HP-SPECTRAL METHODS FOR STRUCTURAL MECHANICS AND FLUID DYNAMICS PROBLEMS

A Dissertation

by

RAKESH RANJAN

Submitted to the Office of Graduate Studies of
Texas A&M University
in partial fulfillment of the requirements for the degree of

DOCTOR OF PHILOSOPHY

May 2010

Major Subject: Mechanical Engineering

HP-SPECTRAL METHODS FOR STRUCTURAL MECHANICS AND FLUID DYNAMICS PROBLEMS

A Dissertation

by

RAKESH RANJAN

Submitted to the Office of Graduate Studies of
Texas A&M University
in partial fulfillment of the requirements for the degree of

DOCTOR OF PHILOSOPHY

Approved by:

Chair of Committee,	Junuthula N. Reddy
Committee Members,	Debjyoti Banerjee
	Theofanis Strouboulis
	Harry Hogan
Head of Department,	Dennis L. ONeal

May 2010

Major Subject: Mechanical Engineering

ABSTRACT

hp-Spectral Methods for Structural Mechanics
and Fluid Dynamics Problems. (May 2010)
Rakesh Ranjan, B.Tech, Indian Institute of Technology, Kharagpur;
M.S., Pennsylvania State University
Chair of Advisory Committee: Dr. Junuthula N. Reddy

We consider the usage of higher order spectral element methods for the solution of problems in structures and fluid mechanics areas. In structures applications we study different beam theories, with mixed and displacement based formulations, consider the analysis of plates subject to external loadings, and large deformation analysis of beams with continuum based formulations. Higher order methods alleviate the problems of locking that have plagued finite element method applications to structures, and they also provide for spectral accuracy of the solutions. For applications in computational fluid dynamics areas, we consider the driven cavity problem with least squares based finite element methods. In the context of higher order methods, efficient techniques need to be devised for the solution of the resulting algebraic systems of equations and we explore the usage of element by element bi-orthogonal conjugate gradient solvers for solving problems effectively, along with domain decomposition algorithms for fluid problems. In the context of least squares finite element methods, we also explore the usage of Multigrid techniques to obtain faster convergence of the the solutions for the problems of interest. Applications of the traditional Lagrange based finite element methods with the Penalty finite element method are presented for modelling porous media flow problems. Finally, we explore applications to some CFD problems namely, the flow past a cylinder and forward facing step.

To my parents in particular my father who completed his Ph.D. a long time back

ACKNOWLEDGMENTS

I would like to take this opportunity to thank my advisor, Dr. J.N.Reddy, for the support that he has extended towards me during the course of this research. I would also like to mention I have appreciated the independence of thought I was able to exercise in the course of my stay here and when I was able to pursue my own interests apart from the main project with which I was involved. Like Dr. J.N. Reddy says "You have your own mind". The fluid mechanics applications of the research were obtained with the help of the supercomputing resources available to the author through the Texas A&M University Supercomputing center and their support of this research is appreciated.

My sincere thanks to my sisters for their constant encouragement and support during my Ph.D. days. I have greatly appreciated their unflinching belief in me and all the encouragement that I have received from them during all these years and some difficult times.

TABLE OF CONTENTS

CHAPTER Page

CHAPTER Page

CHAPTER Page

LIST OF TABLES

TABLE Page

LIST OF FIGURES

FIGURE Page

FIGURE Page

FIGURE Page

CHAPTER I

INTRODUCTION

In the last few decades there is been considerable interest in the h version of finite element methods. In particular the three different methods that advanced in the areas of numerical computations namely, the finite difference, finite element methods, and spectral element methods found fruition in three different decades. Spectral element methods or higher order hp element methods came into existance in the 1970s. Since then there has been huge advances in the spectral element methods community and also both nodal and nodeless methods have been devised for solving problems. In nodal based methods also there are now distinctions between either Legendre based polynomials or the usage of Chebyshev polynomials for the variable approximations. In this work we mainly concern ourselves with the Legendre based polynomials, which are node based.

We have well defined estimates of the errors of the approximations in the lower order finite element or h version finite element setting. These h version finite elements have been applied to solving problems in both structures and computational fluid dynamics, and have met with success in both areas. However, these methods fail to capture the intricacies in the solutions when higher orders of accuracy is desired [1]. In particular in computational fluid dynamics areas where we have many small vortices in the flow field, the accurate resolution requirements that these methods can provide over the lower order elements become indispensable and needs to be properly exploited to obtained highly accurate solutions. In this framework, either the p or hp versions of spectral element methods have been developed. The p and hp versions of finite

---

The journal model is Applied Mathematics and Computation.

elements offer greater accuracy for the solutions of problems.

A. Error estimates

The measure of the accuracy of the formulation lies in the determination of the errors that are obtained when the formulation is used for solving a partial differential equation. As a sample differential equation for determining the errors estimates we consider the Helmholz equation in one dimension. The Helmholz equation is defined as the following;

$$L(u) = \frac{\partial^2 u}{\partial x^2} - \lambda u + f = 0 \tag{1.1}$$

supplemented with the boundary conditions;

$$u(0) = g_D, \quad \frac{\partial u}{\partial x}(l) = g_N \tag{1.2}$$

where we wish to determine the solution of the problem in the interval, $0 < x < l$ which we shall denote by Ω.

1. h-version FEM

Let us define the energy norm of the Helmholz problem as the following;

$$\| u \|_E = \sqrt{a(u,u)} \tag{1.3}$$

Here, $a(u,u)$ is the operator obtained after the integration by parts step in the weak Galerkin finite element approximation of the problem. Carrying out a Taylor series approximation of the error of the finite element approximation which is defined as;

$$e_e\bar{(x)} = u(x) - Iu(x) \tag{1.4}$$

an expression for the h version finite element error can be obtained as follows;

$$\| \epsilon \|_E \leq K_1 C h \tag{1.5}$$

where, C depends on f and λ but is independent of h.

2. p-version FEM

For the p type expansion, with the help of Parsevals identity and the orthogonality of the Legendre polynomials, we obtain the L^2 is bounded by the following;

$$\| \epsilon \|_2 = P^{-k} \| u \|_k \tag{1.6}$$

In the above relationship, $\| u_k \|$ denotes the H^k norm of the function. If $u(k)$ is sufficiently smooth then the above equation tells us that the error decays at the rate, that is faster than any power of P, as $P \rightarrow \inf$. Similarly for the p type expansions the errors in the H^1 norm have been found to decay based on the relationship;

$$\| \epsilon \|_1 = P^{1-k} \| u \|_k \tag{1.7}$$

The proofs for the following prepositions have been carried out in [2].

3. *hp*-version SEM

Again we consider the Helmholz equation on a one dimensional domain Ω. It is assumed that we discretize the domain into equal size elements of size h. In such a case the general error estimate in the energy norm for the h and p type extension is provided by [3];

$$\| \epsilon \|_E = C h^{\mu-1} P^{1-k} \| u \|_k \tag{1.8}$$

where, $\epsilon = u - u^{\delta}$,$\mu = min(k, P+1)$ and C is independent of h,P, and u but depends on k. This shows us that if the polynomial is smooth enough to have bounded (deterministic) derivatives, for $k \geq (P+1)$, then this error estimate shows us that we can achieve exponential convergence as we increase the polynomial order P (p type extension). This is the chief advantage of the usage of higher order hp type expansions for the solutions of partial differential equations and the reason that highly accurate solutions are obtainable with appropriate hp refinements. We show the superior convergence of the errors in the L^2 norms for the linear subcomponents of the problems solved in this work both for the beam theories and the plate theories for which such analytical series solutions exist.

In addition to providing for highly accurate results, in the course of this research it was realized that there is no need to resort to some of the ad-hoc techniques like reduced integration to obtain acceptable results in both structures and computational fluid dynamics (CFD) areas. It should be mentioned here that for CFD applications we are able to equally integrate all the terms because of the usage of least squares finite element methods which circumvent the celebrated Ladyzhenskaya-Babuska-Brezzi (LBB) condition, and not because of usage of higher order spectral element methods. Infact, in CFD applications one of the spectral element methods that is being used is the so called $P_N - P_{N-2}$ element in a Penalty finite element framework.

Apart from the advantages that these methods provide, one of the major drawbacks of the higher order methods lies in the higher order quadrature requirements that are necessary for the evaluation of the stiffness matrices that are obtained with higher order methods. This issue can become specially important when one is concerned with solution of computational fluid dynamics problems, where solutions of the order of millions of equations is routine. To ameliorate some of the disadvan-

tages of the higher order methods for applications to CFD we explore the usage of faster and more efficient solution techniques for the routine solutions of anywhere between 0.2 to 0.50 million equations. In this context we explore the parallel implementations of Domain Decomposition, Element by Element Bi-orthogonal Conjugate Gradient (EBE-BJCG), and Multigrid techniques for solutions of huge linear systems of equations.

CHAPTER II

HP-SPECTRAL METHODS APPLIED TO BEAM THEORIES

A. Introduction

Beams as structural members are of interest in many engineering applications. Some of the applications include pile foundations, spread footings supported on groups of piles, and in structural frames common in a variety of structures. Three different kinematic theories have been used to study beams, namely, the Euler-Bernoulli theory (EBT), the Timoshenko beam theory (TBT), and Reddy third-order shear deformation theory (RBT). A number of different finite element models of these theories have been developed using traditional finite element interpolations. Various finite element models of beams differ from each other in the choice of the interpolation functions used for the transverse deflection w, total rotation ϕ and/or shear strain γ_{xz}, or in the integral (or weak) form used to develop the finite element model [4]. The TBT and RBT are known to exhibit shear locking when using equal-order lower-order interpolation of the generalized displacements w and ϕ. The locking is due to the inconsistency of the interpolation used for w and ϕ. Often reduced-order integration to evaluate the stiffness coefficients associated with the transverse shear strain is used as a means to remove locking. The reduced integration beam elements are known to exhibit spurious energy modes. Others have used so- called consistent interpolation based on the recovery of correct constraints in the thick beam limit [5]. Although such elements do not experience locking, they did not lead to the two-node superconvergent element developed by Reddy [6], who used the Hermite cubic interpolation of w and interdependent quadratic interpolation of ϕ in developing the element. The conventional reduced integration Timoshenko elements as well as consistent interpo-

lated quadratic elements fail to capture the true behaviour of such members unless two or more elements per a structural member are used.

While the displacement-based models for the Timoshenko beam theory (TBT) admit the use of C0 expansions, the use of Euler Bernoulli beam theory (EBT) requires the use of C1-continuous expansions. The mixed formulation in which the stress resultants are incorporated into the fundamental governing equations for the Euler-Bernoulli beam theory does admit the use of C0 expansions, which naturally lends itself to spectral accuracy with the help of *hp*-spectral element methods due to reduced continuity requirements. The TBT, on the other hand, allows the use of C0 approximations for the displacement based formulations. In the thin beam limit, the TBT model should give the same results as the EBT. However, due to the use of equal lower-order approximations for the displacements and rotations, the element fails to realize the thin beam limit and thus experiences shear locking.

Most studies in literature make use of the equispaced Lagrange higher-order expansions for studying the bending response of plates and the same can be extended in one-dimension to study the bending behaviour of TBT. The equispaced Lagrange interpolation suffers from severe ill-conditioning and for high values of the polynomial degree p [1]. At high *p*-levels the discrete problem suffers from a very high condition number of the stiffness matrix and the problem exhibits poor convergence behaviour. Very strong preconditioners are recommended in some cases to parse the discrete problem at such high *p*-levels but the convergence is problem dependent and also dependent on the regularity of the mesh. There has been increased interest in the past decade on using orthogonality of Legendre polynomials to better predict the response of beams when subject to dynamic loadings. Some of the work by P.Z.B-Yoseph [7] is in that area. In their analysis a space-time spectral element method is employed to solve a simply supported Euler-Bernoulli beam undergoing forced lateral

vibrations. The realization by P.Z.B-Yoseph [7] is in the temporal approximation of the dynamics of the beam which is approximated with a spectral space-time mesh rather than a modification of the Taylor series approximations which forms the basis for the other conditionally stable schemes.

It was discovered in the 1980s that the choice of higher-order shape functions has a dramatic effect on the conditioning of the discrete problem. Since then, significant amount of work has been devoted to the improvement of higher-order finite elements or p-version FEM. The search for optimality continues till today [8]. Thus, when higher-order shape functions are used in the finite element method, it is common to examine the condition numbers of the coefficient matrix generated [9]. Condition numbers close to one represent a well-conditioned system where as large condition numbers indicate a poorly conditioned system of equations which is likely to lead to numerical errors in the solution process. The usual definition of the condition number is being used in the present context, that is the $\kappa(.) = \frac{\lambda_{max}(.)}{\lambda_{min}(.)}$.

The spectral/hp based nodal expansions which is based on the Legendre polynomials provide discrete orthogonality and the condition number for the mass matrix of the equispaced expansions grows as 10^p for higher values of p where as the condition number for the Legendre based expansions grows as $O(p)$ [1]. The superior conditioning of both the mass and stiffness matrices produced with the Gauss-Lobatto-Legendre shape functions has been demonstrated in Maitre et al. [9]. The paper by Maitre et al. [9] provides the condition numbers of the Legendre based expansions to a polynomial order of 30 in 2-dimensions and 9 in three dimensions. The above arguments exhibit the fact that equi-spaced Lagrange p-version finite element suffer from strong linear dependence of the solution and special solution techniques have to be used to address the problem unless one contends with spurious results from the discrete model, reasonable solutions to certain problems only under very special

circumstances, or ad-hoc approaches that ameliorate solver breakdowns.

Another issue with finite element formulations for beams, is that it presents computational difficulties when the length-to-thickness ratio of the beam (a/h) is large (i.e. when modelling long beams). A strong stiffening of the element matrices occurs, resulting in spurious shear stress predictions and erroneous results for the generalized displacements [10]. This phenomenon is known as shear-locking. Shear locking develops in formulations which cannot represent a state of zero-shear in the thin beam limit independent of the mesh. This is exhibited as a violation of the Kirchhoff assumption in the thin beam theory, stated as $w_x - \theta$=0. When the beam is thin most of the energy of deformation is due to bending. If a formulation does not admit non-trivial zero shear solutions, then most of the energy of deformation goes into shear deformation, resulting in very little bending–hence locking. This can be seen from the variational form; since the coefficient of the bending term is of the order $O(t^3)$ and the coefficient of the shear term is of the order of $O(t)$, the latter becomes much larger as t approaches zero [10].

This problem is commonly treated by reduced integration techniques, although other remedies may be found [11]-[12]. Shear locking is evident in the Ritz-Galerkin displacement based finite element models with equal-order interpolation of all generalized displacements. The phenomenon is more predominant when the length-to-thickness ratio of the beam is high. Higher-order elements have been explored in literature to be alleviating shear locking phenomenon but they have been mostly been equi-spaced Lagrange based so far. The use of spectral/hp nodal expansions was explored by Pontaza [13] while analyzing plates for both the classical plate theory and FSDT with the least squares finite element formulation however, only a linear analysis was performed and the referenced work is an application to the bending of different beam theories.

The aforementioned reasons compel the use of spectral/hp element refinements as a viable and a robust alternative to studying the bending behaviour of beams which provide spectrally accurate results and at the same time alleviate the perennial problems of locking associated with lower order finite element methods. In this paper the issue of locking has been addressed two different ways, the first is the use of hp-spectral methods within the framework of displacement based formulations, and the second method is the use of mixed formulations. Mixed formulations also do not require the use of reduced integration techniques to solve for the problems studied. The motivation for this study comes from the many advantages that are associated with hp-higher order elements; spectral convergence (accuracy) of the solutions, the removal of locking issues, and the orthogonality property of the nodal expansions which provide excellent results with standard solvers like scaled Gaussian elimination with partial pivoting, alleviating the problem of ill-conditioning of the discrete problem ascribed to the usage of higher-order equi-spaced Langrange based interpolants. For the mixed formulation the Gaussian Elimination with scaled partial pivoting was implemented and was found to work better than the conjugate gradient solver. Different a/h ratios are explored and with appropriate hp-refinements full integration is found to provide consistently good agreement with published results for both linear and non-linear analysis.

B. Literature Review

Urthaler et al. [14] explored the use of mixed formulations for the laminate composite plate analysis based on the first order shear deformation theory (FSDT). They also checked their solutions obtained with the reduced integration techniques with the Navier solutions for the plate problem for the FSDT. It was reported that the mixed

formulations were superior to the displacement based formulations for the prediction of accurate stress resultants and, thus moments and shear forces were incorporated as primary variables in the formulation. In this paper we explore both mixed and the displacement based finite element formulations in the context of *hp*-spectral methods as applied to the bending analysis of beams. A comprehensive review of the different beam theories can be found in Reddy's work [6], where both local and non-local theories for bending of beams are explored. Also, in the document explicit analytical expressions were derived for the linear analysis of both local and non-local theories for the Euler-Bernoulli beam theory, Timoshenko beam theory, Reddy beam theory, and the Levinson beam theories. The evaluation of the deflections and the slopes of the different beam theories are derived based on the Fourier series expansions of each of the terms of the governing differential equation. The analysis by Fourier expansions is based on the fact the Fourier series captures the inherent waves in any system and provided the boundary conditions are being met with the Fourier expansions, the series solutions provide a uniform framework for solving linear partial differential equations across disciplines, subject to simplified boundary conditions. Such an expansion has been used in this document from the above reference to verify the spectral convergence of the EBT and TBT results obtained with that obtained from the series solution. The basic idea is the Fourier expansions converge point wise to any solution of a differential equation to a prescribed tolerance provided the boundary conditions are satisfied. Further details on the series solution will be provided later.

Asta et al [15] have carried out the bending analysis of composite beams, with displacement and mixed elements. A non-linear analysis was performed. The composite beam was considered as made of steel and concrete, where the steel behaviour is typically modelled as elastic-perfectly plastic, where as the concrete material be-

haviour was characterized as non-linear with compressive loads. Reinforcement in the concrete is also characterized to have steel behaviour, even though some interaction effects due to the presence of concrete bonding at the edges can change some of the properties of the composite. In the paper they condensed out the stress and the strain fields because these can be inter-element discontinuous. Numerical tests were carried out on two-span continuous beams which is often the model for design of bridge structures, with simply supported (hinged-pinned) boundary conditions on either sides.

Finite element analysis for a Timoshenko beam subjected to a moving mass was carried out by Lou et al [16]. Dynamic analysis of a Timoshenko beam subjected to a moving mass is of interest because it can study the bending characteristics of a train moving over the rails, design of bridges, and study of milling processes. The second order hyperbolic equation obtained during the formulation part was solved with the Wilson theta method. The main assumption in the analysis was that the beam remains in constant contact with the moving mass which is a reasonable assumption to make for the problems of interest in this area. The external force on the Timoshenko beam was considered due to the moving mass. The effect of damping on the behaviour of the response was neglected. The force components that are obtained from the model due to the moving loads change with the location of the mass that is moving over the beam. Good agreement with the results published in literature were reported.

Edem [17] explored Timoshenko beam finite element models with analytical bending and shear rotation interdependent shape functions. In the paper the exact locking free two-noded Timoshenko beam finite element was formulated. An analytical expression between the bending and a proposed shear rotation was established. In contrast to the Timoshenko beam equations where these two effects are coupled the decoupling causes the locking phenomenon to disappear. Reddy explored the super-

convergent element in [18]. The element provided yields the exact nodal deflections in static analysis for any distribution of the transverse load $q(x)$ and element-wise constant bending stiffness EI and shear stiffness GAKs. They explored the assumed strain-displacement models (ASD) in which the variational form contains the displacements and strains as independent variables. Explicit expressions for the element stiffness matrices for the Timoshenko beam element were provided for different elements i.e. reduced integration element, interdependent interpolation element, and the consistent interpolation element etc. An implicit expression was also obtained for determining the natural frequency of the Timoshenko beams, the solutions of which were checked with the results from the finite element model, and close agreement between both were reported for all cases analysed.

Mixed finite element formulation for Reissner-Mindlin plates when subjected to different types of loads, were explored by Eratll et al. [19]. Different types of boundary conditions were explored, namely the clamped clamped, and simply supported boundary conditions. Also different types of loading were explored, namely, uniform load, concentrated load at the center etc. The elasticity solutions obtained were checked with the finite element results and good agreement was reported. The enforcement of the boundary condition was done both in a strong sense and also for some cases the boundary conditions were enforced with the Lagrange multiplier method into the functional itself, which is also a weak imposition of the boundary condition. The second technique for enforcing boundary condition was found to be more accurate as the information from the contributions from the adjoining elements is not destroyed, and the results are more accurate, it is proposed. A closed form solution to the Reissner plate was obtained using the field equation of three-dimensional elasticity.

A unified finite element model based on the classical and shear deformation theory has been presented in Reddy et al [5]. The three main theories, the EBT,

TBT and RBT are incorporated into one finite element model. Depending upon the choice of the element type the general stiffness matrix can be specialized into any of the three different theories by merely assigning the proper values to the parameters that were used in the development. The element did not experience shear locking and gave exact generalized nodal displacements for Euler-Bernoulli and Timoshenko beam theories when the beam is homogeneous and has constant material property values. A locking-free shear deformation beam finite element is also presented in Reddy [6]. A review of the different finite element models for the three theories have also been presented separately. Exact polynomial solutions to the different theories have also been presented, for the simply supported and the cantilever beams.

Hierarchical finite element analysis of vibration of membranes was carried out by Houmat [20]. Legendre based orthogonal polynomials were used for modelling the membrane. A single finite element with appropriate p-refinement inside the single element was used for the analysis and thus the satisfaction of the C0 continuity at the internal nodes was avoided completely. The values of the integrals were evaluated and saved in a table lookup which was used repeatedly for which ever terms that were needed to be obtained. Highly accurate results were obtained with the hierarchical Legendre based polynomials that were used, and fifth decimal accuracy with analytical solutions was achieved. Based on their analysis and the cited advantages of the hierarchical finite elements that were used by the authors they reported that the p-version of FEM always converges from above to the exact values as the number of hierarchical terms in the expansion are increased and highly accurate results are obtained with very few hierarchical terms.

Houmat [21] have also explored the use of hierarchical trigonometric based shape functions for studying plate vibrations. They developed a new finite element which was formulated based on a number of fixed quintic polynomial shape functions plus

a variable number of trigonometric hierarchical shape functions. The procedure for deriving the shape functions for the problem were also outlined and trigonometric hierarchical functions were derived based on the steps outlined herein. The table look up procedure for the generation of the stiffness matrices was also done in this paper. The specification of the different sets of boundary conditions that were tested for the analysis of the plates followed the traditional *Leissa's* convention.

A new hierarchical finite element basis for the triangular and tetrahedral elements has been proposed by Adjerid [22]. The stiffness matrices that are generated in the document were found to have better conditioning than existing literature. It is mentioned that better conditioning of the stiffness matrices that are obtained for the case of the rectangular and linear domains benefit from the tensorial nature of the same in two dimensions and the orthogonality within the one-dimensional framework. If the hierarchical shape functions are non-tensorial then the conditioning of the stiffness matrices that are produced from the formulation can grow exponentially with the polynomial order making it no better than traditional equi-spaced Lagrange based higher order expansions. To alleviate this problem they have proposed a new set of hierarchical shape functions for triangles and tetrahedron which lead to better conditioned matrices. It is of some value to note that they identified the problem with worse conditioning to be due to the interaction of the face and region shape functions with themselves and each other. In the same context Beslin [23] advocate the use of trigonometric shape functions as opposed to the Legendre based interpolants. Amongst the reasons that they cite the complex high numeric dynamics of the Legendre based polynomials which become unfeasible to be used beyond a p_{value} of 46, where as the trigonometric hierarchical functions that have been used were demonstrated to be predicting correctly the high order plate vibration modes upto to p_{values} of 2048 with possible extensions to this limitation. Amongst the cited advan-

tages of the trigonometric shape functions are computations of the stiffness matrices can be computed exactly, and are easy to compute, and the better numeric dynamics of the trigonometric shape functions which allow one to use extremely high value of p_{levels} where as the Legendre based polynomials are limited to a maximum value of 46 as pointed out by the authors. The trigonometric shape functions of order P_m^s ensure a derivative continuity of C^{s-1}. Another point to note, was the fact that the Legendre polynomials offer a homogeneous resolution over the entire domain, where as the Legendre polynomials present a higher resolution near the boundaries of the domain, and a poor resolution in the center of the domain. This point however can be addressed with an appropriate h-refinement where a better resolution is desired.

Numerical implementation of hybrid-mixed formulation for Reissner-Mindlin plate is presented in Pereira [24]. They independently approximated the stress resultants and the mid-surface displacements in the domain, and the displacements on the boundary of the plate using Legendre polynomials. Because of the orthogonality of the functions in an integral sense the resulting finite element matrices are mentioned to be sparse which was effectively parsed with a sparse matrix solver. Based on the above cited literature different avenues for alleviating problems that beset beam theories have been proposed and implemented, by introducing new variables in the formulation, to eliminate shear locking problems.

The use of higher order equi-spaced, Lagrange based polynomials for alleviating the locking problem has been demonstrated for plates, in two dimensions with Lagrange based finite element methods. Even if higher order equi-spaced Lagrange interpolation functions are used for predicting the behaviour of the beam elements, the higher order Lagrange polynomials yield matrices that are severely ill-conditioned and special techniques have to be resorted to, to solve the discrete problem. It is the objective of this chapter to advocate the use of appropriate hp-spectral element

method in studying the Euler-Bernoulli and Timoshenko beam theories, both with the mixed and displacement based finite element formulations.

C. Governing Equations

The governing equations for the two beam theories have been outlined in this section, the first the equation for the Euler-Bernoulli beam theory are outlined, followed by the equations for the Timoshenko beam theory. The EBT theory is based on the assumption that a straight line transverse to the axis of the beam remains straight, inextensible, and normal to the mid-plane after deformation. These assumptions amount to neglecting the Poisson effect and the transverse strains. The displacement field for beams with moderately large rotations but with small strains can be derived using the displacement field;

$$\begin{aligned} u(x) &= u(x)_0 - z\frac{\partial \omega_0}{\partial x} \\ u_2 &= 0 \\ u_3 &= w_0(x) \end{aligned} \tag{2.1}$$

where, u1,u2,u3 , denote the total displacements along the coordinate directions (x,y,z) and u_0 and w_0 denote the axial and transverse displacements of a point on the neutral axis.

The non-linearity for beam bending figures into the equation in the form of non-linear strain displacement relationships. The sum on the repeated indices is implied.

$$\epsilon_{ij} = \frac{1}{2}\left(\frac{\partial u_i}{\partial x_j} + \frac{\partial u_j}{\partial x_i}\right) + \frac{1}{2}\left(\frac{\partial u_m}{\partial x_i}\frac{\partial u_m}{\partial x_j}\right) \tag{2.2}$$

Omitting the large strain terms but retaining only the square of $\frac{\partial u_3}{\partial x}$ (which represents the rotation of the transverse normal line in the beam), one obtains the Von-Karman

non-linear strain relations.

The Euler-Lagrange equations for the EBT can be derived based on the principle of virtual work or the equilibrium of the forces and moments on a beam section. The virtual work statement for the EBT problem is equivalent to the weak form for the governing differential equations. For details on the virtual work principle the reader is referred to Reddy [11]- [25]. Based on the virtual work principle and separating the virtual displacements we obtain the Euler-Lagrange equations for the EBT as follows:

$$\frac{\partial N_{xx}}{\partial x} + f_x = 0 \tag{2.3}$$

$$\frac{\partial V_{xx}}{\partial x} + q_x = 0 \tag{2.4}$$

$$\frac{\partial M_{xx}}{\partial x} - V + N_{xx}\frac{\partial \omega_0}{\partial x} = 0 \tag{2.5}$$

where, N_{xx} is the axial force measured per unit length, and M_{xx} is the moment measured per unit length. The variables in the equations are defined as follows:

$$N_{xx} = \int_A \sigma_{xx} dA \tag{2.6}$$

$$M_{xx} = \int_A \sigma_{xx} z dA \tag{2.7}$$

And, it should be noted that V is the shear force acting perpendicular to the x-axis and is not the shear force Q(x) acting on a section perpendicular to the deformed beam. In fact, one can show $V = Q - N_{xx}\frac{\partial \omega}{\partial x}$.

Assuming a linearly elastic material the relationship between the shear stress and the strains can be qualified as:

$$N_{xx} = A_{xx}\Big[\frac{\partial u_0}{\partial x} + \frac{1}{2}\Big(\frac{\partial \omega_0}{\partial x}\Big)^2\Big] - B_{xx}\frac{\partial^2 \omega_0}{\partial x^2} \tag{2.8}$$

$$M_{xx} = B_{xx}\Big[\frac{\partial u_0}{\partial x} + \frac{1}{2}\Big(\frac{\partial \omega_0}{\partial x}\Big)^2\Big] - D_{xx}\frac{\partial^2 \omega_0}{\partial x^2} \tag{2.9}$$

In the above, equations;

$$(A_{xx}, B_{xx}, D_{xx}) = \int_A E^e(1, z, z^2)dA \tag{2.10}$$

For a constant crossectional area beam the B_{xx} is typically zero and since we are dealing with regular shaped beams, this value will be considered null.

The Timoshenko beam theory relaxes the normality restriction on the beam as imposed by the Euler-Bernoulli beam theory and allows for arbitrary but constant rotations of the transverse normals [11]. The displacement field of the Timoshenko beam theory can be expressed in the form:

$$u(x, y, z) = u(x) + z\phi_x(x), \quad w(x, y, z) = w_0(x) \tag{2.11}$$

where u_0 is the axial displacement, w_0 the transverse deflection, and ϕ_x is the rotation of a transverse normal about the y axis. The governing equations of the Timoshenko beam theories are outlined below;

$$\frac{\partial N_{xx}}{\partial x} + f_x = 0 \tag{2.12}$$

$$\frac{\partial M_{xx}}{\partial x} - Q_x = 0 \tag{2.13}$$

$$\frac{\partial Q_x}{\partial x} + \frac{\partial}{\partial x}(N_{xx}\frac{\partial w_0}{\partial x}) + q = 0 \tag{2.14}$$

In the above equations N_{xx} is the force per unit length and M_{xx} is the moment per unit length. The variables have been defined earlier, for the EBT, and only new

term that needs to be defined is the Q_x which is being mentioned below;

$$Q_x = K_s \int_A \sigma_{xx} dA \tag{2.15}$$

Here, K_s is the shear correction coefficient that is introduced to account for the parabolic distribution of the transverse shear stress which is not accounted for in the TBT which assumes a constant state of shear. The value of K_s was taken as 5/6 as is the norm. Assuming a linearly elastic material the relationship between the shear stress and the strains have been written out earlier and the new variable that needs to be defined is outlined below as follows;

$$Q_x = S_{xx}\Big(\frac{\partial w_0}{\partial x} + \phi_x\Big) \tag{2.16}$$

S_{xx} is defined as the following;

$$S_{xx} = \int_A G K_s dA = K_x G A \tag{2.17}$$

When the x-axis is taken along the centroidal axis, B_{xx} is zero.

The non-linearity in both theories comes from the Von-Karman non-linear strains as a form of geometric non-linearity in the equations as shown above. The above equations describe the bending response of TBT. Shear modulus for the isotropic beam is given by the following formula:

$$G = \frac{E}{2(1+\nu)} \tag{2.18}$$

where, ν is Poisson ratio for the isotropic beam under consideration.

1. Mixed Model I (EBT)

The governing equations of the Euler-Bernoulli beam theory equations that have been presented above can be manipulated appropriately to obtain different mixed

formulations models that consequently lead to different finite element formulations. The first mixed model we consider is the one in which the shear force is eliminated as a primary variable by substitution of the definition of shear force V into the first order differential equation describing the equilibrium of the shear forces with the externally applied loads. The governing differential equations presented above are modified thus;

$$\frac{\partial N_{xx}}{\partial x} + f_x = 0 \tag{2.19}$$

$$\frac{\partial}{\partial x}\Big[\frac{\partial M_{xx}}{\partial x} + N_{xx}\frac{\partial \omega_0}{\partial x}\Big] + q_x = 0 \tag{2.20}$$

$$N_{xx} = EA\Big[\frac{\partial u_0}{\partial x} + \frac{1}{2}\Big(\frac{\partial \omega_0}{\partial x}\Big)^2\Big] \tag{2.21}$$

$$M_{xx} = -EI\frac{\partial^2 \omega_0}{\partial x^2} \tag{2.22}$$

The primary (PV) and the secondary variables (SV) for the EBT include the specification of either the displacements or the forces on the model as follows: PV:

$$u_0,\ w_0,\ \frac{\partial \omega_0}{\partial x} \tag{2.23}$$

SV:

$$N_{xx},\ V_x,\ M_{xx} \tag{2.24}$$

The above classification of the primary and secondary variables is instructive in determining the appropriate boundary conditions that should be applicable. Although, the deflection and the derivative of the deflection have been mentioned as the primary variables it should be noted that since we are not dealing with a displacement based formulation the formulation admits C^0 continuity as minimially confirming. The non-linearity in the first-order shear deformation theory comes from the Von-Karman non-linear strains as a form of geometric non-linearity in the equations as mentioned above.

Based on the equations that were presented above the shear force is absorbed into the formulation and there are four variables per node, for this mixed model, namely axial displacement u_x, the deflection w_x, the shear force N_{xx}, and the moment M_{xx}.

2. Mixed Model II (EBT)

The governing equations of the Euler-Bernoulli beam theory equations that have been presented above can be manipulated appropriately to obtain different mixed formulations that consequently lead to different finite element formulations. For the second mixed model that was considered for analysis, the equations are left in their primitive forms with no substitutions and the resulting formulation has six degrees of freedom per node. The governing differential equations presented above are modified thus (repeated for clarity);

$$\frac{\partial N_{xx}}{\partial x} + f_x = 0 \tag{2.25}$$

$$\frac{\partial V_x}{\partial x} + q(x) = 0 \tag{2.26}$$

$$V_x - \frac{\partial M_{xx}}{\partial x} - N_{xx}\left(\frac{\partial \omega_0}{\partial x}\right) = 0 \tag{2.27}$$

$$N_{xx} = EA\left[\frac{\partial u_0}{\partial x} + \frac{1}{2}\left(\frac{\partial \omega_0}{\partial x}\right)^2\right] \tag{2.28}$$

$$M_{xx} = -EI\frac{\partial^2 \omega_0}{\partial x^2} \tag{2.29}$$

The primary and secondary variables have already been defined earlier. The finite element formulation starts from these governing equations and the standard weak form Galerkin finite element formulation is obtained with the multiplication of the above with a weight function so that the equations are left with six degrees of freedom per node in the stiffness matrix for this system of equations.

3. Displacement Based Formulation (TBT)

Displacement based formula seeks to find the solution of the following equations, with all equations expressed in terms of the displacements, which after some substitutions on the above equations yields, the following set of coupled non-linear equations that define the displacement based TBT theory:

$$-\frac{\partial}{\partial x}\Big\{A_{xx}\Big[\frac{\partial u_0}{\partial x}+\frac{1}{2}\Big(\frac{\partial w_0}{\partial x}\Big)^2\Big]\Big\}=f \tag{2.30}$$

$$-\frac{\partial}{\partial x}\Big[S_{xx}\Big(\frac{\partial w_0}{\partial x}+\phi_x\Big)\Big]-\frac{\partial}{\partial x}\Big\{A_{xx}\frac{\partial w_0}{\partial x}\Big[\frac{\partial u_0}{\partial x}+\frac{1}{2}\Big(\frac{\partial w_0}{\partial x}\Big)^2\Big]\Big\}=q \tag{2.31}$$

$$-\frac{\partial}{\partial x}\Big(D_{xx}\frac{\partial \phi_x}{\partial x}\Big)+S_{xx}\Big(\frac{\partial w_0}{\partial x}+\phi_x\Big)=0 \tag{2.32}$$

The primary (PV) and the secondary variables (SV) include the specification of either the displacements or the forces on the model as follows:

PV:

$$u_0,\ w_0,\ \phi_x \tag{2.33}$$

SV:

$$N_{xx},\ Q_x,\ M_{xx} \tag{2.34}$$

The non-linearity in the TBT comes from the Von-Kármán non-linear strains as a form of geometric non-linearity in the equations as shown above. The above equations describe the bending response of TBT, where, ν is Poisson ratio for the isotropic beam under consideration.

4. Mixed Formulation (TBT)

The mixed formulation for the Timoshenko beam theory starts with the same equations as the displacement based formulations but the equations are kept in primitive variables as they appear in the equations with no substitutions to bring every equa-

tion in terms of the displacements. The main equations for the variables that enter the finite element formulation are being (repeated here) for clarity.

$$\frac{\partial N_{xx}}{\partial x} + f_x = 0 \tag{2.35}$$

$$\frac{\partial M_{xx}}{\partial x} - Q_x = 0 \tag{2.36}$$

$$\frac{\partial Q_x}{\partial x} + \frac{\partial}{\partial x}(N_{xx}\frac{\partial w_0}{\partial x}) + q = 0 \tag{2.37}$$

$$N_{xx} = EA\ [\frac{\partial u_0}{\partial x} + \frac{1}{2}(\frac{\partial w_0}{\partial x})^2] \tag{2.38}$$

$$M_{xx} = EI\ \frac{\partial \phi_x}{\partial x} \tag{2.39}$$

$$Q_x = K_s GA\Big(\frac{\partial w_0}{\partial x} + \phi_x\Big) \tag{2.40}$$

The derivation of the weak form for the above set of equations follows the standard step of integration by parts after multiplying these equations with a weight function. The above procedure provides the stiffness matrices for the non linear problem with the appropriate substitutions of the weight functions.

D. Spectral/*hp* Finite Element Formulation

The Ritz-Galerkin finite element model development follows reduction of the residuals for the governing differential equations in the weighted residual sense. The mixed model involves the solution of six degrees of freedom per node, namely, the axial displacement (u), the deflection of the beam w, the slope ϕ_x, along with N_{xx}, Q_x, and M_{xx}. At the end of the weak form development the finite element model for each variable is determined and is obtained from the weak finite element formulation. The weak formulation development of the governing equations presented earlier for the Timoshenko beam and Euler-Bernoulli beam theories are standard along with derivation of the tangent stiffness matrix coefficients.

The spectral finite element approximation is stated as follows, the primary variables are each approximated as;

$$\Delta^e = \sum_{j=1}^{n} \Delta_j \psi_j \tag{2.41}$$

where,ψ_j are the nodal expansions, which are provided by the following one-dimensional C^0 spectral nodal basis [1];

$$\psi_i(\xi) = h_i^e(\xi) = \frac{(\xi-1)(\xi+1)L_n'(\xi)}{n(n+1)L_n(\xi_i)(\xi-\xi_i)} \tag{2.42}$$

where, Δ_j are the nodal values due to the Kronecker delta property of the spectral basis. $L_n = P_n{}^{(0,0)}$ is the Legendre polynomial of order p, and ξ_i denotes the location of the roots of $(\xi-1)(\xi+1)L_n'(\xi) = 0$ in the interval $[-1,+1]$. All Jacobi polynomials, $P_n^{\alpha,\beta}$, satisfy a three-term recurrence relation of the form:

$$xP_n^{\alpha,\beta}(x) = a_{n-1,n}^{\alpha,\beta} P_{n-1}^{\alpha,\beta}(x) + a_{n,n}^{\alpha,\beta} P_n^{\alpha,\beta}(x) + a_{n+1,n}^{\alpha,\beta} P_{n+1}^{\alpha,\beta}(x) \tag{2.43}$$

where, $a^{\alpha,\beta}$ only depends on α, β, and n. And the derivatives of Jacobi polynomials satisfy a three-term recurrence relation of the form [26];

$$(1-x^2)\frac{dP_n^{\alpha,\beta}}{dx} = c_{n-1,n}^{\alpha,\beta} P_{n-1}^{\alpha,\beta}(x) + + c_{n+1,n}^{\alpha,\beta} P_{n+1}^{\alpha,\beta}(x) \tag{2.44}$$

For the special case of $\alpha = \beta$=1;

$$xP_n(x) = a_1(n)P_{n-1}(x) + a_2 P_{n+1}(x) \tag{2.45}$$

where,

$$a_1(n) = \frac{n+1}{2n+3} \tag{2.46}$$

and,

$$a_2(n) = \frac{(n+1)(n+3)}{(n+2)(2n+3)} \tag{2.47}$$

For α=β=1, $c_{n,n}^{\alpha,\beta}$=0 and the above equation can be written as;

$$(1-x^2)\frac{dP_n^{\alpha,\beta}}{dx} = c_{n-1,n}^{\alpha,\beta}P_{n-1}^{\alpha,\beta}(x) + c_{n+1,n}^{\alpha,\beta}P_{n+1}^{\alpha,\beta}(x) \tag{2.48}$$

Seeking the recurrance relation for the derivative, we rewrite the above equation by dropping α and β, for the special case of $\alpha = \beta$=1;

$$(1-x^2)\frac{dP_n}{dx} = c_1(n)P_{n-1}(x) + c_2P_{n+1}(x) \tag{2.49}$$

where,

$$c_1(n) = \frac{(n+1)(n+3)}{2n+3} \tag{2.50}$$

and,

$$c_2(n) = \frac{(2n)(n+1)(n+3)}{(2n+3)(2n+4)} \tag{2.51}$$

For an illustration of the proofs of these above mentioned equalities see Osilenker [26].

E. Linearisation

Linearisation can be accomplished with either of two techniques, namely the Picard (direct iteration procedure) and the Newton-Raphson's method. For checking the convergence behaviour of both the methods of linearisation with *hp*-spectral methods both of these were implemented. There was however, no difference found between the results of either of the two methods for most cases and thus only results based on the Newton-Raphson's method will be presented. For all structural problems Newton's method yields a symmetric positive definite matrix system. The mixed model was solved with Gaussian elimination with scaled partial pivoting. Some of the celebrated advantages of the Newton-Raphson's method are a faster convergence rate, since we are using incremental loadsteps for the runs, Newton's method does not noticeably outperform the Picard method of linearisation in *most* cases. The

Picard method faced some convergence issues for the pinned-pinned case for the mixed formulations and failed to converge. The linearised problem with the Newton's method is represented as follows:

$$[\hat{K^e}(\{\Delta^e\}^r)]^{tan}\{\delta\Delta\}^e = -\{R^e\}^r \tag{2.52}$$

The non-linear convergence was declared when L^2 norm of the incremental vector normalized with the norm of the solution vector was less than 10^{-03} for the spectral element method model. In the next section we present the results that we obtained for the linear and non-linear problems that were studied with different types of boundary conditions and also verify the spectral convergence of the solutions in the energy norm (L^2 norm).

F. Boundary Conditions

The specification of the boundary condition for the beam problem can be done based on a number of different ways in which the beam is supported. The different boundary conditions that were examined were the clamped-clamped, pinned-pinned, and the hinged-hinged case. The clamped-clamped case means that at the ends, the specification of the following variables are zero;

$$u = \omega_0 = \frac{\partial \omega_0}{\partial x} = 0 \tag{2.53}$$

The pinned-pinned case requires the specification of the following variables to be zero;

$$u = \omega_0 = 0 \tag{2.54}$$

Also, the specification of the third variable comes from the specification of the end moment, which is zero for the case that the ends are not subject to any external

moments. Finally, the hinged-hinged case involves the specification of the following variables,

$$\omega_0 = 0 \tag{2.55}$$

Also, the different a/h ratios were explored for both the models, subject to different boundary conditions and the results are discussed in the following section.

G. Numerical Results

The TBT beam was solved with the displacement based formulation and the mixed formulations whereas the EBT beam was solved with both mixed finite element formulations. The results that were obtained for both the formulations are presented here. The main differences in the displacement based and the mixed formulation that was found was in the convergence characteristics of the problem. While the displacement based formulation was found to be a better alternative for the solution of the system with iterative solvers, the mixed formulation was found to cause convergence issues with the conjugate gradient solver. The mixed formulation also has zeros along the diagonal, and thus the convergence of the mixed formulation with any variant of Gauss-Seidel iterative solver is pre-empted. However, Gauss- Elimination was found to work well with the mixed formulation with scaled partial pivoting. Amongst the advantages of the mixed formulation are better representation of the secondary variables which are more accurate as they are directly solved for in the formulation, rather than derived quantities with the displacement based formulations. Both linear and non-linear analyses were performed.

1. Linear Series Solutions

Analytical solutions for the Timoshenko beam theory as also the first order shear deformation theory of plates exist in terms of the Navier solutions in two dimensions. For a complete description of the Navier equations the reader is referred to Reddy [18]. The linear solution that corresponds to the solution of the Euler-Bernoulli Beam Theory and Timoshenko beam theory are presented below. The solution to the problem can be expressed in terms of an infinite series which can be extended to any desired level of accuracy with the help of inclusion of an appropriate number of terms in the infinite expansion. The boundary conditions of simply supported beams are expressed as [11]: w=0 and, M=0, at $x = [0, L]$.

The following expressions of the generalized displacements ω, and ϕ_x satisfy the boundary conditions for the EBT;

$$w(x,t) = \sum_{n=1}^{\infty} W_n sin(\frac{n\pi x}{L}) e^{i\omega_n t} \tag{2.56}$$

and,

$$\phi(x,t) = \sum_{n=1}^{\infty} \phi_n cos(\frac{n\pi x}{L}) e^{i\omega_n t} \tag{2.57}$$

The term ϕ_x has the meaning of derivative of the deflection at that location for the Euler-Bernoulli beam theory whereas the Timoshenko beam theory admits an independent slope which gets added to the transverse shear term to generate the total slope of the beam. For static bending, we set all the time derivatives to zero and take the distributed load to be of the form;

$$\begin{aligned} q(x) &= \sum_{n=1}^{\infty} Q_n sin(\frac{n\pi x}{L}) \\ Q_n &= \frac{2}{L} \int_0^L q(x) sin(\frac{n\pi x}{L}) \end{aligned} \tag{2.58}$$

The coefficients Q_n associated with uniform load is obtained as follows $q(x) = \ q_0$;

$$Q_n = \frac{4q_0}{n\pi} \tag{2.59}$$

Substituting the expansions for ω, ϕ, and q into the governing differential equations for the Euler-Bernoulli beam theory we obtain the following expressions for the deflection and slope for the Euler-Bernoulli beam undergoing linear bending deformations;

$$w(x)^T = \sum_{n=1}^{\infty} \lambda_n \frac{Q_n L^4}{n^4 \pi^4 EI} \ sin(\frac{n\pi x}{L}) \tag{2.60}$$

and,

$$\phi(x)^T = -\sum_{n=1}^{\infty} \lambda_n \frac{Q_n L^3}{n^3 \pi^3 EI} \ cos(\frac{n\pi x}{L}) \tag{2.61}$$

where, the non-local parameter λ_n has the effect of increasing the deflection. The definition of λ follows;

$$\lambda_n = (1 + \mu \frac{n^2\pi^2}{L^2}) \tag{2.62}$$

Note, that in the derivation of above equations the linear form of the Euler-Bernoulli beam model has been solved. Incorporation of non-linear effects complicates the solution and such closed form solutions to the problem do not exist. The linear solution that corresponds to the solution of the Timoshenko Beam Theory are provided next. Consider a Timoshenko beam subject to the same boundary conditions as mentioned earlier for the EBT beam for linear analysis. For the case that the beam is subject to a uniform load, the expressions for the quantities of interest are also provided below, and the final expressions for the deflections and the slopes for the Timoshenko beam elements are provided here;

$$w(x,t) = \sum_{n=1}^{\infty} W_n \sin(\frac{n\pi x}{L}) e^{i\omega_n t} \tag{2.63}$$

and,

$$\phi(x,t) = \sum_{n=1}^{\infty} \phi_n \cos(\frac{n\pi x}{L}) e^{i\omega_n t} \tag{2.64}$$

where, the constants introduced are defined as follows;

$$\lambda_n = (1 + n^2\pi^2\Omega), \quad \Omega = \frac{EI}{GAK_sL^2} \tag{2.65}$$

The linear series solutions provided above serve as a very good estimate to the actual results obtained from the solutions of the different beam theories mentioned both to serve as validation benchmarks for the problems solved and also to provide checks on the exponential convergence of the errors in the L^2 norms. The following figure 1 presents the agreement between the linear series solutions obtained and the spectral/*hp* results. The spectral convergence of the series solutions to the analytical

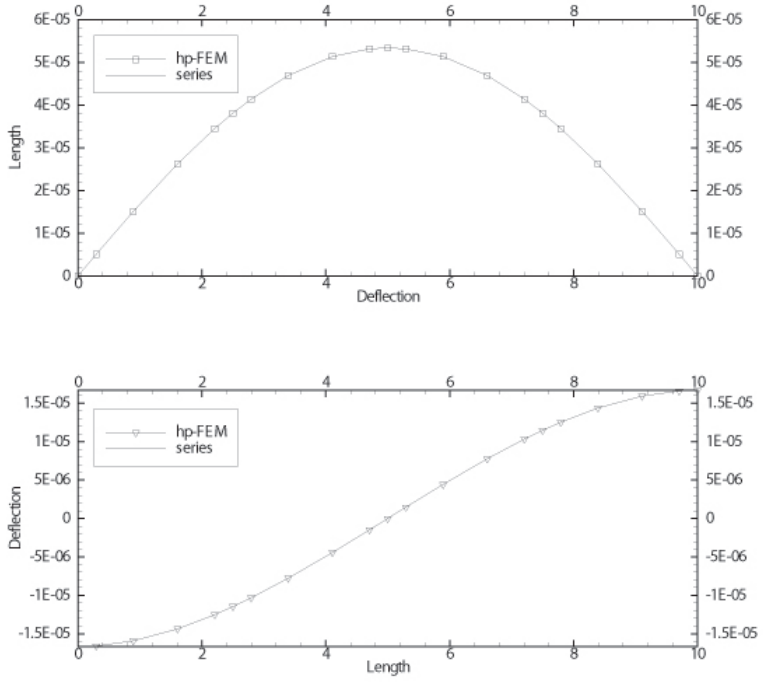

Fig. 1. TBT series solutions comparisons with *hp* spectral results

results has been presented in Fig 2. The *hp* spectral results were checked with a concurrent linear analysis and the agreement between the results can be found to be very good as the error decays exponentially with the increase in the p_{level}.

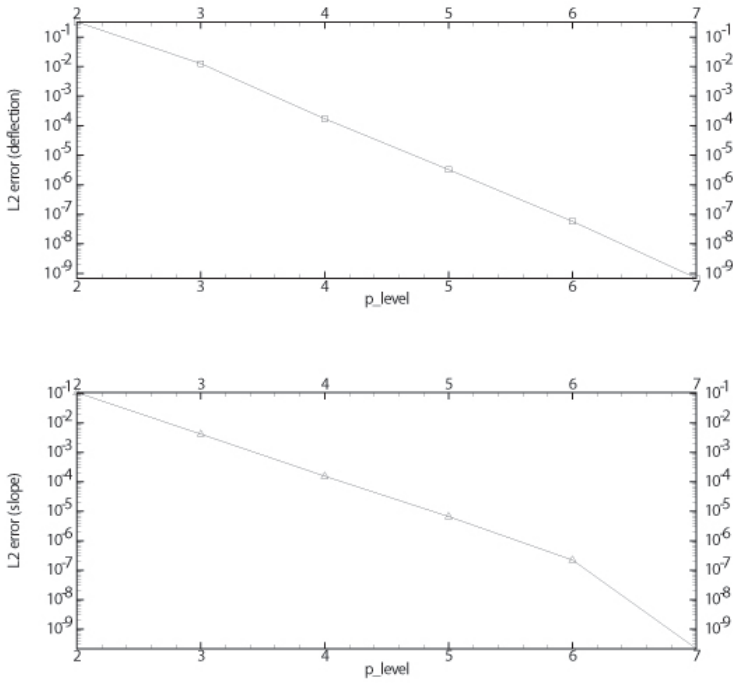

Fig. 2. Convergence of the series solutions and *hp* spectral results

H. Nonlinear Solutions

The non-linear problem was formulated two different ways as mentioned above for the different beam models that were solved. The first formulation is the displacement based formulation, and the second formulation is the mixed formulation. Both of these will be described in the following sections for both beam theories studied.

1. Euler-Bernoulli Beam Theory

The non-linear problem was formulated two different ways as mentioned above. Results from finite element mixed model I and FE mixed II are both discussed in the following sections.

a. Hinged-hinged B.C. (EBT)

Consider a EBT beam which is subject to hinged-hinged boundary conditions at both ends. The beam length $L = 100in.$, $1in \times 1in$ crossection, made of steel ($E = 30msi$), and subjected to a uniform loading of intensity q_0 lb/in. The Poisson ratio for the beam was taken as 0.25. For mixed model I the whole domain of the beam was modelled. The geometric boundary conditions for the beam hinged-hinged boundary condition has been specified earlier. The non-dimensionalization of the deflection was carried out based on equation [2.66]: The non-dimensional deflections at the center of the beam are also being reported for this beam in Table I. As can be seen from Table I the agreement with the *hp*-spectral results and the results of Reddy [11] is excellent. A total of 10 elements were used for this analysis, with uniformly spaced levels and uniform p_{level}]. The discrete problem resulted in a total of 124 degrees of freedom of the system. A constant p_{value}] of 3 was used in each element. The uniform load parameter of 1.0 was used for stepping through the loads till a maximum value of 10 (as reported in Table I) was reached. For the mixed model II ten elements were used in the analysis with a p_{value} of 7. A relatively high p_{level} was used for this analysis. For the mixed formulation II each node has a total of six degrees of freedom. The discrete problem consisted of a total of 426 degrees of freedom. The non-linear convergence criterion was set at a value of 10^{-03}. The linearisation was carried out with Newton-Raphson's method of non-linear iteration. Hinged-hinged

Table I. Hinged-Hinged EBT results

q(xx)	Mixed Model I (MX1)		Mixed Model II (MXII)		Reddy [11]
	$w_0\ in.$	$w\ (dmlss)$	$w_0\ in.$	$w\ (dmlss)$	$w_0\ in.$
1	0.5208	1.302	0.5208	1.302	0.5208
2	1.0416	2.6041	1.0416	2.6041	1.0417
3	1.5625	3.9062	1.5625	3.9062	1.5625
4	2.0833	5.2083	2.0833	5.2083	2.0833
5	2.6041	6.5104	2.6041	6.5104	2.6042
6	3.125	7.8125	3.125	7.8125	3.125
7	3.6458	9.1145	3.6458	9.1145	3.645
8	4.1666	10.4166	4.1666	10.4166	4.1667
9	4.6875	11.7187	4.6875	11.7187	4.6875
10	5.2083	13.0208	5.2083	13.0208	5.2083

case is the most sensitive case for checking locking issues and it was realized that with appropriate p_{level} refinement there was no need to use reduced integration to obtain excellent results.

b. Pinned-Pinned B.C. (EBT)

Consider a beam with the material properties defined earlier subject to pinned-pinned boundary condition. For the pinned-pinned (PP) boundary condition the Newton's method of linearisation was used to obtain the results. The non-dimensional deflections at the center of the beam are also being reported for this beam in Table II. As can be seen from Table II the agreement with the *hp*-spectral results and the results of Reddy [11] is excellent. Reddy [11] results were obtained with 4 quadratic elements

Table II. Pinned-Pinned EBT results

q(xx)	Mixed Model I (MX1)		Mixed Model II (MXII)		Reddy [11]
	w_0 $in.$	w $(dmlss)$	w_0 $in.$	w $(dmlss)$	w_0 $in.$
1	0.3697	0.9244	0.3685	0.9212	0.3685
2	0.5478	1.3696	0.5454	1.3636	0.5454
3	0.6675	1.6687	0.6643	1.6607	0.664
4	0.7593	1.8983	0.7556	1.8891	0.7555
5	0.8353	2.0884	0.8313	2.0783	0.8312
6	0.9008	2.2521	0.8964	2.2412	0.8964
7	0.9586	2.3966	0.954	2.3851	0.954
8	1.0107	2.5267	1.0059	2.5147	1.0058
9	1.0582	2.6455	1.0532	2.633	1.0531
10	1.102	2.755	1.0968	2.7421	1.0967

with reduced integration techniques for this case. A total of 10 elements were used for this analysis, with gradation at the edges of the beam as explained earlier. The discrete problem resulted in a total of 124 degrees of freedom of the system. A constant p_{value} of 3 was used in each element. The uniform load parameter of 1.0 was used for stepping through the loads till a maximum value of 10 (as reported in Table II) was reached. For the mixed finite element formulations for the Euler-Bernoulli beam models a higher value of p was used in some cases (as illustrated later) to generate more confidence in the results and also to resolve the stresses and moments to a high level of accuracy. For mixed model II twenty elements were used in the analysis with a p_{level} of 9. For the mixed formulation each node has a total of six degrees of freedom. The discrete problem consisted of a total of 1086 degrees of freedom. The non-linear

convergence criterion was set at a value of 10^{-03}. The non- dimensional deflections for the different a/h ratios for the pinned-pinned cases were also explored and are presented in Table III. The following figure 3 highlights the bending characteristics

Table III. Pinned-Pinned EBT results different a/h ratios

Results	Pinned Pinned different a/h ratios			
q_{xx}	w_{10}	w_{20}	w_{25}	w_{100}
1	1.3020	1.3020	1.3020	0.9213
2	2.6041	2.6041	2.6040	1.3637
3	3.9062	3.9061	3.9058	1.6609
4	5.2083	5.2081	5.2072	1.8893
5	6.5104	6.5100	6.5083	2.0785
6	7.8124	7.8119	7.8089	2.2414
7	9.1145	9.1136	9.1090	2.3854
8	10.4166	10.4152	10.4083	2.5150
9	11.7187	11.7167	11.7068	2.6332
10	13.0208	13.0180	13.0045	2.7423

for several load-steps when subjected to uniformly distributed loads for increasing length of the beam.

c. Clamped-clamped B.C. (EBT)

Consider a beam which is subjected to clamped-clamped boundary conditions at both ends. The beam length L=100 in., $1in \times 1in$ crossection, made of steel ($E = 30msi$), and subject to a uniform loading of intensity q_0 lb/in. The Poisson ratio for the beam was taken as 0.25. Table IV reports the deflections of the center of the beam

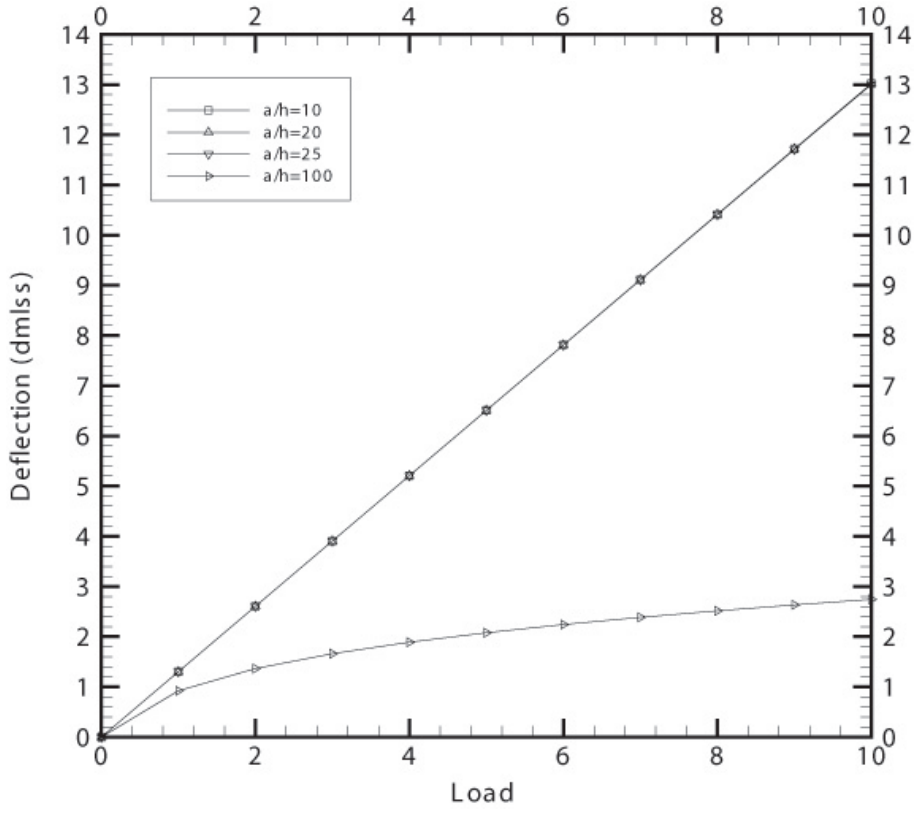

Fig. 3. EBT results for pinned-pinned B.C. for different a/h ratios

subjected to the clamped-clamped boundary condition and also the non-dimensional deflections at the center of the beam. A total of 10 elements were used for this analysis for mixed model I, with uniform elements with a uniform p_{level} in each element. The discrete problem resulted in a total of 204 degrees of freedom of the system. A constant p_{value} of 5 was used in each element. The uniform load parameter of 1.0 was used for stepping through the loads till a maximum value of 10 (as reported in Table IV) was reached. A high value of p_{level} was used in certain cases to generate more confidence in the results. The discrete problem was solved with Gaussian-Elimination with scaled partial pivoting. The run presented above is for the case where $a/h = 100$. Different a/h ratios were analysed and Table V reports the non-dimensionalised center deflection as a function of the changing length of the beam. For

Table IV. Clamped-Clamped EBT results

q(xx)	Mixed Model I (MX1)		Mixed Model II (MXII)		Reddy [11]
	$w_0\ in.$	$w\ (dmlss)$	$w_0\ in.$	$w\ (dmlss)$	$w_0\ in.$
1	0.1033	0.2584	0.1033	0.2584	0.1035
2	0.2024	0.5061	0.2023	0.5057	0.2025
3	0.2944	0.7361	0.294	0.735	0.2943
4	0.3784	0.946	0.3775	0.9438	0.3777
5	0.4545	1.1364	0.4531	1.1329	0.4534
6	0.5237	1.3092	0.5218	1.3045	0.522
7	0.5867	1.4669	0.5843	1.4608	0.5845
8	0.6445	1.6114	0.6416	1.604	0.6418
9	0.6979	1.7449	0.6945	1.7362	0.6946
10	0.7474	1.8687	0.7435	1.8588	0.7436

the analysis of the beam deflection with changing lengths of the beam, 10 elements were used, and the full beam was modelled. The p_{level} used was set at a uniform value of 9 to generate these results. A high value of p_{level} was also used to bring out the differences in numerics between the tip deflections of the beams at different a/h ratios. The model consisted of a total of 546 degrees of freedom which was stepped with Newtons method. Based on the above observations the non-dimensional load vs. deflection curves for clamped-clamped Euler-Bernoulli beams is constant with varying lengths from a range of $a/h = 10$ through a value of $a/h = 75$ and varies significantly only for the case of a slender beam of slenderness ratio $a/h = 100$.

Figure 4 shows the non-dimensional deflection vs. loads for studying the bending deformation analysis of EBT. Figure 5 provides the load vs. the deflection curves for

Table V. Clamped-Clamped EBT results different a/h ratios

Results	Clamped Clamped different a/h ratios			
q_{xx}	w_{10}	w_{20}	w_{25}	w_{100}
1	0.2604	0.2604	0.2604	0.2584
2	0.5208	0.5208	0.5208	0.5057
3	0.7812	0.7812	0.7812	0.7350
4	1.0416	1.0416	1.0416	0.9438
5	1.3020	1.3020	1.3020	1.1329
6	1.5624	1.5624	1.5624	1.3045
7	1.8229	1.8229	1.8229	1.4608
8	2.0833	2.0833	2.0833	1.6040
9	2.3437	2.3437	2.3437	1.7362
10	2.6041	2.6041	2.6041	1.8588

the EBT theory, for increasing loadsteps. As can be seen from the load vs. deflection curves there is considerable non-linear response in the bending of the EBT beam with the increasing loadsteps.

2. Timoshenko Beam Theory

The non-linear results obtained with the solutions of the Timoshenko beam theory with the displacement (DX) and the mixed formulation (MX) have been outlined below along with published results in literature on the above. The classifications of the results have been done based on the different types of the boundary conditions that were applied for solving the beam problem. The deformed shapes of the Timoshenko beam theories with the clamped-clamped and the pinned-pinned boundary conditions

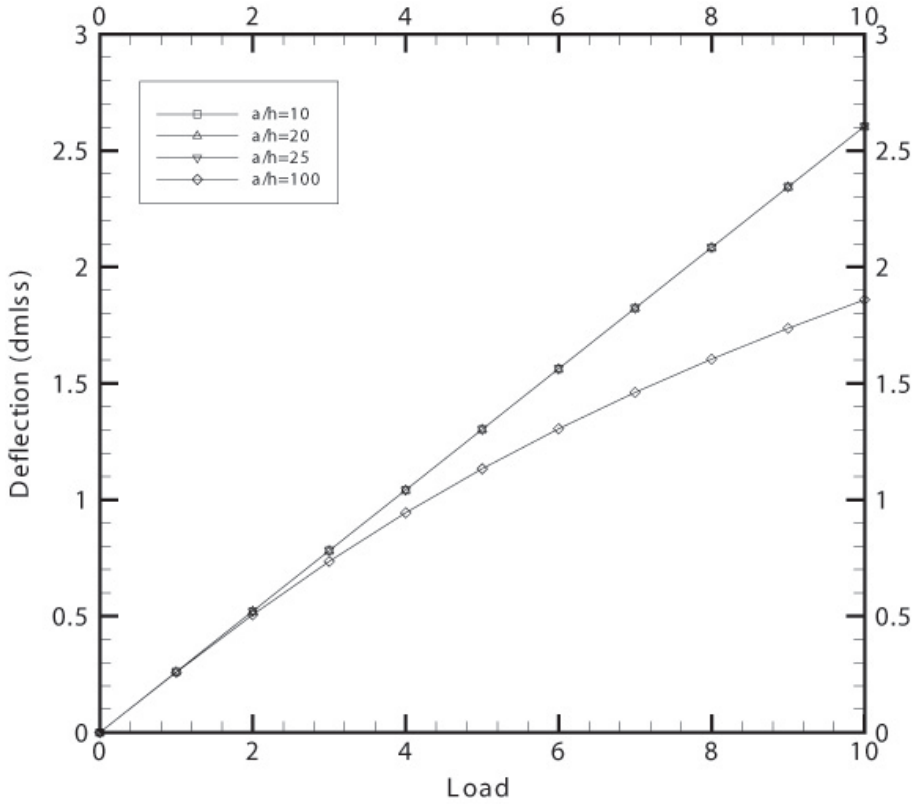

Fig. 4. EBT results for clamped-clamped B.C. for different a/h ratios

is being provided in Fig 6.

a. Hinged-Hinged B.C. (TBT)

Consider a beam which is subjected to hinged-hinged boundary conditions at both ends. The beam length $L = 100in.$, $1 \times 1\ in^2$ cross section, made of steel $E = 30$ msi, subject to a uniform loading of intensity q_0 lb/in. The Poisson ratio for the beam was taken as 0.25. The non-dimensionalization of the deflection was based on the following formula;

$$w = \frac{1000 * w_{max} * D_{xx}}{L^4} \tag{2.66}$$

Also, the results obtained in the above cited reference were obtained using reduced

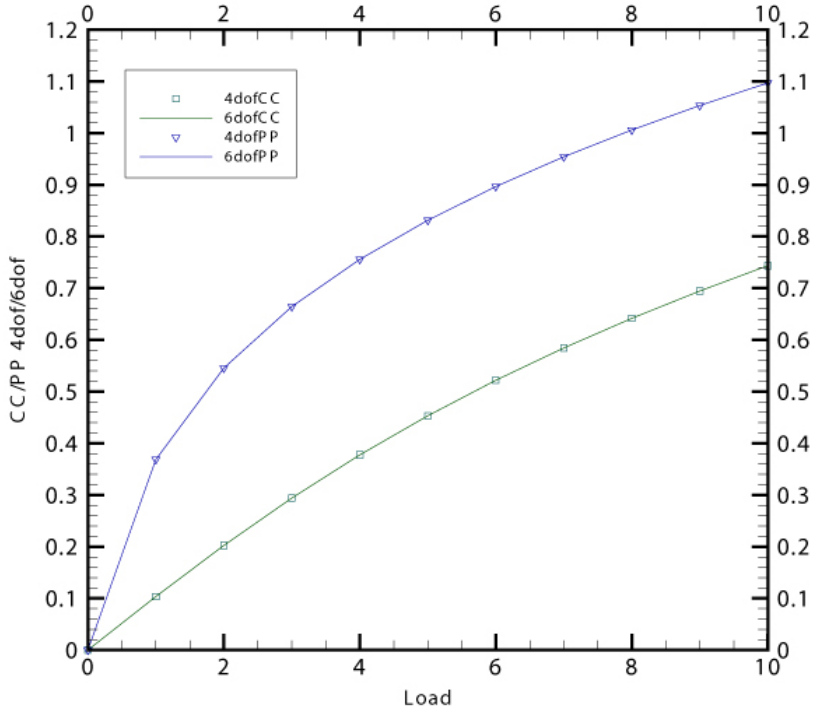

Fig. 5. Load vs. deflection for EBT beam with CC and PP B.C.

integration techniques and in this case usage of full integration has been advocated with appropriate *hp*-refinements. No acceleration parameter was used for obtaining the above results. The non-dimensional deflections at the center of the beam are also being reported for this beam in Table VI. As can be seen from Table VI the agreement with the *hp*-spectral results and the results of Reddy [11] is excellent. It is expected that the present results are more accurate because of the spectral convergence of the solutions. A total of 10 elements were used for this analysis, with gradation at the edges of the beam to capture the development of strain and stress concentrations at the end of the beam (boundary layers). The gradation of half beam is being presented below;

$$\Delta(x) = 0.25, 0.25, 0.25, 0.25, 4.0, 9.0, 9.0, 9.0, 9.0, 9.0 \tag{2.67}$$

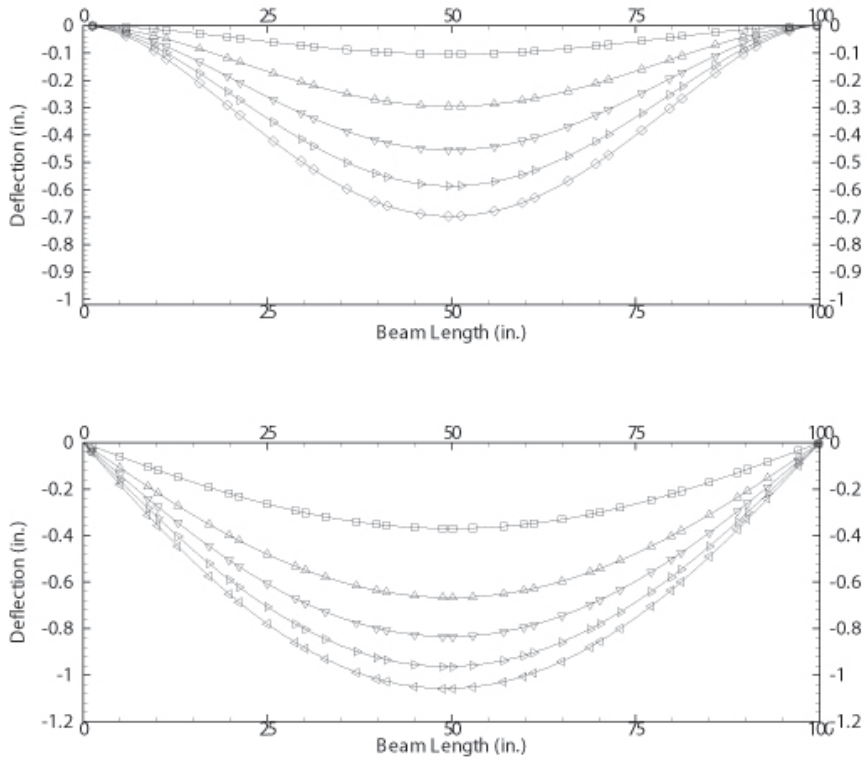

Fig. 6. TBT deformed shapes for clamped-clamped and pinned-pinned B.C.

The discrete problem resulted in a total of 153 degrees of freedom of the system for the displacement based formulation. A constant p_{value} of 5 was used in each element. The uniform load parameter of 0.50 was used for stepping through the loads till a maximum value of 10 (as reported in Table VI) was reached. Bi-orthogonal conjugate gradient was used as a solver for this system of equations with Jacobi preconditioning and was found to work well for the discrete problem obtained from the displacement based formulation. For the mixed formulation since, the shear forces and the moments at the center of the beam are not known the full beam was modelled. Ten elements were used in the analysis with a p_{value} of 14. Such high p_{levels} were used to generate confidence in the results. For the mixed formulation each node has a total of six degrees of freedom. The discrete problem consisted of a total of 846 degrees

Table VI. Hinged-Hinged TBT results

q(xx)	Displacement Model (DX)		Mixed Model (MX)		Reddy [11]
	$w_0\ in.$	$w\ (dmlss)$	$w_0\ in.$	$w\ (dmlss)$	$w_0\ in.$
1	0.5209	1.3024	0.5209	1.3023	0.5208
2	1.0386	2.5966	1.0419	2.6047	1.0417
3	1.5629	3.9072	1.5628	3.9071	1.5625
4	2.0838	5.2096	2.0838	5.2095	2.0833
5	2.6048	6.5119	2.6047	6.5119	2.6042
6	3.1258	7.8144	3.1257	7.8143	3.125
7	3.6467	9.1167	3.6467	9.1167	3.6458
8	4.1677	10.419	4.1676	10.4191	4.1667
9	4.6887	11.722	4.6886	11.7215	4.6875
10	5.2096	13.024	5.2095	13.0239	5.2083

of freedom. The non- linear convergence criterion was set at a value of 10^{-03}. The linearization was carried out with Newton-Raphsons method of linearisation.

b. Pinned-Pinned B.C. (TBT)

Consider a TBT beam with material properties defined earlier subject to the pinned-pinned boundary condition. For the pinned-pinned (PP) boundary condition the Picard method of linearisation reported some convergence problems beyond certain load steps, and thus the Newton-Raphson method was used for obtaining the results. The inclusion of acceleration parameter into the program caused the convergence to be reached which was difficult otherwise for the Picard method. The non-dimensional deflections at the center of the beam are also being reported for this beam in Table VII.

Table VII. Pinned-Pinned TBT results

q(xx)	Displacement Model (DX)		Mixed Model (MX)		Reddy [11]
	$w_0\ in.$	$w\ (dmlss)$	$w_0\ in.$	$w\ (dmlss)$	$w_0\ in.$
1	0.3685	0.9212	0.3693	0.9234	0.3685
2	0.5454	1.3636	0.5467	1.3669	0.5454
3	0.6645	1.6614	0.6655	1.6638	0.664
4	0.7556	1.8891	0.7536	1.8841	0.7555
5	0.8312	2.0781	0.8316	2.079	0.8312
6	0.8963	2.2409	0.8993	2.2483	0.8964
7	0.9539	2.3848	0.9588	2.397	0.954
8	1.0058	2.5144	1.0205	2.5514	1.0058
9	1.0531	2.6327	1.0525	2.6312	1.0531
10	1.0967	2.7417	1.1139	2.7849	1.0967

As can be seen from Table VII the agreement with the *hp*-spectral results and the results of Reddy [11] is excellent. Reddy results were obtained with 4 quadratic elements with reduced integration techniques for this case. A total of 10 elements were used for this analysis, with gradation at the edges of the beam as explained earlier. The discrete problem resulted in a total of 183 degrees of freedom of the system for the displacement based formulation. A constant p_{value} of 6 was used in each element. The uniform load parameter of 0.50 was used for stepping through the loads till a maximum value of 10 (as reported in Table VII) was reached. For the mixed finite element formulations for the Timoshenko beam models a higher value of p was used in some cases to generate more confidence in the results and also to resolve the stresses and moments to a high level of accuracy. The non-dimensional deflections

for the different a/h ratios for the pinned-pinned cases were also explored and have been presented in Table VIII. The following figure 7 presents the non-dimensional

Table VIII. Pinned-Pinned TBT results different a/h ratios

Results	Clamped Clamped different a/h ratios			
q_{xx}	w_{10}	w_{20}	w_{25}	w_{100}
1	1.3333	1.3099	1.3071	0.9212
2	2.6667	2.6198	2.614	1.3636
3	4	3.9296	3.9208	1.6614
4	5.3333	5.2394	5.2273	1.8891
5	6.6667	6.5491	6.5333	2.0781
6	8	7.8588	7.8389	2.2409
7	9.3333	9.1683	9.1439	2.3848
8	10.667	10.478	10.448	2.5144
9	12	11.787	11.752	2.6327
10	13.333	13.096	13.054	2.7417

deflections vs. the loadings for a pinned-pinned TBT beam. As can be seen from the figure there is not appreciable differences in the non-dimensional deflections for a few different a/h ratios and only when the a/h ratio increases to more than 100 does the deviations become appreciable.

c. Clamped-Clamped B.C. (TBT)

Consider a beam which is subjected to clamped-clamped boundary conditions at both ends. The beam length $L = 100in.$, $1 \times 1\ in^2$ cross section, made of steel ($E = 30$ msi), and subjected to a uniform loading of intensity q_0 lb/in. The Poisson ratio

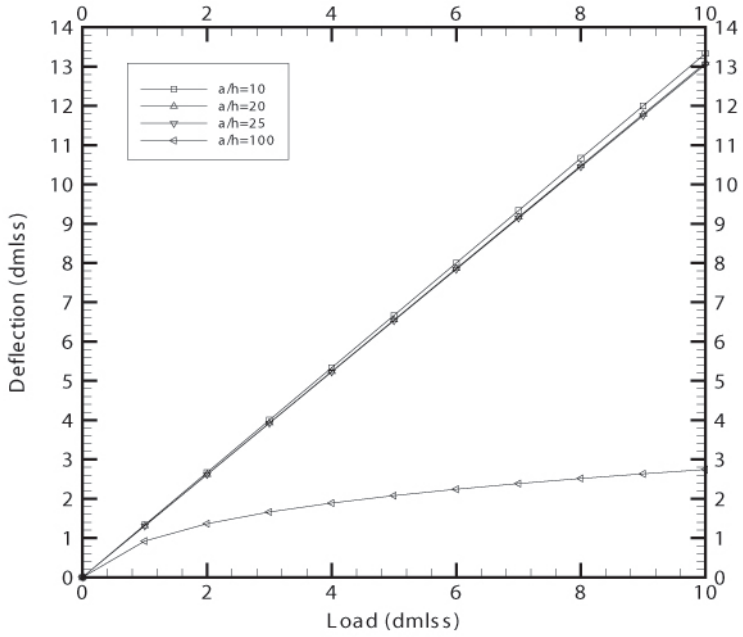

Fig. 7. Different a/h vs. deflections for TBT beam subject to PP B.C.

considered was taken as 0.25. Using the symmetry of the beam around the center of the beam, one half of the beam needed to have been modelled. Table IX reports the deflections of the center of the beam subject to the clamped-clamped boundary condition and also the non-dimensional deflections at the center of the beam for both the mixed and displacement based formulations. Reddy [11] results were obtained with 4 quadratic elements with reduced integration techniques for this case. A total of 10 elements were used for this analysis, with gradation at the edges of the beam as explained earlier. The discrete problem resulted in a total of 153 degrees of freedom of the system. A constant p_{value} of 5 was used in each element. The uniform load parameter of 0.50 was used for stepping through the loads till a maximum value of 10 was reached. The run presented above is for the case where $a/h = 100$. Different a/h ratios analysis were carried out and Table X reports the non-dimensionalized center

Table IX. Clamped-Clamped TBT results

q(xx)	Displacement Model (DX)		Mixed Model (MX)		Reddy [11]
	$w_0\ in.$	$w\ (dmlss)$	$w_0\ in.$	$w\ (dmlss)$	$w_0\ in.$
1	0.1034	0.2587	0.1034	0.2587	0.1035
2	0.2025	0.5063	0.2025	0.5063	0.2025
3	0.2942	0.7356	0.2943	0.7358	0.2943
4	0.3777	0.9444	0.3779	0.9449	0.3777
5	0.4533	1.1335	0.4537	1.1343	0.4534
6	0.5219	1.3049	0.5224	1.3061	0.5220
7	0.5843	1.4610	0.5850	1.4626	0.5845
8	0.6416	1.6041	0.6424	1.6061	0.6418
9	0.6944	1.7361	0.6954	1.7385	0.6946
10	0.7434	1.8586	0.7445	1.8613	0.7436

deflection as a function of the changing length of the beam. For the analysis of the beam deflection with changing lengths of the beam, 10 elements were used, and the full beam was modelled. The p_{level} used was set at a uniform value of 9 to generate the results. This resulted in a total of 546 degrees of freedom, the non-linear problem was stepped with Newton's method. As can be seen from the results presented here, an increase in the length of the beam did not cause any deterioration of the results and all the results were obtained with *full integration* techniques.

The following figure 8 demonstrates the non- dimensional deflections vs. the different a/h ratios for the TBT beam subject to clamped-clamped boundary condition. To demonstrate the convergence behaviour of the TBT beam with the bi-orthogonal conjugate gradient solver Fig 9 has been included. The higher residuals are for the

Table X. Clamped-Clamped TBT results different a/h ratios

Results	Clamped Clamped different a/h ratios			
q_{xx}	w_{10}	w_{20}	w_{25}	w_{100}
1	0.2916	0.2682	0.2654	0.2587
2	0.5833	0.5364	0.5308	0.5064
3	0.8749	0.8046	0.7962	0.7361
4	1.1666	1.0729	1.0616	0.9454
5	1.4583	1.3411	1.3270	1.1351
6	1.7499	1.6093	1.5924	1.3073
7	2.0416	1.8776	1.8579	1.4642
8	2.3333	2.1458	2.1233	1.6080
9	2.6249	2.4140	2.3887	1.7407
10	2.9166	2.6822	2.6541	1.8638

lower value of p_{level} of 4 whereas the the higher values of 7 exhibits a lower value of residuals and faster convergence as expected.

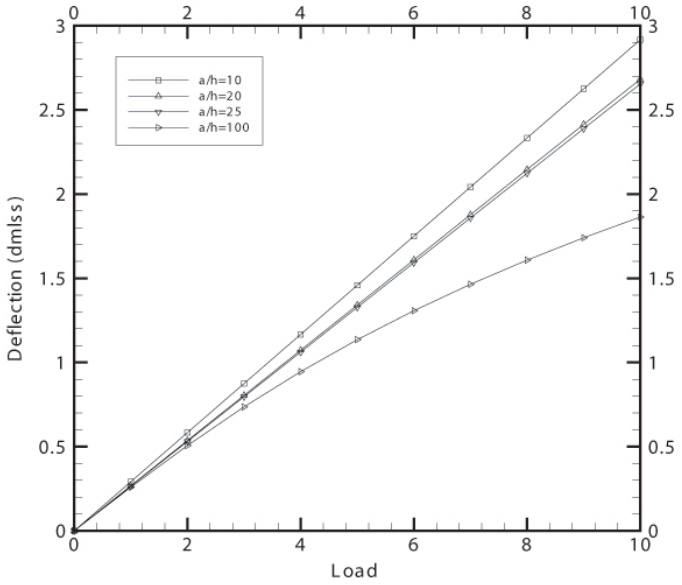

Fig. 8. a/h vs. deflections for TBT beam subject to CC B.C.

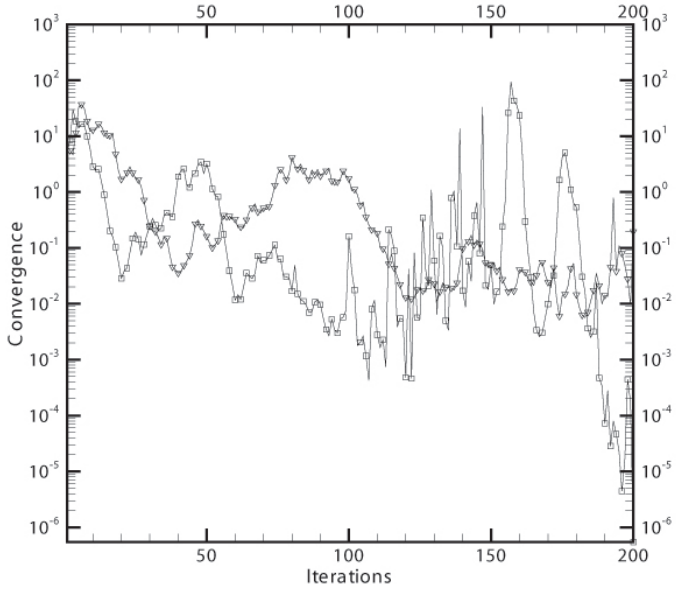

Fig. 9. Convergence history of the CG solver for TBT solutions

CHAPTER III

HP-SPECTRAL METHODS APPLIED TO PLATE THEORY

A. Introduction

In this chapter we further explore the usage of higher order *hp*-spectral element methods applied to solving both linear and non-linear analysis associated with the solutions of the Reissner-Mindlin plates in two dimensions. We start out with a literature review in this field of the usage of such methods in different related areas, and describe the governing equations along with the linearisation procedures for problems in bending of plates followed by results and comparisons with published results in literature.

There are different formulations that are in place for predicting the bending behaviour of Reissner-Mindlin plates with different types of resulting finite element approximations. Mostly the literature abounds with traditional equi-spaced Lagrange based low order finite element approximations of the first-order shear deformation theory of plates which are either displacement based or mixed based methods. However, the traditional methods of using either bilinear (Q4) or bi-quadratic (Q9) elements has suffered from locking problems which has been alleviated with the help of primarily reduced/selective integration techniques to obtain acceptable solutions amongst some other techniques [11]. These kinds of 'fixes' have come into existence because the element stiffness matrix becomes excessively stiff with low-order interpolation functions. Here we propose an alternative spectrally accurate *hp*/spectral method to model the first order shear deformation theory of plates (FSDT) to solve shear locking problems. Both linear and non-linear isotropic and orthotropic plates are studied in this document subject to clamped, and simply supported boundary conditions. Re-

sults obtained herewith are compared to both analytical solutions (where available) and non-linear solutions from literature and excellent agreement is found for all cases. Full integration scheme is employed for all cases.

B. Background

Studying the bending deformation of plates is of interest in many applications in engineering. Some of the applications of this are in geotechnical engineering, structural design of foundations, design of spread footings, soil-structure interaction studies etc. There are primarily three models in place for studying this subject and can be classified into the classical plate theory, Reissner-Mindlin plate theory, and Reddy third order shear deformation theory. The plate bending problem has been studied in literature and different methods have been used for solving problems. The Ritz-Galerkin method for laminated composite plates [27], weak formulations for first order shear shear deformation theory (FSDT) [11], and least-squares finite element method for studying FSDT and classical plate theories [13].

While the displacement based models for the first-order shear deformation theory (FSDT) admit the use of C_0 expansions the use of classical plate theory and the Reddy theory require the use of C_1 continuous expansions. The classical plate theory has a relatively simpler formulation, however the theory does not account for the transverse shear strains, and therefore the results are inadequate for the prediction of the global response of thick plates. When using the first order shear deformation (FSDT) to model plates, shear correction factors are introduced to correct for the discrepancy between the actual parabolic transverse shear stress distribution and those compared using the kinematic assumptions of the FSDT. Higher order plate theories provide a slight increase in the accuracy relative to the FSDT solution, at the expense of a

significant increase in the computational effort. Based on the above arguments the FSDT provides the best compromise between economy, simplicity, and accuracy in prediction of the global response of thin to moderately thick plates [14].

While some studies have been carried out in literature on the use of equi-spaced Lagrange based higher order expansions for studying the bending response of plates, the traditional equi-spaced Lagrange based expansions suffer from ill-conditioning and for high p_{levels} equi-spaced Lagrange based expansion is not recommended [1]. It has been mentioned in literature that higher than a p_{level} of 4 is not recommended. At high p_{level} the discrete problem suffers from a very high conditioning of the stiffness matrix. Very strong pre-conditioners, can be recommended in some cases to parse the discrete problem at such high p_{levels} but the convergence is problem dependent and also dependent on the regularity of the mesh.

Another issue with displacement-based FSDT finite element models is that it presents computational difficulties when the side-to-thickness ratio of the plate (a/h) is large (i.e. when modelling thin plates). A strong stiffening of the element matrices occurs, resulting in spurious shear stress predictions and erroneous results for the generalized displacements [10]. This phenomenon is known as shear-locking. Shear locking develops in formulations which cannot represent a state of zero-shear in the thin beam limit independent of the mesh. This is exhibited as a violation of the Kirchoff assumption in the thin beam theory, stated as $w, x - \theta = 0$. When the beam is thin most of the energy of deformation is due to bending. If a formulation does not admit non-trivial zero shear solutions, then most of the energy of deformation goes into shear deformation, resulting in very little bending–hence locking. This can be seen from the variational form; since the coefficient of the bending term is of the order t^3 and the coefficient of the shear term is of the order of $O(t)$, the latter becomes much larger as t approaches zero [10].

This problem is commonly treated by reduced integration techniques, although other remedies may be found [11]. Shear locking is evident in the Ritz- Galerkin displacement based finite element models with equal-order interpolation of all generalized displacements. The phenomenon is more pre-dominant when the side-to-thickness ratio of the plate is high. Higher-order elements have been explored in literature to be alleviating the shear locking phenomenon but they have been mostly equi-spaced Lagrange based so far. The use of *hp*-spectral nodal expansion was explored by Pontaza while analysing plates for both the classical plate theory and the FSDT with the least squares finite element formulation however, only a linear analysis was performed [13].

The aforementioned reasons compel the use of *hp*-element refinements as a viable and a robust alternative to studying the bending behaviour of plates which provide both spectrally accurate results and at the same time alleviate perennial problems of locking associated with lower order finite element methods. This study proposes to advance the use of appropriate *hp*-refinements for studying the plate bending behaviour and cures the problem of locking for all cases that are studied. The motivation for this study comes from the many advantages that are associated with *hp*-higher order elements; spectral convergence (accuracy) of the solutions, the removal of locking issues, and the orthogonality property of nodal expansions which provide excellent results with standard solvers like the preconditioned bi-orthogonal conjugate gradient (BPCG) alleviating the problem of ill-conditioning of the discrete problem ascribed to the usage of higher-order equi-spaced Lagrange based interpolants. The convergence history of the bi-orthogonal conjugate gradient solver with preconditioning is also reported to get further insight into the problem formulation and convergence behaviour with *hp*-spectral methods. Different a/h ratios are explored and with appropriate *hp*-refinements full integration is found to provide consistently good agreement with published results. Both straight and skewed *hp*-spectral meshes are explored in this

study and it is found that there is no drastic deterioration in the results when using skewed meshes. Skewed meshes (after respecting the development of boundary layers), provide very good results as well as the straight non-uniform meshes and one such comparison is demonstrated.

C. Governing Equations

The first order shear deformation theory extends the classical plate theory by relaxing the normality restriction on the plate and allows for arbitrary but constant rotations on the transverse normals [25]. The displacement field of the first order shear deformation theory can be expressed in the form:

$$\begin{aligned} u(x,y,z) &= u(x,y,z) + z\phi_x(x,y) \\ v(x,y,z) &= v(x,y,z) + z\phi_y(x,y) \\ w(x,y,z) &= w_0(x,y,z) \end{aligned} \tag{3.1}$$

The displacements u_0, v_0, and w_0 denote the mid-plate displacements and ϕ_x and, ϕ_y are the rotations of the transverse normals about the y and x-axis respectively.

The Euler-Lagrange equations for the first-order shear deformation theory can be derived based on the principle of virtual work. The virtual work statement for the FSDT problem is equivalent to the weak form (integral form) for the governing differential equations. For details on the virtual work principle the reader is referred to the following references [11]. Based on the virtual work principle and separating the virtual displacements we obtain the Euler-Lagrange equations for the FSDT as follows:

$$\frac{\partial N_{xx}}{\partial x} + \frac{\partial N_{xy}}{\partial y} = 0 \tag{3.2}$$

$$\frac{\partial N_{xy}}{\partial x} + \frac{\partial N_{yy}}{\partial y} = 0 \tag{3.3}$$

$$\frac{\partial Q_x}{\partial x} + \frac{\partial Q_y}{\partial y} - kw_0 + N + q = 0 \tag{3.4}$$

$$\frac{\partial M_{xx}}{\partial x} + \frac{\partial M_{xy}}{\partial y} - Q_x = 0 \tag{3.5}$$

$$\frac{\partial M_{xy}}{\partial x} + \frac{\partial M_{yy}}{\partial y} - Q_y = 0 \tag{3.6}$$

In the above equations N_{xx}, N_{xy}, and N_{yy} are the forces per unit length and M_{xx}, M_{xy}, and M_{yy} are the moments per unit length, k is the foundation modulus (which has meaning in soil-structure interaction studies, spread footing designs etc.),and N is defined as follows:

$$N = \frac{\partial}{\partial x}\left(N_{xx}\frac{\partial \omega_o}{\partial x} + N_{xy}\frac{\partial \omega_o}{\partial y}\right) + \frac{\partial}{\partial y}\left(N_{xy}\frac{\partial \omega_o}{\partial x} + N_{yy}\frac{\partial \omega_o}{\partial y}\right) \tag{3.7}$$

The primary (PV) and the secondary variables (SV) include the specification of either the displacements or the forces on the model as follows: PV:

$$u_{0n}, u_{0s}, w_0, \phi_n, \phi_s \tag{3.8}$$

SV:

$$N_{nn}, N_{ns}, Q_n, M_{nn}, M_{ns} \tag{3.9}$$

The plate constitutive equations relate the forces and the moments to the displacement fields for the plate. For the plate under consideration the constitutive equations can be expressed as:

$$\begin{Bmatrix} \epsilon_{xx} \\ \epsilon_{yy} \\ \gamma_{yz} \\ \gamma^0_{xz} \\ \gamma_{xy} \end{Bmatrix} = \begin{Bmatrix} \epsilon^0_{xx} \\ \epsilon^0_{yy} \\ \gamma^0_{yz} \\ \gamma_{xz} \\ \gamma^0_{xy} \end{Bmatrix} + z\begin{Bmatrix} \epsilon^1_{xx} \\ \epsilon^1_{yy} \\ 0 \\ 0 \\ \gamma^1_{xy} \end{Bmatrix} = \begin{Bmatrix} \frac{\partial u_0}{\partial x} + \frac{1}{2}\left(\frac{\partial \omega}{\partial x}\right)^2 \\ \frac{\partial v_0}{\partial y} + \frac{1}{2}\left(\frac{\partial \omega}{\partial y}\right)^2 \\ \frac{\partial \omega_0}{\partial y} + \phi_y \\ \frac{\partial \omega_0}{\partial x} + \phi_x \\ \frac{\partial u_0}{\partial y} + \frac{\partial v_0}{\partial x} + \frac{\partial \omega_0}{\partial x}\frac{\partial \omega_0}{\partial y} \end{Bmatrix} + z\begin{Bmatrix} \frac{\partial \phi_x}{\partial x} \\ \frac{\partial \phi_y}{\partial y} \\ 0 \\ 0 \\ \frac{\partial \phi_x}{\partial y} + \frac{\partial \phi_y}{\partial x} \end{Bmatrix} \tag{3.10}$$

The non-linearity in the first-order shear deformation theory comes from the Von-Karman non-linear strains as a form of geometric non-linearity in the equations as shown above. The above equations describe the bending response of both orthotropic and isotropic plates. Shear modulus for the isotropic plate is given by the following formula:

$$G = \frac{E}{2(1+\nu)} \tag{3.11}$$

where, ν is Possion ratio for the isotropic plate under consideration. For the orthotropic plate formulae for a definition of the different coefficients that are part of the weak formulation, and stiffness matrices, the reader is referred to Reddy [11].

Post computation of the stresses is also done with *full integration* techniques. The calculation follows up based on the above formula for both isotropic and orthotropic plates:

$$\left\{ \begin{array}{c} N_{xx} \\ N_{yy} \\ N_{xy} \end{array} \right\} = \left\{ \begin{array}{ccc} A_{11} & A_{12} & 0 \\ A_{12} & A_{22} & 0 \\ 0 & 0 & A_{66} \end{array} \right\} \left\{ \begin{array}{c} e^0_{xx} \\ e^0_{yy} \\ \gamma^0_{xy} \end{array} \right\} \tag{3.12}$$

In the above equation we have neglected the thermal effects on the stresses which can also be accounted for if required.

D. Finite Element Formulation

The FSDT model involves the solution of five degrees of freedom per node, namely, the components of the displacement vector (u, v), the deflection of the plate w, and the slopes ϕ_x and ϕ_y. At the end of the weak form development the finite element model for each variable is determined based on the following equations at the element

level:

$$\begin{bmatrix} K_{11} & K_{12} & K_{13} & K_{14} & K_{15} \\ K_{21} & K_{22} & K_{23} & K_{24} & K_{25} \\ K_{31} & K_{32} & K_{33} & K_{34} & K_{35} \\ K_{41} & K_{42} & K_{43} & K_{44} & K_{45} \\ K_{51} & K_{52} & K_{53} & K_{54} & K_{55} \end{bmatrix} \begin{Bmatrix} \Delta^1 \\ \Delta^2 \\ \Delta^3 \\ \Delta^4 \\ \Delta^5 \end{Bmatrix} = \begin{Bmatrix} R^1 \\ R^2 \\ R^3 \\ R^4 \\ R^5 \end{Bmatrix} \tag{3.13}$$

Each of the coefficients have been defined elsewhere [11] and will not be repeated in the interest of brevity. Thus the discretized problem is represented as an assemblage of 5×5 sub matrices at the element level. This stiffness matrix presented above is the discrete equivalent to the non-linear differential equation and the components of the stiffness matrix depends upon the type of iterative linearisation used in the solution of the problem.

The linearisation process can be accomplished with either of two techniques, namely the Picard (direct iteration procedure) and the Newton-Raphson's method. For checking the convergence behavior of both the methods of linearisation with *hp*-spectral methods both of these were implemented. There was however, no difference found between the results of either of the methods and thus only results based on the Newton-Raphson's method will be presented. For all structural problems the Newton's method yields a symmetric positive definite matrix system which can be solved by conjugate gradient (Krylov subspace methods) solvers, although the solver implemented for the solution of the above discrete problem is BPCG which can handle non-symmetric matrix systems with relative ease. Some of the celebrated advantages of the Newton-Raphsons method are a faster convergence rate, but here again since we are using incremental loadsteps for the runs, Newton's method does not noticeably outperform the Picard method of linearisation. Picard method, on the other

hand is comparatively straightforward to implement and is more intuitive in a sense with a larger radius of convergence. However we are reporting the results based on the Newton Raphson's method as is the norm for solving structural problems. The linearised problem with the Newton's method is represented as follows:

$$[\hat{K^e}(\{\Delta^e\}^r)]^{tan}\{\delta\Delta\}^e = -\{R^e\}^r \tag{3.14}$$

The linear convergence criterion was set at a reduction in the L^2 norm of the residuals to a tolerance value of 10^{-06}, where as the non-linear convergence was declared when L^2 norm of the incremental vector normalized with the norm of the solution vector was less than 10^{-04}. No acceleration parameter was necessary to achieve convergence for all problems studied. In the next section we present the results that we obtained for the linear and non-linear problems that were studied with different types of boundary conditions.

E. Boundary Conditions

The specification of the boundary conditions is very important for the FSDT model, and certain boundary conditions like the simply supported are more susceptible to shear-locking issues. For the Reissner-Mindlin plates there exists a boundary layer which is usually the thickness of the plate at the edges of the plate where there are acute gradients in the stresses and the moments [27]-[28]. Such boundary layers need to be resolved with appropriate *hp*-refinements such that the elements are smaller at the edges of the plate and the same was done in the *hp*-finite element discretization of the domains.

Different problems were studied and analysed and various combinations of boundary conditions were used. The boundary conditions for the FSDT plates require the

specification of the primary or the secondary variables. For most cases, that were explored the strong form of the boundary conditions were applied, with the tractions where ever not specified was satisfied in an integral sense to be zero. This is an advantage of Ritz-Galerkin models where the traction boundary condition resolves to a 'do nothing' boundary condition in an integral sense. While alternative Least squares finite element models usually need special treatment of the boundary conditions which can also be problem specific and quite involved for inclined boundaries. Different boundary conditions were explored and they are being outlined below. Simply Supported boundary (SS1) (parallel to x-axis):

$$u_0 = w_0 = \phi_x = 0 \tag{3.15}$$

Simply Supported boundary (SS1) (parallel to y-axis):

$$u_0 = w_0 = \phi_y = 0 \tag{3.16}$$

Simply supported boundary condition (SS3):

$$u_0 = v_0 = w_0 = 0 \tag{3.17}$$

Clamped-clamped boundary:

$$u_0 = v_0 = w_0 = \phi_x = \phi_y = 0 \tag{3.18}$$

Symmetry Line x-axis:

$$v_0 = \phi_y = 0 \tag{3.19}$$

Symmetry Line y-axis:

$$u_0 = \phi_x = 0 \tag{3.20}$$

A combination of these boundary conditions has been used for all the problems anal-

ysed. They are being mentioned here to avoid repetition elsewhere. The non-linearity as it appears in structural problems stepping of the laod-steps is necessary for convergence of the solution. For the more concise description of the problem often a non-dimensionless parameter of the problem namely the laod-parameter is introduced which is defined below.

$$\bar{P} = \frac{q_0 a^4}{E_2 h^4} \tag{3.21}$$

While defining the loads that were applied to the problems studied, specifying the load parameter greatly simplifies the presentation. Stepping through the loadsteps with the above definition of the load parameter generates the load vector. In some cases, the load vector itself has been provided.

F. Numerical Results

In this section we present the results for the FSDT bending of plates for a diverse set of boundary conditions and for both isotropic and orthotropic plates. Both straight non-uniform meshes and skewed meshes are explored and both linear and non-linear results for both types of meshes show excellent agreement with available results in literature.

1. Linear Solution

First the linear solution to the FSDT was validated with analytical solutions to the equations. Consider a clamped-clamped isotropic plate with ν= 0.25, and K_s= 5/6, subject to uniformly distributed loading of intensity q_0. The following non-dimensionalization of the variables have been used in reporting the results:

$$\bar{w} = w_0(0,0)\frac{E_2 h^3}{a^4 q_0}$$

$$\bar{\sigma}_{xx} = \sigma_{xx}(0, 0, h/2)\frac{h^2}{b^2 q_0}$$
$$\bar{\sigma}_{yy} = \sigma_{yy}(0, 0, h/4)\frac{h^2}{b^2 q_0}$$
$$\bar{\sigma}_{xy} = \sigma_{xy}(a/2, b/2, -h/2)\frac{h^2}{b^2 q_0} \tag{3.22}$$

In the above equations a and b are the dimensions of the plate. Due to the symmetry of the plate and the boundary conditions only a quarter of the plate needed to have been modelled. The simply supported boundary condition of the SS1 type was used to obtain solutions to the problem and compare with analytical solutions to the same published elsewhere. A uniform 2×2 *hp*-spectral discretization with a $p = 8$, was used for determining the bending response for the low a/h ratio of 10 and a non-uniform 8×8 *hp*-spectral refinement of the domain with a p refinement of 4 was done to obtain the linear solution to the problem for an a/h of 100. The acceleration parameter was set to zero for all cases examined. Different a/h ratios were tried, a/h of 10 and 100 to check the effect of shear locking on the latter case. Figure10 presents the two different

Table XI. Series solutions vs. *hp*-SEM results

a/h	*Results*	w_{xx}	$\bar{\sigma}_{xx}$	$\bar{\sigma}_{xy}$
10	Present	0.047914	0.276267	0.208793
10	Analytic	0.047914	0.2762	0.2085
10	Skewed	0.047914	0.2763	0.2093
100	Present	0.0457234	0.276269	0.208822
100	Analytic	0.045698	0.2762	0.2085

types of *hp*- discretized meshes that were used for solving the linear problem for an

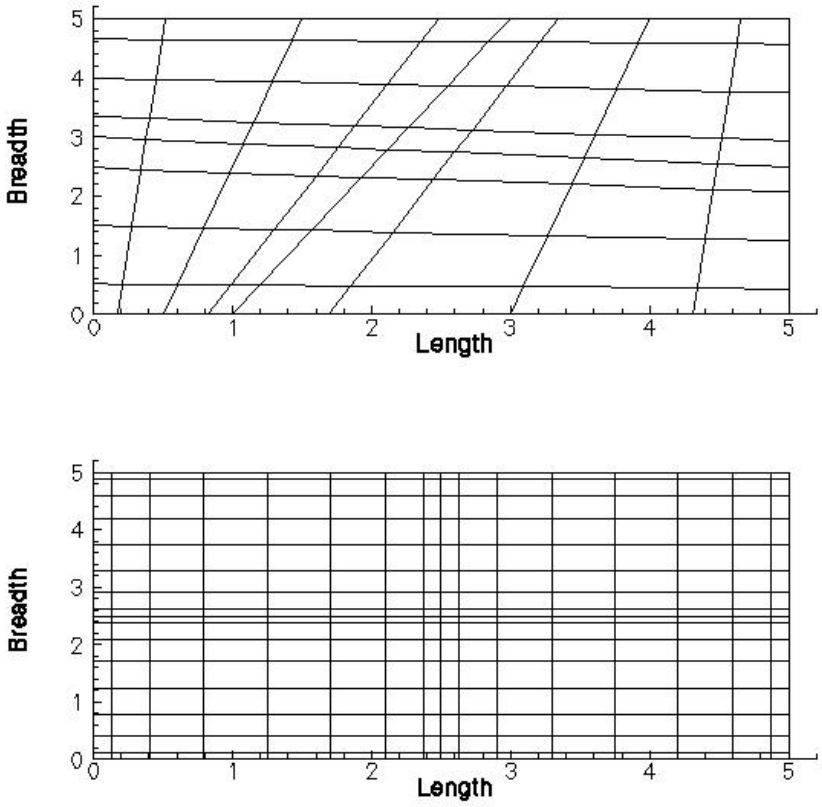

Fig. 10. *hp* spectral meshes used for linear problem

$a/h = 10$. The straight mesh consisted of a 2×2 mesh with an polynomial expansion of eight (8). The 2×2 skewed mesh is also presented in the figure. Considerable skew was introduced in the mesh however, as can be seen from Table XI there was no drastic deterioration in the results because of the skewness of the spectral mesh. The p_{value} tested for the skewed mesh was also relatively low at a value of four (4). The slight difference in the non-dimensional stress σ_{xy} can be attributed to the low value of p and for the following reason.

Some loss of accuracy during the calculation of the stresses during post-computation can attribute to the slight deviation of the results (fifth decimal place discrepancy)

from the analytical solution. Also, displacements for the $a/h = 100$ were found to be off also in the fifth decimal place which in high likelyhood was because in the evaluation of the series solution to the plate problem only the first nineteen terms were used. The problem posses bi-axial symmetry and therefore, only a quarter domain of the mesh needs to be modelled. However, it is also interesting to note that with one of the guass-points being at the end of the plate helps us to determine the center deflection at the exact center of the plate and no approximation with increasing order polynomials reaching the center of the plate asymptotically needs to be done for the *hp*-spectral mesh. This is invariably the case if Lagrange based higher-order elements are used and some form of interpolation has to be done to calculate the variables at the exact center of the plate. This note will also be found to affect the stress calculations slightly in the non-linear analysis.

hp-spectral element method naturally allows for such calculation of the primary and secondary variables at the edges of the plates and the center of the plate as demonstrated for the present example. It took three iterations to converge to the solution above. The problem was discretized with 1089 nodes and with five degrees of freedom per node resulted in a global system with 5445 degrees of freedom that were solved for the linear problem for the $a/h = 100$ case, whereas for the skewed mesh the number of equations solved to get reasonably accurate results, was 405. The above example demonstrates the relative ease with which the linear analysis of plates can be accomplished with fairly low degrees of freedom that need to be solved *without* the use of any reduced integration techniques and also demonstrates the possible extensions to non-rectangular and non-square shaped plates that can be studied even with fairly low computational resources available to the analyst. The *hp* convergence of the deflections, slopes, and stresses is being presented in Figure11. Some deviations from the linear curve at higher p_{levels} can be attributed to the numerical truncation

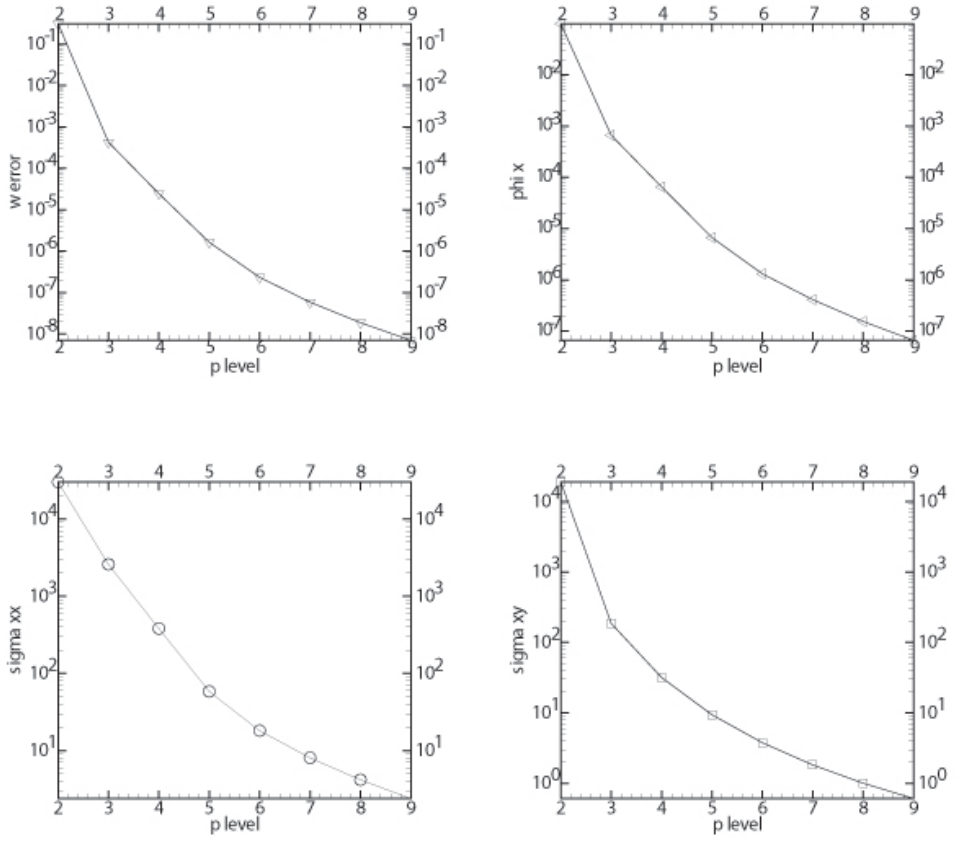

Fig. 11. *hp* convergence of variables for the linear problem

errors at such high resolutions of the errors.

2. Non-Linear Analysis of Isotropic Plates

Plates can be characterized as isotropic or orthotropic based on the inherent symmetries in the material property variations inside the plate. When there are no preferred directions in a material, the number of elastic constants used to characterize the material reduce to two namely the modulus of elasticity and the Poisson's ratio of the material. Plates made of such materials are characterized as isotropic plates. Here we consider the isotropic plates for non-linear analysis with the *hp*- spectral method sub-

ject to SS1, SS3, and Clamped-Clamped boundary conditions. In the FSDT model for the Reissner-Mindlin there exists a "'boundary layer"' extending into the plate a distance roughly equal to the thickness of the plate where there are large gradients in the stresses and the reactions [28],[29],[30]. Because of the presence of the boundary layer one has to discretize the *hp*-mesh to capture this effect and a graded mesh (graded towards the end of the plate) was utilized for the straight meshes. For the skewed mesh, also capturing the boundary layer is important in order not to lose the physics of the problem and the skewness of the mesh was enforced at the inside elements, the boundary layer was left, intact. The two different meshes that were used for the plate problem are shown in Figure12 below. The first mesh consisted of 6×6 *hp* refinements, and a 8×8 mesh with $p = 4$.

a. Isotropic Plates with SS1/SS3 Boundary Conditions

Consider a square plate uniformly loaded with a load intensity of q_0. The material parameters for the isotropic plate are:

$$a = b = 10\ in., h = 1\ in., E = 7.8 \times 10^6 psi, \nu = \ 0.30$$

The load steps that were used for the analysis are mentioned below:

$$\{\Delta P\} = \{6.25\ 6.25\ 12.5\ 25.0\ 25.0\ 25.0\ 25.0\ 25.0\ 25.0\ 25.0\ 25.0\ 25.0\} \qquad (3.23)$$

Table XII presents the development of the stresses, and deflections inside the isotropic plate subject to $SS1$ and $SS3$ boundary conditions with the different loads. The agreement between the present results and the published results is very good. Some differences in the stress calculations are evident and this is because of the slightly different locations of the Gauss-Points where the stress calculation was done. For the low-order bi-linear elements and the bi-quadratic elements there can be a substantial

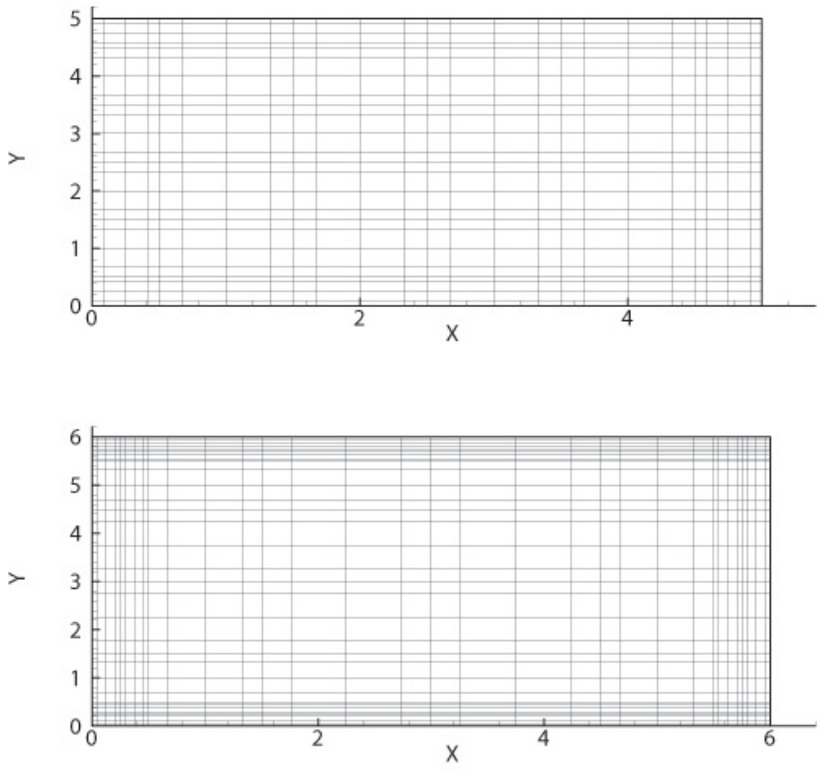

Fig. 12. *hp* spectral meshes for isotropic plate non-linear analysis

approximation in the location of the first Gauss point for the evaluation of the deflections. Also for the low order elements the stresses are evaluated at the reduced integration points which are even lower order (and further) from the edge of the plate.

As can be expected from the nature of the boundary conditions the SS1 boundary condition is less restrictive and allows for more deflection at the center of the plate as compared to the SS3 boundary condition. Figure 13 demonstrates this fact and it is clear that the clamped-clamped boundary condition is more restrictive in allowing deflections at the center of the plate as compared to the SS3 boundary condition.

Table XII. SS1/SS3 boundary conditions- isotropic plate

Results	SS3		SS1		Lagrange SS3		Lagrange SS1	
$\bar{P}$	w_0	$\bar{\sigma}_{xx}$	w_0	$\bar{\sigma}_{xx}$	w_0	$\bar{\sigma}_{xx}$	w_0	$\bar{\sigma}_{xx}$
6.25	0.2790	1.9140	0.2822	1.8387	0.2790	1.861	0.2813	1.779
12.5	0.4654	3.4128	0.5205	3.4980	0.4630	3.305	0.5186	3.396
25	0.6964	5.4793	0.8783	6.1552	0.6911	5.319	0.8673	5.882
50	0.9638	8.1746	1.3369	9.6490	0.9575	8.001	1.3149	9.159
75	1.1339	10.1160	1.6255	11.4085	1.1333	9.983	1.6241	11.458
100	1.2689	11.7917	1.8690	13.3794	1.2688	11.663	1.8687	13.299
125	1.3907	13.3285	2.0763	14.8577	1.3809	13.084	2.0758	14.878
150	1.4828	14.5801	2.2684	16.5013	1.4774	14.396	2.2567	16.278
175	1.5671	15.7737	2.4228	17.7798	1.5628	15.608	2.4194	17.553
200	1.6432	16.9205	2.5725	18.9404	1.6398	16.741	2.5681	18.733
225	1.7128	18.0861	2.7099	20.1026	1.7102	17.811	2.7056	19.837
250	1.7774	19.1010	2.8389	21.1629	1.7752	18.828	2.8338	20.880

For both the analysis presented above a *hp*-discretization of 6×6 graded mesh was found to be adequate. There were 625 nodes in the mesh with a total of 3125 degrees of freedom in the problem (ref. Figure 12). No relaxation parameter was utilized for convergence. Non-linear convergence was declared when the L^2 norm was less than 10^{-03} and the matrix solution convergence was declared when the L^2 norm was less than 10^{-06}. The problem typically required 3 iterations for the first few loadsteps, after which once the linear portion of the load-deflection behaviour was achieved; required 2 non-linear iterations for convergence. Figure 14 presents the development of the mid-fiber stress with the increasing loadsteps. The non-linear

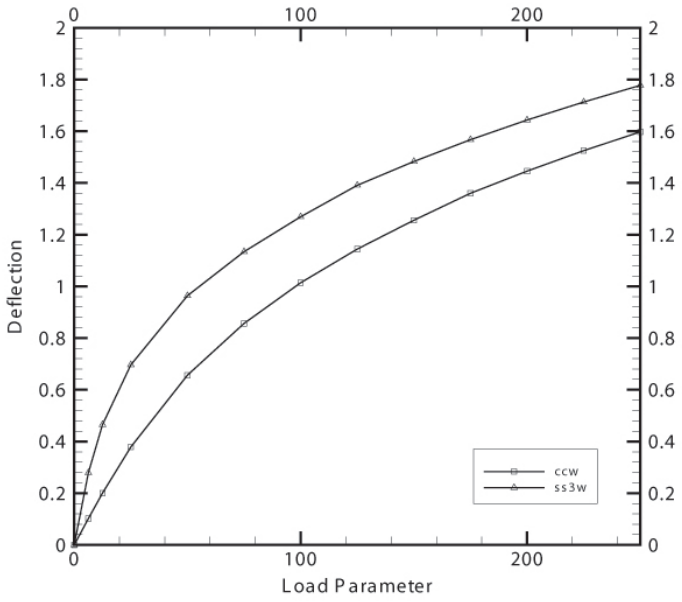

Fig. 13. *hp* convergence of variables for the linear problem

behaviour of the stresses as a function of the loading is evident. Figure 15 presents the development of displacement, slope, and stress fields inside the quarter isotropic plate of dimensions and material properties defined earlier. The whole development of fields can give an index of the stress concentrations and the contour plots of the deflections inside the plate.

3. Non-Linear Analysis of Orthotropic Plates

Orthotropic materials have two different principal axis for the material property variations. The number of independent elastic coefficients for an orthotropic plate are reduced to nine in three dimensions from a total of 81 constants of the fourth order tensor C_{ijkl}.

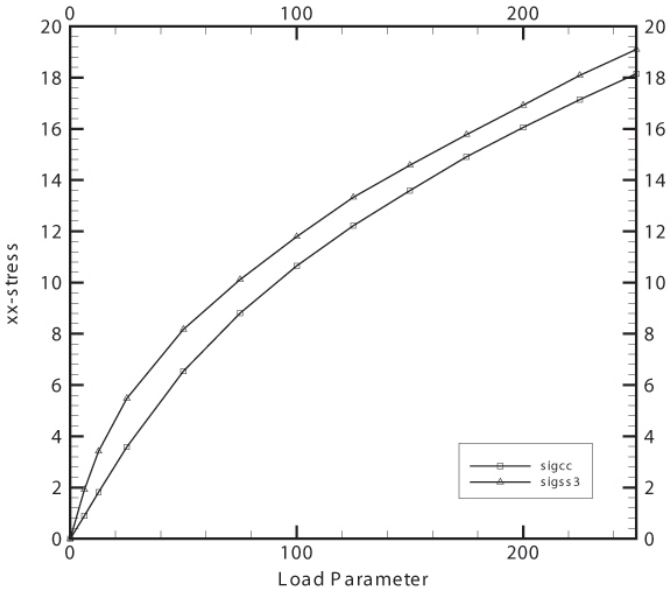

Fig. 14. σ_{xx} vs. the loading for isotropic plate

a. Orthotropic Plates with SS1/SS3 Boundary Conditions

Consider a square plate uniformly loaded with a load intensity of q_0. The material parameters for the orthotropic plate are:

$$a = b = 12\ in., h = 0.138\ in., E_1 = 3.0 \times 10^6\ psi, E_2 = 1.28 \times 10^6\ psi$$
$$G_{12} = G_{13} = G_{23} = 0.37 \times 10^6\ psi, \nu_{12} = \ 0.32$$

The incremental load vector that was used for the analysis:

$$\{\Delta P\} = \{0.05\ 0.05\ 0.10\ 0.10\ 0.10\ 0.10\ 0.10\ 0.10\ 0.10\ 0.10\ 0.10\ 0.10\} \qquad (3.24)$$

Figure 16 shows the deflections and stresses inside the orthotropic plate subject to the SS1 and SS3 boundary conditions with increasing load parameters. Figure 17 shows the development of deflections, angles, and stresses, inside the orthotropic plate when subject to the SS1 boundary condition. The difference in the development of these

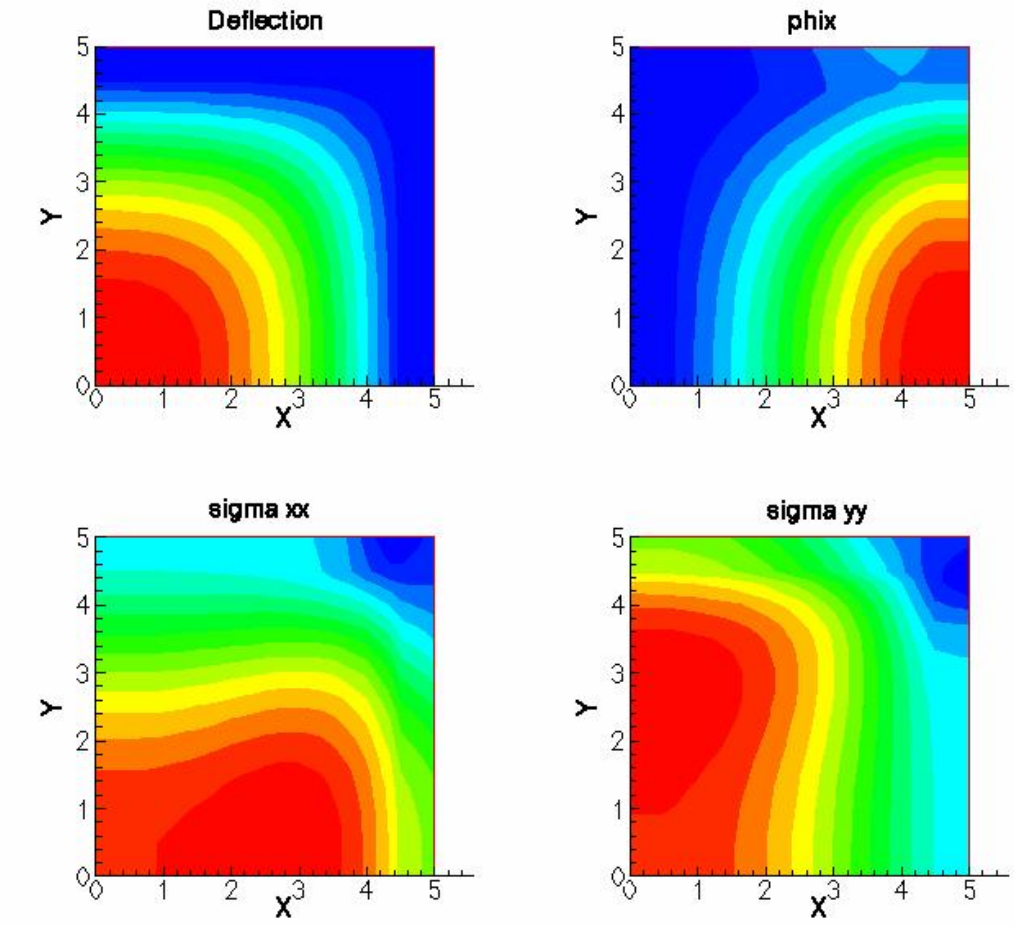

Fig. 15. Displacement, slopes, and stresses inside an isotropic plate

fields with the isotropic case is evident. An 8×8 *hp*-spectral mesh was used with 1089 nodes and 5445 degrees of freedom. No relaxation parameter was utilized for convergence. Non-linear convergence was declared when the L^2 norm was less than 10^{-03} and the matrix solution convergence was declared when the L^2 norm was less than 10^{-06}. For this analysis the Direct method or the Picard method was used to iterate for non-linear convergence. The problem typically required between 3 to 6 iterations for convergence. The corresponding results that were obtained with Lagrange based

Table XIII. SS1/SS3 boundary conditions- orthotropic plate

Results	SS1		SS3		Lagrange SS1		Lagrange SS3	
$\bar{P}$	w_0	$\bar{\sigma}_{xx}$	w_0	$\bar{\sigma}_{xx}$	w_0	$\bar{\sigma}_{xx}$	w_0	$\bar{\sigma}_{xx}$
0.05	0.0112	1.0724	0.0112	1.0989	0.0112	1.0663	0.01126	1.0938
0.10	0.0224	2.1495	0.0218	2.2023	0.0224	2.1365	0.02182	2.1923
0.20	0.0438	4.2604	0.03973	4.2264	0.0437	4.2174	0.03970	4.2045
0.40	0.0815	8.0472	0.0649	7.3772	0.0819	8.0669	0.06497	7.3441
0.60	0.1122	11.1570	0.0824	9.7487	0.1125	11.139	0.08244	9.7088
0.80	0.1382	13.6495	0.0961	11.7074	0.1379	13.669	0.09589	11.6310
1.00	0.1596	15.8089	0.1070	13.3426	0.1781	17.478	0.106861	13.2487
1.20	0.1785	17.6151	0.1163	14.7870	0.1864	18.305	0.11622	14.6995
1.40	0.1952	19.0488	0.1245	16.0939	0.1960	19.303	0.12442	16.0021
1.60	0.2104	20.7772	0.1318	17.2903	0.2106	20.7526	0.13174	17.2083
1.80	0.2242	21.8133	0.1384	18.4052	0.2245	22.0648	0.1383	18.3138
2.00	0.2371	23.0114	0.1445	19.4510	0.2373	23.2709	0.14446	19.3539

interpolation functions with reduced integration has also been included in Table XIII to provide a context for comparison with present results.

b. Clamped Clamped Isotropic/Orthotropic Plates

Consider a square plate uniformly loaded with a load intensity of q_0. The material parameters and load steps/load vectors that were used for the analysis of the isotropic and orthotropic plates have been listed above separately. The orthotropic plate with the material properties defined above when subjected to an load intensity of q_0 is of interest in this section, and the boundary condition explored for this analysis was a

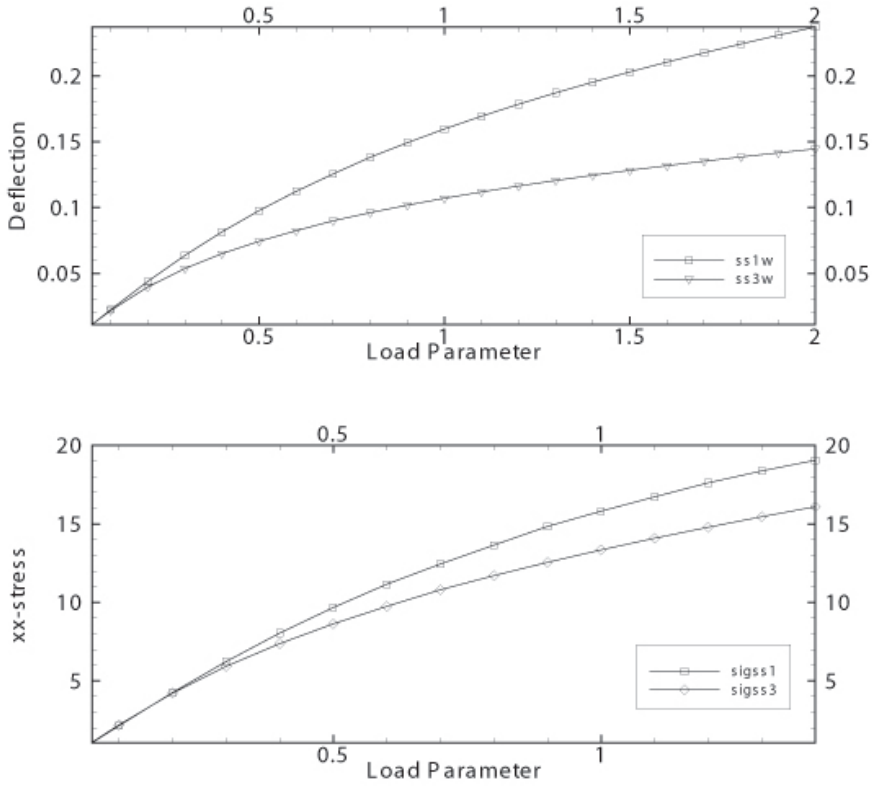

Fig. 16. Deflections and stress inside an orthotropic plate

clamped- clamped case. An 8×8 *hp*-spectral mesh was used with 1089 nodes and 5445 degrees of freedom for the above analysis. No relaxation parameter was found necessary for convergence. Non-linear convergence was declared when the L^2 norm was less than 10^{-03} and the matrix solution convergence was declared when the L^2 norm was less than 10^{-06}. For this analysis the the Newton-Raphson's method was used to iterate for non-linear convergence. The problem typically required 3 iterations for convergence. The corresponding results that were obtained with Lagrange based low-order expansions with reduced integration techniques has also been included in

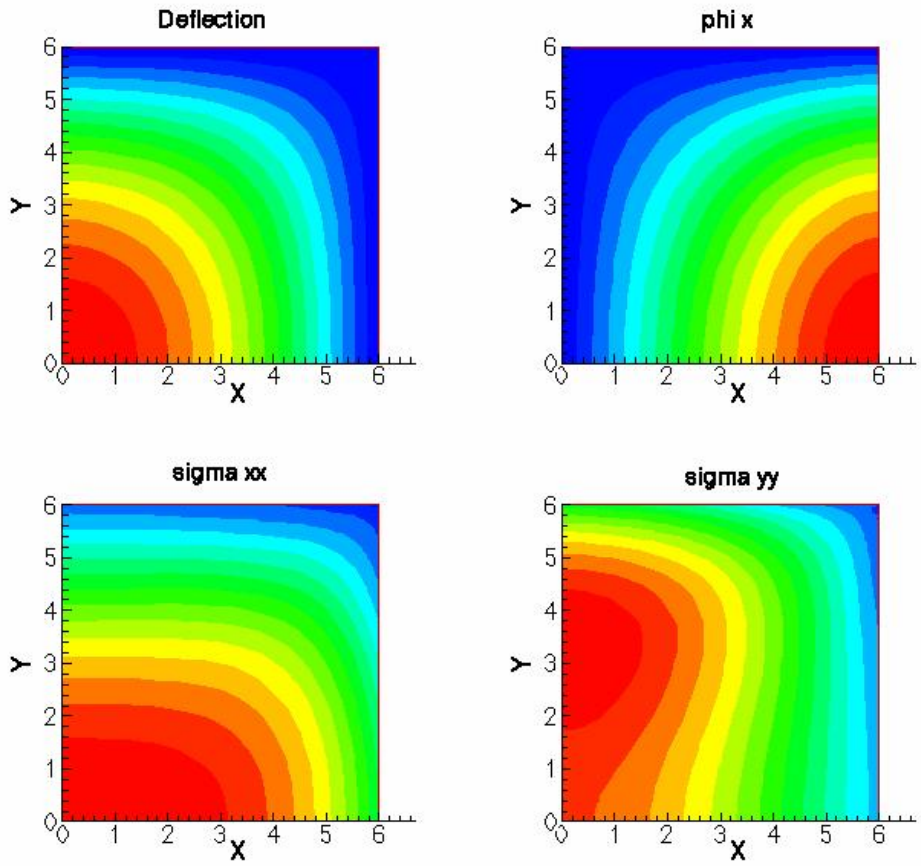

Fig. 17. Displacement, slopes, and stresses inside an orthotropic plate

Table XIV to demonstrate the efficacy of the *hp*-element methods over the traditional reduced integration techniques.

c. Clamped-Clamped Orthotropic Plate on Opposite Edges

Let us consider a orthotropic plate subjected to a uniformly distributed load of intensity q_0. The plate is clamped at the two opposite ends of the domain. Material parameter values that characterize the plate are described below:

$$a = b = 10\ in., h = 0.138\ in., E_1 = 3.0 \times 10^6\ psi, E_2 = 1.28 \times 10^6\ psi$$

Table XIV. CC boundaries isotropic/orthotropic plate results

Isotropic		Present		Lagrange	
$\bar{P}$	ref.	w_0	$\bar{\sigma}_{xx}$	w_0	$\bar{\sigma}_{xx}$
0.05	Results	0.1020	0.8961	0.1021	0.8877
0.10	Results	0.2006	1.8156	0.2007	1.7987
0.20	Results	0.3787	3.5860	0.3787	3.5536
0.40	Results	0.6564	6.5420	0.6546	6.4794
0.60	Results	0.8564	8.8040	0.8561	8.7397
0.80	Results	1.0138	10.6509	1.0142	10.5819
1.00	Results	1.1441	12.2197	1.1445	12.1558
1.20	Results	1.2557	13.5905	1.2561	13.5478
1.40	Results	1.3599	14.9101	1.3542	14.8086
1.60	Results	1.4456	16.0543	1.4421	15.9683
1.80	Results	1.5247	17.1388	1.5218	17.0565
2.00	Results	1.5973	18.1523	1.5950	18.0803

$$G_{12} = G_{13} = G_{23} = 0.37 \times 10^6 \; psi, \nu_{12} = \; 0.32$$

An 8×8 *hp*-spectral mesh was used with 1089 nodes and 5445 degrees of freedom for Table XV. No relaxation parameter was utilized for convergence. Non-linear convergence was declared when the L^2 norm was less than 10^{-03} and the matrix solution convergence was declared when the L^2 norm was less than 10^{-06}. For this analysis the Newton-Raphson's method was used to iterate for non-linear convergence. The problem typically required 3 iterations for convergence. The corresponding results that were obtained with Lagrange based low-order expansions with reduced integration techniques has also been included in Table XV to demonstrate the efficacy of the

Table XV. CC boundaries orthotropic plate results

Orthotropic	Present		Lagrange	
$\bar{P}$	w_0	$\bar{\sigma}_{xx}$	w_0	$\bar{\sigma}_{xx}$
0.10	0.0060	0.9141	0.0060	0.9041
0.40	0.0236	3.7307	0.0237	3.6904
0.80	0.0453	7.4096	0.0454	7.3341
1.00	0.0552	9.1383	0.0552	9.0470
1.20	0.0643	10.7718	0.0643	10.6682
1.60	0.0805	13.7586	0.0806	13.6295
2.00	0.0949	16.4386	0.0947	16.2583
4.00	0.1466	26.3920	0.1455	26.0928
8.00	0.2054	38.6526	0.2054	38.3693
12.00	0.2462	47.7959	0.2448	47.1947
16.00	0.2760	55.1212	0.2752	54.7676
20.00	0.3011	61.8126	0.3005	61.4079
22.00	0.3123	64.9234	0.3117	64.4918
24.00	0.3227	67.8604	0.3223	67.4446

hp-element methods over the traditional reduced integration techniques. Figure 18 shows the development of the deflections and stresses inside the orthotropic plate subject to the CFFC boundary conditions with increasing load parameters. Figure 19 exhibits the linear convergence history for a thin plate a/h=100 subject to different boundary conditions. From the convergence history also one can infer that the clamped-clamped boundary condition leads to the best conditioning of the global system which can be solved more easily with the preconditioned conjugate gradient

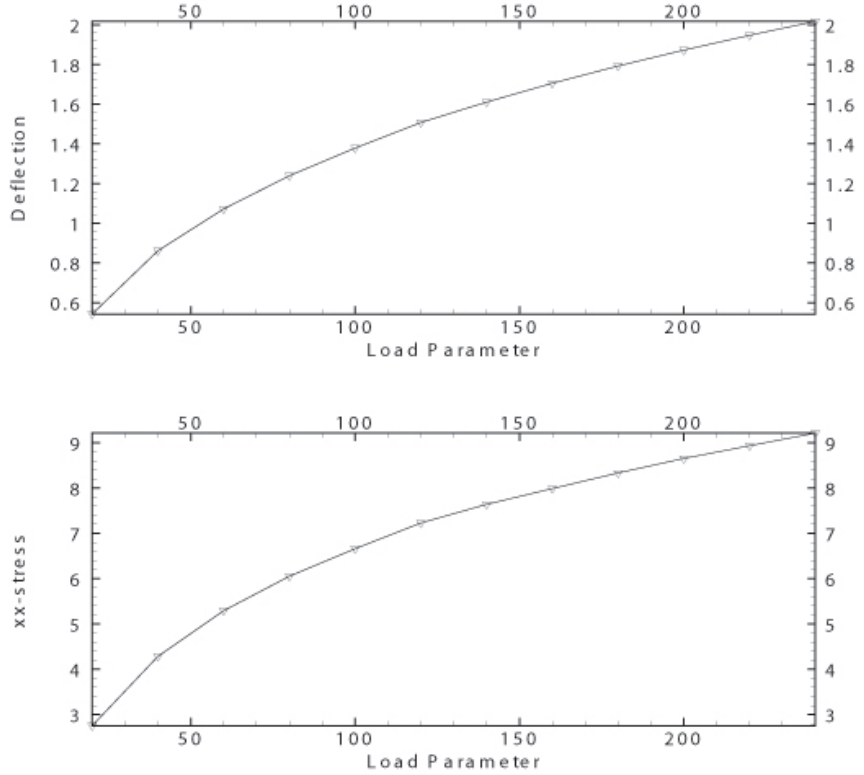

Fig. 18. Deflections/stress development subject to CC B.C.

solver.

d. Skewed Mesh Comparison with Straight Mesh

Let us consider an orthotropic plate subject to uniformly distributed load of intensity q_0 for non-linear analysis with skewed *hp*-spectral mesh discretization. The material property values used for the problem have been described earlier and a quarter plate was modelled subject to SS1 boundary conditions. The mesh that was used for the analysis has been presented in Figure12. Table XVI presents the agreement between the results from the *hp*-spectral mesh with the results found by using straight mesh

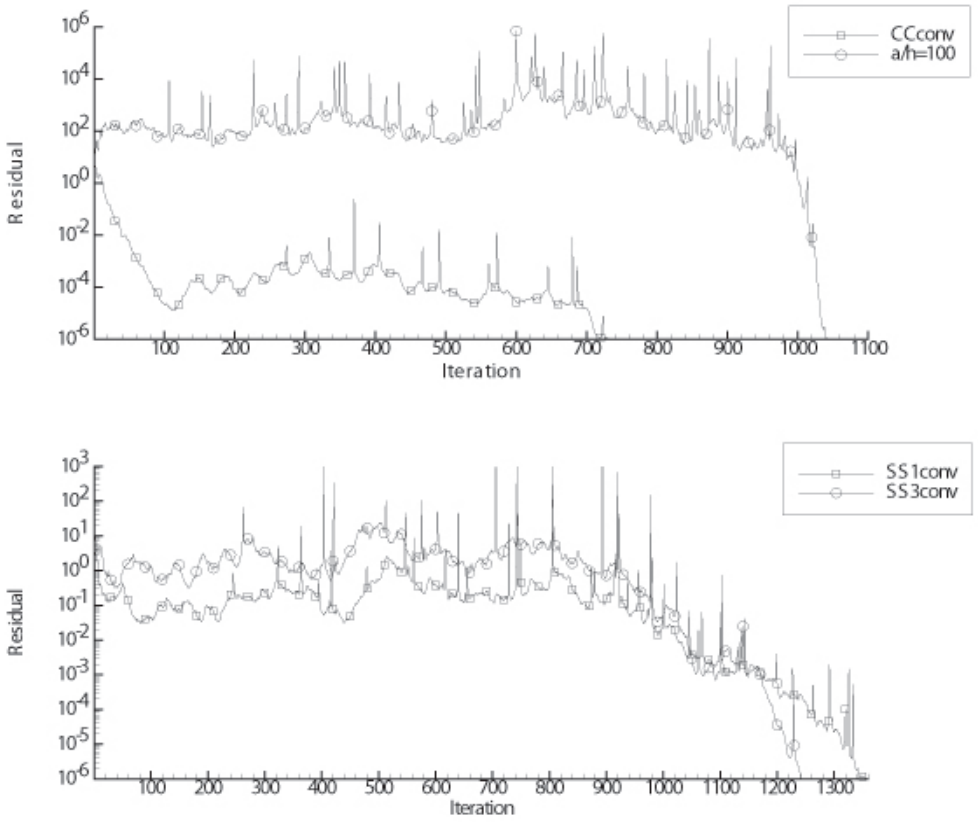

Fig. 19. Convergence history for different boundary conditions

both with inclusion of the boundary layer refinements. As can be seen from the Table XVI there is excellent agreement found between the straight mesh results and the skewed mesh results. The R^2 between the deflections predictions for both cases was found to be 0.99999, demonstrating the predictive capabilities of *hp*-spectral element skewed meshes. The stress predictions had an R^2 value of 0.99978, which was slightly lower than the agreement with the deflections. However, for both cases the predictions can be considered excellent. The aforementioned Table XVI also conclusively shows that there is no perceptible deterioration in accuracy of results

from the *hp*-spectral skewed meshes as compared to the straight meshes for both the linear and non-linear problems. Figure 20 presents the skewed mesh used for the

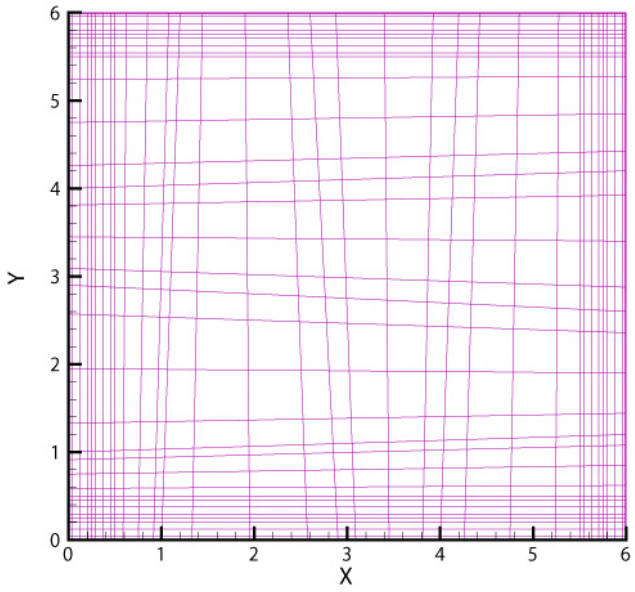

Fig. 20. Skewed mesh used for non-linear analysis

non-linear analysis for the orthotropic plate. The refinements at the boundary layers is necessary for capturing the correct stress concentrations at the ends of the plate and in predicting the correct bending response.

Table XVI. Skewed mesh results vs. straight mesh

Orthotropic		Skew		Straight	
$\bar{P}$	Ref.	w_0	$\bar{\sigma}_{xx}$	w_0	$\bar{\sigma}_{xx}$
0.05	present	0.0112	1.0715	0.0112	1.0724
0.1	present	0.0224	2.1467	0.0224	2.1495
0.2	present	0.0438	4.2545	0.0438	4.2604
0.3	present	0.0636	6.2393	0.0636	6.2330
0.4	present	0.0815	8.0440	0.0815	8.0472
0.5	present	0.0976	9.6782	0.0976	9.6739
0.6	present	0.1122	11.1739	0.1122	11.1570
0.7	present	0.1255	12.4775	0.1255	12.4430
0.8	present	0.1382	13.7507	0.1382	13.6495
0.9	present	0.1492	14.7966	0.1492	14.8382
1.0	present	0.1596	15.8112	0.1596	15.8089
1.1	present	0.1693	16.7230	0.1693	16.7185
1.2	present	0.1785	17.6126	0.1785	17.6151
1.3	present	0.1871	18.4448	0.1871	18.3689
1.4	present	0.1952	19.1858	0.1952	19.0488
1.5	present	0.2030	19.9645	0.2030	19.9596
1.6	present	0.2104	20.7010	0.2104	20.7772
1.7	present	0.2175	21.3376	0.2175	21.2264
1.8	present	0.2243	22.0986	0.2242	21.8133
1.9	present	0.2308	22.7217	0.2308	22.7114
2	present	0.2371	23.4157	0.2371	23.0114

CHAPTER IV

SPECTRAL/HP METHODS FOR LARGE DEFORMATION ANALYSIS

A. Introduction

In this chapter we explore the usage of higher order hp-spectral element methods applied to solving Continuum mechanics based large deformation analysis of structures in particular with the Updated Lagrangian description of motion. We start with a literature review in this field regarding large deformation analysis of structures, and then describe the governing equations and the formulation followed by results.

The motion of a body can be described with the help of a material or a spatial formulation. The spatial formulation studies the conservation equations that are applied to a fixed region in space whereas the material formulation studies the changes in these equations as the body undergoes deformation. The material/Lagrangian description of motion is the norm for application to structures problems. The Lagrangian description is natural for a solid body since one is more interested in the deformation of the body as opposed to the changes that are taking place in the control volume that was initially occupied by the body. Applications of hp-spectral methods in the current context has been explored, as these provide exponentially accurate spatial resolutions of the motion of the body undergoing deformation. Two cases, of the deformation of a cantilever beam, and a fixed beam at both ends are explored and results are checked with the benchmark solutions and good agreement with the published results are reported. The use of hp-spectral methods applied to solving these continuum mechanics formulations is advocated to generate more confidence in the results, as during the equilibrium iterations for reducing the residuals of the unbalanced virtual work, these higher order methods provide better spatial resolutions

of the results as compared to lower order finite element formulations and provide for a better minimization statement.

There are two different methods by which the description of motion of a body can be formulated. The first is the Total Lagrangian formulation where the final configuration of the body is described with reference to the initial undeformed configuration of the body. The second is the Updated Lagrangian formulation where the latest known configuration of the body is the reference configuration. The applications of the Total and Updated Lagrangian formulations have been performed by different researchers [31],[32], [33]. It has been mentioned that the Total and Updated Lagrangian formulations are both equivalent in the description of the motion of bodies, and for most cases the Updated Lagrangian formulation is recommended because of the relative simplicity of the formulation [34].

During the process of non-linear equilibrium iterations for the Updated Lagrangian formulations the displacements of the body undergoing deformation is updated with the corresponding increments. It is therefore, an issue with *hp*-spectral methods, that the deformed configuration of the body be incremented with accurate predictions of these displacement increments. It is in this context, that *hp*-spectral methods provide spectrally accurate spatial resolutions of these increments as compared to Lagrange based finite element methods which can at best provide error estimates in the order of O^{hp+1} in spatial resolutions; when bi-quadratic elements are used p=2. In comparison *hp*-spectral methods can provide exponential decay of the errors in the increments for the problem of interest [1]. It is anticipated that the convergence characteristics, and the spatial resolutions provided by the spectral methods for the linear problem are also spectrally convergent to the non-linear solutions of the more general problems solved, thus guaranteeing better results as compared to the usage of Lagrange based finite element methods.

Continuum mechanics formulations based on both the Updated and Total Lagrangian formulations have been used by different researchers for example for modelling plane elastic problems [31], for the analysis of stiffened composite laminates [35], for studying the large deformation analysis for beam structures amongst others [36]-[37]. Bathe et al. [34] noted that for the small strain cases of a beam bending the stiffness matrices for the Total and Updated Lagrangian formulations for the three dimensional beam element studied are equal. A comparison of the Eulerian and the Updated Lagrangian finite element formulations for simulating the film casting process has been studied by [32]. They also checked the closed form solutions to the velocity, thickness, and stress for 1D film casting of a viscous fluid. The errors that they found between the analytical results and the series solutions were found to decay in the appropriate norms with algebraic rates of convergence. They also concluded that the Updated Lagrangian formulation is more robust as compared to the Eulerian formulation that they had employed because it more naturally picks up the steady state solution whereas the Eulerian formulation has a smaller convergence radius, meaning that the initial solution has to be fairly close to the actual solution to obtain correct results and avoid divergence. The use of Updated Lagrangian formulations for studying contact problems was explored in [37]. Geometric and material nonlinearities were incorporated with the Updated Lagrangian formulations. They used regularization technique for handling the friction terms in their formulation.

This study proposes to advance the use of appropriate *hp*-refinements for studying the Updated Lagrangian formulation for studying the bending response of beams. The motivation for this study comes from the many advantages that are associated with *hp*-higher order elements; spectral convergence (accuracy) of the solutions, and the orthogonality property of nodal expansions which provide excellent results with standard solvers like the preconditioned bi-orthogonal conjugate gradient (BPCG)

alleviating the problem of ill-conditioning of the discrete problem ascribed to the usage of higher-order equispaced Lagrange based interpolants. The convergence history of the bi-orthogonal conjugate gradient solver with preconditioning is also reported to get further insight into the problem formulation and convergence behaviour with *hp*-spectral methods.

B. Governing Equations

Consider the motion of a body in a fixed Cartesian coordinate system. Suppose that the body can experience large displacements, large strains, and non-linear mechanical behaviour. We wish to determine the configuration of the body for different times and loads. The configuration to be described assumes that the configuration of the body C_1, due to P_1 at time t, is known and seeks the configuration C_2 at time $t + \Delta t$. This type of description where we follow the material from the configuration C_1 to C_2 is known as the material description or the Lagrangian description of motion, which differs from the Eulerian description of motion that is common for fluid mechanics applications. In the Lagrangian description of motion the configuration of the body has to be known with respect to one of the earlier configurations which we have the flexibility of deciding, which we want to choose as the reference configuration [38]. A description in which the last known configuration is taken as the reference configuration is called the Updated Lagrangian description (UL) of motion. The configuration in which all variables are referred to the initial configuration is called the Total Lagrangian (TL) description of motion [11]. It has been mentioned that the Updated and Total Lagrangian descriptions of motion are equivalent and the decision of which of these formulations to use is really a matter of personal choice or ease of programming in most cases. The results obtained from either formulations are identical in

the limit of the incremental decompositions reaching zero, between two successive configurations. In the present work, thus only UL formulation has been addressed, based on the above arguments, as no significant advantage is expected from using a TL formulation. The basic principle that is used in the formulation for either of the formulations is the principle of virtual work (that is virtual displacements, virtual forces, or mixed virtual displacements and virtual forces). The principle of virtual work requires that the sum of the internal work done by the virtual work stored in the body, and the external applied body forces and tractions is equal to zero.

$$\int_{V_2}^{2} \sigma_{ij}\delta_2(e_{ij})dV - \delta({}^2F) = 0 \tag{4.1}$$

where,

$$\delta({}^2F) = \int_{V_2}^{2} f_i \delta u_i dV + \int_{S_2}^{2} t_i \delta u_i dS \tag{4.2}$$

and, ${}^2\sigma_{ij}$ are the Cartesian components of the Cauchy stress tensor, in configuration C_2 at time, $t + \Delta t$, occupying the volume V_2, e_{ij} are the Cartesian components of the infinitesimal strain tensor associated with the displacements, u_i in going from configuration C_1 at time t to C_2 at time $t + \Delta t$.

$$e_{ij} = \frac{1}{2}\left(\frac{\partial u_i}{\partial x_j} + \frac{\partial u_j}{\partial x_i}\right) \tag{4.3}$$

x_i are the Cartesian components of a point in C_2. ${}^2f_i$ are the Cartesian components of the body force vector, measured in C_2. ${}^2t_i$ are the Cartesian components of the surface stress vector, measured in C_2. In the above notation, δ denotes the variational symbol, (that is δu_i denotes virtual displacement) and dV and dS denote the volume and surface elements in the configuration over which the integrals are defined. The main problem with the statement of the virtual work as presented in equation [11] is that the final deformed volume V_2 and the surface area, S_2 of the body is yet unknown.

In a linear analysis of the body it is assumed that the initial configuration of the body is unchanged and thus equation 4.1 is applied to the undeformed configuration of the body. The fact that the configuration of the body is changing continuously requires us to be careful of the stress and strain measures and Bathe's notation [34] is employed for clarity. In order to completely specify the configuration C_2 that is obtain, the measures of stress, strain, and displacements in C_2 it is necessary to make some assumptions. A description of the procedure based on the UL formulation is given below. The coordinates of the body in the configuration C_0, C_1, and C_2 is denoted by $(X_1^0,\, X_2^0,\, X_3^0)$, $(X_1,\, X_2,\, X_3)$, and $(x_1,\, x_2,\, x_3)$ respectively. The displacements of a point in C_1 are given by $({}^1u_1, {}^1u_2, {}^1u_3)$. In C_2 they are given by the following;

$$ {}^2u_i = {}^1u_i + u_i \tag{4.4} $$

for, i= 1,2, and 3. where, u_i are the components of the displacement vector from configuration C_1 to C_2. When the body that is deforming it is undergoing change in its configuration and the stresses, configurations, densities, volumes and surface area, all change with this deformation. Thus different measures of the stresses are needed to appropriately describe this motion of the body. The Cauchy stress σ is defined to be the current force per unit deformed area of the body. The second Piola-Kirchhoff stress tensor is introduced as a symmetric tensor which measures the transformed current force per unit undeformed area. The Cauchy stress tensor is defined by the following relationship:

$$ (\hat{n}t)\; dS = dF \tag{4.5} $$

where, the force $d\mathbf{F}$ acts on the surface area dS in configuration C_2. Here t is the Cauchy stress tensor. Note that the Cauchy stress tensor is the force per unit deformed area that is measured in C_2 and referred to C_2. The second Piola Kirchhoff stress

tensor, at time $t + \Delta t$ measured in C_1, is defined by the following;

$$(\hat{n_0}\ {}^2_1S)\ dS_0 = dF \tag{4.6}$$

where, n_0 is the normal to the surface element dS_0 in C_1. The force dF_0 is related to the force dF by, the following;

$$dF_0 = J^{-1}dF \tag{4.7}$$

where,

$$J^{-1} = \left(\frac{\partial X}{\partial x}\right)^T \tag{4.8}$$

The second Piola-Kirchhoff tensor is thus measured in the configuration C_2 but referred to C_1. It can be shown that [11] the components of the stress tensor, ${}^2_1S_{ij}$ and ${}^2_2C_{ij}$, are related according to;

$${}^2_1S_{ij} = \frac{{}^1\rho\ \partial^1 x_i\ \partial^1 x_j}{{}^2\rho\ \partial^2 x_p\ \partial^2 x_q}\ {}^2\sigma_{pq} \tag{4.9}$$

In the above derivations, the densities at the appropriate locations in the C_1 and C_2 configurations have been included. Note, that the second Piola-Kirchhoff stress tensor is symmetric whenever the Cauchy stress tensor is symmetric by construction. Similarly, the Green-Lagrange strain tensor E_{ij} is related to the Almansi stress tensor with the following relationships:

$${}^2_1E_{ij} = \frac{\partial^1 x_i\ \partial^1 x_j}{\partial^2 x_p\ \partial^2 x_q}\ {}^2\sigma_{pq} \tag{4.10}$$

In continuum mechanics various measures of stress and strains enter the formulations for describing the different deformed shapes of a body undergoing large deformations. However, some anchoring of these ideas also has to be done and in this context, the work conjugacy of different measures of stresses and strains is of interest. The second Piola-Kirchhoff stress tensor is energetically conjugate to the Green-Lagrange strain

tensor, and the Cauchy stress tensor is energetically conjugate to the Almansi stain tensor. In other words, the work done with the inner products of the respective pairs amount to the same amount of virtual work done. In integral form this relationship can be expressed as;

$$\int_{V_1}^{2} {}^{2}_{1}S_{ij}\ \delta\left({}^{2}_{1}E_{ij}\right)\ dV = \int_{V_2}^{2} {}^{2}_{1}\sigma_{ij}\ \delta\left({}^{2}_{2}e_{ij}\right)\ dV \tag{4.11}$$

substituting the above relationship into the virtual work principle equation 4.1 one obtains;

$$\int_{V_1}^{2} {}^{2}_{1}S_{ij}\ \delta\left({}^{2}_{1}E_{ij}\right) dV - \delta({}^{2}F) = 0 \tag{4.12}$$

The main advantage with the present formulation is that the same amount of virtual work is done with the evaluations of the above integrals in equation 4.1 as compared to the equation 4.12 in terms of the known volume of the configuration C_1. The next, step is the incremental decompositions of the stress and the strain measures. The stresses are decomposed based on the assumption that the second Piola-Kirchoff stress components in measured in C_1 but occurring in C_2, can be decomposed into Cauchy component in the known configuration and an unknown stress component. The equations for the incremental stress and strain components are described below;

$$\begin{aligned} {}^{2}_{1}S_{ij} &= {}^{1}\sigma_{ij} + {}_{1}S_{ij} \\ {}^{1}_{1}S_{ij} &= {}^{1}_{1}\sigma_{ij} \end{aligned} \tag{4.13}$$

and,

$${}^{2}_{1}\varepsilon_{ij} = {}_{1}e_{ij} + {}_{1}\eta_{ij} \tag{4.14}$$

where, ${}_1S_{ij}$ is the incremental components of the second Piola-Kirchhoff stress tensor, e_{ij} is the (linear) components of the Green-Lagrange strain tensor, given as;

$$ {}_1e_{ij} = \frac{1}{2}\left(\frac{\partial u_i}{\partial X_j} + \frac{\partial u_j}{\partial X_i}\right) \tag{4.15} $$

and,

$$ {}_1\eta_{ij} = \frac{1}{2}\left(\frac{\partial u_m \partial u_m}{\partial X_i \partial X_j}\right) \tag{4.16} $$

Recall that u_i is the i^{th} displacement component of a generic point in C_1 (in going from C_1 to C_2). Also, the Cauchy stress tensors and the strain tensors are related by the stiffness tensor as the following;

$$ \begin{aligned} {}^1\sigma_{ij} &= C_{ijkl}\ {}^1_1\varepsilon_{kl} \\ {}_1S_{ij} &= C_{ijkl}\ {}^2_1\varepsilon_{kl} \end{aligned} \tag{4.17} $$

Substituting the above equations into the virtual work statement, we obtain the virtual work statement expressed in the following form;

$$ \int_{V_1} {}_1S_{ij}\ \delta\left({}^2_1e_{ij}\right)\ d^1V - \int_{V_1} {}^1\sigma_{ij}\ \delta\left({}_1\eta_{ij}\right)\ d^1V = \delta\left({}^2_1R\right) - \int_{V_1} {}^1\sigma_{ij}\ \delta\left({}_1e_{ij}\right)\ d^1V \tag{4.18} $$

The linearization of the above equation is achieved with the help of the following approximations [11]:

$$ \begin{aligned} {}_1S_{ij} = {}_1C_{ijkl}\ {}^2_1\varepsilon_{kl} &\approx {}_1C_{ijkl}\ {}_1e_{kl} \\ \delta_1 e_{kl} &\approx \delta e_{ij} \end{aligned} \tag{4.19} $$

Along with the above linearizations (approximations) we obtain the final form of the principle of virtual work as follows;

$$ \int_{V_1} {}_1C_{ijkl}\ e_{kl}\ \delta\left({}_1e_{ij}\right)\ d^1V - \int_{V_1} {}^1\sigma_{ij}\ \delta\left({}_1\eta_{ij}\right)\ d^1V = \delta\left({}^2_1R\right) - \int_{V_1} {}^1\sigma_{ij}\ \delta\left({}_1e_{ij}\right)\ d^1V \tag{4.20} $$

The right hand side in equation 4.20 represents the out of balance virtual work, prior to the calculation of the increments in the displacements whereas the left hand side represents the out of balance virtual work after the solution, as a result of the linearizations performed [34]. We set out to perform the equilibrium iterations to solve for the out of balance virtual work in the incremental procedure of iterating for the solution of the non-linear problem. In some sense, this is similar to the Newton Raphsons method for iterating for the increments which is extensively used in standard finite element procedures. In the present formulation we have confined ourselves to studying the displacement based incremental formulations with the Updated Lagrangian description of motion. As demonstrated elsewhere, mixed formulations based on the above principles is also an option and has been studied in the context of UL formulations [38].

C. Finite Element Formulation

The complete derivation of the principle of virtual work with the incremental formulation was mentioned in the last section. Here we highlight some of the main issues while deriving the stiffness matrices for UL formulations. The main issue with the derivations is the expressions of the strain tensor in the Cartesian coordinate systems where they are defined as follows;

$$\left\{ \ {}_1e \ \right\} = \left\{ \begin{array}{c} \frac{\partial \bar{u}}{\partial x} \\ \frac{\partial \bar{v}}{\partial y} \\ \frac{\partial \bar{u}}{\partial y} + \frac{\partial \bar{v}}{\partial x} \end{array} \right\} \tag{4.21}$$

Therefore, taking the variation the strain tensor; we obtain the following;

$$\left\{ \begin{array}{c} {}_1\delta e \end{array} \right\} = \left\{ \begin{array}{c} \frac{\partial \delta \bar{u}}{\partial x} \\ \frac{\partial \delta \bar{v}}{\partial y} \\ \frac{\partial \delta \bar{u}}{\partial y} + \frac{\partial \delta \bar{v}}{\partial x} \end{array} \right\} \tag{4.22}$$

And non-linear components of the strain tensor are defined as follows;

$$\left\{ \begin{array}{c} {}_1\eta \end{array} \right\} = \frac{1}{2} \left\{ \begin{array}{c} \frac{\partial \bar{u}}{\partial x}\frac{\partial \bar{u}}{\partial x} + \frac{\partial \bar{v}}{\partial x}\frac{\partial \bar{v}}{\partial x} \\ \frac{\partial \bar{u}}{\partial y}\frac{\partial \bar{u}}{\partial y} + \frac{\partial \bar{v}}{\partial y}\frac{\partial \bar{v}}{\partial y} \\ \frac{\partial \bar{u}}{\partial x}\frac{\partial \bar{u}}{\partial y} + \frac{\partial \bar{v}}{\partial x}\frac{\partial \bar{v}}{\partial y} \end{array} \right\} \tag{4.23}$$

Taking the variation of the above quantity we obtain the following;

$$\left\{ \begin{array}{c} {}_1\delta\eta \end{array} \right\} = \left\{ \begin{array}{c} \frac{\partial \delta \bar{u}}{\partial x}\frac{\partial \bar{u}}{\partial x} + \frac{\partial \delta \bar{v}}{\partial x}\frac{\partial \bar{v}}{\partial x} \\ \frac{\partial \delta \bar{u}}{\partial y}\frac{\partial \bar{u}}{\partial y} + \frac{\partial \delta \bar{v}}{\partial y}\frac{\partial \bar{v}}{\partial y} \\ \frac{\partial \delta \bar{u}}{\partial x}\frac{\partial \bar{u}}{\partial y} + \frac{\partial \delta \bar{v}}{\partial x}\frac{\partial \bar{v}}{\partial y} + \frac{\partial \bar{u}}{\partial x}\frac{\partial \delta \bar{u}}{\partial y} + \frac{\partial \bar{v}}{\partial x}\frac{\partial \delta \bar{v}}{\partial y} \end{array} \right\} \tag{4.24}$$

For an orthotropic material in plane stress elastic constitutive equations provides the relationship between the stresses and the strains and involves four constants namely, C_{11}, C_{12}, C_{22}, and C_{66}. The above relations when substituted into the virtual work statement provides the stiffness matrices at the element level for the incremental displacements in two dimensions.

$$([K_L] + [K_{NL}])\ \bar{\Delta} = {}^2_1F \tag{4.25}$$

where;

$$[K_L] = \int_{{}_0V} [B_L^0]^T\, [{}_1C]\, [B_L^0]\, d^1V$$
$$[K_{NL}] = \int_{{}_0V} [B_{NL}]^T\, [{}_1\sigma]\, [B_{NL}^0]\, d^1V$$
$$[{}^1_1F] = \int_{{}_0V} [B_L^0]^T\, [{}_1\sigma]\, d^1V$$
$$[{}^2_1F] = \int_{{}_1V} [\psi]^T\, [{}^2_1f]\, d^1V + \int_{{}_1S} [\psi]^T\, [{}^2_1t]\, d^1S$$

where, the matrices $[{}^1\sigma]$ and are $[{}^1\varepsilon]$ are defined as follows;

$$[{}^1\sigma] = \left\{ \begin{array}{c} {}^1\sigma_{xx} \\ {}^1\sigma_{yy} \\ {}^1\sigma_{xy} \end{array} \right\} = \left[\begin{array}{ccc} {}_1C_{11} & {}_1C_{12} & 0 \\ {}_1C_{12} & {}_1C_{22} & 0 \\ 0 & 0 & {}_1C_{66} \end{array} \right] \left\{ \begin{array}{c} {}^1_1e^0_{xx} \\ {}^1_1e^0_{yy} \\ {}^1_1\gamma^0_{xy} \end{array} \right\} \tag{4.26}$$

$$[{}^1\varepsilon] = \left\{ \begin{array}{c} {}^1_1\varepsilon_{xx} \\ {}^1_1\varepsilon_{yy} \\ 2{}^1_1\varepsilon_{xy} \end{array} \right\} = \left[\begin{array}{c} \frac{\partial u}{\partial x} - \frac{1}{2}\left[\left(\frac{\partial u}{\partial x}\right)^2 + \left(\frac{\partial v}{\partial x}\right)^2\right] \\ \frac{\partial v}{\partial y} - \frac{1}{2}\left[\left(\frac{\partial u}{\partial y}\right)^2 + \left(\frac{\partial v}{\partial y}\right)^2\right] \\ \frac{\partial u}{\partial y} + \frac{\partial v}{\partial x} - \left(\frac{\partial u}{\partial x}\frac{\partial u}{\partial y} + \frac{\partial u}{\partial x}\frac{\partial u}{\partial y}\right) \end{array} \right] \tag{4.27}$$

Finally, the stiffness matrices at the element level are expressed as follows [11];

$$\left[\begin{array}{cc} K^{11L} + K^{11N} & K^{12L} \\ K^{21L} & K^{22L} + K^{22N} \end{array} \right] \left\{ \begin{array}{c} \bar{u} \\ \bar{v} \end{array} \right\} = \left\{ \begin{array}{c} {}^2_1F^1_i - {}^1_1F^1_i \\ {}^2_1F^2_i - {}^1_1F^2_i \end{array} \right\} \tag{4.28}$$

where, the explicit forms of the stiffness matrices are obtained as follows;

$$\begin{aligned} K^{11L}_{ij} &= h_e \int_{\Omega_e} \left({}_1C_{11}\frac{\partial\psi_i}{\partial x}\frac{\partial\psi_j}{\partial x} + {}_1C_{66}\frac{\partial\psi_i}{\partial y}\frac{\partial\psi_j}{\partial y}\right)\, dxdy \\ K^{12L}_{ij} = K^{21L}_{ij} &= h_e \int_{\Omega_e} \left({}_1C_{12}\frac{\partial\psi_i}{\partial x}\frac{\partial\psi_j}{\partial y} + {}_1C_{66}\frac{\partial\psi_i}{\partial y}\frac{\partial\psi_j}{\partial x}\right)\, dxdy \\ K^{22L}_{ij} &= h_e \int_{\Omega_e} \left({}_1C_{22}\frac{\partial\psi_i}{\partial x}\frac{\partial\psi_j}{\partial x} + {}_1C_{66}\frac{\partial\psi_i}{\partial y}\frac{\partial\psi_j}{\partial y}\right)\, dxdy \\ K^{11N}_{ij} = K^{22N}_{ij} &= h_e \int_{\Omega_e} \left({}_1\sigma_{xx}\frac{\partial\psi_i}{\partial x}\frac{\partial\psi_j}{\partial x} + {}_1\sigma_{yy}\frac{\partial\psi_i}{\partial y}\frac{\partial\psi_j}{\partial y} + \sigma_{xy}\left[\frac{\partial\psi_i}{\partial y}\frac{\partial\psi_j}{\partial x} + \frac{\partial\psi_i}{\partial x}\frac{\partial\psi_j}{\partial y}\right]\right)\, dxdy \end{aligned} \tag{4.29}$$

The forcing function terms are defined as follows;

$$\begin{aligned} {}^2_1F^1_i &= h_e \int_{\Omega_e} \left({}^2_1f_x\psi_i\right)\, dxdy + h_e \int_{\Gamma_e} \left({}^2_1t_x\psi_i\right)\, ds \\ {}^2_1F^2_i &= h_e \int_{\Omega_e} \left({}^2_1f_y\psi_i\right)\, dxdy + h_e \int_{\Gamma_e} \left({}^2_1t_y\psi_i\right)\, ds \\ {}^1_1F^1_i &= h_e \int_{\Omega_e} \left(\frac{\partial\psi_i}{\partial x}\ {}^1\sigma_{xx} + \frac{\partial\psi_i}{\partial y}\ {}^1\sigma_{xy}\right)\, dxdy \\ {}^1_1F^2_i &= h_e \int_{\Omega_e} \left(\frac{\partial\psi_i}{\partial x}\ {}^1\sigma_{xy} + \frac{\partial\psi_i}{\partial y}\ {}^1\sigma_{yy}\right)\, dxdy \end{aligned} \tag{4.30}$$

For a description of the steps in the derivation of the stiffness matrices the reader is referred to the following reference [11]. Most of the steps for the derivation of

these element matrices have been described above, and the iterations which have been mentioned as equilibrium iterations are utilized to balance the out of balance virtual work to attain the converged displacements and the stresses at each change of configuration.

D. Boundary Conditions

The cantilever beam was subject to traction loading on the sides of the beam. The traction loading was equally distributed on the top and bottom face of the beam. The change in the length and deformed configurations of the beam were automatically incorporated into the formulation since line integrals were performed at every load-step for calculating the traction surface integrals which enter the forcing function terms. Two different types of boundary conditions were considered. The first one was the case of a cantilever beam subject to traction loading. In this case because of the rigidity of the support at one end the u and v components of the displacement are equal to zero. In the second case the beam is subject to an equi-distributed traction loading and fixed at both ends. In this case both the components of the displacements are specified to be zero on both ends. The linear solution for the cantilever beam was also analysed and results compared with the analytical solution available.

E. Numerical Results

In this section we present results for the large deformation analysis of bending of beams subject to two different types of boundary conditions for both linear and non-linear analysis and validate the linear case, with published results in literature.

1. Linear Solution

Consider a cantilever beam of length $a =$ 10 in, height $b =$ 1 in, and thickness of $h =$ 1 in. For the linear analysis two different meshes of 5×1 spectral elements are used, with a p_{level} of five, and 10×1 elements with a p_{level} of 10 were used. The higher p_{value} of 10 was used to generate confidence in the results against the lower p_{level} values. The modulus of elasticity of the beam was taken as; E= 1.2×10^4 psi, and the Poisson ratio was taken as 0.20. The beam was assumed to be in the plane state of stress and thus no distinction was made between the material properties ${}^1C_{ij}$ and, ${}^0C_{ij}$ which were also assumed to remain constant during the deformation process. The v-component of the center deflection for the mesh of 5×1 spectral element was reported at a value of -0.627542 which is in good agreement with the values reported in literature [11] which reports a value of -0.6227. A better agreement was obtained with the spectral mesh with a higher resolution of p_{level} of 10, for which the center deflection $v(10, 0, 50)$ was found to be -0.627367. The linear analysis performed was also used as a validation for the results that have been reported in literature along with the convergence of the deflections to the same values between different values of p_{levels} tried. Further validation of the problem is also performed as the center deflections for the non-linear analysis was checked with published results. Some of the results that follow will serve as validation of the present results with results of Reddy [11].

2. Non-Linear Analysis

a. Cantilever Beam under Traction Loading

A cantilever beam with the material property values mentioned earlier was analysed for a non-linear analysis for the case of equi-distributed traction loading. The v-

component of the deflections that was obtained with the above analysis was compared to the results obtained in literature, as mentioned in Table XVII and good agreement was found for all load-steps. Some differences in the deflections at higher load-steps

Table XVII. Cantilever beam non-linear analysis UL formulation

	Results	Position		Deformed	
q_0	$u(10, 0.5)$ [11]	x	y	$u(10, 0.5)$	$v(10, 0.5)$
1.0	-0.086	9.91323	-0.7421	-0.08677	-1.24209
2.0	-0.326	9.66724	-1.9151	-0.33276	-2.41508
3.0	-0.673	9.30659	-2.9512	-0.69341	-3.45117
4.0	-1.080	8.88282	-3.8297	-1.11718	-4.32971
5.0	-1.507	8.56083	-4.3836	-1.43917	-4.88364
6.0	-1.930	8.16144	-4.9603	-1.83856	-5.4603
7.0		7.72631	-5.4941	-2.27369	-5.99413
8.0	-2.714	7.29368	-5.9537	-2.70632	-6.4537
9.0		6.88781	-6.3347	-3.11219	-6.83472
10.0	-3.391	6.51702	-6.648	-3.48298	-7.14801
11.0		6.18297	-6.9061	-3.81703	-7.40614
12.0	-3.965	5.88343	-7.1208	-4.11657	-7.6208
13.0		5.61339	-7.3022	-4.38661	-7.80224
14.0	-4.450	5.36786	-7.4582	-4.63214	-7.95818
15.0		5.14321	-7.5939	-4.85679	-8.09394
16.0	-4.863	4.93682	-7.7133	-5.06318	-8.21329

can be attributed to the higher spatial accuracy of the spectral method, and it is anticipated that the present results are more accurate. The non linear analysis was

performed on a set of different meshes to generate grid independent results and the results for a mesh of 10×5 spectral elements with a p_{level} of 4 is being reported. The development of the Cauchy and second Piola-Kirchoff stresses for the same beam are being reported in Table XVIII. The calculation of the stresses was done on the top

Table XVIII. Cantilever beam stresses non-linear analysis

Results		Cauchy Stresses		Piola Kirchhoff	
q_0	σ_{xx}	σ_{yy}	σ_{xy}	${}^1_0S_{xx}$	${}^1_0S_{yy}$
1.0	-345.751	-69.1501	-40.5306	-335.643	-67.1287
2.0	-699.166	-139.833	-77.7164	-659.24	-131.848
3.0	-1044.91	-208.982	-110.377	-958.544	-191.709
4.0	-1380.49	-276.099	-139.054	-1234.1	-246.821
5.0	-1678.09	-335.617	-163.076	-1466.96	-293.393
6.0	-1980.68	-396.137	-184.944	-1693.58	-338.715
7.0	-2283.29	-456.658	-204.545	-1910.6	-382.12
8.0	-2578.35	-515.67	-221.921	-2113.46	-422.692
9.0	-2862.52	-572.505	-237.238	-2301.12	-460.224
10.0	-3135.2	-627.04	-250.761	-2474.4	-494.881
11.0	-3397.12	-679.424	-262.808	-2634.88	-526.977
12.0	-3649.66	-729.931	-273.588	-2784.31	-556.863
13.0	-3894.66	-778.933	-283.296	-2924.51	-584.902
14.0	-4133.79	-826.759	-292.078	-3056.99	-611.398
15.0	-4368.25	-873.65	-300.046	-3182.85	-636.57
16.0	-4598.87	-919.774	-307.297	-3302.9	-660.579

left uppermost fiber of the beam. The usage of *hp*-spectral expansions allows us to

determine the exact location of the top left corner as one of the Gauss-integration points lies on the end of each element and no further approximations with the Gauss point reaching the top left asymptotically with mesh refinements needs to be done.

b. Beam Fixed at Both Ends Undergoing Deformation

Here we consider a beam with the same material property values as in the last section undergoing deformations however both the ends of the beam are fixed to rigid supports, allowing zero, deflections in both the x and z directions. In Table XIX we present the deflections of the center of the beam as a function of the increasing traction loading on either side of the beam along with the development of the Cauchy stresses at the top-center of the beam. The development of the Piola-Kirchhoff stresses as a function of the loading on the corner of the beam at the top left corner of the beam is being presented in Table XX. The development of the stresses in Table XX were obtained at the top left corner of the beam whereas the deflections in Table XIX have been reported to be the deflection of the center of the beam. The appropriate locations have been marked in the respective tables.

Figure 21 presents the transverse deflections of the end of the cantilever beam with the load steps that were applied on the top and the bottom faces of the beam. Figure 22 presents the development of Cauchy and the second Piola-Kirchhoff stresses at the top left corner of the Cantilever beam as discussed in Figure 21. A partial deformation history and the development of the Cauchy stresses inside the cantilever beam have been presented in Figure 23. The stress concentrations is evident with the contour plots, at the corner near the fixed edge. Figure 24 presents the deflections of the center of the cantilever beam as subject to increasing traction loadings applied equally to the top and the bottom of the beam for the case where both ends of the beam are fixed. The development of the Cauchy stresses and the Second Piola-

Table XIX. Beam non-linear analysis UL formulation

Results	Deflections		Cauchy Stresses		
q_0	$u(5,0)$	$v(5,0)$	$cxx(5,0)$	$cyy(5,0)$	$cxy(5,0)$
1.0	9.29E-12	-0.02883	25.40503	0.49987	2.17E-05
2.0	-4.44E-09	-0.05758	51.0077933	0.99993687	3.98E-05
3.0	9.27E-09	-0.08617	76.7160033	1.49989787	0.00021067
4.0	-2.98E-08	-0.11455	102.449066	1.99977348	0.000255882
5.0	2.30E-07	-0.14259	128.001747	2.43525019	0.000594432
6.0	4.82E-08	-0.1703	153.48433	2.92206514	0.000727948
7.0	8.27E-08	-0.19762	178.759235	3.40974019	0.000811384
8.0	4.33E-08	-0.22451	203.75745	3.8973405	0.000956216
9.0	4.09E-07	-0.25093	228.428024	4.38591696	0.001394485
10.0	2.97E-08	-0.27685	252.727833	4.87534593	0.001714965
11.0	6.53E-08	-0.30228	276.622908	5.36517074	0.001886332
12.0	2.00E-08	-0.32718	300.086859	5.85564377	0.002099622
13.0	2.07E-07	-0.35157	323.100536	6.3473639	0.002681038
14.0	3.86E-07	-0.37543	345.651077	6.83957252	0.002950302
15.0	3.41E-08	-0.39877	367.73063	7.33203955	0.003129701
16.0	2.37E-07	-0.42161	389.33572	7.82551688	0.003436536

Kirchhoff stresses at one of the fixed ends, and the center of the beam; respectively are presented in Figure 25. Finally, the convergence history for the Preconditioned Bi-orthogonal conjugate gradient solver with for the cantilever beam is being presented in Figure 26. As can be seen from the convergence history the problem also appears to be ill-conditioned as there is rapid convergence only at the end of the convergence history. From the above figures it is clear that the *hp*-spectral method performs well in all cases studied while considering the non-linear deformations of the beam undergoing large deformations with the UL formulations. For all cases analysed and

Table XX. Beam non-linear analysis Piola-Kirchhoff stresses

Loads	Cauchy Stresses		
q_0	$cxx(0, 0.0)$	$cyy(0, 0.0)$	$cxy(0, 0.0)$
1.0	-61.1519	-12.2304	-9.8230475
2.0	-121.685	-24.3371	-19.511989
3.0	-181.501	-36.3002	-29.055779
4.0	-240.53	-48.106	-38.448437
5.0	-299.224	-59.8449	-47.73406
6.0	-356.479	-71.2958	-56.802084
7.0	-412.785	-82.5569	-65.706928
8.0	-468.081	-93.6163	-74.446716
9.0	-522.351	-104.47	-83.021004
10.0	-575.588	-115.118	-91.433921
11.0	-627.798	-125.56	-99.6897
12.0	-678.999	-135.8	-107.79423
13.0	-729.204	-145.841	-115.75242
14.0	-778.437	-155.687	-123.56895
15.0	-826.721	-160.538	-127.42665
16.0	-874.1	-174.82	-138.80836

linear and non linear problems solved the results were obtained using full-integration of the stiffness matrices and no under integration procedures were employed for the problems solved.

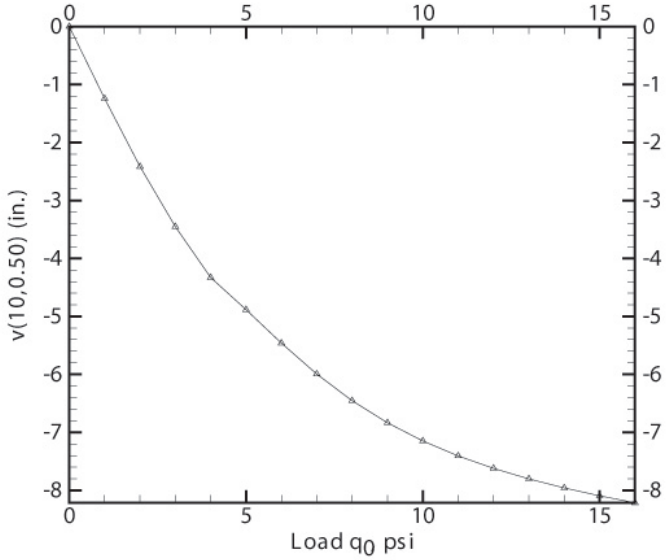

Fig. 21. Center deflection vs. loading for cantilever beam vs. loadsteps

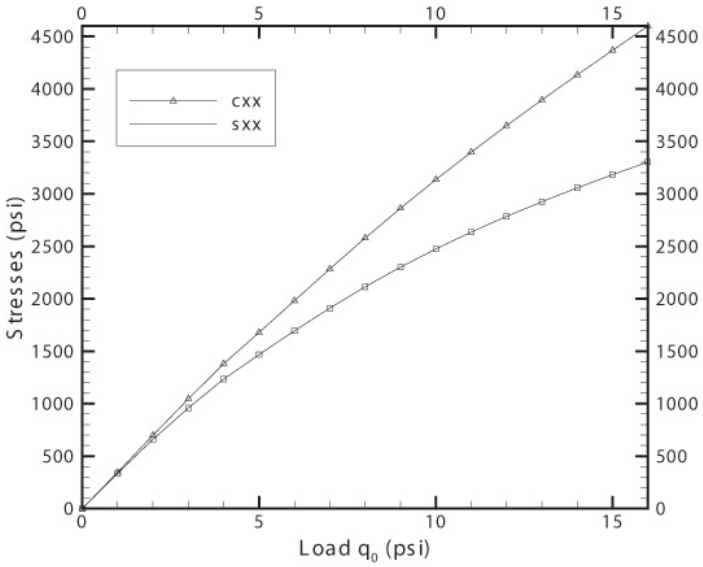

Fig. 22. Stresses at the top left corner of cantilever beam

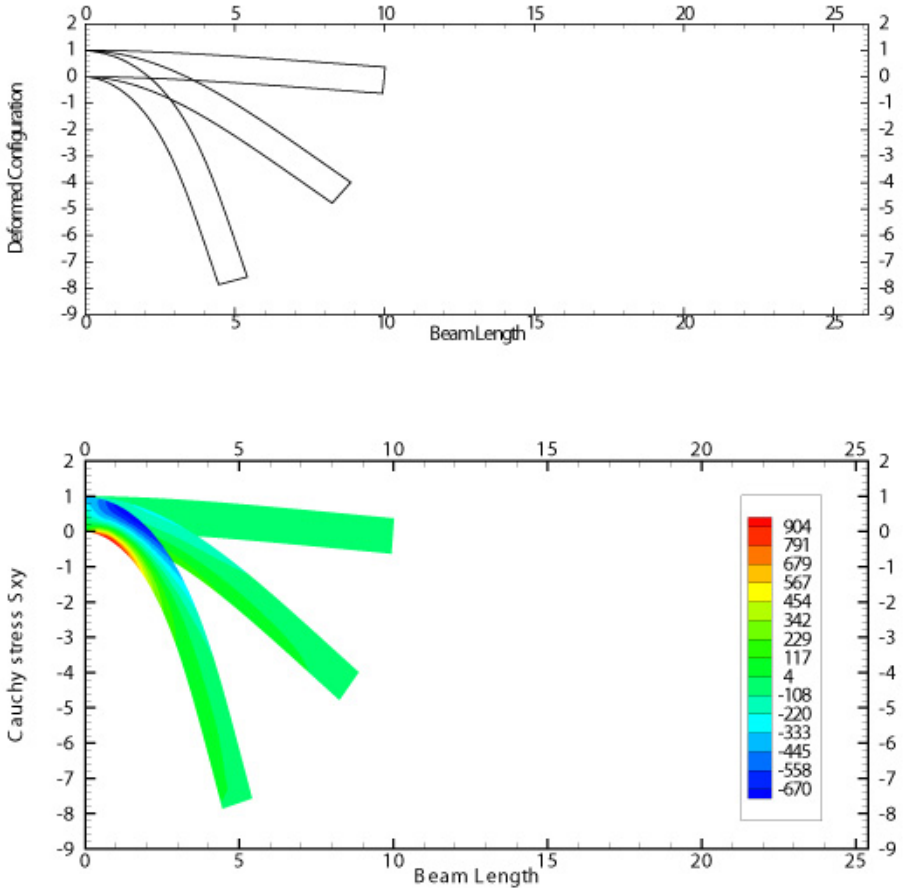

Fig. 23. Deformed shapes and Cauchy stresses inside the cantilever beam

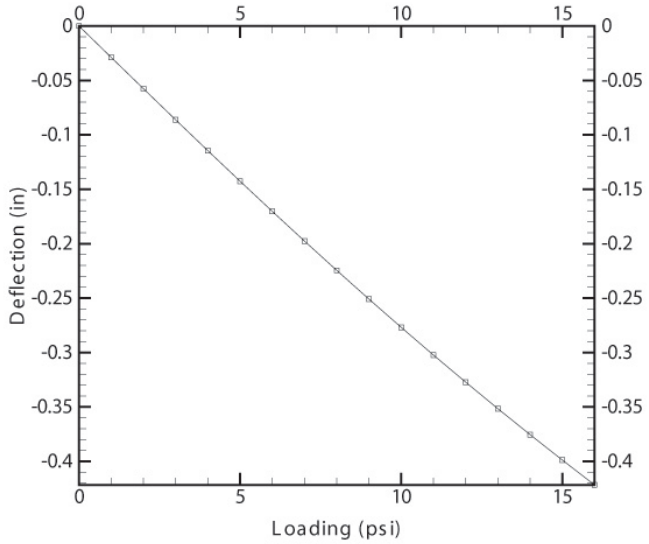

Fig. 24. Development of center deflection for both sides clamped beam

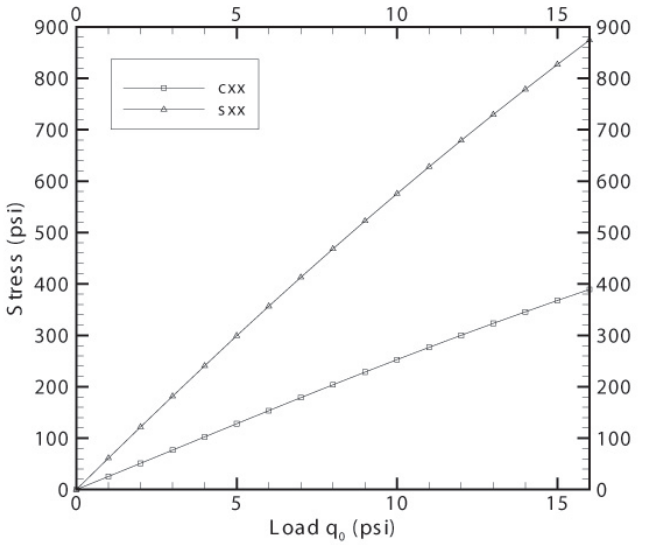

Fig. 25. Cauchy and second Piola-Kirchhoff stresses at the corner of beam

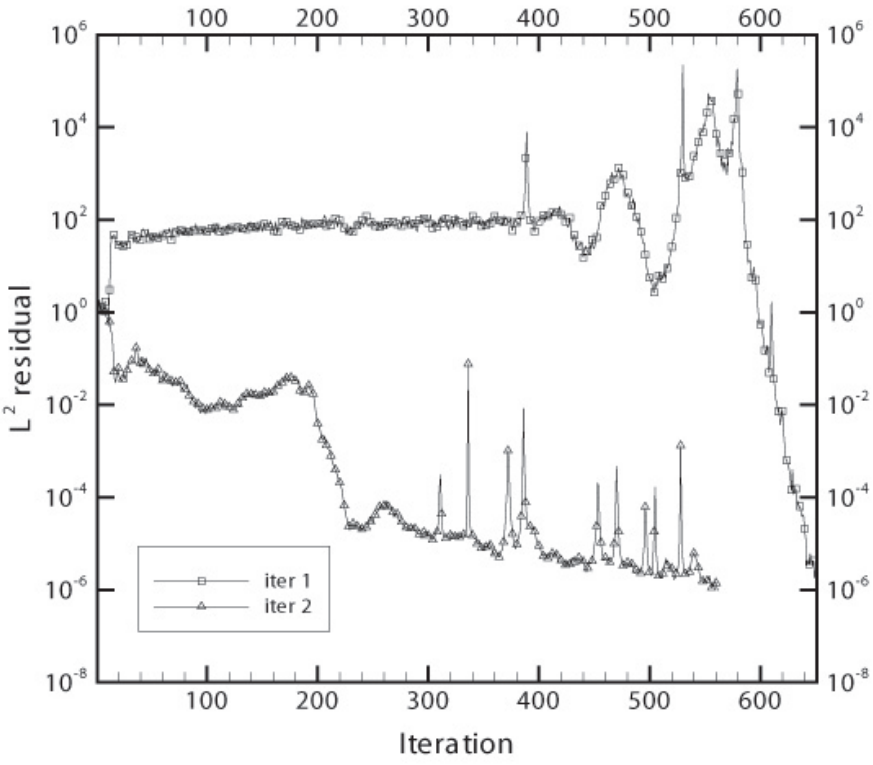

Fig. 26. Convergence of preconditioned bi-orthogonal conjugate gradient solver

CHAPTER V

DOMAIN DECOMPOSITION METHODS FOR LEAST SQUARES PROBLEMS

A. Introduction

There is a vast literature on least squares finite element methods that have been applied to solving problems in computational fluid mechanics areas. The *hp* version of the least squares problems has computationally expensive quadrature requirements which necessitate the usage of elegant methods for solving the resulting systems of equations. Amongst some of the schemes for solving large systems of equations is the Domain Decomposition technique. In this paper we explore one such highly parallel Domain decomposition technique namely the Additive Schwarz method for the solution of linear systems of equations in parallel and demonstrate the effectiveness and speedup that is obtained for solving the Navier-Stokes equations in parallel. Another new technique for solving huge unsymmetric systems, namely the element by element Jacobi preconditioned Bi-orthogonal Conjugate gradient (EBE-BJCG) technique is developed for applications in fluids problems and an unsymmetric solution is demonstrated. In doing so, we provide for effective means for solving fluid flow problems for both unsymmetric and symmetric operators and demonstrate their efficacy for solutions of fluid flow problems. We also demonstrate the usage of domain decomposition techniques in the solutions of both the linear stokes operator with the least squares finite element methods as also the full non-linear Navier-Stokes equations with least squares finite element methods. In all cases we report super linear to linear speedup and thus the optimality of the methods for parallelism is exemplified. Some of the issues related with such applications to least squares problems are also addressed and remedies suggested.

B. Background

Amongst the different methods used for solving fluid flow problems, a relatively new addition is the least squares finite element method (LSFEM). Amongst the celebrated advantages of the least squares finite element methods are the symmetric systems produced from these formulations; and also the velocity and the pressure spaces do not have to adhere to the Ladyzhenskaya-Babuska-Brezzi (LBB) compatibility restrictions for obtaining the correct velocity and pressure metrics. It has been mentioned in literature that the least squares finite element methods (LSFEM) lead to symmetric systems by construction, for the solutions of problems, and the problems thus are more amenable to conjugate gradient techniques for the solution of the linear systems thus generated. In this regard, it should be pointed out that the least squares formulations also suffer from some drawbacks when solutions of linear systems of equations are sought. One of the drawbacks is that in the context of least squares applications to solving real world fluid flow problems, the there are issues with regard to obtaining the coarse grid correction step. The projection of the *hp*-spectral mesh onto a bi-linear discretization does not work because the problem locks as is well known with least squares methods. Thus least squares problems at the same time, although generators for symmetric systems, do not have a very sound foundation which permit the applications of multigrid techniques, and or coarse grid corrections, in a more general setting. It is this issue that this chapter wishes to address to develop a consistent technique for being able to solve large systems of algebraic equations efficiently with the LSFEM and Penalty finite element formulations. We provide two different techniques to be employed for the solutions of problems. For the symmetric problems, we would recommend the usage of domain decomposition methods, in specific the *Additive* Schwarz methods for cases, were high level of parallelism is desired,

and element by element bi-orthogonal conjugate gradient solver for cases, where it is known that the system of equations is unsymmetric/ non self adjoint. For both these cases, we demonstrate the effectiveness of the algorithms for the solutions of problems and compare the results with the benchmark/analytical results. The usage of spectral element methods for solving elliptic problems obtained from the Galerkin finite element methods has been demonstrated in Paverino thesis and some papers [39]. In the above work spectral element methods were used for decomposing the problems on given domains, and consequently solving the equations with the help of the Domain Decomposition techniques. *Additive* Schwarz was used along with the multiplicative versions to solve problems efficiently. The formation of an overlay of the spectral element grid with a bilinear finite element grid was explored by Heys et al. [40] and they have explored the usage of such overlays along with an accompanying "black box" algebraic multigrid method to act as preconditioners to the conjugate gradient solver. They also demonstrated the use of the direct application of the algebraic multigrid method for solving problems obtained from higher order discretizations. Convergence histories independent of the polynomial orders were obtained for the solution of the Poisson problem on a two dimensional domain with specified boundary conditions. An accompanying work in the use of higher order discretizations for solving problems was reported in Darao et al [41]. They explored the usage of a substructuring method in order to solve the Stokes problem with the construction of the Schur complement. Good parallelism achieved with the construction of the Schur complement was demonstrated. However, the construction of the Schur complement is beset by a very specific numbering system that needs to be adopted for the problem that is being solved. Extensions of the Schur complement to problems is not straight forward, and special care needs to be exercised in deciding the numbering system to condense out the interior degrees of freedom. Domain decomposition methods on the other hand as

expressed in the form of either multiplicative or additive Schwarz methods allows the user very good flexibility in the sense that one can choose whichever gridpoints numbering scheme one wishes to adopt. In this sense, domain decomposition techniques are superior to the Schur complement methods. Also in the above cited reference, only the stokes equations were solved, whereas the inclusion of the non-linearity can cause significant difficulties with convergence for the LSFEM formulations. In light of the above cited problems there is a need to explore the use of Domain Decomposition techniques in the context of LSFEM formulations, as only heuristics exist at present, and the aforementioned has not been demonstrated yet. We only address the steady Navier-Stokes equations as is well known in most cases the solutions of the steady state problems can be far complicated as compared to the unsteady variants, as the convergence is more relaxed in the latter case and the previous time estimates provide excellent estimates to the new time step during marching in time.

C. Navier-Stokes Equations

The behaviour of the steady incompressible flows can be modelled with the Navier-Stokes equations. The Navier-Stokes equations in the pressure-velocity formulation can be written as follows;

$$(\mathbf{u} \cdot \nabla)\,\mathbf{u} + \nabla p + \frac{1}{Re}\Delta\mathbf{u} = \mathbf{f} \quad in\ \Omega \tag{5.1}$$

and,

$$\nabla \cdot \mathbf{u} = 0 \quad in\ \Omega \tag{5.2}$$

with, $\mathbf{u}$ the velocity vector, $\mathbf{f}$ is the forcing term per unit mass, Re is the Reynolds number and $\Omega \subset \Re^d$, where d, is the space dimension in which the problem is defined. To allow the use of practical C^0 expansions, in the least squares finite element formu-

lation, the governing equations must be recast, as an equivalent first-order system. So, the least squares functional is defined in terms of the L_2 norms only. Introducing the vorticity, and using the identity, $\omega = \nabla \times \mathbf{u}$, and using the vector identity,

$$\nabla \times \nabla \times \mathbf{u} = -\Delta u + \nabla (\nabla \cdot \mathbf{u}) \tag{5.3}$$

The Navier-Stokes equations in the first order form are thus expressed as follows;

$$\begin{aligned} (\mathbf{u} \cdot \nabla)\, \mathbf{u} + \nabla p - \frac{1}{Re} \nabla \times \omega = \mathbf{f} \quad & in\ \Omega \\ \omega - \nabla \times \mathbf{u} = 0 \quad & in\ \Omega \\ \nabla \cdot \mathbf{u} = 0 \quad & in\ \Omega \\ \nabla \cdot \omega = 0 \quad & in\ \Omega \end{aligned} \tag{5.4}$$

It is important to note the requirement that the vorticity be solenoidal, is needed for the three dimensional case where as not for the two dimensional case. For the three dimensional case, this additional constraint makes the system uniformly elliptic, meaning the determinant of the first order system formed with these matrices is positive. The stokes component of the Navier- Stokes is obtained from the above equations by dropping the non-linear terms from the above equations set as follows;

$$\nabla p - \frac{1}{Re} \nabla \times \omega = \mathbf{f} \quad in\ \Omega \tag{5.5}$$

The above equations need to be supplemented with the appropriate boundary conditions to complete the definition of the boundary value problem. The non linear term, $\mathbf{u} \cdot \nabla \mathbf{u}$ has no effect on the classification of the system, and thus, the same boundary conditions as the Stokes equations are admissible boundary conditions for the above equations.

D. Linearization Procedure

Before, the application of the LSFEM, the convective term, needs to be linearized by using successive substitution or Newtons method. We adopted the Newtons method for linearization of the LSFEM, and for this case the method is linearized as follows;

$$(\mathbf{u_0} \cdot \nabla)\,\mathbf{u} + (\mathbf{u} \cdot \nabla)\,\mathbf{u_0} + \nabla p + \frac{1}{Re}\nabla \times \omega = \mathbf{f} + (\mathbf{u_0} \cdot \nabla)\,\mathbf{u_0} \quad in\ \Omega \tag{5.6}$$

Newtonś method is known to have a smaller radius of convergence, however the convergence to the solutions is expected to be faster as compared to the Picard method or the method of successive substitutions. Newton's method of linearization is the preferred choice of linearization procedure when a guess close to the solution is available [42]. The LSFEM functional is setup with the help of the reduction of the individual residuals for each of the equations expressed above and is provided by;

$$J(\mathbf{u}, p, \omega; \mathbf{f}) = \frac{1}{2}\Big(\parallel (\mathbf{u} \cdot \nabla)\,\mathbf{u} + \nabla p + \frac{1}{Re}\nabla \times \omega - \mathbf{f} \parallel_0^2 + \parallel \omega - \nabla \times \mathbf{u} \parallel_0^2 + \parallel \nabla \cdot \mathbf{u} \parallel_0^2 + \parallel \nabla \cdot \omega \parallel_0^2 \Big) \tag{5.7}$$

The following functional minimization statement provides the stiffness matrix for the formulation. The minimization statement is mentioned as follows;
Find $(\mathbf{u},\ \mathbf{p},\ \omega) \in\ X(\Omega)$, such that;

$$\lim_{\epsilon \to 0} \frac{d}{d\epsilon} J\left(\mathbf{u} + \epsilon \mathbf{v}; \mathbf{f}\right) = 0 \quad \forall \mathbf{v} \in X(\Omega) \tag{5.8}$$

where, $X(\Omega)$ is the space of admissible functions,

$$X = \{(\mathbf{u}, p, \omega) \in \mathbf{H}_0^1(\Omega) \times \mathbf{H}^1(\Omega) \cap \bar{L}_2(\Omega) \times \mathbf{H}^1(\Omega)\} \tag{5.9}$$

In an abstract notation, the linear system is expressed as the following;

Find $(\mathbf{u},\ p,\ \omega) \in\ X(\Omega)$, such that;

$$\mathcal{A}(\mathbf{U},\mathbf{V}) = \mathcal{F}(\mathbf{V})\ \ \forall \mathbf{V} \in X(\Omega) \tag{5.10}$$

with;

$$\mathcal{A}(\mathbf{U},\mathbf{V}) = \langle \mathcal{L}(\mathbf{U}), \mathcal{L}(\mathbf{V}) \rangle_{Y(\Omega)} \tag{5.11}$$

and;

$$\mathcal{F}(\mathbf{V}) = \langle \mathcal{G}, \mathcal{L}(\mathbf{V}) \rangle_{Y(\Omega)} \tag{5.12}$$

where, $\mathcal{L}$, represents the Navier-Stokes operator, $\mathcal{F}$ is the corresponding source term, $\mathcal{A} : X \times X \rightarrow \mathcal{R}$, is a symmetric, continuous bilinear form, and $\mathcal{F} : X \rightarrow R$, is a continuous linear form. A description of the operator $\mathcal{L}$ follows as expressed in the first order form. We have described a method for the derivation of these matrices in a following chapter VIII. Following the convention used in [42], the first order system can be expressed in the following form;

$$A\underline{u} = \underline{f} \tag{5.13}$$

and therefore;

$$A_1 \frac{\partial \underline{u}}{\partial x} + A_2 \frac{\partial \underline{u}}{\partial y} + A_0 \underline{u} = \underline{f} \tag{5.14}$$

and, the above matrices are defined as follows;

$$A_1 = \begin{bmatrix} u_0 & 0 & 1 & 0 \\ 0 & u_0 & 0 & -\frac{1}{Re} \\ \omega & 0 & 0 & 0 \\ 0 & -1 & 0 & 0 \end{bmatrix}, \quad A_2 = \begin{bmatrix} v_0 & 0 & 0 & \frac{1}{Re} \\ 0 & v_0 & 1 & 0 \\ 0 & \omega & 0 & 0 \\ 1 & 0 & 0 & 0 \end{bmatrix} \tag{5.15}$$

,

$$A_0 = \begin{bmatrix} \frac{\partial u_0}{\partial x} & \frac{\partial u_0}{\partial y} & 0 & 0 \\ \frac{\partial v_0}{\partial x} & \frac{\partial v_0}{\partial y} & 0 & 0 \\ 0 & 0 & 0 & 0 \\ 0 & 0 & 0 & 1 \end{bmatrix}, \quad f = \begin{bmatrix} f_x + u_0\frac{\partial u_0}{\partial x} + v_0\frac{\partial u_0}{\partial y} \\ f_y + u_0\frac{\partial v_0}{\partial x} + v_0\frac{\partial v_0}{\partial y} \\ 0 \\ 0 \end{bmatrix} \tag{5.16}$$

Finally, instead of using the infinite dimensional function space $X(\Omega)$ to seek for the minimizer, the searching process is performed in a finite dimensional space X_h, i.e. $\mathbf{U_h} \in \mathbf{X_h}(\mathbf{\Omega})$. Then the least squares formulation can be stated as;
Find $\mathbf{U_h} \in \ \mathbf{X}(\mathbf{\Omega})$, such that;

$$\mathcal{A}(\mathbf{U_h}, \mathbf{V_h}) = \mathcal{F}(\mathbf{V_h}) \ \ \forall \mathbf{V_h} \in X_h(\Omega) \tag{5.17}$$

For modelling of the transients, the development follows the above very closely and has a few more terms in the first order system of equations.

E. Additive Schwarz Domain Decomposition

Domain decomposition methods are parallel, potentially fast, robust algorithms for the solution of the linear or nonlinear equations that arise from discretization of partial differential equations. Some of the motivations for the use of these methods include: (1) potential for efficient parallelization through the use of data locality (2) ability to deal with PDEs on complicated physical geometries (3) ability to deal with PDEs that demonstrate different behaviour on different parts of the domain (stiff systems) (4) superior convergence properties of the iterative method even on sequential machines [43]-[44]. Domain Decomposition methods fall into two categories- those using the overlapping subdomains, and those using non overlapping subdomains, which are sometimes called substructuring methods. Even with the overlapping domain

decomposition methods there are two distinct variants the first is the Multiplicative variant of the domain decomposition method, and the second is the Additive Schwarz method. The Additive Schwarz method which utilizes data locality and has a much lower sequential component and is more suited to parallelization even though it takes more iterations as compared to the multiplicative Schwarz method. Based on these arguments, Additive Schwarz is a much better suited for parallelization and this is the method that was adopted in this study. In the following sections we describe the Additive Schwarz algorithm along with the parallelization issues and follow through with results which were compared with the benchmark results for the driven cavity problem, in two dimensions. Extensions to three dimensions is straight forward even though it is considerable more involved. Let us denote the symmetric linear system of equation that we wish to solve with;

$$A\mathbf{u} = \mathbf{f} \tag{5.18}$$

where, A is a $n \times n$ positive definite matrix, and, $f \subset R^n$. The matrix version of the Additive Schwarz algorithm for the above equation $Pu = f_*$, has the form;

$$\Big(\sum_{i=0}^{p} R_i^T A_i^{-1} R_i A\Big)\mathbf{u} = \mathbf{w}_* \tag{5.19}$$

where,

$$\mathbf{w}_* = \Big(\sum_{i=0}^{p} R_i^T A_i^{-1} R_i\Big)\mathbf{f} \tag{5.20}$$

The system for equation [45] corresponds to a preconditioned system of the form $M^{-1}A\mathbf{u} = M^{-1}\mathbf{f}$. This yields the additive Schwarz preconditioner as:

$$M^{-1} = \Big(\sum_{i=0}^{p} R_i^T A_i^{-1} R_i\Big) \tag{5.21}$$

Assimilating the ideas in the algorithm for the Additive Schwarz preconditioner we obtain the following;

```
Input r:
1.  For  i=0,1,2.......,p in parallel do:
```

$$\mathbf{w_i} = \left(\sum_{i=0}^{p} R_i^T A_i^{-1} R_i\right)$$

```
2.  End for.
3.  Sum:
```

$$\mathbf{w} \equiv \mathbf{w_0} + \mathbf{w_1} + \mathbf{w_2} + \mathbf{w_3} + ... + \mathbf{w_n}$$

It has been mentioned in literature [46] that the *Additive* Schwarz algorithm performs well for a small number of subdomains, and also the performance of the algorithm is dependent on the number of subdomains and some deterioration of the performance of the *Additive* Schwarz algorithm is to be expected with an increase in the number of subdomains. For this reason it has been recommended for Galerkin methods to account for the coarse grid correction step for obtaining better performance of the algorithms. The algorithm for the *Additive* Schwarz preconditioner with the coarse grid correction for a matrix A is given by the following;

$$B_{add}^{-1} = R_0^T A_0^{-1} R_0 + \sum_{k=1}^{K} R_k^T A_k^{-1} R_k \tag{5.22}$$

in the above notation, k is the number of subdomains over over which the *Additive* Schwarz preconditioner is defined. Coarse grid correction step is a good idea for solving Galerkin based finite element formulations. However, for least squares finite element methods, there are a few issues with the inclusion of the coarse grid. It is well known that the solution of extremely large problems with multigrid methods

always leads to *load balancing* issues on parallel processors. The same is anticipated for the spectral element discretization and the coarse grid problem. Another issue is that it is well known that the bilinear finite element basis for the least squares problems locks and the velocity metrics obtained are very high. In such a case, thus the coarse grid correction cannot be implemented based on the above formula, and one has to resort to reduced integration techniques to provide a collocation solution which can perhaps serve as a representation of the least squares errors on the coarser grid. Another reason, is that LSFEM problems, suffer from extremely high loss of mass for most problems with open boundaries and for large contraction regions. To ameliorate this problem one has to include a weight into the continuity equation for these problems, and minimize the weighted functional thus, to better conserve mass, and such projections into the coarse grid also has to be achieved before, the coarse grid faithfully represents the coarse components of the errors. In addition one does not know *apriori* which *mesh refinements* will avoid loss of mass or how much the continuity equation has to be weighted to solve the problem. The weights can range anywhere from the range of 25, to 100. These are some of the issues which have beset researchers in the LSFEM community however, it is not been highlighted clearly enough for new practitioners to get better acquainted with the method. In light of the above issues raised, we did not implement the coarse grid correction step as it does not seem to provide a generic solution to large scale LSFEM solution methodologies which are beset with different numerical issues which need to be studied first.

F. Partition of the Domain

In addition to identifying which subdomains to use, it is also necessary to identify them. We identified each element to comprise of a subdomain. This choice was made

based on the fact, that each spectral element infact can be a large problem itself, in particular for the cases of high order approximations. The overlap regions is also of some importance in the determination of the convergence rates. We used the case of $\delta = 0$ overlap, as this allows for effective implementations and a minimal communication overhead between multiprocessors that are solving the problem. However, it is recognized, that even better convergence rates can be reported based on further exploration into these areas, the main interests of which will in high likely hood center around some of these performance enhancements. In this context infact, some of Pavirino's papers [47] can be very useful, because they have explored the increase in the overlap regions increasing the efficiency of Galerkin based spectral element methods. Also, a related issue is the choice of the subdomain solver. It has been recommended by different researchers to possibly use a GMRES type *inner* iteration solver for the subdomain problems, as it can be sometimes effective in approximating the solutions and relaxing the convergence criterion on these solvers can also aid in *faster* implementations. We implemented unsymmetric Gauss-Elimination elimination for the above. Amongst the advantages of the Gauss-Elimination is that it avoids the use of these *inner* iterations for obtaining fast solutions to the linear systems of equations and for relatively smaller size problems can be an effective implementation because its operation count scales as $O(N^3)$. It should be noted that we can also use a solver based on an incomplete Cholesky factorization for the same, and store only the non-zero entries in a sparse format. However, for the LSFEM formulations the element matrices are usually dense, and sparse storage formats for faster implementations do not offer any considerable advantage to the solution algorithm.

G. Spectral/*hp* Finite Element Formulation

The spectral finite element approximation is stated as follows, the primary variables are each approximated as;

$$\Delta^e = \sum_{j=1}^{n} \Delta_j \psi_j \tag{5.23}$$

where,ψ_j are the nodal expansions, which are provided by the following one-dimensional C^0 spectral nodal basis [1];

$$\psi_i(\xi) = h_i^e(\xi) = \frac{(\xi-1)(\xi+1)L_n'(\xi)}{n(n+1)L_n(\xi_i)(\xi-\xi_i)} \tag{5.24}$$

where, Δ_j are the nodal values due to the Kronecker delta property of the spectral basis. $L_n = P_n{}^{(0,0)}$ is the Legendre polynomial of order p, and ξ_i denotes the location of the roots of $(\xi-1)(\xi+1)L_n'(\xi) = 0$ in the interval $[-1,+1]$. All Jacobi polynomials, $P_n^{\alpha,\beta}$, satisfy a three-term recurrence relation of the form:

$$xP_n^{\alpha,\beta}(x) = a_{n-1,n}^{\alpha,\beta}P_{n-1}^{\alpha,\beta}(x) + a_{n,n}^{\alpha,\beta}P_n^{\alpha,\beta}(x) + a_{n+1,n}^{\alpha,\beta}P_{n+1}^{\alpha,\beta}(x) \tag{5.25}$$

where, $a^{\alpha,\beta}$ only depends on α, β, and n. And the derivatives of Jacobi polynomials satisfy a three-term recurrence relation of the form [48];

$$(1-x^2)\frac{dP_n^{\alpha,\beta}}{dx} = c_{n-1,n}^{\alpha,\beta}P_{n-1}^{\alpha,\beta}(x) + +c_{n+1,n}^{\alpha,\beta}P_{n+1}^{\alpha,\beta}(x) \tag{5.26}$$

For the special case of $\alpha = \beta$=1;

$$xP_n(x) = a_1(n)P_{n-1}(x) + a_2P_{n+1}(x) \tag{5.27}$$

where,

$$a_1(n) = \frac{n+1}{2n+3} \tag{5.28}$$

and,

$$a_2(n) = \frac{(n+1)(n+3)}{(n+2)(2n+3)} \tag{5.29}$$

For α=β=1, $c_{n,n}^{\alpha,\beta}$=0 and the above equation can be written as;

$$(1-x^2)\frac{dP_n^{\alpha,\beta}}{dx} = c_{n-1,n}^{\alpha,\beta}P_{n-1}^{\alpha,\beta}(x) + c_{n+1,n}^{\alpha,\beta}P_{n+1}^{\alpha,\beta}(x) \tag{5.30}$$

Seeking the recurrence relation for the derivative, we rewrite the above equation by dropping α and β, for the special case of $\alpha = \beta$=1;

$$(1-x^2)\frac{dP_n}{dx} = c_1(n)P_{n-1}(x) + c_2P_{n+1}(x) \tag{5.31}$$

where,

$$c_1(n) = \frac{(n+1)(n+3)}{2n+3} \tag{5.32}$$

and,

$$c_2(n) = \frac{(2n)(n+1)(n+3)}{(2n+3)(2n+4)} \tag{5.33}$$

H. Penalty Formulation Navier-Stokes (Unsymmetric System)

In this section we consider the Penalty finite element method, applied to solving Navier-Stokes equations in two dimensions which has been the primary generator for un-symmetric systems in the computational mechanics areas. The problem under consideration is that of a parallel channel flow, in which the top channel has an inlet fully developed profile, called the membrane channel, and the flow in the bottom channel (also called the permeate channel), develops because of the fluid trickling along the channel length, through a semi-permeable membrane. Some applications of such a configuration are in salt purification systems etc. For this exposition however, the main interest is in the un-symmetric nature of the algebraic system generated from the Lagrange finite element discretization of the resulting partial differential

equations. If the flow of the fluid in such a process is assumed to be governed by the incompressible Navier-Stokes equations then the equations for the two channel membrane flow comprise of the continuity equation and the momentum transport equations as follows.

$$\nabla \cdot u = 0 \tag{5.34}$$

The global mass conservation equation for the system of equations is expressed as equation 5.2. The momentum transport equations are mentioned below [49]:

$$(\mathbf{u} \cdot \nabla)\,\mathbf{u} = -\nabla p + \mu \nabla^2 \mathbf{u} + \rho \mathbf{g} \quad in\ \Omega \tag{5.35}$$

The above equations thus, for the momentum transfer are solved along with the mass conservation interpreted as a constraint into the momentum equations with the Penalty finite element method, to obtain the velocities for the equations in two dimensions. The specification of the problem is complete with the specification of the boundary conditions. The vertical component of the velocity thus at the bottom of the membrane channel, and the top of the permeate channel are specified, both set equal to the permeate velocity which was taken equal to be a constant.

$$v_y = v_w \tag{5.36}$$

At the left side of the permeate channel, the u-velocity component is assumed to be fully developed, with the v-component of the velocity set to zero. Inside the permeate channel on the left wall, both components of the velocities are set to zero, as there is a no-slip/no-penetration boundary condition at that face. At the top face, insulated boundary conditions are specified for the membrane channel. For the bottom wall of the feed channel, both components of the velocity are set to zero. The specification of these boundary conditions along with the differential equation

makes the problem well posed and solvable. The primary variables that are being solved for are thus, the the velocities, subject to the appropriate boundary conditions as specified above. Penalty finite element formulation was utilized to solve for the velocities with the penalization of the momentum equations with the velocity terms [49]. The formulation for this problem along with the discretized system of equations is being described in the following section.

1. Weak Finite Element Formulation

The Penalty finite element model includes the incompressibility as a constraint into the governing equations for fluid flow. The modified functional for the Naiver-Stokes equations are as follows [11];

$$I_p(v) = I_0(v) + \frac{\gamma_e}{2}\left[G(v)\right]^2 \tag{5.37}$$

In the above equation, $G(v)$ is the global mass conservation for the flow equations. For a description of the functional for the steady incompressible Navier-Stokes equations the reader is referred to [49]. Note, that the incompressibility constraint is included in a least squared sense into the functional. The Penalty finite element method for Navier-Stokes equations is derived based on seeking the minimum of this modified functional as;

$$\delta I_p(v) = 0 \tag{5.38}$$

The weak-form development involves reducing the differentiability of the equations after multiplication of the same with a weighing function and trading of the differentiability between the primary variables (velocities) and the corresponding weighting functions. For the Navier-Stokes equations it is sufficient to use a Lagrange family of interpolation functions as the basis functions. The x-component of the weak form

finite element model for the Navier-Stokes equations is given by;

$$\int_{\Omega_e} \left[2\mu \frac{\partial \psi_i}{\partial x} \frac{\partial \psi_j}{\partial x} u_j + \mu \frac{\partial \psi_i}{\partial y} \left(\frac{\partial \psi_j}{\partial y} u_j + \frac{\partial \psi_j}{\partial x} v_j \right) \right] d\mathbf{x} - \int_{\Omega_e} \rho_s f_x \psi_i d\mathbf{x} + \int_{\Omega_e} \gamma_e \frac{\partial \psi_i}{\partial x} \left(\frac{\partial \psi_j}{\partial x} u_j + \frac{\partial \psi_j}{\partial y} v_j \right) d\mathbf{x} = 0 \tag{5.39}$$

The y-component of the weak form finite element model for the Navier-Stokes equations is given by;

$$\int_{\Omega_e} \left[2\mu \frac{\partial \psi_i}{\partial y} \frac{\partial \psi_j}{\partial y} v_j + \mu \frac{\partial \psi_i}{\partial x} \left(\frac{\partial \psi_j}{\partial y} u_j + \frac{\partial \psi_j}{\partial x} v_j \right) \right] d\mathbf{x} - \int_{\Omega_e} \rho_s f_y \psi_i d\mathbf{x} + \int_{\Omega_e} \gamma_e \frac{\partial \psi_i}{\partial y} \left(\frac{\partial \psi_j}{\partial x} u_j + \frac{\partial \psi_j}{\partial y} v_j \right) d\mathbf{x} = 0 \tag{5.40}$$

In the above equations, γ_e denotes the penalty parameter, f_x is the x-component of the body force, and μ is the viscosity of the fluid. For the fluid flowing along the length of the two channel configuration described earlier, inclined at an angle θ with the horizontal the x-and y-component of the body forces are obtained as follows;

$$f_x = \ \rho g sin(\theta), f_y = \ \ -\rho g cos(\theta) \tag{5.41}$$

For the above equations the x-coordinate was taken aligned with the length of the separator and the y-coordinate was taken perpendicular to the x-axis. Thus, the gravity acts on the negative direction with respect to the positive y-axis for the problem under consideration. It should be noted that the penalty parameter terms are evaluated with a reduced integration rule than that used for the remaining coefficients. Specifically, the order of the Gauss integration rule used for the numerical evaluation of the penalty terms should be at least one order less than that is needed for the exact integration of the terms. For example, when bilinear approximation ($Q4$) of the primary variables is used, 3×3 Gauss rule is used to evaluate all coefficients in Equations [49], except for the penalty term, which is evaluated using 1×1

Gauss rule. Bilinear interpolation functions for the velocity components are an admissible combination of interpolation functions for generating stable and convergent solutions for flow problems. The element with $Q4$ interpolation is known to satisfy the Ladyzhenskaya-Babuska-Brezzi (LBB) condition [49]. The penalty parameter was taken as 10^{+06} in the simulations. It is recommended to use a sufficiently large value of the penalty parameter to satisfy the continuity equation and reach the convergence in the velocity vector solutions.

The above equations are assembled to obtain the element stiffness matrices. For an elaborate description of the assembly procedure and incorporation of the boundary conditions refer to [49] and for the Penalty finite element implementation [11]. The above set of equations have been linearized with the Picard method of linearization as this permits a direct implementation and at the same time the results converged to the solutions for this problem. Navier-Stokes equations with the weak finite element method have been mentioned to be the primary generators for non self adjoint operators, and the same was realized in the generation of the stiffness matrices. Considerations of the previous issue required thus the linear solver to be to be able to handle non-symmetric systems. The solver that was implemented thus to solve the problem was element by element Bi-orthogonal conjugate gradient solver with Jacobi preconditioning which can handle non-symmetric systems. The linear convergence criterion for the global residual was set at 10^{-06}. Non-linear convergence was declared when the non-linear convergence residual was reduced to a value lesser than 10^{-03} for the velocity metrics. A relaxation factor of 0.50 was found to work well for the solution of the non-linear problem. In the following section we describe the parallel implementation issues with the unsymmetric solver, namely the element by element bi-orthogonal conjugate gradient (EBE-BiJCG).

I. Element by Element Bi-orthogonal Conjugate Gradient

The solver that was implemented for the solution of the unsymmetric system of equations generated with the Penalty Finite element method, was the element by element bi-orthogonal conjugate gradient (Bi-CG) solver with Jacobi preconditioning. Conjugate gradient like methods for nonsymmetric linear systems can generally be divided into three classes-orthogonalization methods (e.g. GMRES), biorthogonalization methods (e.g. Bi-CG), and, methods based on the normal equations (e.g. CGNR). Bi-orthogonalization methods have received much attention recently because of its demonstrated computational efficiency and small storage requirements which is a result of short recurrences. Bi-orthogonal conjugate gradient solver has been mentioned to be a very robust solver, that takes lesser iterations to converge as compared to the conjugate gradient solver. In addition the capability of being able to solve, unsymmetric systems makes this solver a very attractive choice for solutions of linear systems in particular because a whole array of *Krylov* subspaces do not have to be saved for this type of solver, as opposed to the GMRES type implementations. In addition the Bi-CG constructs a three term recurrence sequence; the extra storage needed for the solver is at a minimum as compared to the GMRES type implementations. Amongst the weaknesses of the Bi-CG algorithm is the possibility of a breakdown, however, for such problems, and conditioning issues, even GMRES type algorithms suffer from the same problem. Infact, restarted versions of the GRMRES, and some look ahead strategies with the GRMRES algorithm have been researched to alleviate some of the problems that plague both methods. Thus, GMRES does not sufficiently outperform the Bi-CG algorithm for most linear systems, however requires considerably more storage. Based on the above arguments, Bi-CG solver is the method of choice, for solving unsymmetric systems at a minimal cost. Nevertheless,

the extensions of the same ideas to GMRES type solvers can be accomplished with relative ease. Let us denote the global stiffness matrix obtained from the summation of the element stiffness matrices with the following notation;

$$A = \sum_{e=1}^{Nel} A_{[e]} \tag{5.42}$$

and, the element stiffness matrices are obtained as follows;

$$A_{[e]} = P_e A_{K_e} P_e^T \tag{5.43}$$

where, P_e is the Boolean connectivity matrix which maps the coordinates of the element stiffness matrix into the global stiffness matrix. In this context, to ensure minimal overlap of data between processors, elements with independent degrees of freedom were sent to different elements with the help of some sort of colouring scheme, the most straight forward being the red-black colouring. The evaluation of the transpose which is required for the bi-orthogonal conjugate gradient algorithm, was achieved with the help of the transpose evaluations for each of the elements in the matrix based on the following;

$$A_{[e]}^T = \left(P_e A_{K_e} P_e^T\right)^T \tag{5.44}$$

With the Bi-CG algorithm, there can be a few different preconditioners that are feasible options. However, the main interest here being the computational efficiency in parallel, leaves us with relatively fewer choices, amongst them the best, and computationally cheapest is the Jacobi preconditioner. Jacobi preconditioning is relatively cheap to construct, and provides an effective means of solving preconditioned problems in parallel on multiprocessors. Gauss-Seidel is another preconditioner that has been explored, but its an inherently sequential algorithm, with some sort of colouring required to remove the inherent sequential dependencies. To avoid complications, in

implementations and in order to stay sufficiently generic and widely accessible as an algorithm, we only implement the Jacobi preconditioning for solving the system of equations. Also, because of the inclusion of the penalty terms, the diagonal dominance of the system of equations is preserved and thus, this preconditioning works very well for the penalized momentum equations.

1. Bi-JCG EBE Algorithm

Here we describe the element by element bi-orthogonal conjugate gradient algorithm, for solving unsymmetric systems of equations. This methodology was implemented to solve the membrane separation process problem.

Compute $r^{(0)} = b - Ax^{(0)}$

Choose $r1^{(0)} = r^{(0)}$;

for $i = 1, 2, 3, 4, ...$

$M\ z^{(i-1)} = r^{(i-1)}$

$M^T\ z1^{(i-1)} = r1^{(i-1)}$

$\rho_{i-1} = {z_{i-1}}^T r1^{i-1}$

$\rho_{i-1} = 0$, **report Lancoz breakdown**

if i=1;

$p^{(i)} = z^{(i-1)}$

$p1^{(i)} = z1^{(i-1)}$

else $\beta_{i-1} = \frac{\rho^{i-1}}{\rho^{i-2}}$

$p^{(i)} = z^{(i-1)} + \beta_{i-1} p^{(i-1)}$

$p1^{(i)} = z^{(i-1)} + \beta_{i-1} p1^{(i-1)}$

end if

$q^{(i)} = \Sigma_{e=1}^{Nel} A_e p^{(i)}$

$q1^{(i)} = \Sigma_{e=1}^{Nel} A_e^T p1^{(i)}$

$\alpha_{(i)} = \rho_{i-1}/p1^{i^T}qi$

$x^{(i)} = x^{(i-1)} + \alpha_i p^{(i)}$

$r^{(i)} = r^{(i-1)} - \alpha_i q^{(i)}$

$r1^{(i)} = r1^{(i-1)} - \alpha_i q1^{(i)}$

check for convergence

end

This above method can in theory breakdown however, in reality the case is rare even if there are some cases where there might be a temporary singular recurrence term, there may be a spike in the convergence curve, however the robustness of Bi-CG to such spikes have been demonstrated by authors [50] and [51] even in finite precision arithmetic of a computer. In the following section we demonstrate the results that were obtained with both the algorithms that have been reported above, for the solution of both symmetric and unsymmetric operators and demonstrate the scalability of the algorithms.

J. EBE-BJCG Results

The problem characteristics and some scalability issues are being presented herewith. We implemented the EBE-BJCG algorithm in parallel, and the distribution of the work to different processors, provided super linear to linear speedup for flow past a cylinder solved with the Fictitious Domain method (only speedup presented here). The linear convergence history for the first non-linear step of the problem solved with a scalar version of the code and the parallel version of the same on 8 processors is provided below. A comparison of the convergence history for *nprocs* (number of processors) set to 8 is also provided. It can be seen from Figure 27 that the parallel version of the convergence history is slightly different from the scalar version and a

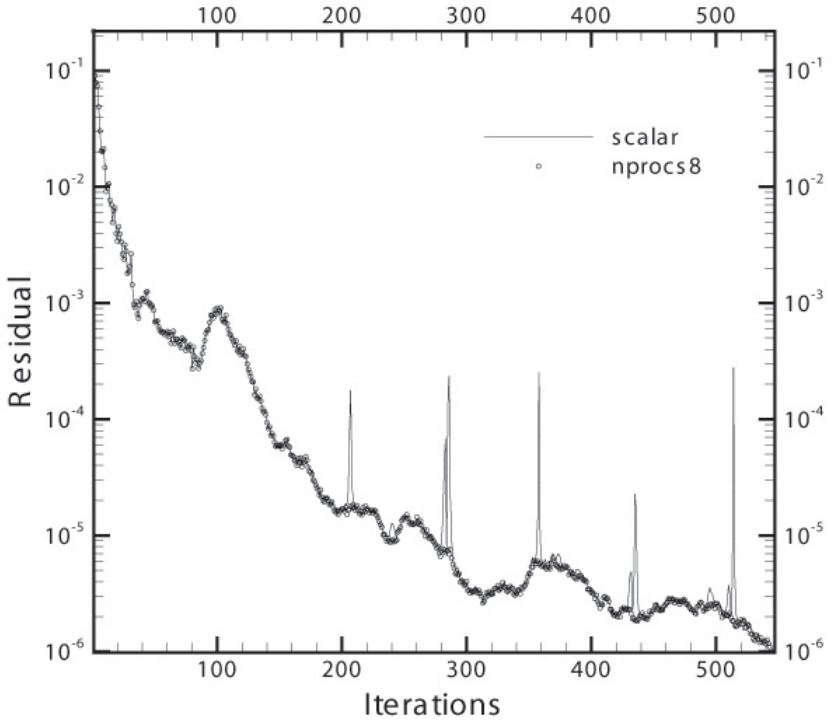

Fig. 27. Parallel convergence history for EBE-BJCG solver

more careful look at the graph shows that the parallel version of the code is more robust, in avoiding nearly singular search directions that are sometimes obtained with the conjugate gradient solver type solvers, and relatively high jumps in the convergence histories are evidence of the same with the scalar version of the solver. However, the parallel version avoids the same and has a relatively smoother convergence history. These deviations are mostly confined by small peaks where the scalar version of the problem deviated slightly from the parallel version. Small perturbations caused by round off errors, of the scalar version of the problem vs. the parallel version of the problem can alternatively account for the slight discrepencies reported. Whichever maybe the reason nevertheless, the parallel version of the solver is found to be more effective in reducing these round off errors, or singular search directions, with high

residuals. Figure 28 presents the time taken by the scalar version of the program for

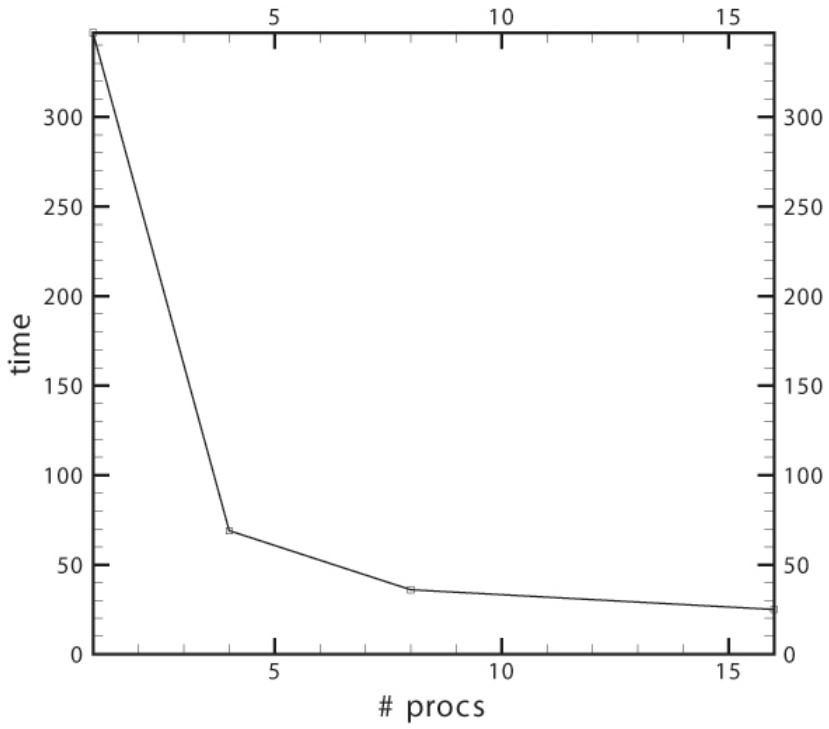

Fig. 28. Solution times for the EBE-BJCG solver

solving the problem mentioned above, and the time taken by the parallel versions of the program with four (4), eight (8), and sixteen (16) processors in parallel. As can be seen from the figure the scalar version of the program takes 347 seconds for one iteration, whereas the parallel version of the program takes 69 seconds for the same operation with four processors. This provides a speedup of approximately 5, which is higher than a linear speedup. The 8-processor run for the same input generates results in 36 seconds, which gives a speedup of 9.6. Some of the advantages in the program can also be attributed to the effective cache memory utilization which can effect super-linear speedup. The sixteen processor run on the same problem provided the results in 25 seconds which evaluates to a speedup of 13.88 ($\sim$ 14.0). The above

speedups greatly support our claim that element by element bi-orthogonal conjugate gradient solver is effectively parallelizable, with the solver achieving superlinear and slightly lesser than linear speedup in all cases. The total number of degrees of freedom that were solved for for this problem were 14884 for a cylinder encased in a small channel width with a consequently large blockage ratio. Figure 29 compares the u-velocity

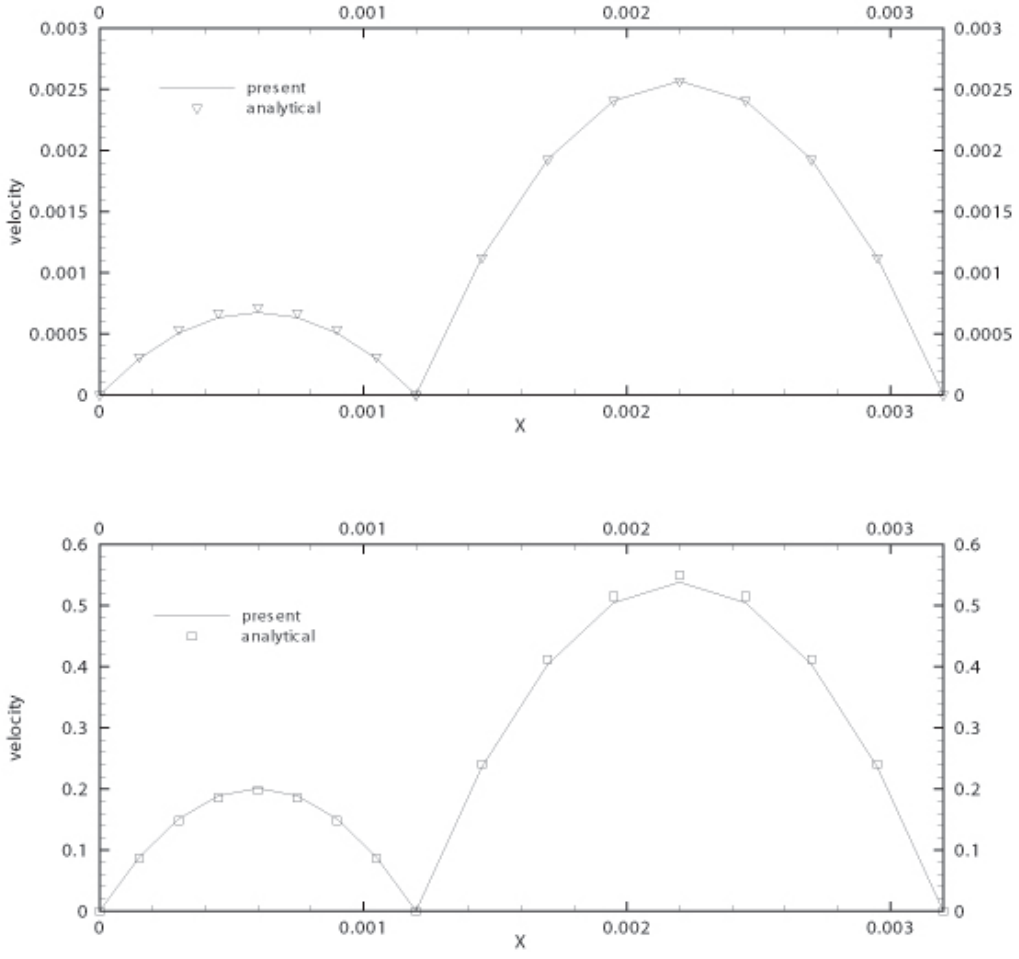

Fig. 29. Velocity comparison with analytical solution

component with the analytical solution for the feed and permeate channels, for both horizontal and vertical configurations for the two channel system with permeation ve-

locity set to a constant. The analytical solutions show very good agreement with the present results, showing the effectiveness of the EBE-BJCG algorithm in solving the unsymmetric system along with the reduced integrated penalty terms. The horizontal channel had the forcing function set to zero, where as for the vertical case the forcing function per unit volume was set to the acceleration due to gravity. The EBE-BJCG implementation was also used to obtain the benchmark results on the driven cavity problem in two dimensions with the LSFEM formulation. The LSFEM formulation can have some unsymmetry in the stiffness matrices because of the non-linear terms in the problem and thus Biconjugate gradient algorithm was tested for the solution of the equations. These results are not repeated here in the interest of brevity. For the flow past a cylinder problem for which the EBE-solution times have been reported, in two dimensions, we are reporting the speedups in the Table XXI with Jacobi preconditioning during the course of solution of the system of equations. Also, with

Table XXI. Speedups for EBE-BJCG solver

Index	Ideal		Time	Speedup
No.	*Processors*	*ideal*	(*sec*)	*Ratio*
1	1	1	347	1.00
2	4	4	69	5.02
3	8	8	36	9.64
4	16	16	25	13.88

the element by element Bi-conjugate gradient solver we can see from Table XXI that there is some deterioration from linear speedup with an increase in the number of processors, however for all cases, the scalability of the problem can be considered to be very good. Super linear speedup is the ideal situation in parallel and for the cases

we test with the EBE-BJCG implementations also we achieved super linear speedup and slightly lesser than linear speedup for the worst case.

K. *Additive* Schwarz Results

Figure 30 presents the streamline and contour plots of the velocities, pressure, and vorticity for Stokes flow obtained with the *Additive* Schwarz domain decomposition technique. This run was performed using a mesh of 6×6, *hp*-SEM, mesh with each element containing a spectral mesh of order 4. Qualitative agreement of these plots with the results presented in [42] is excellent. Figure 31 presents the streamline and contour plots of the velocities, pressure, and vorticity for a Reynolds number of 100 obtained with the *Additive* Schwarz domain decomposition technique. Figure 32 presents the streamline and contour plots of the velocities, pressure, and vorticity for a Reynolds number of 400, for the driven cavity problem obtained with *Additive* Schwarz domain decomposition. As can be seen from the figure, the presence of the vortex near the right end of the cavity is clearly visible and was smaller in size for the $Re = 100$ case presented earlier. Figure 33 presents the agreement of the present results with published results of Ghia et al. [52] for the u-velocity at the midplane of the driven cavity problem, where as Figure 34 presents the v-velocity at the midplane, of the cavity. The agreement for both cases is good, and the results thus are validated for effective implementations of the Domain Decomposition technique. Agreements for the other Reynolds numbers were similarly found to be very good however, they have not been presented in the interest of brevity. The Figure 35 presents the number of iterations taken by the Jacobi preconditioned conjugate gradient and the *Additive* Schwarz algorithm for the driven cavity problem for Reynolds numbers of 100 and 400. As can be seen from the figure, *Additive* Schwarz algorithm converges with around

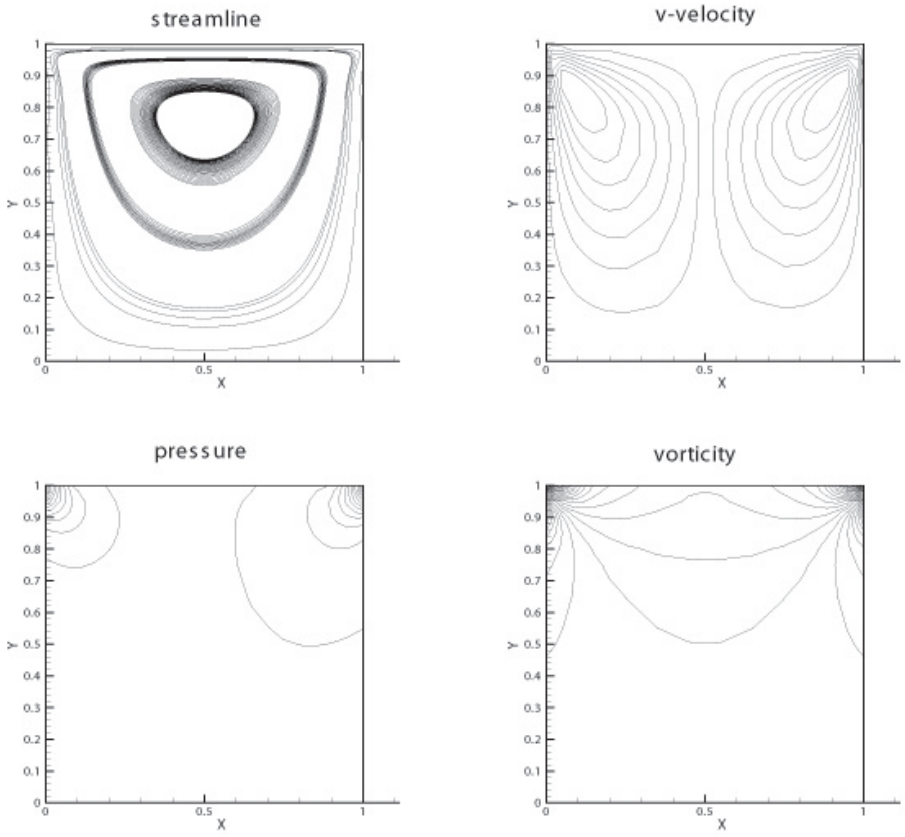

Fig. 30. Contour plots for stokes flow

1/3 the number of iterations for most cases. There is deterioration of the performance of the *Additive* Schwarz methods for the solutions of problems with increase in the number of subdomains, and this has been well documented with the Galerkin finite element formulations. The same behaviour is observed with the LSFEM problems as shown here, however as is well known the solution of this issue lies in a judicious choice of the number of subdomains along with a concurrent increase in the overlap region. Some of these refinements dependent on the specific problem under consideration is left for further research work. We anticipate however that there can be considerable advantages and even higher speedups with implementations of some of the these ideas.

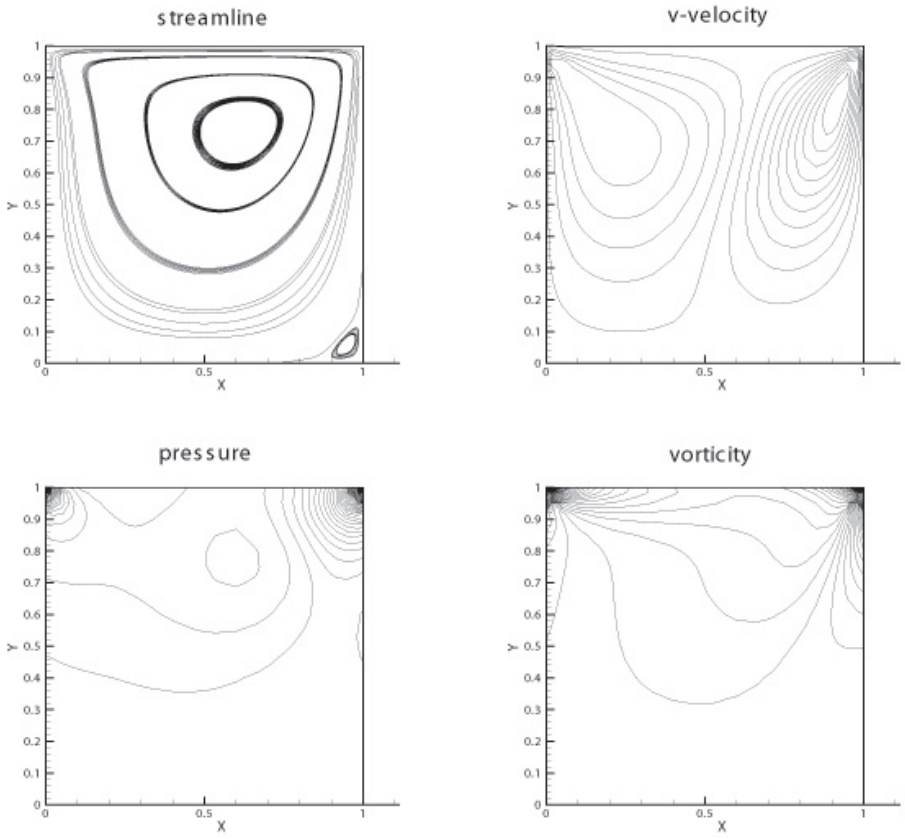

Fig. 31. Contour plots for Re=100

L. Parallel Performance Measures

The computations were performed using the supercomputing resources provided by the Texas A& M University supercomputing center. The specific compiler used was the IBM compiler for AIX, V10.1. The simulations were performed using the IBM Cluster 1600 (hydra.tamu.edu), which has 832 cores. The Additive Schwartz algorithm shows superlinear speedup for smaller number of domains, and there is deterio-

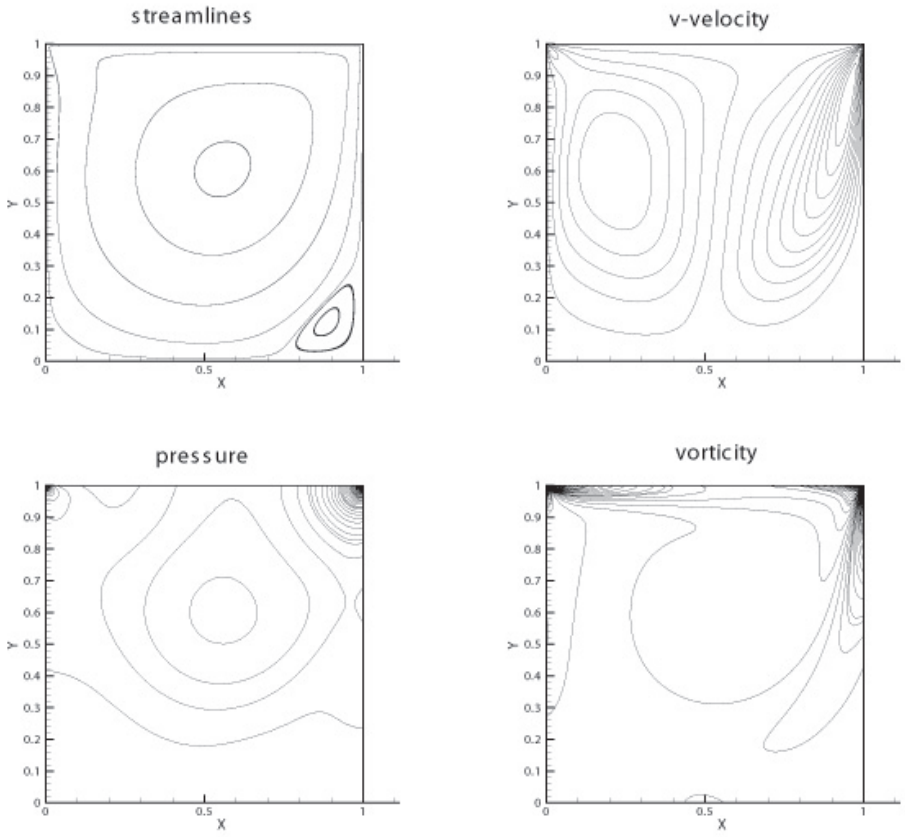

Fig. 32. Contour plots for Re=400

ration in the speedup ratio with an increase in the number of subdomains. This is an expected trend, and even for large number of subdomains, we notice the performance is ideal to slightly lesser than ideal for all cases. The linear convergence tolerance for all cases was set at a reduction of the final residual with respect to the initial residual at a a value of 10^{-06}. Non-linear convergence was declared when the non-linear residual defined by the following formula reduced to a value of 10^{-03}.

$$\epsilon = \frac{\| \mathbf{U^{i+1}} - \mathbf{U^{i}} \|_0^2}{\| \mathbf{U^{i}} \|_0^2} < 10^{-03} \tag{5.45}$$

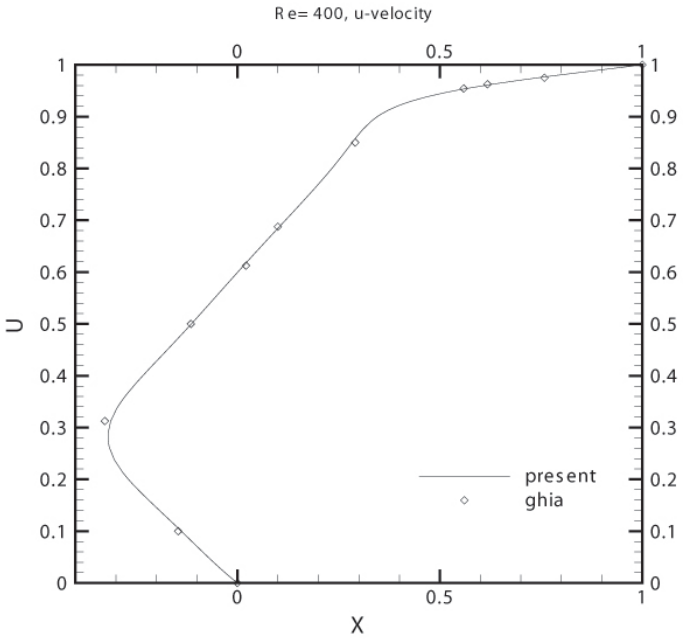

Fig. 33. u-velocity mid-plane for Re=400

An important measure of the parallel performance is speedup. For a fixed size of the problem, the speedup is defined as;

$$S_p = \frac{T_1}{T_p} \tag{5.46}$$

where, T_1 is the elapsed time on one processor, and T_p is the elapsed time for the same problem on P processors. The efficiency is defined as the speedup ratio over the number of processors used ($nprocs$).

$$\epsilon_p = \frac{S_p}{n} \tag{5.47}$$

We report the speedup ratios for both the Additive Schwarz algorithm, and the EBE-BJCG algorithm, in Figure 36. Efficiency of both the EBE Bi-JCG algorithm implemented in parallel, and the Additive Schwarz algorithm was found to be greater than 1, which is the ideal case efficiency, as mentioned earlier, because of effective

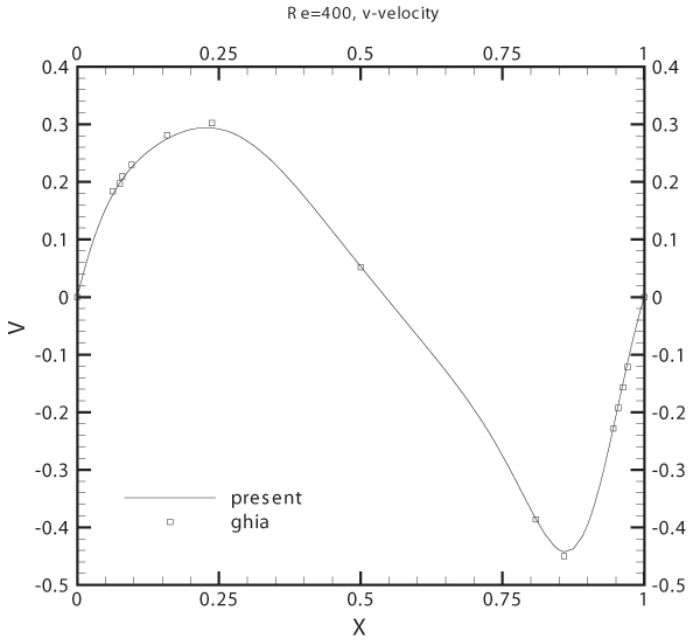

Fig. 34. v-velocity mid-plane for Re=400

cache memory utilization. Thus, only the speedups are being reported in Figure 36 against the ideal speedups expected with an increase in the number of processors. A tabulation of the values of the speedups with the Additive Schwarz algorithm has been presented in Table XXII which also presents the super-linear to linear speedup reported for all cases.

M. Conclusion

In this chapter we presented the parallel implementations of two new algorithms for solving huge systems of linear equations. Scalability of the implementations were described and their effective implementations demonstrated for solving both adjoint, and non-self adjoint operators. For both algorithms, we demonstrated superlinear to linear speedups which pave the way for effective usage of the above methods for solving problems in the CFD areas. A few sample problems were solved, and results validated

Table XXII. Speedups for different Reynolds numbers

Iteration	Re	No. of	Speedup		Iterations	
No.		*Domains*	*ideal*	*present*	*ASchwarz*	*BJCG*
1	100	64	6	13.58	55	124
2	100	64	6	14.13	221	554
3	100	64	6	13.67	229	592
4	100	64	6	15.97	150	502
1	400	400	8	8.46	59	138
2	400	400	8	10.20	1264	3443
3	400	400	8	9.54	1571	4133
4	400	400	8	7.91	759	1639
5	400	400	8	10.05	963	2516
6	400	400	8	9.67	1059	2889
7	400	400	8	9.98	1453	3907

with benchmark/analytical results. New research areas for further exploiting the usage of the above mentioned schemes by further refinements were highlighted.

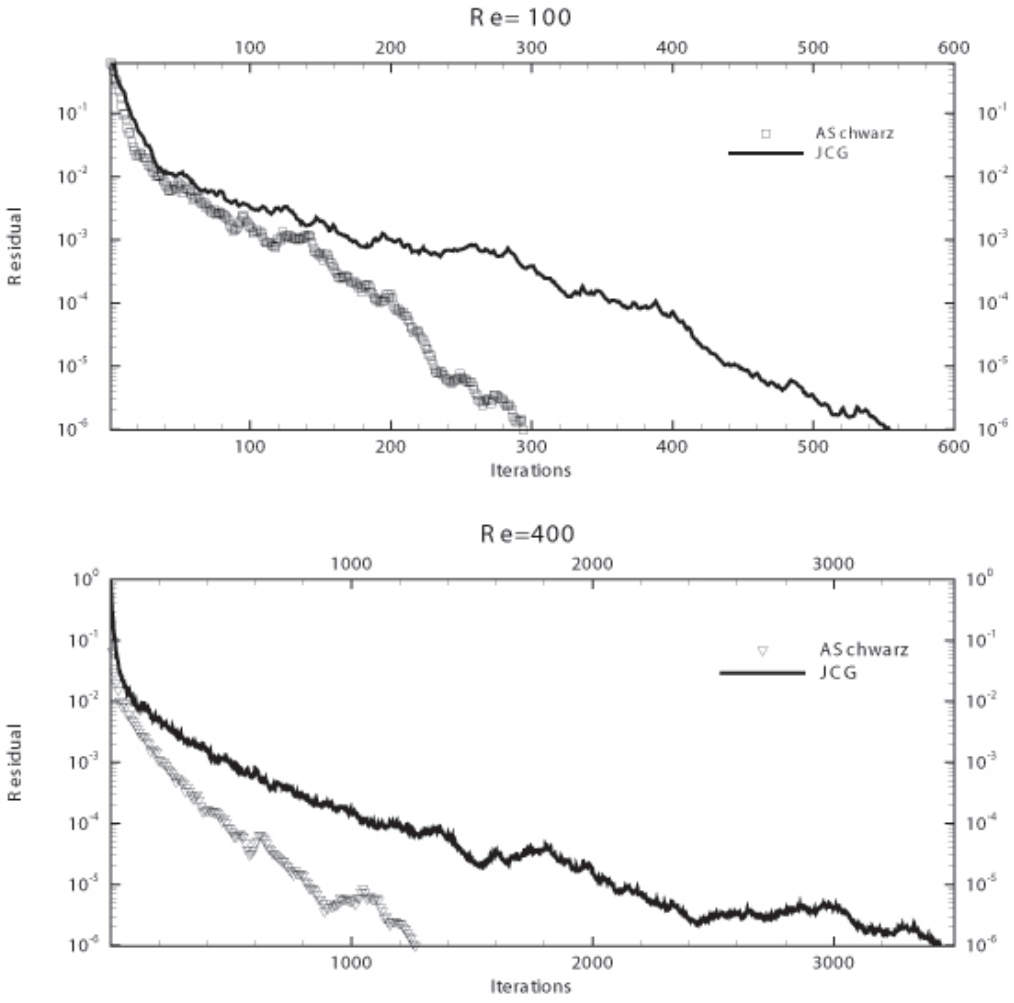

Fig. 35. BJCG vs. Additive Schwarz iterations

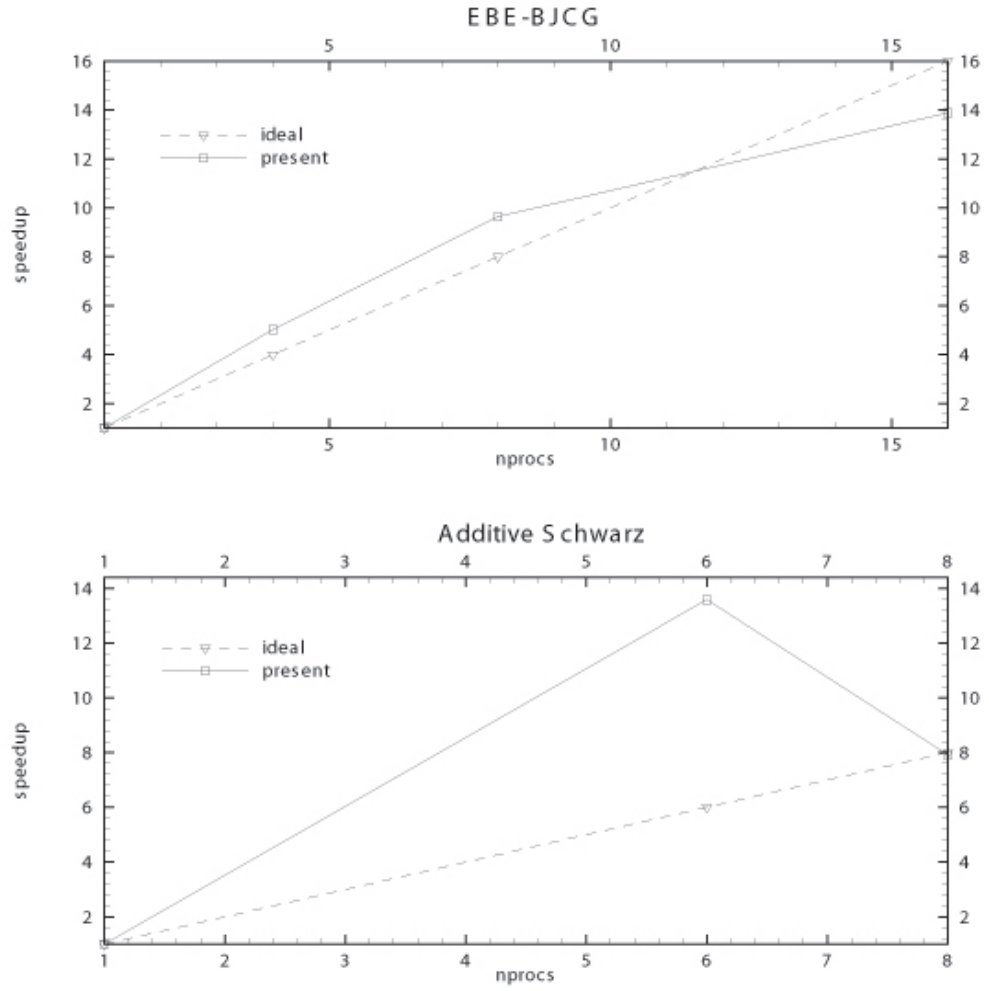

Fig. 36. BJCG vs. Additive Schwarz speedups

CHAPTER VI

MULTIGRID METHODS FOR LEAST SQUARES PROBLEMS

A. Introduction

There is a vast literature on least squares finite element methods that have been applied to solving problems in computational fluid dynamics areas. The *hp* version of the least squares problems has computationally expensive quadrature requirements which necessitate the usage of elegant methods for solving the resulting systems of equations. Amongst some of the schemes for solving large systems of equations is the element by element solution (EBE) technique which has found widespread use in the papers [53] -[54] of in the context of the *hp* version of the least squares finite element methods. Although such techniques are very efficient memory wise, as one can solve 0.5 million degrees of freedom problem with not more than 176 MB of memory in parallel, the use of element by element techniques for solving CFD problems is generally not recommended because of extremely high computational times. The basic quadrature requirement with the *p*-version spectral element methods requires a $O(p^6)$ operation on each element and this becomes the performance bottleneck. It is thus not uncommon to have solution times in days with EBE algorithms running even on multiprocessors. When seeking a collocation solution, based on bilinear finite element meshes in two dimensions, where a reduced integration technique has been used in the context of collocation least square finite element methods, the use of EBE may be a good idea, and has been extensively explored by Jiang [42] as it is computationally cheap. For the *hp* least squares formulation one is left to evaluate higher order quadratures and necessarily is compelled to explore other options to generate the solutions of the systems faster than possible with EBE techniques. Thus

exploring of other highly parallel schemes in the context of *hp* least squares problems is of interest. In the previous chapter we explored the usage of one such highly parallel scheme namely the Schwarz method for solutions of least squares problems. In this chapter we bring together the ideas of collocation and *hp* version of least squares in the context of a Multigrid method to attain even better convergence performance, in the context of LSFEM.

B. Background

Amongst the different methods used for solving fluid flow problems, a relatively new addition is the least squares finite element method (LSFEM). Amongst the celebrated advantages of the least squares finite element methods are the symmetric systems produced from these formulations; and also the velocity and the pressure spaces do not have to adhere to the Ladyzhenskaya-Babuska-Brezzi (LBB) compatibility restrictions for obtaining the velocity and pressure metrics. It has been mentioned in literature that the least squares finite element methods (LSFEM) leads to symmetric systems by construction, for the solutions of problems, and the problems thus are more amenable to conjugate gradient techniques for the solution of the linear systems generated. The element by element technique however, as has been mentioned above leads to extremely large solution times for the solutions of problems even in parallel. In the previous chapter we explored the usage of Additive Schwarz methods as preconditioners for the solutions of LSFEM problems. We also demonstrated the deterioration of the performance of the Additive Schwarz techniques for the solutions of LSFEM problems as the number of subdomains increases. It has been mentioned that single level methods are most effective for the solutions of a small number of subdomains.

For smooth errors over a small subdomain, the error may be written as $\varepsilon = \bar{\varepsilon} + \varepsilon_{small}$. Since no reduction in the $\bar{\varepsilon}$ term may be obtained through a local solve, one can expect little reduction in the entire error ε over the entire subdomain. This also reflects the deterioration of the performance of the Schwarz decomposition techniques when the number of subdomains is increased. One thus is compelled to explore options to be able to reduce the smooth errors. One such technique that attains this is the multigrid method [55],[56],[57], [58] and we explore this technique for the solutions of least squares problems. The Galerkin finite element method does not produce the an H^1 elliptic form and multigrid schemes typically perform very poorly. An alternative formulation based on reformulating the Navier-Stokes equations based on the first-order system and minimizing the least- squares norm of residuals in the resulting system-the FOSLS (first order system least squares) formulation produces the H^1 elliptic form and is the formulation adopted in this study.

C. Navier-Stokes Equations

The behaviour of slow and creeping flows can be modelled well with the Stokes equations. The Stokes equations are written as;

$$-\nabla p + \nabla^2 \mathbf{u} = 0 \quad in\ \Omega, \tag{6.1}$$

$$-\nabla \cdot \mathbf{u} = 0 \quad in\ \Omega, \tag{6.2}$$

$$\mathbf{u} = \mathbf{g} \quad in\ \Gamma, \tag{6.3}$$

where, p is the pressure scaled by the viscosity, and $\mathbf{u}$ is the velocity vector. Expressing the Stokes equations for the easy application of the FOSLS formulation and introducing the vorticity as a new variable into the formulation $\omega = (\omega_x,\ \omega_y,\ \omega_z) = \nabla \times \mathbf{u}$;

we obtain;

$$\nabla p + \nabla \times \omega = \mathbf{f} \quad in\ \Omega, \tag{6.4}$$

$$\nabla \cdot \omega = 0 \quad in\ \Omega, \tag{6.5}$$

$$\omega - \nabla \times \mathbf{u} = 0 \quad in\ \Omega, \tag{6.6}$$

$$-\nabla \cdot \mathbf{u} = 0 \quad in\ \Omega, \tag{6.7}$$

For simplicity the domain is considered two-dimensional, open, bounded, and simply connected with a smooth boundary Γ. For a two dimensional consideration we immediately drop the condition on the solenoidality of ω as it is identically equal to zero.

The non-linear Navier-Stokes equations in the pressure-velocity formulation can be written as follows;

$$(\mathbf{u} \cdot \nabla)\,\mathbf{u} + \nabla p + \frac{1}{Re}\Delta \mathbf{u} = \mathbf{f} \quad in\ \Omega \tag{6.8}$$

$$\nabla \cdot \mathbf{u} = 0 \quad in\ \Omega \tag{6.9}$$

with, $\mathbf{u}$ the velocity vector, $\mathbf{f}$ is the forcing term per unit mass, Re is the Reynolds number and $\Omega \subset \Re^d$, where d, is the space dimension in which the problem is defined. To allow the use of practical C^0 expansions, in the least squares finite FOSLS formulation, the governing equations must be recast, as an equivalent first-order system. So, the least squares functional is defined in terms of the L_2 norms only. Introducing the vorticity, and using the identity, $\omega = \nabla \times \mathbf{u}$, and using the vector identity,

$$\nabla \times \nabla \times \mathbf{u} = -\Delta u + \nabla\,(\nabla \cdot \mathbf{u}) \tag{6.10}$$

The Navier-Stokes equations in the first order form are thus expressed as follows;

$$(\mathbf{u} \cdot \nabla)\,\mathbf{u} + \nabla p - \frac{1}{Re}\nabla \times \omega = \mathbf{f} \quad in\ \Omega$$

$$\omega - \nabla \times \mathbf{u} = 0 \quad in\ \Omega$$
$$\nabla \cdot \mathbf{u} = 0 \quad in\ \Omega$$
$$\nabla \cdot \omega = 0 \quad in\ \Omega \tag{6.11}$$

The above equations need to be supplemented with the appropriate boundary conditions to complete the definition of the boundary value problem. The non linear term, $\mathbf{u} \cdot \nabla \mathbf{u}$ has no effect on the classification of the system, and thus, the same boundary conditions as the Stokes equations are admissible boundary conditions for the non-linear Navier-Stokes equations also.

D. Linearization Procedure

Before, the application of the LSFEM, the convective term, needs to be linearized by using successive substitution or Newtons method. We adopted both methods in our analysis. For illustration purposes we demonstrate the Newtons method of linearization of the LSFEM;

$$(\mathbf{u_0} \cdot \nabla)\,\mathbf{u} + (\mathbf{u} \cdot \nabla)\,\mathbf{u_0} + \nabla p + \frac{1}{Re}\nabla \times \omega = \mathbf{f} + (\mathbf{u_0} \cdot \nabla)\,\mathbf{u_0} \quad in\ \Omega \tag{6.12}$$

Newtonś method is known to have a smaller radius of convergence, however the convergence to the solutions is expected to be faster as compared to the Picard method or the method of successive substitutions (if it converges). Newton's method of linearization is the preferred choice of linearization procedure when a guess close to the solution is available [42]. The LSFEM functional is setup with the help of the reduction of the individual residuals for each of the equations expressed above and is provided by;

$$J(\mathbf{u}, p, \omega; \mathbf{f}) = \frac{1}{2}\Big(\parallel (\mathbf{u} \cdot \nabla)\,\mathbf{u} + \nabla p + \frac{1}{Re}\nabla \times \omega - \mathbf{f} \parallel_0^2 + \parallel \omega - \nabla \times \mathbf{u} \parallel_0^2 +$$

$$\| \nabla \cdot \mathbf{u}\|_0^2 + \| \nabla \cdot \omega\|_0^2 \Big) \quad (6.13)$$

The following functional minimization statement provides the stiffness matrix for the formulation. The minimization statement is mentioned as follows;

Find $(\mathbf{u},\ \mathbf{p},\ \omega) \in\ X(\Omega)$, such that;

$$\lim_{\epsilon \to 0} \frac{d}{d\epsilon} J\left(\mathbf{u} + \epsilon \mathbf{v}; \mathbf{f}\right) = 0 \quad \forall \mathbf{v} \in X(\Omega) \tag{6.14}$$

where, $X(\Omega)$ is the space of admissible functions,

$$X = \{(\mathbf{u}, p, \omega) \in \mathbf{H}_0^1(\Omega) \times \mathbf{H}^1(\Omega) \cap \bar{L}_2(\Omega) \times \mathbf{H}^1(\Omega)\} \tag{6.15}$$

In an abstract notation, the linear system is expressed as the following;

Find $(\mathbf{u},\ p,\ \omega) \in\ X(\Omega)$, such that;

$$\mathcal{A}(\mathbf{U}, \mathbf{V}) = \mathcal{F}(\mathbf{V}) \ \ \forall \mathbf{V} \in X(\Omega) \tag{6.16}$$

with;

$$\mathcal{A}(\mathbf{U}, \mathbf{V}) = \langle \mathcal{L}(\mathbf{U}), \mathcal{L}(\mathbf{V}) \rangle_{Y(\Omega)} \tag{6.17}$$

and;

$$\mathcal{F}(\mathbf{V}) = \langle \mathcal{G}, \mathcal{L}(\mathbf{V}) \rangle_{Y(\Omega)} \tag{6.18}$$

where, $\mathcal{L}$, represents the Navier-Stokes operator, $\mathcal{F}$ is the corresponding source term, $\mathcal{A} : X \times X \to \mathcal{R}$, is a symmetric, continuous bilinear form, and $\mathcal{F} : X \to R$, is a continuous linear form. A description of the operator $\mathcal{L}$ follows as expressed in the first order form. We have described a method for the derivation of these matrices in a following chapter VII. Following the convention used earlier, the first order system can be expressed in the following form;

$$A\underline{u} = \underline{f} \tag{6.19}$$

and therefore;

$$A_1\frac{\partial \underline{u}}{\partial x} + A_2\frac{\partial \underline{u}}{\partial y} + A_0\underline{u} = \underline{f} \tag{6.20}$$

and, the above matrices are defined as follows;

$$A_1 = \begin{bmatrix} u_0 & 0 & 1 & 0 \\ 0 & u_0 & 0 & -\frac{1}{Re} \\ \omega & 0 & 0 & 0 \\ 0 & -1 & 0 & 0 \end{bmatrix}, \quad A_2 = \begin{bmatrix} v_0 & 0 & 0 & \frac{1}{Re} \\ 0 & v_0 & 1 & 0 \\ 0 & \omega & 0 & 0 \\ 1 & 0 & 0 & 0 \end{bmatrix} \tag{6.21}$$

,

$$A_0 = \begin{bmatrix} \frac{\partial u_0}{\partial x} & \frac{\partial u_0}{\partial y} & 0 & 0 \\ \frac{\partial v_0}{\partial x} & \frac{\partial v_0}{\partial y} & 0 & 0 \\ 0 & 0 & 0 & 0 \\ 0 & 0 & 0 & 1 \end{bmatrix}, \quad f = \begin{bmatrix} f_x + u_0\frac{\partial u_0}{\partial x} + v_0\frac{\partial u_0}{\partial y} \\ f_y + u_0\frac{\partial v_0}{\partial x} + v_0\frac{\partial v_0}{\partial y} \\ 0 \\ 0 \end{bmatrix} \tag{6.22}$$

Finally, instead of using the infinite dimensional function space $X(\Omega)$ to seek for the minimizer, the searching process is performed in a finite dimensional space X_h, i.e. $\mathbf{U_h} \in \mathbf{X_h(\Omega)}$. Then the least squares formulation can be stated as;

Find $\mathbf{U_h} \in \ \mathbf{X(\Omega)}$, such that;

$$\mathcal{A}(\mathbf{U_h}, \mathbf{V_h}) = \mathcal{F}(\mathbf{V_h}) \ \ \forall \mathbf{V_h} \in X_h(\Omega) \tag{6.23}$$

The Picard method for the LSFEM formulation follows the development very closely with the following linearization;

$$(\mathbf{u_0} \cdot \nabla)\,\mathbf{u} + \nabla p + \frac{1}{Re}\nabla \times \omega = \mathbf{f} \ \ in\ \Omega \tag{6.24}$$

With the above procedure we obtain the discrete form of the least squares finite element model.

E. Conjugate Gradient Method

The matrix that result from the least squares finite element formulation is sparse, symmetric, and positive definite. Preconditioned conjugate gradient methods are a popular Krylov method, commonly used to solve such systems. Let us denote the symmetric linear system of equation that we wish to solve with;

$$A\mathbf{x} = \mathbf{b} \tag{6.25}$$

where, A is a $N \times N$ positive definite matrix, and, $f \subset R^n$. Krylov subspace methods for solving the above linear system are iterative methods, that pick the j^{th} iterate from the following affine subspace:

$$x_j \in x_0 + K_j(A_j, r_0) \tag{6.26}$$

where, x_0 is the initial guess, r_0 is the corresponding residual vector$= b - Ax_0$, and the Krylov subspace $K_j(A, r_0)$ is defined as;

$$K_j(A_j, r_0) = span\{r_0, Ar_0, ..., A^{j-1}r_0\} \tag{6.27}$$

The different versions of the Krlov methods differ in the different choices of the subspaces. Amongst the popular methods for the solutions of linear systems with Krylov subspace are the Preconditioned Conjugate Gradient (PCG), Bi-orthogonal Stablized (Bi-CGSTAB), Bi-Orthogonal Conjugate gradient (BCG), Generalized Minimum Residual (GMRES). Amongst these methods, also the most competitive are PCG, and GMRES. GMRES suffers from one major drawback in that the storage requirements of all the subspaces are needed during their formation in course of the iteration process. To get around this limitation, restarted versions of this algorithm are popular, in particular one variant with k restarts provides us with $GMRES(k)$.

To work with shorter recurrence relations, and also to economize on storage requirements, one is often lead to CG as the most competitive for the solution of huge linear systems. In this chapter, we will only explore the usage of multigrid methods in conjugation with CG algorithms. However, it should be noted that a non-trivial extension of these ideas are possible to any Krylov subspace method.

If a real $N \times N$ matrix A is symmetric and positive definite, the solution of the linear system with the conjugate gradient is equivalent to seeking the solution of the following quadratic form;

$$Q(x) = \frac{1}{2} x^T A x - \mathbf{b}^T \mathbf{x} \tag{6.28}$$

In this interpretation the CG algorithm can be interpreted to be the solution of the generalized least squares problem where the minimization takes place over a particular vector space in particular the Krylov space defined above.

The conjugate gradient is one of the minimization methods that uses A-conjugate vectors as direction vectors which are generated sequentially. Theoretically, this method has the property that the number of steps until convergence is at most N steps. The theory behind this being that at the end of N steps one runs out of mutually orthogonal directions for searching the solutions. However, this property is only valid in infinite precision, in practice during programming of some of these methods, the convergence is slightly higher than N for some problems due to round off errors. It has been shown that Conjugate gradient method reduces the initial error $|\mathbf{U^0} - \bar{\mathbf{U}}|$ to ε times the final error $|\mathbf{U^n} - \bar{\mathbf{U}}|$ in the following number of iterations;

$$n \geq \frac{1}{2} \sqrt{\kappa(\mathbf{K})}\ log \frac{1}{\varepsilon} \tag{6.29}$$

where, κ is defined as the ratio of the maximum eigenvalue of the matrix $\mathbf{K}$ to the

smallest,

$$\kappa = \frac{\lambda_{max}}{\lambda_{min}} \tag{6.30}$$

where,

$$\lambda_{max} = max_{U \neq 0} \frac{U^T K U}{U^T U} \quad \lambda_{min} = min_{U \neq 0} \frac{U^T K U}{U^T U} \tag{6.31}$$

In the above, **U** denotes the global vector of nodal values.

F. Multigrid Method

For the conjugate gradient algorithms, the number of iterations required for convergence increases with the increase in the problem size, as the conditioning continues to worsen, with increasing sizes of the problem. Jacobi preconditioning which has found widespread use in the least squares community is very similar to using identity as a preconditioner and offers very low performance gain as compared to the unpreconditioned system. One can ameliorate some of the problems mentioned above, if we implement multigrid as a stand alone solver, or as a preconditioner to the Krylov Subspace method of choice. It has been mentioned in literature that multigrid preconditioned conjugate gradient is superior to the standalone solver, and is upto 40% faster in some cases [59],[60], [61]. With due consideration to the above issue we chose to implement multigrid as a preconditioner to the FOSLS linear system both for the Stokes and the full non-linear Navier-Stokes equations. For some of the difficult problems that are encountered with the FOSLS formulations, even if the multigrid algorithm does not converge fast, and exhibits oscillatory convergence, then conjugate gradient acceleration is an easy and often very efficient way to adopt for solving the problem quickly. The reason for this often spectacular convergence of a weakly convergent, multigrid or a Jacobi preconditioned conjugate gradient is as follows. In

the case of deterioration of the multigrid convergence, or inevitably the Jacobi preconditioned CG convergence, for ill-conditioned problems, only a few eigenmodes are slow to converge. It is these very eigenmodes, that the conjugate gradient algorithm reduces and thus a conjugation of the multigrid and conjugate gradient is a very robust alternative for the solutions of difficult problems.

By using the multigrid method we can make the iterations to convergence almost independent to the problem size, and the conditioning of the system. However, there are also some issues that beset the extensive usage of multigrid, mostly related to the load balancing issues when implemented in parallel with properly parsing the coarse grid problem, on a single processor. Another issue being for very large problems the coarse grid problem solution can become computationally extensive, usage of direct solvers which provide a $O(N^3)$ performance, become prohibitive. In order to gain two order of magnitude speedup as compared to the usage of Gauss Elimination solver we implement the Jacobi preconditioned Conjugate Gradient solver as it is $O(N)$ process. Further to relieve the algorithm of coarse grid problem size limitations we implement the solution of the coarse grid problem in parallel, with a Jacobi preconditioned element by element algorithm. This idea is not new and has been used based on the implementations of Mahinthakumar [62]. This step renders the algorithm completely independent of the size of the problem, and brings all the merits of multigrid into our implementation. Thus we implement a two grid algorithm, as a preconditioner to the FOSLS formulation [40]-[63]. The usage of Gauss-Elimination as the standalone solver for the coarse grid was also explored for the Stokes operator and some of the smaller problems that were solved, and JCG/EBE-JCG was used for larger problems.

The classic Multigrid is geometric in nature (GMG) where the operator is defined on the coarser grid, and also the error components are defined in a geometric sense as well. The goal in GMG is to properly define a relaxation strategy (e.g. Ja-

cobi or Gauss-Seidel) to reduce the oscillatory errors on a given grid, and rely on the predetermined interpolation to effectively represent the remaining smooth error components on coarser levels. Another approach to multigrid methods, is algebraic multigrid, where the coarse grid operators are defined on the fly, to handle various components of the error. In our implementation to be able to use a non-locking discretization on the coarse grid, we chose to use the geometric multigrid. The two grid implementation of the multigrid algorithm (MG) is described below;

for i= 1,2,3,..... until convergence

$$\begin{aligned} h^{-} &= S(h_i, A, f, m) \\ r^{c} &= R(f - Ah^{-}) \\ e^{c} &= (A^{c})^{-1} r^{c} \\ h^{+} &= h^{-} + Pe^{c} \\ h_{i+1} &= S(h^{+}, A, f, m) \end{aligned} \tag{6.32}$$

In the above, algorithm we perform m steps of smoothing operation, restrict the residual to the coarse grid. Following this, we solve the coarse grid problem with the Jacobi preconditioned element by element conjugate gradient solver. Further the coarse grid error is then prolonged to the fine grid to obtain the current final grid solution approximation. There are a few choices for the determination of the smoothing operator, amongst them being Point Jacobi, and Gauss-Seidel. Since, the intent is to implement the whole algorithm in parallel, we are left with relatively fewer options. Gauss-Seidel has some inherent dependencies which can create issues with parallel implementations even though this smoothing is relatively superior to Jacobi smoothing. However Jacobi smoothing provides a simpler implementation and is also relatively easily parallelized. Based on these considerations we implement the

damped Point Jacobi smoothing in our algorithm. Thus for the problem, $Ax = b$, and, $A = D - L - U$, we obtain;

$$x^{n+1} = \left[(1-\omega)I + \omega D^{-1}(L+U)x^n + \omega D^{-1}b \right] \tag{6.33}$$

In the above equation, ω refers to the damping of the Jacobi smoothing operation. We perform only 1 presmoothing step and the conjugate gradient algorithm is taken as the postsmoother. For a rigorous proof of the theory behind both pre and post smoothing and also only pre-smoothing during the multigrid algorithm the reader is referred to Osamu [64].

G. Spectral/*hp* Finite Element Formulation

The spectral finite element approximation is stated as follows, the primary variables are each approximated as;

$$\Delta^e = \sum_{j=1}^{n} \Delta_j \psi_j \tag{6.34}$$

where,ψ_j are the nodal expansions, which are provided by the following one-dimensional C^0 spectral nodal basis [1];

$$\psi_i(\xi) = h_i^e(\xi) = \frac{(\xi-1)(\xi+1)L_n'(\xi)}{n(n+1)L_n(\xi_i)(\xi-\xi_i)} \tag{6.35}$$

where, Δ_j are the nodal values due to the Kronecker delta property of the spectral basis. $L_n = {P_n}^{(0,0)}$ is the Legendre polynomial of order p, and ξ_i denotes the location of the roots of $(\xi-1)(\xi+1)L_n'(\xi) = 0$ in the interval $[-1,+1]$. All Jacobi polynomials, $P_n^{\alpha,\beta}$, satisfy a three-term recurrence relation of the form:

$$xP_n^{\alpha,\beta}(x) = a_{n-1,n}^{\alpha,\beta}P_{n-1}^{\alpha,\beta}(x) + a_{n,n}^{\alpha,\beta}P_n^{\alpha,\beta}(x) + a_{n+1,n}^{\alpha,\beta}P_{n+1}^{\alpha,\beta}(x) \tag{6.36}$$

where, $a^{\alpha,\beta}$ only depends on α, β, and n. And the derivatives of Jacobi polynomials satisfy a three-term recurrence relation of the form [26];

$$(1-x^2)\frac{dP_n^{\alpha,\beta}}{dx} = c_{n-1,n}^{\alpha,\beta}P_{n-1}^{\alpha,\beta}(x) + +c_{n+1,n}^{\alpha,\beta}P_{n+1}^{\alpha,\beta}(x) \tag{6.37}$$

For the special case of $\alpha = \beta$=1;

$$xP_n(x) = a_1(n)P_{n-1}(x) + a_2P_{n+1}(x) \tag{6.38}$$

where,

$$a_1(n) = \frac{n+1}{2n+3} \tag{6.39}$$

and,

$$a_2(n) = \frac{(n+1)(n+3)}{(n+2)(2n+3)} \tag{6.40}$$

For α=β=1, $c_{n,n}^{\alpha,\beta}$=0 and the above equation can be written as;

$$(1-x^2)\frac{dP_n^{\alpha,\beta}}{dx} = c_{n-1,n}^{\alpha,\beta}P_{n-1}^{\alpha,\beta}(x) + c_{n+1,n}^{\alpha,\beta}P_{n+1}^{\alpha,\beta}(x) \tag{6.41}$$

Seeking the recurrence relation for the derivative, we rewrite the above equation by dropping α and β, for the special case of $\alpha = \beta$=1;

$$(1-x^2)\frac{dP_n}{dx} = c_1(n)P_{n-1}(x) + c_2P_{n+1}(x) \tag{6.42}$$

where,

$$c_1(n) = \frac{(n+1)(n+3)}{2n+3} \tag{6.43}$$

and,

$$c_2(n) = \frac{(2n)(n+1)(n+3)}{(2n+3)(2n+4)} \tag{6.44}$$

H. Restriction and Interpolation Maps

Let us denote the discrete elliptic boundary value problem, by

$$L_h u_h = f_h \qquad in\ \Omega_h \tag{6.45}$$

Let Ω_H be the coarse grid $(H > h) \Rightarrow L_H e\hat{m}_H = r_H^m$. Then, the transfer operators, between Ω_h and Ω_H, are considered. The restriction operator maps the residuals from the fine grid to the coarse grid, as:

$$I_h^H : G(\Omega_h) \rightarrow G(\Omega_H) \tag{6.46}$$

and, the interpolation operator is defined as;

$$I_H^h : G(\Omega_H) \rightarrow G(\Omega_h) \tag{6.47}$$

Consider the space of piecewise Legendre polynomials, of degree p on the fine elements V^h. On the coarse elements construct the space of continuous polynomials of degree $q \leq p$, V^H. Then V^H is the coarse subspace of the fine space V^h, i.e. $V^H \subset V^h$. Let ψ_i denote the nodal expansions for V^h, and ϕ_k denote the bilinear nodal basis for V^H. Then, any function in V^h can be expressed as;

$$\mathbf{u} = \sum_i u_i \psi_i \tag{6.48}$$

and similarly any function in V^H can be expressed as;

$$\mathbf{u_C} = \sum_k u_{C_k} \phi_k \tag{6.49}$$

Since, $V^H \subset V^h$, we can express the coarse grid functions ϕ_k, as linear combinations of the fine grid functions, ψ_i;

$$\phi_k = \sum_j R_{kj} \psi_j \tag{6.50}$$

Based on the above arguments, we obtain the following relationship;

$$\begin{aligned} \mathbf{u_C} &= \sum_k u_{C_k}\phi_k \\ &= \sum_k u_{C_k} \sum_j R_{kj}\phi_j \\ &= \sum_j \sum_k u_{C_k} R_{kj}\phi_j \\ &= \sum_j [R^T u_C]_j \phi_j \end{aligned} \tag{6.51}$$

Thus, for our purposes we deal with nested subspaces and the interpolation operator was determined as the transpose of the restriction operator. The theory behind the use of restriction operator being the transpose of the interpolation lies in the appropriate minimization of the errors in the appropriate matrix $\|.\|_A$ norm. Infact the usage of transpose of the restriction as the interpolation guarantees the proper reduction of the errors.

I. Coarse Grid Problem

Construction of the operator for the coarse grid problem is elucidated here. In the least squares finite element collocation solution, an approximate solution is constructed so that it satisfies the boundary conditions in advance, and nodal values of the finite element expansion are then determined so that the approximation satisfies the differential equation at a number of distinct points in the domain. In order to have a determined system we should choose a proper number of interior collocation points in each element such that the total number of equations is equal to the total number of known nodal values. This requirement can be expressed as;

$$N_{elem} + N_{Gauss} \times N_{eq} = N_{node} \times m - N_{bc} \tag{6.52}$$

In the above equation, N_{eq} is the number of equations, N_{node} is the total number of nodes, m is the number of components of u or the number of degrees of freedom at each node, N_{bc} is the total number of nodal values at boundary nodes. An alternative to the use of collocation least squares finite element operator description on the coarse mesh is to use the *Galerkin* approximation or the variational coarse grid correction. In this procedure we construct the operator, on the fly with the help of the appropriate description of the fine to coarse grid maps and also generate successively coarser grids from this information. Such a procedure is mentioned as the *Algebraic Multigrid* (AMG). In this formulation the coarse grid is constructed as;

$$A_C = R_0 A R_0^T \tag{6.53}$$

This method of construction of the coarse grid operator has been gaining acceptance and popularity in recent years since it allows the use of the multigrid algorithm as a stand alone solver, with a "black box" implementation independent of the physics of the problem. A requisite attention of the degree of dependence of the neighbouring connections in the form of independent sets have to be addressed for such an implementation. However, we choose to construct the operator based on the geometric Multigrid framework.

Mesh independent convergence rates of the two grid method has been proved for the case of post smoothing only in Weissling [55]-[65] for a 1-dimensional problem. For an elaborate exposition of the proofs for the solution of Laplace equation in two dimensions, we refer the reader to Greenbaum [66]. In both cases, the main premise is the fact that we have representations of the eigenvalues for the finite difference discretizations of the Laplace operator on a two dimensional mesh, and also we have analytical expressions for the maximum and minimum eigenvalues. Thus, if the smallest eigenmodes are being annihilated on the coarser mesh then, we are left with

a ratio of the largest to the smallest eigenvalues which is of the order $O(1)$, which can be quickly parsed with the Conjugate gradient solver with a a very few number of iterations as compared to the Jacobi preconditioned element by element implementation of the same. Based on these proofs, we carried out a two grid implementation of acceleration of conjugate gradient. As mentioned before, the coarse grid problem was implemented in a completely matrix free fashion, to alleviate the main performance bottleneck for the multigrid method.

With the solutions of the coarse grid problems two different methods were tried. We implemented Gauss-Elimination method for the solutions of the coarse grid problem. Direct methods are competitive for the solutions of small systems of linear equations and the cost of computation for the inversion of the matrix with these is of order $O(N^3)$ and the storage cost is of the order of $O(N^2)$. For the solutions of the Stokes equations for example, this method of solution was found to be appropriate and did not require the usage of an inner iteration which can substantially increase the complexity of implementation. For the solutions of larger problems the usage of Gauss-Elimination itself can become an issue and realizing the above limitation we implemented a matrix free technique for solving the problem. In this context, either Gauss-Seidel or Point Jacobi could have been chosen and we chose the Jacobi preconditioning to simplify the implementation of the algorithm, as different levels of complexities have already been introduced into the implementation with the issues mentioned.

J. Stokes Solution

We examine the problem of a driven cavity and seek the least squares solution to the problem at a very low Reynolds number. We used 6×6 spectral elements, with

a p_{level} of 4 in each element. The Newton's method of linearization was used for solving this problem. We explored the solutions of this problem both in serial and in parallel on sixteen (16) processors. The linear convergence criterion was set at a reduction in the error with respect to the initial residual to a value of 10^{-06}. Non-linear convergence was declared when the change in the solution based on the norm to be defined later reached a value of 10^{-03}. Qualitative agreement of these plots

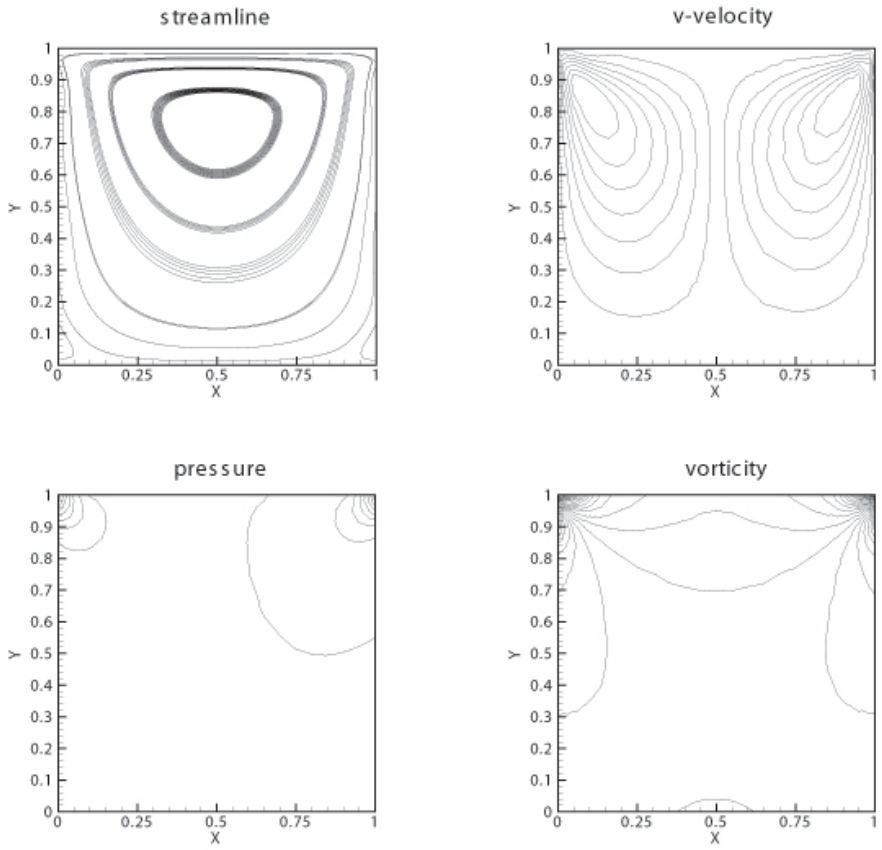

Fig. 37. Contour plots for Stokes flow

with the results presented in [42] is excellent. Also the quality of the solution can be judged from the least squares functional which remained below 10^{-06} for all elements other than very near the driven surface. Figure 37 presents the streamlines, vorticity,

and the pressure contours for the flow field generated. For the case of Stokes flow the iterations taken for convergence was found to be approximately 1/2 of that required with Jacobi preconditioning. This has also been proved by different researchers, that for the Stokes operator, Multigrid method does not perform well in the context of least squares problems. However, in the course of our analysis we show in the later sections that Multigrid performance greatly improves with increasing Reynolds numbers which is a welcome change and of some consequence because for most real flows we usually intend to exercise the full non-linear Navier-Stokes equations. For the Stokes operator a comparison between the number of iterations taken by Jacobi preconditioned conjugate gradient (JCG) vs. the multigrid accelerated Conjugate gradient algorithm is shown in Figure 38. Gauss-Elimination was used for the solution

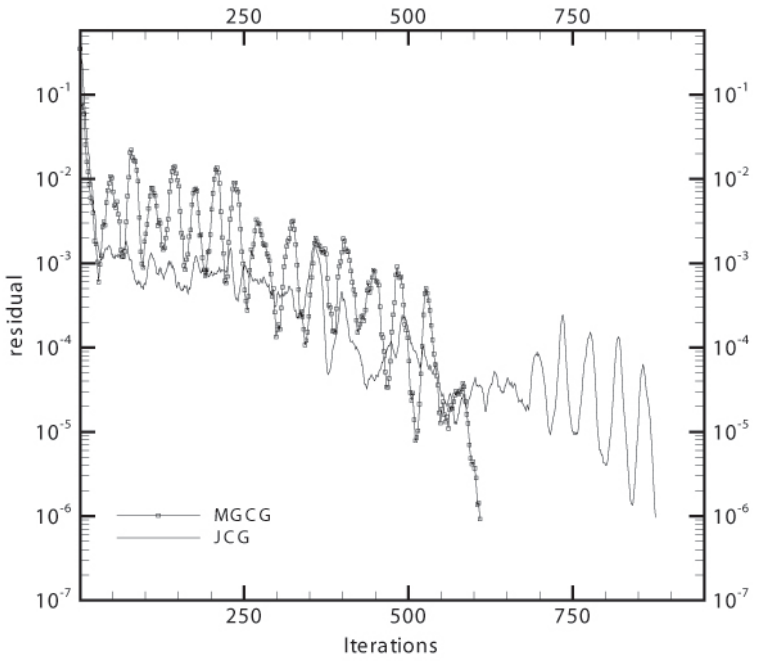

Fig. 38. MG vs. JCG iterations for Stokes flow

of the coarse grid problem in this case as there was no need felt to complement the

solution with a EBE implementation of the coarse grid solve for this problem.

K. Non-Linear Navier-Stokes Solutions

The agreement for the results for $Re = 100$, and 400 have not been presented in the interest of brevity. However, Figure 39 presents a comparison between the iterations taken by Jacobi preconditioned conjugate gradient and the Multigrid algorithm for these Reynolds numbers. As can be seen from the figure, Multigrid algorithm converges with around 1/5 to even 1/20 the number of iterations. This offers remarkable savings on time when one wishes to solve the Navier-Stokes equations for higher Reynolds numbers. In light of the fact that the coarse grid problem was increasing in size, we examined the use of Gauss Elimination for $Re = 100$, and the Jacobi Preconditioned Conjugate gradient for $Re = 400$. This allows for considerable savings since $Re = 400$ case 20×20, grid was used, and the reduction in the operation count from an $O(N^3)$, to $O(N)$, reduces the computational time substantially. In this section we exercise the Multigrid method for the solutions of high Reynolds numbers flows for the driven cavity problem. In specific we intend to bring out the advantages that accrue with the multigrid algorithm as compared to JCG algorithms for high Re flows. Figure 40 presents the streamline and contour plots of the velocities, pressure, and vorticity for a Reynolds number of 1000 obtained with the Multigrid method. As can be seen from the figure, the presence of two vortices are clearly visible at either ends of the cavity for this Reynolds number. Figure 41 presents the agreement of the present results with published results of Ghia et al. [52] for the u-velocity at the mid-plane of the driven cavity problem, where as Figure 42 presents the v-velocity at the midplane of the cavity. The agreement for both cases is good, and the results thus are validated for effective implementations of the Multigrid method. Picard method

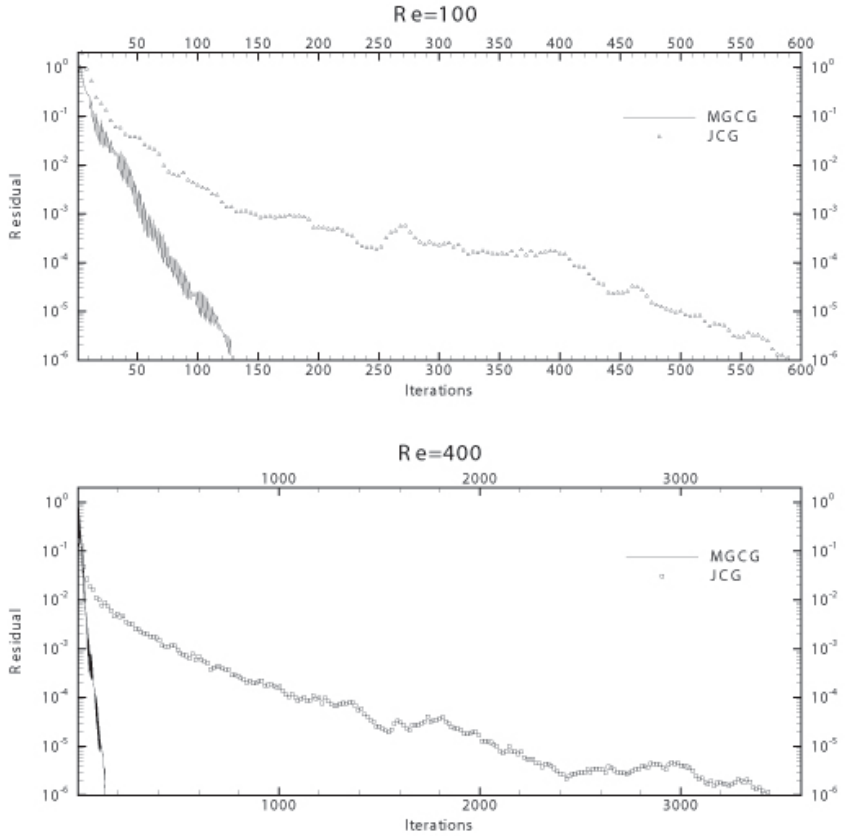

Fig. 39. JCG and Multigrid algorithm iterations

was used for linearizing the non-linear problem. The problem was also solved on a single processor, with JCG and the reduction in the number of iterations varied from multigrid being, 17 to 36 times faster. Also, a real comparison cannot even be done for this case, because the multigrid algorithm only took 7 non-linear iterations to converge, where as the JCG took 11 iterations to convergence, only further showing the spectacular convergence of the present formulation. The value of the least squares functional was found to be lesser than 10^{-08}, and in fact was lower than 10^{-10} for the majority of the elements away from the driven surface. A convergence history comparison for the Multigrid method is presented in Figure 43 as compared to the

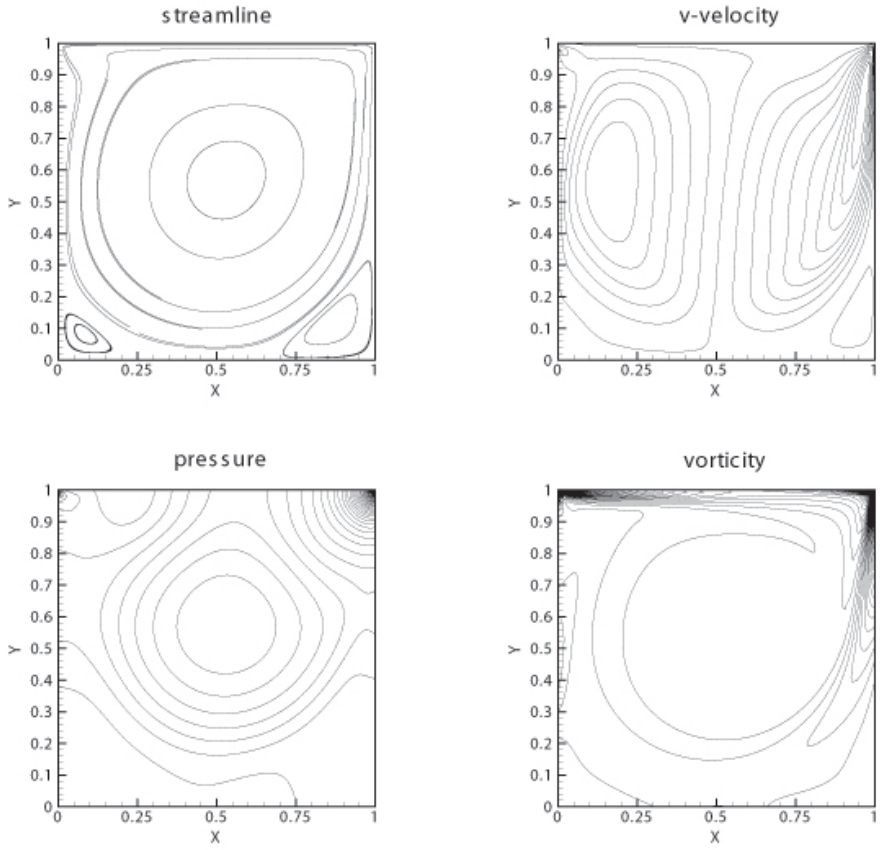

Fig. 40. Contour plots for Re=1000

Jacobi preconditioned EBE algorithm. The effectiveness of the multigrid over the EBE-JCG is evident in the steep march towards the solution as compared to Jacobi preconditioning. Figure 43 also presents the convergence history for the EBE-JCG method for the coarse grid problem. The average number of iterations for the coarse grid solution were found to be of the order of 53 to 230 iterations. To verify the effect of inaccurate coarse grid solve, and maximize the performance of the Least squares multigrid algorithm–in terms of the decrease in the outer iterations vs. the increase in the inner iterations needed for a stricter convergence criterion we relaxed the convergence of the inner iterations to a value of 10^{-03}. It was realized however

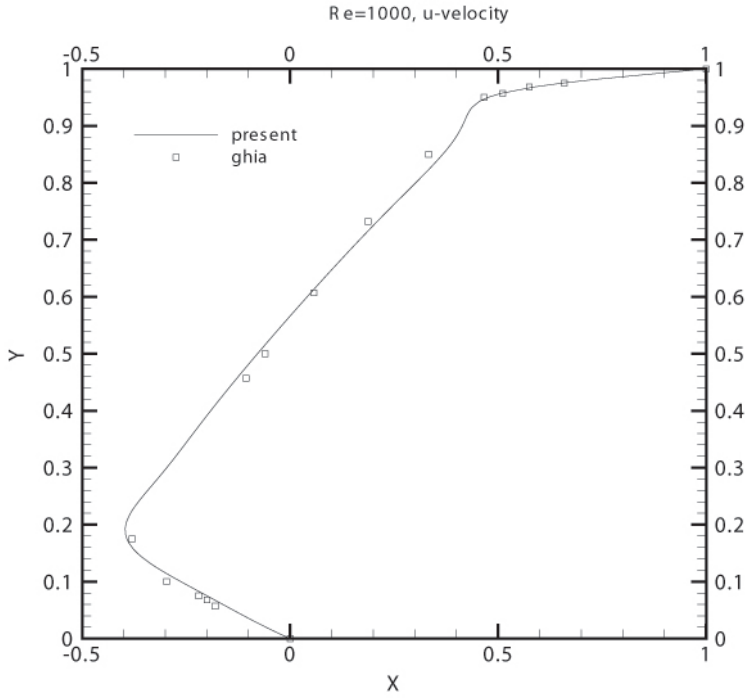

Fig. 41. u-velocity comparison with Ghia results for Re=1000

that the number of outer iterations increased for this "very" inaccurate solve. Based, on this result we use a uniform value of the tolerance to 10^{-04}. This value is also in agreement with multigrid applications to Galerkin finite element formulations also with consequent EBE-JCG implementations as proposed by Mathinthakumar [62]. The relationship between the different tolerances for the coarse grid solve has been presented in Figure 44. Figure 45 presents the contour plots for a Reynolds number of 3200. The non-linear convergence criterion was identified as a reduction in the norm of the initial residual to 10^{-03}. The problem was solved in parallel utilizing 16 processors. It took eight iterations for reaching the non-linear convergence with the Picard method of linearization.

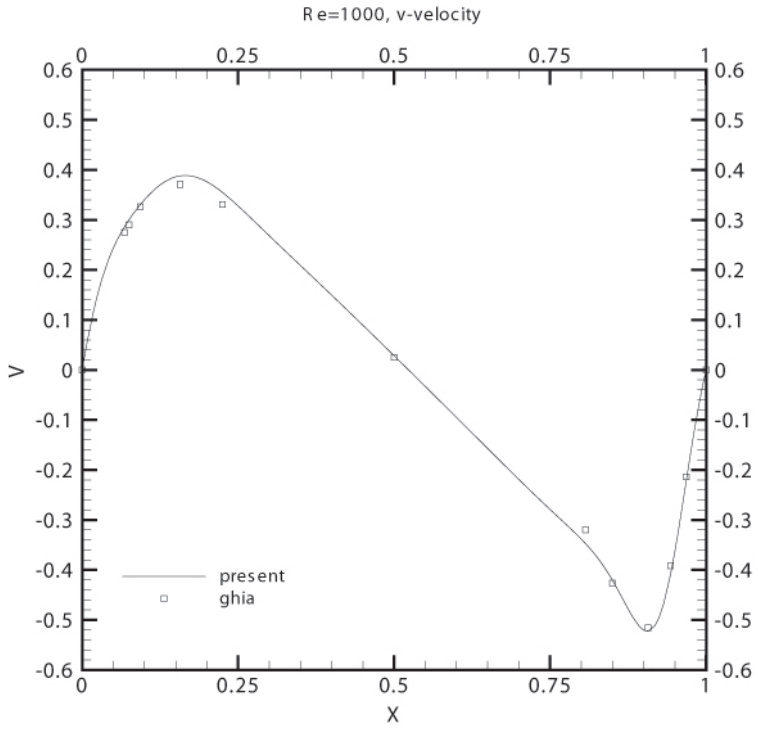

Fig. 42. v-velocity comparison with Ghia results for Re=1000

L. Parallel Performance Measures

The computations were performed using the supercomputing resources provided by the Texas A& M University supercomputing center. The specific compiler used was the IBM compiler for AIX, V10.1. The simulations were performed using the IBM Cluster 1600 (hydra.tamu.edu), which has 832 cores.

An important measure of the parallel performance is speedup. For a fixed size of the problem, the speedup is defined as;

$$S_p = \frac{T_1}{T_p} \tag{6.54}$$

where, T_1 is the elapsed time on one processor, and T_p is the elapsed time for the same problem on P processors. The efficiency is defined as the speedup ratio over

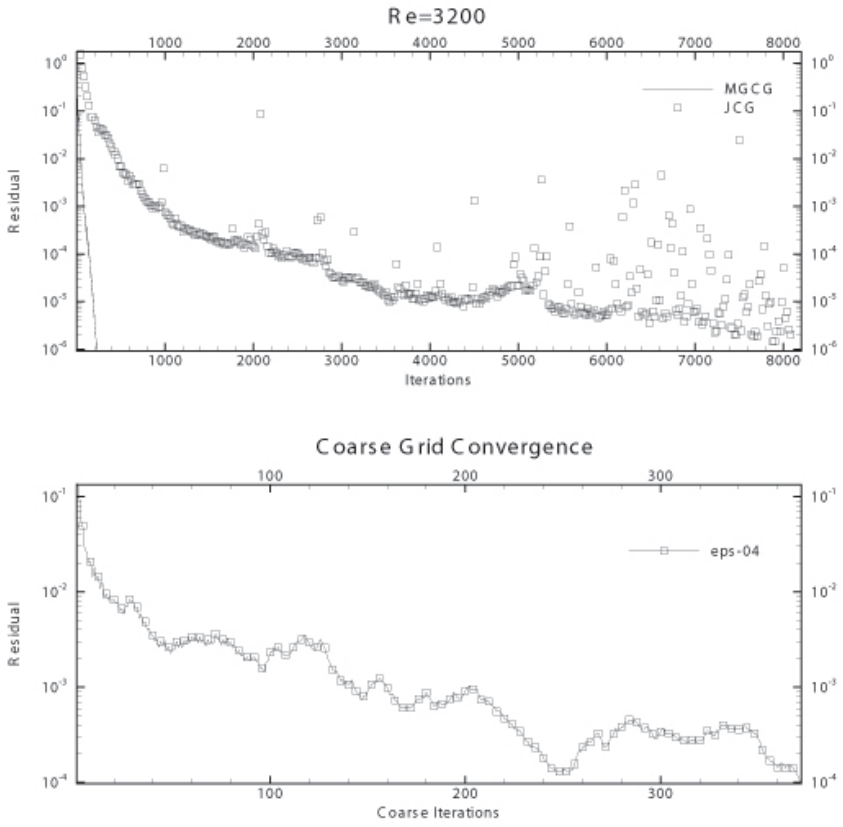

Fig. 43. Convergence of Mutigrid and coarse grid solves

the number of processors used (*nprocs*).

$$\epsilon_p = \frac{S_p}{n} \tag{6.55}$$

For effecting the solutions of the problem in parallel, elements with independent degrees of freedom were sent to different processors. The processors operate on their independent sets of elements, and thus performance enhancements for the algorithm implementations are achieved at the rate which is at least equal of the number of processors *nprocs* that are operating on the problem concurrently. The distribution of the elements to different processors can be effected with the help of a multi-colouring

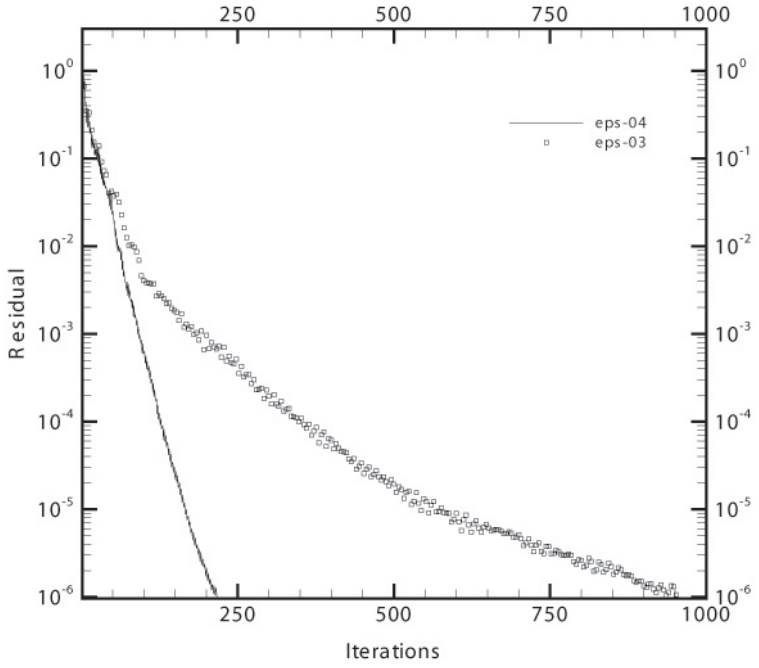

Fig. 44. Inaccurate solve increase in iterations

scheme, which assigns a color to elements which are associated with each part of the domain [67].

There is some time lag associated with communication overheads while transferring information between processors, however it did not seem to deteriorate the overall performance of the multigrid algorithm appreciably as evidenced with the performance of the algorithm in parallel for the different sets of processors that were tested. Table XXIII presents the speedup obtained with the Multigrid algorithm for the driven cavity for different sets of Reynolds numbers tested.

The linear convergence tolerance for all cases was set at a reduction of the final residual with respect to the initial residual at a value of 10^{-06}. Non-linear convergence was declared when the non-linear residual defined by the following formula reduced

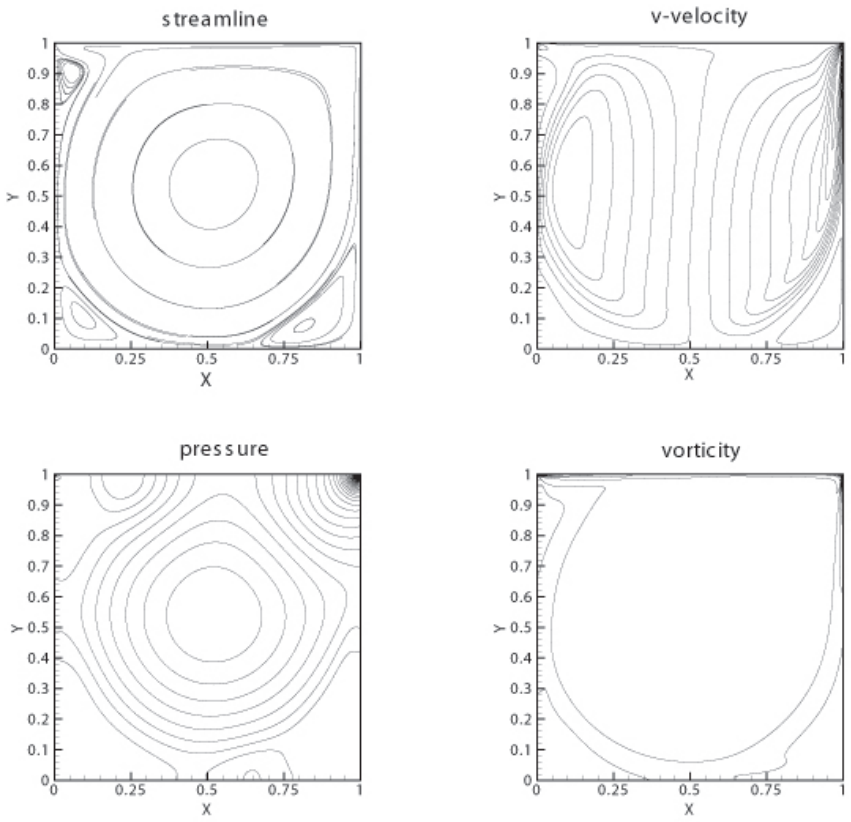

Fig. 45. Contour plots for Re=3200

to a value of 10^{-03}.

$$\epsilon = \frac{\| \mathbf{U^{i+1}} - \mathbf{U^{i}} \|_0^2}{\| \mathbf{U^{i}} \|_0^2} < 10^{-03} \tag{6.56}$$

We report the speedup ratio for the Multigrid algorithm, in Figure 46. Efficiency of the Multigrid algorithm implemented in parallel, was found to be greater than 1, which is the ideal case efficiency, as mentioned earlier, because of effective cache memory utilization. The speedups are being reported in Figure 46 against the ideal speedups expected with an increase in the number of processors. The lowest speedup between the different non-linear iterations are being reported as a conservative estimate. For a lower number of proceessors, there is an initial phase where the multigrid

algorithm does not perform as well for some non-linear steps, however it improves drastically for larger problems. The increase in the number of iterations as a function of the increasing degrees of freedom have also been presented. The performance of the multigrid for higher degrees of freedom, is also acceptable in particular because it is able to solve the linear system at $O(N/75)$ for the worst case tested where N is the total degrees of freedom in the problem. The reason for superlinear speedup

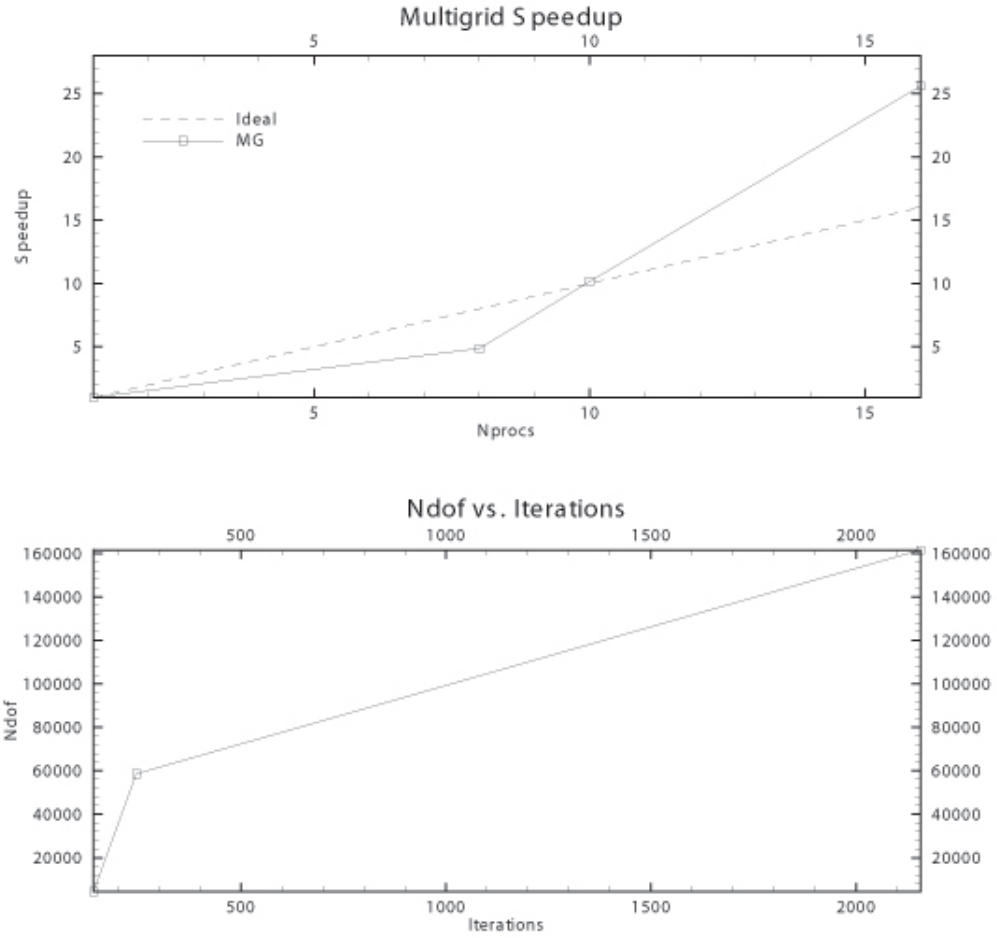

Fig. 46. BJCG vs. Multigrid speedups

for the problems under consideration is the fact that the problems were solved with a very effective implementation, in view. The main performance bottleneck with the parallelization of the multigrid algorithm, and the reason for load balancing issues in a parallel implementation as encountered often with the method, was removed with the solution of the coarse grid problem with a Jacobi preconditioned element by element solution in parallel. Smaller problems where Gauss Elimination was found to be appropriate, were solved with the direct solver. For different number of processors the speedup was found to be greater than ideal to suboptimal in the worst case, which is very encouraging for the effective implementations of the above algorithm for the solution of huge linear systems that arise in computational fluid dynamics areas, and in specific that are associated with the p-version of the least squares formulations which have been plagued with high quadrature costs so far. Here we demonstrated, not only the vastly superior performance of the multigrid algorithm but also detail the implementation aspects of the same in parallel.

M. Backward Facing Step LSFEM Solutions

Next, we consider two-dimensional steady flow over a backward-facing step at $Re = 800$ for solution with Multigrid Least Squares finite element method. The geometry and boundary conditions, taken from the benchmark solution of Gartling [68], are shown in Fig 47. The two dimensional domain in $\Re^2$ of dimensions $[0, 30] \times [0, 1]$ units was discretized into 280 hp/spectral mesh with a seventh order expansion in each element. The mesh was fine in the vicinity of the inlet of the backward facing step and was coarse near the exit of the step. No-slip boundary condition is imposed on all walls. Boundary condition of $u(y) = 0$ is imposed for $y \in [0, 1]$ along the left face of the backward facing step. A parabolic velocity profile given by $u_x(y) = 12(y-1)(1-2y)$

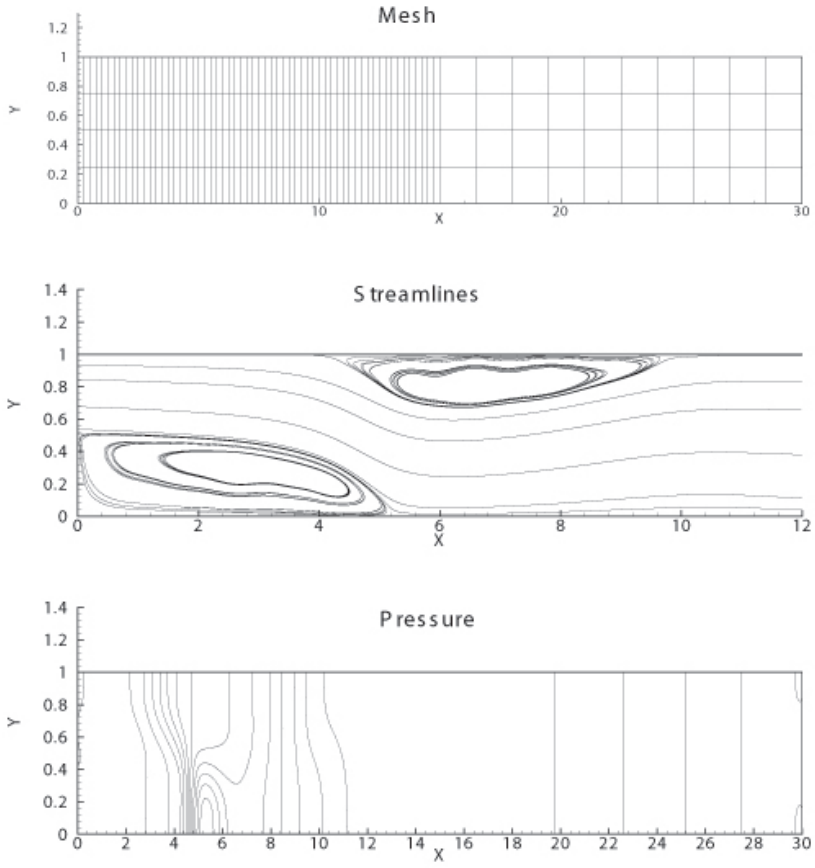

Fig. 47. Backward facing step

is specified at the inlet for $y \in [0.5, 1]$. This produces a maximum inflow velocity of $u_{max} = 1.5$ and a mean inflow velocity of $u_{avg} = 1.0$. The Reynolds number is based on the mean inflow velocity and the characteristic height of the entrance region.

At the outflow, the desired boundary condition (as with some Galerkin finite element implementations) are as follows; $-p + \frac{1}{Re}\frac{\partial u}{\partial x} = 0$ and, $\frac{1}{Re}\frac{\partial v}{\partial x} = 0$. Both of the above requirements have been specified as the boundary conditions for open ended domains, for solving CFD problems in a Galerkin finite element setting. The above boundary conditions were enforced in a least squared sense into the functional for the LSFEM minimization statement. The finer mesh and coarse mesh operators both

have this specification in a LSFEM sense along the outflow boundaries. Thus the modified functional for the new minimization statement for the boundary elements are specified as follows;

$$J(\mathbf{u},p,\omega;\mathbf{f}) = \frac{1}{2}\Big(\parallel (\mathbf{u}\cdot\nabla)\,\mathbf{u} + \nabla p + \frac{1}{Re}\nabla\times\omega - \mathbf{f}\parallel_0^2 + \parallel \omega - \nabla\times\mathbf{u}\parallel_0^2 + \\ \parallel \nabla\cdot\mathbf{u}\parallel_0^2 + \parallel -p + \frac{1}{Re}\frac{\partial u}{\partial x}\parallel_{0,\Gamma_{outflow}}^2 + \parallel \frac{1}{Re}\frac{\partial v}{\partial x}\parallel_{0,\Gamma_{outflow}}^2 \Big) \quad (6.57)$$

There were a total of 56956 degrees of freedom in the problem. The results obtained from the development of the pressure fields and the recirculation zones match qualitatively very well with the published results of Reddy [11] who used the Penalty finite element method to obtain the results. The location of primary reattachment length was found at $x = 5.3$, secondary separation started at $x = 4.2$, and secondary reattachment point was found at approximately, $x = 9.9$. After reattachment of the upper wall eddy, the flow slowly recovers towards a fully developed Poiseuille flow. Flow is almost fully developed at the exit ($x = 30$) with no pressure gradient in the direction of flow. The value of the L_2 least-squares functional remained below 10^{-07} for the elements near the entrance region of the backward facing step and below, 10^{-11} for the majority of the elements. The L_2-norm of the residual of the continuity equation was found to be below 10^{-07} for most elements. The quality of the solution can also be judged based on the low values of the residuals as reported above and in specific the residuals of the continuity equation reflect on the excellent mass conservation properties of the spectral element method for this Least Squares problem.

The u-velocity profiles along the channel height at $x = 7$ and $x = 15$ are compared with the benchmark results of Gartling [68] in Fig 48. We find excellent agreement for both sections along the length of the Backward Facing step. Pressure profiles along the length of the channel are plotted in Fig. 49 for both the top and bottom walls

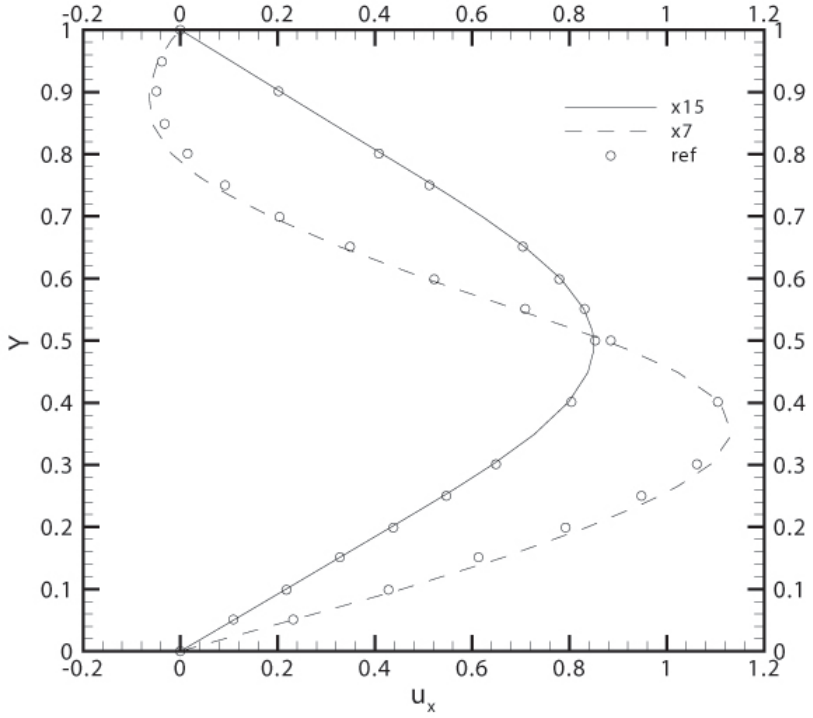

Fig. 48. u-velocity along length of step

of the Backward Facing Step and compared with the published results of Pontaza and Reddy [69]. The number of elements inside the backward facing step was kept at 280 elements as shown in Fig 47. The coarse grid convergence history for the corresponding coarse mesh is presented in Figure 50. A representative convergence history has been presented. As can be seen from the figure approximate number of iterations for the solution of the coarse grid problem varied from anywhere between 150 to 200 iterations for reaching the linear convergence tolerance of the coarse grid problem set at 10^{-04}.

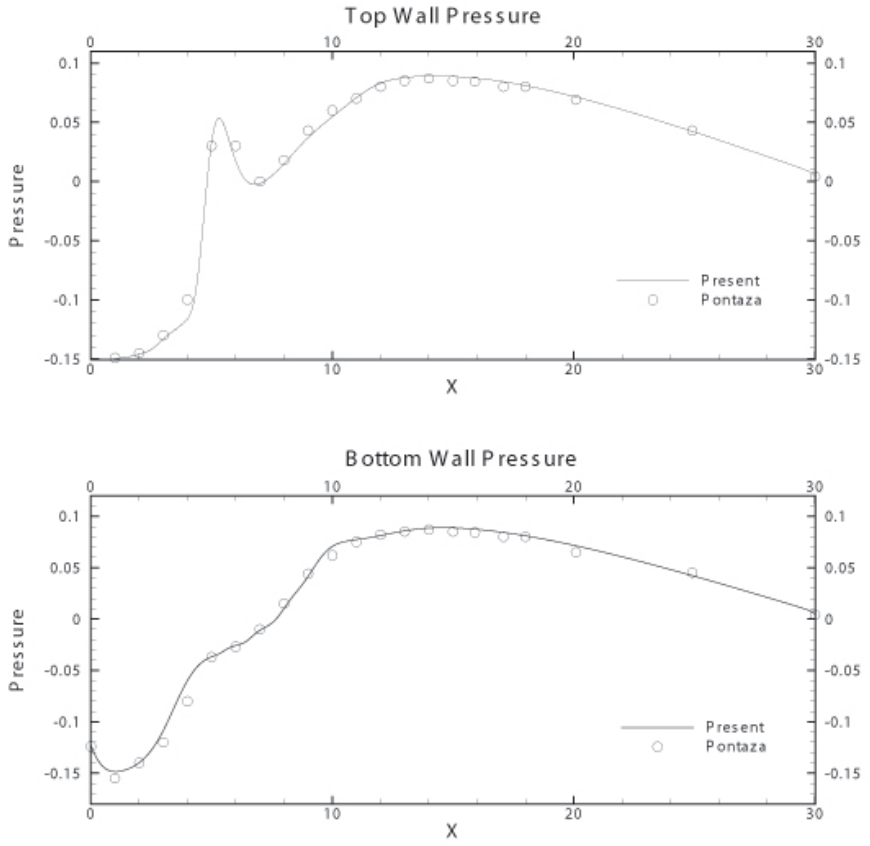

Fig. 49. Pressure along top/bottom of backward facing step

N. Conclusion

In this chapter we presented the parallel implementations of the multigrid algorithm for solving the Least squares finite element formulations applied to fluid flow. We explored problems subject to both Dirichlet and open type boundary conditions. Scalability of the implementations were described and their effective implementations demonstrated for solving self-adjoint operators. We demonstrated superlinear to linear speedup for the Multigrid algorithm which paves the way for effective usage of the above methods for solving *hp*-version of Least Squares problems.

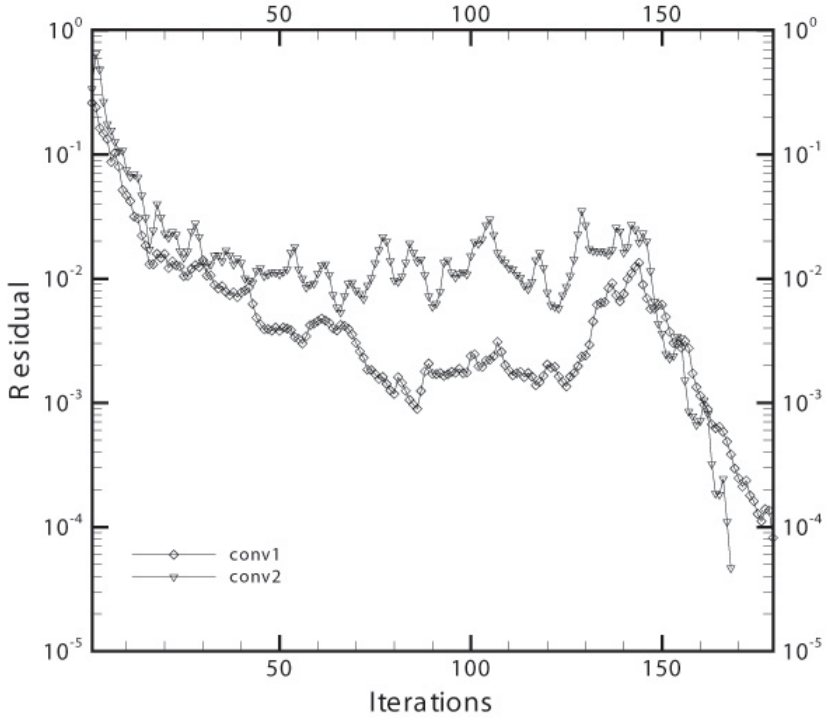

Fig. 50. Backward facing step coarse grid iterations

Table XXIII. Multigrid speedups for different Reynolds numbers

Iteration	Re	No. of	Ndof	Speedup		Iterations	
No.		*Elements*		*ideal*	*present*	*Multigrid*	*JCG*
1	0.01	36	2500	8	4.8	392	656
2	0.01	36	2500	8	6.8	609	876
3	0.01	36	2500	8	7.33	656	911
4	400	400	26244	10	14.04	56	138
5	400	400	26244	10	10.17	141	3443
6	400	400	26244	10	10.79	244	4133
7	400	400	26244	10	15.38	218	1639
8	400	400	26244	10	12.96	157	2516
9	400	400	26244	10	-	-	2889
10	400	400	26244	10	-	-	3907
11	1600	1000	58564	16	28.76	82	172
12	1600	1000	58564	16	29.15	245	3737
13	1600	1000	58564	16	29.11	211	6076
14	1600	1000	58564	16	25.58	207	8094
15	1600	1000	58564	16	29.09	222	5133
16	1600	1000	58564	16	26.04	234	8166
17	1600	1000	58564	16	26.04	195	5142
18	1600	1000	58564	16	-	-	7929
19	1600	1000	58564	16	-	-	5347
20	1600	1000	58564	16	-	-	7602
21	1600	1000	58564	16	-	-	5163

CHAPTER VII

MODELLING THE POROUS MEDIA FLOW PROBLEM

A. Introduction

In this chapter we digress a little bit from the main topic of the usage of *hp*-spectral element methods applied to solving different problems and concentrate on the usage of Lagrange based FEM methods to solving the porous media problem. The bi-quadratic basis is used with the help of Penalty finite element method to solve the porous flow problem in two dimensions. We solve the porous media flow problem for the case of different permeabilities and in the context of the Generalized Navier-Stokes equations.

The fluid flow inside a porous matrix has been modelled with the help of generalized Navier-Stokes equations inside a porous domain. A finite element formulation of the transient porous flow problem is presented and resulting finite element equations are solved on a simple geometry to understand the behaviour of such a flow in porous materials. Estimates to the variation of the average Nusslet number, which is an index for the evolving heat transfer, is presented for a specific porosity and permeabilities of the matrix and it is compared with the pure fluid case to see the difference in the heat transfer due to the presence of the porous matrix.

B. Background

The flow of moisture inside a porous material during the course of a drying operation or addition of moisture during adsorption is a very important and interesting problem with applications in food drying operations etc. Flows of fluids (different components of the moisture transfer in liquid and vapor forms) inside the a porous medium are

governed by the conservation laws of mass, momentum, and energy[1]. Different physical phenomenon occur simultaneously when a porous sample such as a food material exposed to convective heating is being dried. There is a transfer of fluid inside the porous material along with a concurrent transfer of vapour inside the porous material making the actual problem a multi-phase transport problem.

Depending on the different phases of transfer inside the porous medium, the problem becomes highly complicated because of the multi-physics involved. In this study the transfer of vapour inside the porous material has been neglected and only a single component of transfer of the fluid is considered to simplify the problem and to serve as a first approximation to a more elaborate analysis. Also, the transfer of the fluid has been assumed to be occurring at 100% saturation.

A number of researchers have solved the heat and mass transfer coupled equations for modelling the coupled heat and moisture transfer inside a porous flow medium with different approximations [70]. The approach primarily has been to obtain the moisture distribution with diffusive transfer with slight variations in the governing equations amongst different efforts. Different moisture diffusivity values have been considered when solving for the moisture loss equations from the porous material, and also different drying scenarios have been explored [71]. A concomitant problem to the determination of the moisture loss by diffusive effects is the consideration of the complete flow field inside the porous medium, which incorporates the effect of the convective components simultaneously with diffusive transport. To the best of the author's knowledge there has not been any work in the determination of the actual flow regime with the solution of the fundamental conservation laws of mass, and momentum equations in a porous medium with applications in food engineering areas with the generalized Navier stokes equations.

The model when considering the conservation of mass, and momentum in two di-

mensions for a porous medium manifests in the form of either Brinkman-Forchheimer equations or in the form of Generalized Navier-Stokes equations for porous media [72]. In this study, coupled equations relating the conservation of mass, and the conservation of linear momentum and coupled heat transfer as applicable to a porous medium are presented and solved in the context of Generalized Navier-Stokes equations in two dimensions as a transient. The solution procedure employed is the finite element reduced integration penalty (RIP) formulation to solve the coupled equation set for the convective heat transfer problem. This study also compares the change in the heat transfer coefficient along the vertical wall due to the presence of the porous medium as opposed to the absence of the porous matrix (for the clear fluid case).

C. Porous Flow Equations

The porous medium is assumed to be isotropic and homogeneous and the fluid and the solid are assumed to be in isothermal equilibrium. It is also assumed that the flow equations are valid over the domain of interest, and the domain is treated as two-dimensional, isothermal and isotropic, porous medium. Conservation of mass inside the domain takes the form (in the absence of mass generation terms);

$$\nabla \cdot \mathbf{u} = 0 \tag{7.1}$$

Conservation of linear momentum equations in two dimensions is expressed as;

$$\rho \frac{\partial \mathbf{u}}{\partial t} + \frac{\rho}{\epsilon} (\mathbf{u} \cdot \nabla) \mathbf{u} = -\nabla (\varepsilon p) + \mu_e \nabla^2 \mathbf{u} + \mathbf{F} \tag{7.2}$$

Here, $\mathbf{u}$ is the velocity vector for the fluid inside the porous matrix, ϵ is the porosity of the medium, $||\mathbf{u}||$is the magnitude of the velocity vector, is the dynamic viscosity of the fluid, ρ is the density of the fluid saturating the porous matrix, and $\mathbf{F}$ is the

body force vector for the flow problem, which can be expressed as

$$\mathbf{F} = -\frac{\varepsilon\mu}{K}\mathbf{u} - \frac{\rho\varepsilon F_{\varepsilon}|\mathbf{u}|}{\sqrt{K}}\mathbf{u} + \rho\varepsilon\mathbf{G} \tag{7.3}$$

where,

$$F_{\varepsilon} = \frac{1.75}{\sqrt{150\varepsilon^3}} \tag{7.4}$$

K is the permeability of the porous medium (m^2), and G is the gravitational acceleration vector. Equations 7.1-7.4 are referred to as the Generalized Navier-Stokes equation for porous flow. The behaviour of the above set of equations closely follows the Navier Stokes equations for the fluid flow problem. Specification of the porosity of the medium to 0.999 and a high permeability of the porous medium reduces the Generalized Navier-Stokes to the pure fluid case which can be used for validation purposes for the code. Recent advances have been made where the solution procedure employed in certain cases for solving the porous flow problem has been with Lattice-Boltzmann's method among other solution methodologies [73]-[74].

The forcing function F has contributions from the velocity vector (making the forcing vector non-linear in nature), and also from the acceleration due to gravity for the specific direction in which the forcing function works [75]. There is a correlation for the permeability of the medium which is related to the solid particle diameter [76], which is not used because the permeability of the porous matrix was entered directly as an input to the model.

The mathematical description of the flow problem formulation is complete after the specification of the boundary conditions and initial conditions for the above set of equations (because of the transients in the partial differential equations). The porous flow problem admits the same boundary conditions as that specified for the Navier-Stokes equations [77]. Therefore, there are primarily two different types of

admissible boundary conditions for the Generalized-Navier Stokes equations, the first is the specification of Dirichlet boundary condition and the second is the specification of Neumann boundary condition. Dirichlet or essential boundary conditions, require the specification of the velocity components u_i, on the boundaries of the domain. Neumann or natural boundary conditions, involve the specification of traction on the boundaries. In the actual problem that has been solved only the first type or the Dirichlet boundary condition had to be specified on the boundaries.

The problem domain was taken as a square enclosure which was meshed subsequently with bi-quadratic finite elements in two dimensions. The domain dimensions were taken to be a square with dimensions of 1m×1m. Buoyancy driven flow with differentially heated walls were used with the left side wall at a higher temperature as compared to the right side wall. The finite element reduced integration penalty formulation with the Galerkin approximation was used in the analysis for the discretization of the equations in two dimensions. Initial conditions were assumed to be a state of quiescence in the fluid and at time $t = 0$ it was assumed that the top of the domain containing the porous material obtains a specified velocity in the positive x-direction.

D. Penalty Finite Element Formulation

Penalty finite element method is a method of discretizing the finite element equations for the generalized Navier-Stokes equations set where the continuity equation is interpreted as a constraint on the momentum equations and the coupled set is solved together with the help of a Lagrange multiplier that serves as the penalty parameter [49]-[78]. Galerkin finite element method entails reducing the differentiability of the equations after multiplication of the same with a weighting function and trad-

ing of the differentiability between the partial differential equation and the weighting function [49]. For the porous flow equations it is sufficient to use a Lagrange family of interpolation functions as the basis functions in the framework of Galerkin finite element method [49]. Only the first derivative of the weighting function (basis function) needs to be continuous between elements, and cubic Hermite interpolation functions are not needed for flow problems. The incompressibility requirement in the penalty method formulation is interpreted as a constraint to the momentum equations and the solution of the constrained problem is sought with the Lagrange multiplier being the penalty parameter. With the above considerations in mind, the finite element equation weight functions are required to apply Green's theorem on the momentum equations only and have been presented for the RIP method [49];

Momentum Equation(s):

$$\begin{aligned}\left[\int_{\Omega_e} \rho\psi\psi^T dx_1 dx_2\right] \overset{*}{u}_i + \left[\int_{\Omega_e} \frac{\rho}{\phi}\psi\left(\psi^T u_j \frac{\partial\psi^T}{\partial x_j} dx_i dx_2\right)\right] u_i \\ + \left[\int_{\Omega_e} \mu_e \frac{\partial\psi}{\partial x_j}\frac{\partial\psi^T}{\partial x_j} dx_1 dx_2\right] u_i + \left[\int_{\Omega_e} \mu_e \frac{\partial\psi}{\partial x_j}\frac{\partial\psi^T}{\partial x_i} dx_1 dx_2\right] u_j \\ + \left[\int_{\Omega_e} \gamma_e \frac{\partial\psi}{\partial x_j}\frac{\partial\psi^T}{\partial x_j} dx_1 dx_2\right] u_i = \left[\int_{\Omega_e} F\psi dx_1 dx_2\right]\end{aligned} \tag{7.5}$$

Here, the forcing function contains contributions from the unknown velocity components as given by Equation 7.3 and the integrations evaluated over the area of the domain (for a two-dimensional problem) have been presented below;

$$\oint_{\Omega_e} \mathrm{F}\psi dx_1 dx_2 = -\int_{\Omega_e} \left[\frac{\varepsilon\mu}{K}\mathrm{u} + \rho\frac{\varepsilon F_\varepsilon}{\sqrt{K}}\|\mathrm{u}\|\,\mathrm{u} - \rho\varepsilon\mathrm{G}\right]\psi dx_1 dx_2 \tag{7.6}$$

In the above equation the penalty terms have been denoted with the γ term, where γ is the penalty parameter. It should be noted that the penalty parameter terms are evaluated with a reduced integration rule than that used for the velocity com-

ponents. Specifically, the order of the Gauss integrations that are involved with the penalty terms should be at least one order less than that is needed for the exact integration of the terms [49]. The velocity approximations are bi-quadratic, and for a quadratic domain there are nine interpolation functions for each velocity component. Bi-quadratic interpolation functions for the velocity components are an admissible combination of interpolation functions for generating stable and convergent solutions for the flow problem and these are often mentioned as $Q9$ interpolation functions. This combination of the $Q9$ interpolation function has been known to satisfy the inf-sup criterion for the solution of the flow problems, and yield stable and convergent solutions. Other elements that are not LBB stable may yield acceptable solutions for some problems but are not reliable for general applications.

Penalty finite element model for the porous flow equations involve the solution of two penalized momentum equations in two dimensions. The momentum equations provide for the two components of the velocity vectors of flow in the porous medium. The porous flow problem involves the determination of different matrices, with the help of an appropriate Gauss-Quadrature scheme for the numerical evaluation of the integral. The element matrices for the porous flow problems were evaluated with a 4 Gauss Quadrature for the velocity matrices that were found to integrate the matrices exactly, and the 2×2 Gauss Quadrature was used for the penalty matrices. It has been noted that determination of the penalty terms has to be done with the help of an order of Gauss Quadrature of one order less than the quadrature points needed to integrate the matrices exactly. This is necessary because Gauss-Quadrature when employed to integrate the penalty terms exactly system of equations becomes unsolvable due to locking. The penalty parameter was taken as 10^{+8} for the simulations. It is recommended to use a sufficiently large value of the penalty parameter to reach convergence in the velocity vector solutions, often the value is chosen as a trade

off between the prediction accuracy of the velocity components against obtaining the trivial solution of the equations ($u = v = 0$).

The boundary integrals were evaluated with a 4-point Gauss Quadrature with a quadratic interpolation along the sides of the domain. The boundary condition for the flow problem required the specification of the velocity components on the right, left, bottom, and, top faces of the domain. The left, right, and the bottom faces of the domain were required to have both the velocity components specified to zero. This was accomplished with zeroing out all the terms in the final assembled global finite element matrix of the problem, except the diagonal terms which were set to unity for these specific nodes, and the global b vector for the same nodes were all set to zero (notation referring to solving for the linear system $Ax = b$). The top nodes required the specification of the diagonal terms to unity, zeroing out all the other coefficients of the respective equations and the specification of the b vector elements to the lid velocity for the specific nodes. The singular points on the top corners of the domain were specified to have zero velocity of the fluid. Initial conditions were specified at the time plane $t = 0$, to have zero velocity vectors, a state of quiescence in the fluid.

E. Coupled Convective Heat Transfer

Convective heat transfer involves solving both the momentum and the heat transfer equation with convective transport in a coupled fashion to determine the velocity and the temperature profiles inside the domain of solution. The coupling between the temperature and the velocity profiles make it a difficult problem to solve and the two penalized momentum equations and the heat transfer equation have to be solved in a segregated form. Thus two separate non-linear convergence criterion have to be specified for the non-linear convergence of the temperature and the velocity

predictions. Also separate linear matrix convergence criterion were also set for the solution of the equations which were being solved in a segregated form.

The temperature partial differential equation for the generalized Navier-stokes equations come into the formulation as follows;

$$\rho_e c_e \frac{\partial T}{\partial t} + \rho_f c_f \left(\mathrm{u} \cdot \nabla\right) T = \left[\nabla \left(k_e \nabla T\right)\right] \tag{7.7}$$

The forcing function for the buoyancy driven convection is expressed as (repeated for clarity):

$$\mathrm{F} = -\frac{\varepsilon \mu}{K}\mathrm{u} - \rho \frac{\varepsilon F_\varepsilon}{\sqrt{K}} \left\|\mathrm{u}\right\| \mathrm{u} + \rho \varepsilon \mathrm{G} \tag{7.8}$$

where, the component of the forcing function G is defined as:

$$\mathrm{G} = -\mathrm{g}\beta(T - T_0) \tag{7.9}$$

Here, $\mathbf{g} = \mathbf{ge_2}$is the acceleration due to gravity, β is the thermal expansion coefficient, and T_0 is the average reference temperature of the system. It should be noted that for the buoyancy driven convection example studied the term has been assimilated with the pressure term and does not appear explicitly in the formulation thus. The above equations along with the appropriate boundary and initial conditions define the problem at hand. Conditions of insulated boundary at the sides of the enclosure were simulated with the specification of a large value for the convective heat transfer coefficient of 10^6.

Certain non-dimensional numbers had to be defined to characterize the flow in two dimensions for the problem, namely the Darcy number (Da), Prandl number (Pr), and the Rayleigh number (Ra) which are defined below;

$$\mathrm{Da} = \left(\frac{K}{L^2}\right) \tag{7.10}$$

$$\mathrm{Pr} = \left(\frac{\mu \rho_e c_e}{k_e \rho_f} \right) \tag{7.11}$$

$$\mathrm{Ra} = \left(\frac{g \beta \Delta T^3 \rho_e c_e}{k_e \upsilon} \right) \tag{7.12}$$

Here, k_e is the effective conductivity of the porous medium, $\rho_e c_e$ is the effective specific heat of the porous medium, ΔT is the temperature difference between the two walls of the cavity, and ν is the kinematic viscosity of the fluid. The above equations define certain non-dimensional characteristics of the flow field for the buoyancy driven convection problem and would be used in the following discussion.

The temperature equation was also discretized with bi-quadratic elements at the element level. For low Ra numbers in the generalized Navier-Stokes equation there is almost no derivation from the conduction solution and the temperature profiles along the domain show a linear drop from the higher end wall temperature to the lower end wall temperature. However, for increasing Rayleigh number there is a considerable deviation from the conduction solution for the temperature solutions as the convective effects dominate the solution. However, since the study deals with porous materials there is a further consideration that needs to be taken into account. The effect of porosity also reduces the convective currents inside the domain of the problem which further reduces the temperature gradients in the cavity as opposed to the clear fluid case.

Nusselt number was plotted along the wall of the cavity. The determination of nusselt number needs some explanation as the evaluation of the above requires some complex post-processing evaluations. Nusselt number is evaluated as a post-processing operation on the primitive variables. The local Nusselt number is defined by the following integral of the normal component of the temperature variation at

the hotter (or colder) vertical wall [76];

$$Nu = -\frac{1}{l}\int_0^l \frac{\partial T}{\partial x}(leftwall, y)dy \tag{7.13}$$

Introducing the finite element approximation for the temperature which has already been calculated (at the post processing stage);

$$Nu = -\frac{1}{l}\int_0^l T_k \frac{\partial N_k}{\partial x}(leftwall, y)dy \tag{7.14}$$

Here, N denotes the shape function for the bi-quadratic element. This integration when performed in the finite element context resolves to;

$$\frac{\partial N_k}{\partial x} = \left[J_{11}^* \frac{\partial \psi_k}{\partial \varepsilon} + J_{12}^* \frac{\partial \psi_k}{\partial \eta}\right] \tag{7.15}$$

where, $[J_{11}^* J_{22}^*]$ denote the inverse of the Jacobian matrix for the element. The Jacobian matrix is the transformation from the specific coordinate system for each finite element to the master square finite element in the localized coordinates.

Thus, the Nu at the element level for each element resolves to the following summation over the gauss points;

$$Nu = \frac{1}{l}\sum_{kk=1}^{10}\sum_{k=1}^{9} T_k \left[J_{11}^* \frac{\partial \psi_k}{\partial \varepsilon} + J_{12}^* \frac{\partial \psi_k}{\partial \eta}\right] w_{kk} \left\|J_s\right\| \tag{7.16}$$

J_s is the surface Jacobian for the finite element edge of the element, and w_{kk} are the Gauss weights, and l is the length of the side of the domain over which the integration is carried out. A ten-point (10) Gauss-quadrature was used for the evaluation of the above integral.

Local Nusslet number along the vertical wall of the cavity was evaluated along with the average Nusselt number for the whole wall. The average Nusselt number is the arithmetic average of the Nusselt numbers evaluated for all the edge elements. Validation of the code developed for the solution of the partial differential equations

was done before the results were generated. The code was first validated with the clear fluid case (a high permeability and a porosity of 0.99) and, a very good agreement with published literature [78] was found. The average Nusselt number evaluated for the vertical wall for the clear fluid case for an Ra of 10^4 was found as 2.25 which shows an excellent agreement with reported results for the same Ra number[75]. Also the present value of the average Nusselt number for the clear fluid case for an Ra of 10^5 was found to be 4.89 which is slightly higher than the reported value of 4.77 by Marshall et al. [77].

The porous cavity results were also checked for the validation of the code with published literature. A very good agreement was found with the published results with an average R-squared between the predictions at 0.98. Nithiarasu et al. [70] have determined the average Nusselt number for the problem with a Da of 0.01, Ra of 10^5, and a porosity of 0.40, and reported a value of 2.98 which was found to be agreement with the present value of 3.19 for steady state for the same parameters. Evaluations of the Nusselt number for a different boundary condition can be found in Basak et al. [76].

F. Applications

A lot of research has been conducted in the areas of food drying in the context of microwave heating, convective drying, infrared drying etc. The problem usually involves coupled heat and moisture transport equations which can be solved with any of the available discretization strategies. When porous materials are subjected to intense drying there are considerable convective effects. In particular, in light of the complex nature of the porous matrices, it is anticipated that there will be dominant effects from convective effects in highly porous materials in particular when subjected

to intense drying operations.

In-spite of the above mentioned literature that exists in the field, most of the problems solved to date have been diffusive, heat and moisture transport equations in two or three dimensions with some variants. There has not been much work on considering convective effects inside a porous material when subjected to intense drying. This work seeks to be a first step towards modelling convective effects in these areas.

Drying problem also involves multi-phase flow transport with different phases of the vapour and water convecting together inside the porous material matrix. The vapour transport however small can contribute to an enhancement of the heat flux transport inside the porous matrix as can the liquid water transfer. Consideration of these effects have to be incorporated in a coupled fashion with the fluid flow and the heat transfer equations. Some of the above mentioned considerations have been addressed with some implicit averaging with the effective porosity and the permeability of the porous media herein. Also an insight is to be gained on the behaviour of the temperature fields inside the food matrix in the presence of convective effects and as mentioned earlier the deviations from a pure conduction solution (with diffusive transport) can be substantial. The deviations of the temperature field from the purely convective fluid flow transport and in the presence of porous matrix also has been brought out clearly.

G. Numerical Results

The dimensions of the cavity in were taken as a square of $1m \times 1m$. The hotter vertical wall of the cavity was subjected to a temperature of 60 degree centigrade and the colder side was maintained a temperature of 40 degree centigrade. The average

temperature for the effects of the change in density of the fluid in a Boussinesq sense was taken as the average of the above two temperatures at 40 degrees. Figure 51

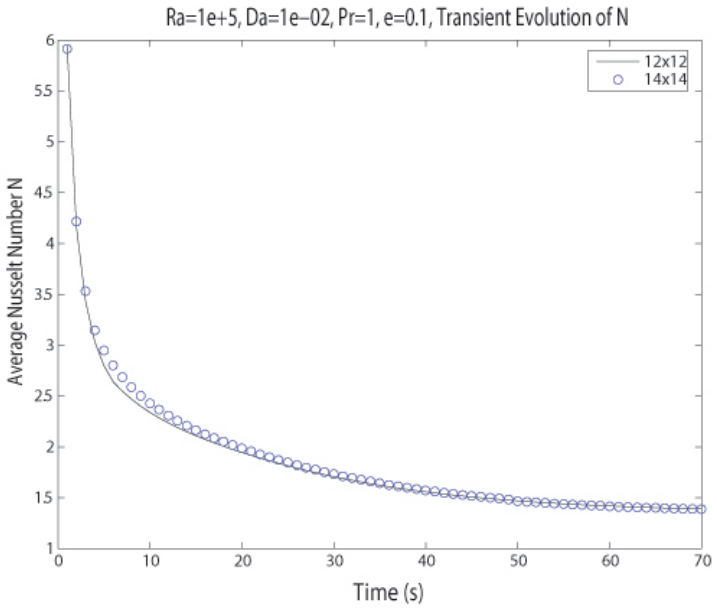

Fig. 51. Transient evolution of average Nusselt number

presents the transient evolution of the average Nusselt number with time for the convective heat transfer problem as presented earlier. As can be seen from the figure, the Nusselt number reaches reaches a constant asymptotically. Figure 52 compares the present results for the *local* variation of the Nusselt number along the vertical wall of the cavity for the clear fluid case to the values obtained from Marshall et al.[12] for an Ra of 10^4. There is a very good agreement between the two results with an R-square of 0.998. The average Nusselt number for an Ra of 10^4 was found to be 2.27 which is the same as reported by the above authors. The lower graph presents the local variation of the Nusselt number along the wall for a Darcy number of 0.01, and a porosity of 0.10, and Ra of 10^5. From this figure it is clear that there is a considerable reduction in heat transfer due to the presence of the porous matrix

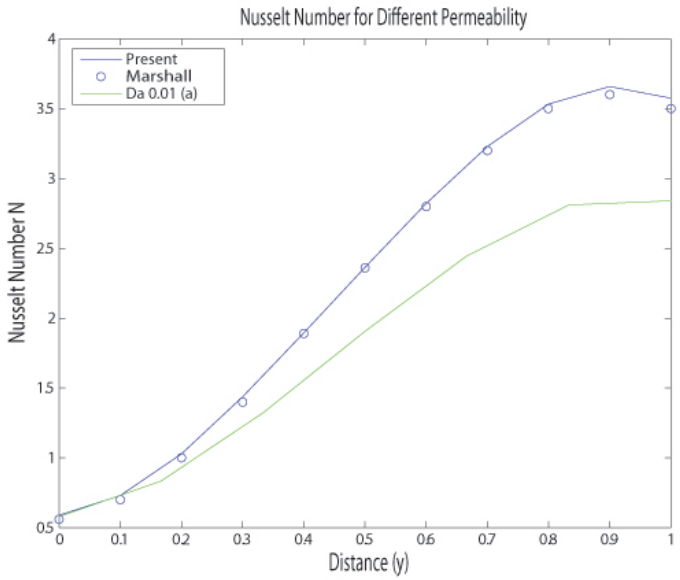

Fig. 52. Nusselt number for different permeabilities

inside the domain of study as compared to if the domain was filled with a fluid only. In spite of an increase in Ra by a factor of 10 the Nusselt number is still smaller as compared to the fluid only case. The average Nusselt number for Ra 10^5, Darcy number 0.01, and Prandtl number 1 was found to be 1.81. Figure 53 presents the u-velocity at the midsection of the buoyancy driven cavity for the clear fluid case along a horizontal line for an Ra of 10^5 and a Prandtl number of 1.0. Figure 54 compares the concomitant v-component of the velocity at the horizontal midsection of the cavity for an Ra number of 10^5 and Pr of 1 along with published results of Reddy[9]. There is a very good agreement between the two results with an R-square of 0.999. Figure 55 compares the non-dimensional temperature predictions along the horizontal midsection of the cavity with published results of Reddy [75] for Ra of 10^5. In this case also, there is a very good agreement of the present results with published results. Generalized Navier-Stokes equations resolves to the clear fluid case

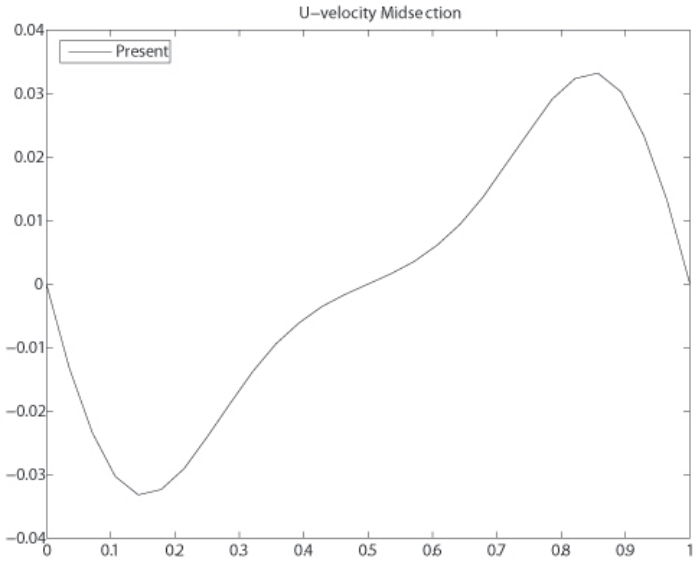

Fig. 53. u-velocity at mid-section of clear fluid

for a porosity of 0.999 and a very high Darcy number as mentioned earlier. Figure 56 presents the transient evolution of the velocity vectors inside the porous domain for an Ra of 10^5, Da of 0.01 and a porosity of 0.10. It can be seen that most of the development of the velocity inside the porous matrix occurs during the early stages of the convective heat transfer problem after which some minor adjustment of the velocity vectors continues till steady state is reached. The transient evolution of the temperature profile inside the porous matrix for an Ra of 10^5, $Da = 0.01$, and a porosity of 0.10 is presented in Figure 57. The temperatures distribution inside the porous matrix takes considerable more time and the transient evolves all along the time plane till it reaches a steady state as evident from the figure.

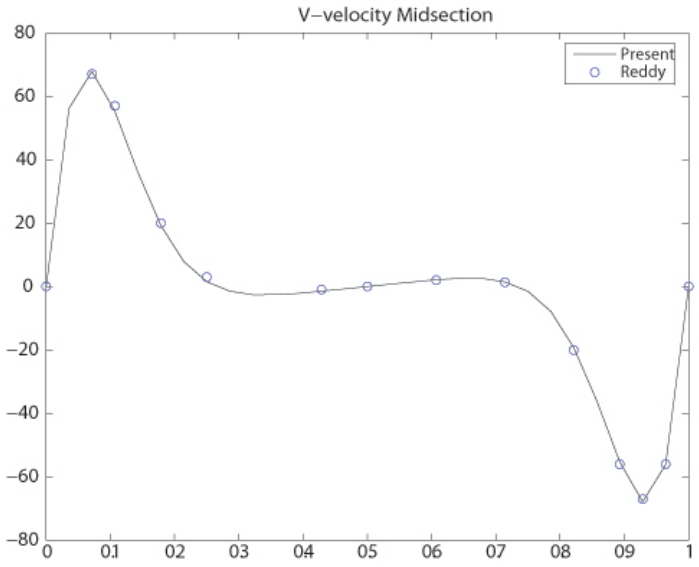

Fig. 54. v-velocity at mid-section of clear fluid

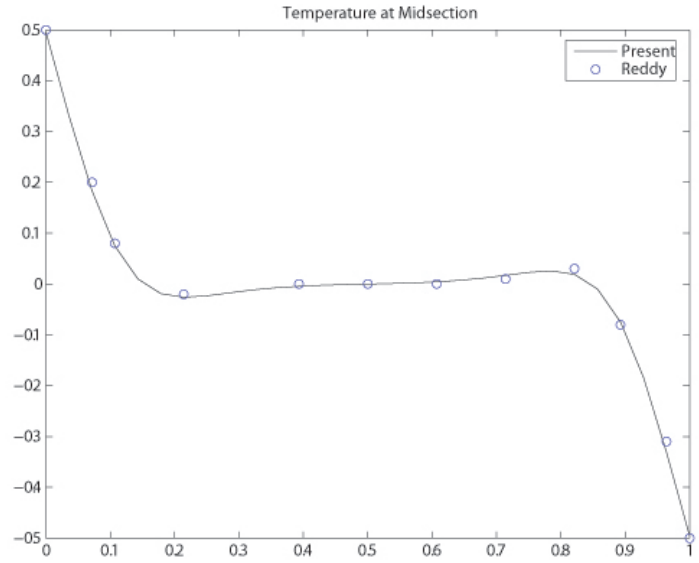

Fig. 55. Non-dimensional temperature comparison with published results

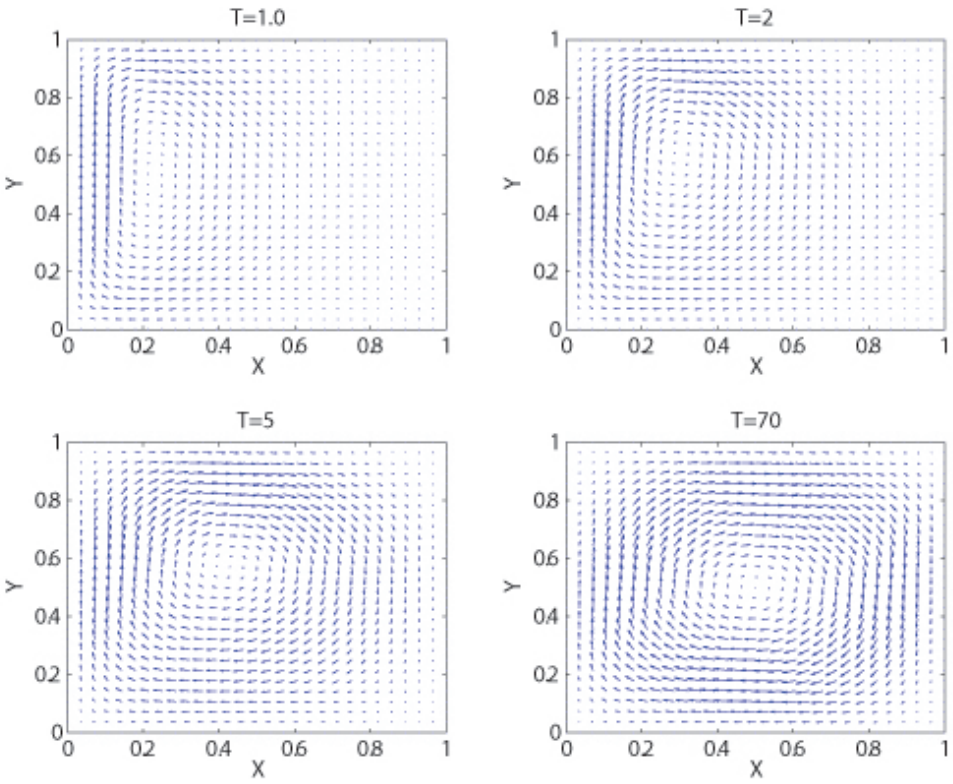

Fig. 56. Velocity vectors for the transient flowfield

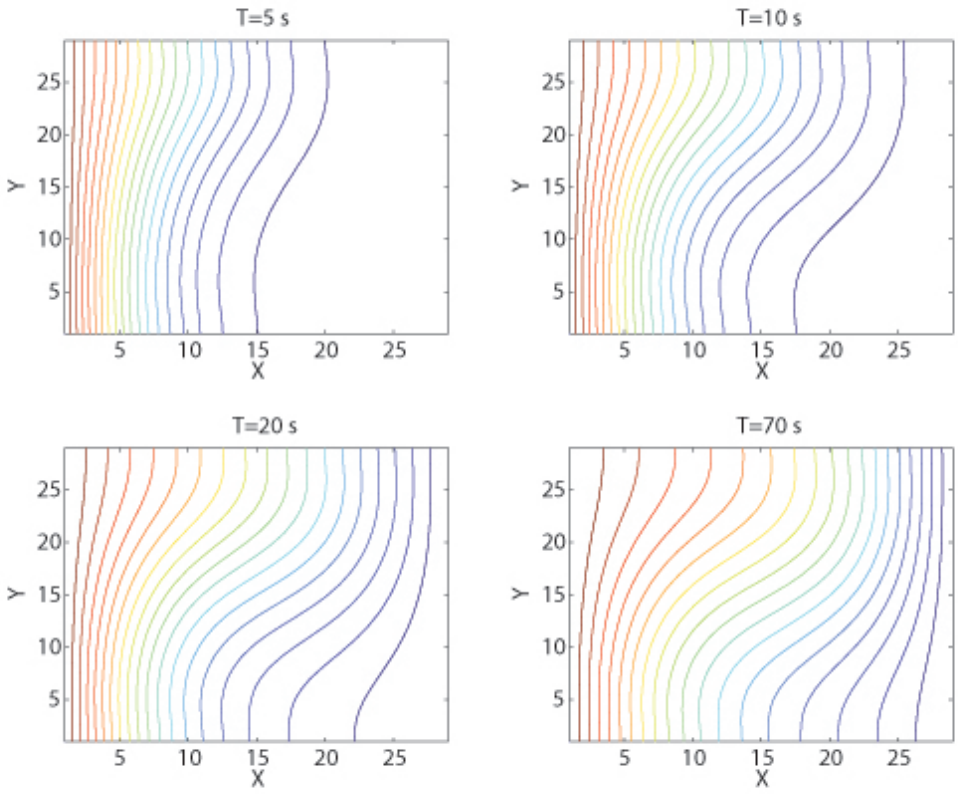

Fig. 57. Transient temperature contours

CHAPTER VIII

HP LEAST SQUARES FORMULATIONS/APPLICATIONS

A. Introduction

We highlighted the usage of least squares formulations for solutions of Navier-Stokes equations with different techniques, namely the Domain decomposition and Multigrid methods in earlier chapters. In this chapter we present the formulation for the development of the stiffness matrices with the Picard method of linearisation for least squares finite element methods (LSFEM) and also explore the usage of LSFEM for the solutions of computational fluid dynamics problems like the flow past a cylinder, and forward facing step. While doing so, we also highlight some of the weaknesses of the formulation itself, and try to establish through applications, the lack of robustness in correctly capturing pressure fields in particular in conjugation with fictitious domain methods (FDM). A lot of research has been devoted to the usage of LSFEM formulations for different applications. While in some cases LSFEM performs well, LSFEM formulations have issues with capturing the correct metrics in a more general setting. The formulation itself is very different in its basic premise of carrying out a minimization statement for the solutions of the partial differential equations in consideration. The main area of interest here is that while the method seeks to find a global minimizer to the PDEs that are solved, there can be some local errors near the boundary layers which can corrupt the pressure solutions for the whole domain of interest. In addition, with the extensive meshing requirements that the method needs as compared to the established Penalty finite element methods (which has been misleadingly disputed by different researchers), makes this method a relatively unattractive choice for the solutions of Navier-Stokes equations. The advantage that

this method provides is the solution of a symmetric operator, which can easily be alleviated if one uses any of the GMRES(k) or BiCGSTAB type solvers for solving the un-symmetric systems that arise from the Penalty finite element formulations. In the following section we detail the derivation of the stiffness matrices for the LSFEM, and follow through with the CFD applications.

B. Method of Direct Substitution (Picard Method)

The Navier-Stokes equations in the first-order form are summarized below for the 2-D case. The continuity equation (conservation of mass) is expressed as:

$$\frac{\partial u}{\partial x} + \frac{\partial v}{\partial y} = 0 \tag{8.1}$$

where (u, v) are the velocity components. The x-component of the momentum equation is expressed as;

$$\frac{\partial u}{\partial t} + u\frac{\partial u}{\partial x} + v\frac{\partial u}{\partial y} + \frac{\partial P}{\partial x} + \frac{1}{\mathrm{Re}}\frac{\partial \omega_z}{\partial y} = f_x \tag{8.2}$$

The y-component of the momentum equation is expressed as

$$\frac{\partial v}{\partial t} + u\frac{\partial v}{\partial x} + v\frac{\partial v}{\partial y} + \frac{\partial P}{\partial y} - \frac{1}{\mathrm{Re}}\frac{\partial \omega_z}{\partial x} = f_y \tag{8.3}$$

where the vorticity ω_z is expressed in terms of the velocity components (u,v) as

$$\omega_z + \frac{\partial u}{\partial y} - \frac{\partial v}{\partial x} = 0 \tag{8.4}$$

Here (f_x, f_y) denote the components of the body force vector and Re denotes the Reynolds number.

C. Least-Squares Functional

In the least-squares formulation, we construct the residuals of each equation and write the sum of the squares of the residuals as the least-squares functional to be minimized. We begin with the Navier-Stokes equation in the first-order form. The residuals of equations [42] are given by

$$R_1 = \frac{\partial u_h}{\partial x} + \frac{\partial v_h}{\partial y} \tag{8.5}$$

$$R_2 = \frac{\partial u_h}{\partial t} + u_h\frac{\partial u_h}{\partial x} + v_h\frac{\partial u_h}{\partial y} + \frac{\partial P_h}{\partial x} + \frac{1}{\mathrm{Re}}\frac{\partial \omega_{zh}}{\partial y} - f_x \tag{8.6}$$

$$R_3 = \frac{\partial v_h}{\partial t} + u_h\frac{\partial v_h}{\partial x} + v_h\frac{\partial v_h}{\partial y} + \frac{\partial P_h}{\partial y} - \frac{1}{\mathrm{Re}}\frac{\partial \omega_{zh}}{\partial x} - f_y \tag{8.7}$$

$$R_4 = \omega_{zh} + \frac{\partial u_h}{\partial y} - \frac{\partial v_h}{\partial x} \tag{8.8}$$

where $(u_h, v_h, P_h, \omega_{zh})$ denote the finite element approximations of (u, v, P, ω_z), respectively. Before we proceed with the least-squares formulation, we must make some approximations of the time-derivative terms and the non-linear terms. For a decoupled time-space formulation, i.e., the formulation in which the space and time are approximated separately, the residuals R_i are replaced with their time-approximated counterparts. Using single-step backward difference scheme, we can write the time derivative of a variable $w(x, y, t)$ as

$$\dot{w}_h^s \approx \frac{w_h^s - w_h^{s-1}}{\Delta t}, \quad \Delta t = t_s - t_{s-1} \tag{8.9}$$

where w^s denotes the value $w(x, y, t_s)$. Then the residuals are linearized by assuming that $u(\partial u/\partial x)$, for example, is equal to $\bar{u}(\partial u/\partial x)$, where $\bar{u}$ is the value computed using the previous iteration. Then the residuals R_2 and R_3 take the form;

$$R_2 = \frac{u_h^s - u_h^{s-1}}{\Delta t} + \bar{u}_h^s\frac{\partial u_h^s}{\partial x} + \bar{v}_h^s\frac{\partial u_h^s}{\partial y} + \frac{\partial P_h^s}{\partial x} + \frac{1}{\mathrm{Re}}\frac{\partial \omega_{zh}^s}{\partial y} - f_x^s \tag{8.10}$$

$$R_3 = \frac{v_h^s - v_h^{s-1}}{\Delta t} + \bar{u}_h^s \frac{\partial v_h^s}{\partial x} + \bar{v}_h^s \frac{\partial v_h^s}{\partial y} + \frac{\partial P_h^s}{\partial y} - \frac{1}{\mathrm{Re}} \frac{\partial \omega_{zh}^s}{\partial x} - f_y^s \tag{8.11}$$

The least-squares functional for a typical finite element Ω_e is;

$$I^e(u_h^s, v_h^s, \omega_{zh}^s, P_h^s) = \int_{\Omega_e} ({R_1}^2 + {R_2}^2 + {R_3}^2 + {R_4}^2) dxdy \tag{8.12}$$

The necessary condition for the minimum of I^e is

$$\begin{aligned}
\delta I^e(u_h^s, v_h^s, \omega_{zh}^s, P_h^s) &= 2\int_{\Omega_e} \Big(R_1\, \delta R_1 + R_2\, \delta R_2 + R_3\, \delta R_3 + R_4\, \delta R_4 \Big) dxdy \\
&= 2\int_{\Omega_e} \Big[\Big(\frac{\partial u_h^s}{\partial x} + \frac{\partial v_h^s}{\partial y} \Big) \Big(\frac{\partial \delta u_h^s}{\partial x} + \frac{\partial \delta v_h^s}{\partial y} \Big) \\
&\quad + \Big(\frac{u_h^s - u_h^{s-1}}{\Delta t} + \bar{u}_h^s \frac{\partial u_h^s}{\partial x} + \bar{v}_h^s \frac{\partial u_h^s}{\partial y} + \frac{\partial P_h^s}{\partial x} + \frac{1}{\mathrm{Re}} \frac{\partial \omega_{zh}^s}{\partial y} - f_x^s \Big) \\
&\quad \times \Big(\frac{\delta u_h^s}{\Delta t} + \bar{u}_h^s \frac{\partial \delta u_h^s}{\partial x} + \bar{v}_h^s \frac{\partial \delta u_h^s}{\partial y} + \frac{\partial \delta P_h^s}{\partial x} + \frac{1}{Re} \frac{\partial \delta \omega_{zh}^s}{\partial y} \Big) \\
&\quad + \Big(\frac{v_h^s - v_h^{s-1}}{\Delta t} + \bar{u}_h^s \frac{\partial v_h^s}{\partial x} + \bar{v}_h^s \frac{\partial v_h^s}{\partial y} + \frac{\partial P_h^s}{\partial y} - \frac{1}{\mathrm{Re}} \frac{\partial \omega_{zh}^s}{\partial x} - f_y^s \Big) \\
&\quad \times \Big(\frac{\delta v_h^s}{\Delta t} + \bar{u}_h^s \frac{\partial \delta v_h^s}{\partial x} + \bar{v}_h^s \frac{\partial \delta v_h^s}{\partial y} + \frac{\partial \delta P_h^s}{\partial y} - \frac{1}{Re} \frac{\partial \delta \omega_{zh}^s}{\partial x} \Big) \\
&\quad + \Big(\omega_{zh}^s + \frac{\partial u_h^s}{\partial y} - \frac{\partial v_h^s}{\partial x} \Big) \Big(\delta \omega_{zh}^s + \frac{\partial \delta u_h^s}{\partial y} - \frac{\partial \delta v_h^s}{\partial x} \Big) \Big] dxdy
\end{aligned} \tag{8.13}$$

Collecting the coefficients of δu_h, δv_h, δP_h, and $\delta \omega_z$ separately, and setting the expressions to zero (because of the linear independence of the variations), we obtain;

$$\begin{aligned}
0 &= \int_{\Omega_e} \Big[\frac{\partial \delta u_h^s}{\partial x} \Big(\frac{\partial u_h^s}{\partial x} + \frac{\partial v_h^s}{\partial y} \Big) + \Big(\frac{\delta u_h^s}{\Delta t} + \bar{u}_h^s \frac{\partial \delta u_h^s}{\partial x} + \bar{v}_h^s \frac{\partial \delta u_h^s}{\partial y} \Big) \\
&\quad \times \Big(\frac{u_h^s - u_h^{s-1}}{\Delta t} + \bar{u}_h^s \frac{\partial u_h^s}{\partial x} + \bar{v}_h^s \frac{\partial u_h^s}{\partial y} + \frac{\partial P_h^s}{\partial x} + \frac{1}{Re} \frac{\partial \omega_{zh}^s}{\partial y} - f_x^s \Big) \\
&\quad + \frac{\partial \delta u_h^s}{\partial y} \Big(\omega_{zh}^s + \frac{\partial u_h^s}{\partial y} - \frac{\partial v_h^s}{\partial x} \Big) \Big] dxdy
\end{aligned} \tag{8.14}$$

$$\begin{aligned}
0 &= \int_{\Omega_e} \Big[\frac{\partial \delta v_h^s}{\partial y} \Big(\frac{\partial u_h^s}{\partial x} + \frac{\partial v_h^s}{\partial y} \Big) + \Big(\frac{\delta v_h^s}{\Delta t} + \bar{u}_h^s \frac{\partial \delta v_h^s}{\partial x} + \bar{v}_h^s \frac{\partial \delta v_h^s}{\partial y} \Big) \\
&\quad \times \Big(\frac{v_h^s - v_h^{s-1}}{\Delta t} + \bar{u}_h^s \frac{\partial v_h^s}{\partial x} + \bar{v}_h^s \frac{\partial v_h^s}{\partial y} + \frac{\partial P_h^s}{\partial y} - \frac{1}{Re} \frac{\partial \omega_{zh}^s}{\partial x} - f_y^s \Big) \\
&\quad - \frac{\partial \delta v_h^s}{\partial x} \Big(\omega_{zh}^s + \frac{\partial u_h^s}{\partial y} - \frac{\partial v_h^s}{\partial x} \Big) \Big] dxdy
\end{aligned} \tag{8.15}$$

$$
\begin{aligned}
0 &= \int_{\Omega_e}\Big[\frac{\partial\delta P_h^s}{\partial x}\Big(\frac{u_h^s-u_h^{s-1}}{\Delta t}+\bar{u}_h^s\frac{\partial u_h^s}{\partial x}+\bar{v}_h^s\frac{\partial u_h^s}{\partial y}+\frac{\partial P_h^s}{\partial x}+\frac{1}{Re}\frac{\partial\omega_{zh}^s}{\partial y}-f_x^s\Big) \\
&\quad +\frac{\partial\delta P_h^s}{\partial y}\Big(\frac{v_h^s-v_h^{s-1}}{\Delta t}+\bar{u}_h^s\frac{\partial v_h^s}{\partial x}+\bar{v}_h^s\frac{\partial v_h^s}{\partial y}+\frac{\partial P_h^s}{\partial y}-\frac{1}{Re}\frac{\partial\omega_{zh}^s}{\partial x}-f_y^s\Big)\Big]dxdy \qquad (8.16)\\
0 &= \int_{\Omega_e}\Big[\frac{1}{Re}\frac{\partial\delta\omega_{zh}^s}{\partial y}\Big(\frac{u_h^s-u_h^{s-1}}{\Delta t}+\bar{u}_h^s\frac{\partial u_h^s}{\partial x}+\bar{v}_h^s\frac{\partial u_h^s}{\partial y}+\frac{\partial P_h^s}{\partial x}+\frac{1}{Re}\frac{\partial\omega_{zh}^s}{\partial y}-f_x^s\Big) \\
&\quad -\frac{1}{Re}\frac{\partial\delta\omega_{zh}^s}{\partial x}\Big(\frac{v_h^s-v_h^{s-1}}{\Delta t}+\bar{u}_h^s\frac{\partial v_h^s}{\partial x}+\bar{v}_h^s\frac{\partial v_h^s}{\partial y}+\frac{\partial P_h^s}{\partial y}-\frac{1}{Re}\frac{\partial\omega_{zh}^s}{\partial x}-f_y^s\Big) \\
&\quad +\delta\omega_{zh}^s\Big(\omega_{zh}^s+\frac{\partial u_h^s}{\partial y}-\frac{\partial v_h^s}{\partial x}\Big)\Big]dxdy \qquad (8.17)
\end{aligned}
$$

D. Picard Method LSFEM Stiffness Matrices

The following decoupled time-space finite element approximation of the field variables $(u_h, v_h, P_h, \omega_{zh})$ is assumed:

$$
u_h^s=\sum_{j=1}^{n}u_j(t_s)\psi_j(x,y),\quad v_h^s=\sum_{j=1}^{n}v_j(t_s)\psi_j(x,y), \qquad (8.18)
$$

$$
P_h^s=\sum_{j=1}^{m}P_j(t_s)\phi_j(x,y),\quad \omega_{zh}^s=\sum_{j=1}^{p}\omega_{zj}(t_s)\varphi_j(x,y) \qquad (8.19)
$$

Here, m, n, and p denotes the number of nodes in the element used for the velocity field, pressure, and vorticity, respectively. Substitution of the finite element approximations from the above equation into the least-squares statements gives the following least-squares finite element model:

$$
\begin{bmatrix}
[M^{11}] & [0] & [M^{13}] & [M^{14}] \\
[0] & [M^{22}] & [M^{23}] & [M^{24}] \\
[M^{31}] & [M^{32}] & [0] & [0] \\
[M^{41}] & [M^{42}] & [0] & [0]
\end{bmatrix}
\begin{Bmatrix}\{u\}\\ \{v\}\\ \{P\}\\ \{\omega\}\end{Bmatrix}^s
+
\begin{bmatrix}
[K^{11}] & [K^{12}] & [K^{13}] & [K^{14}] \\
[K^{21}] & [K^{22}] & [K^{23}] & [K^{24}] \\
[K^{31}] & [K^{32}] & [K^{33}] & [K^{34}] \\
[K^{41}] & [K^{42}] & [K^{43}] & [K^{44}]
\end{bmatrix}
\begin{Bmatrix}\{u\}\\ \{v\}\\ \{P\}\\ \{\omega\}\end{Bmatrix}^s
$$

$$= \begin{Bmatrix} \{G^1\} + \{F^1\} \\ \{G^2\} + \{F^2\} \\ \{F^3\} \\ \{F^4\} \end{Bmatrix} + \begin{bmatrix} [\tilde{M}^{11}] & [0] & [0] & [0] \\ [0] & [\tilde{M}^{22}] & [0] & [0] \\ [\tilde{M}^{31}] & [\tilde{M}^{32}] & [0] & [0] \\ [\tilde{M}^{41}] & [\tilde{M}^{42}] & [0] & [0] \end{bmatrix} \begin{Bmatrix} \{u\} \\ \{v\} \\ \{P\} \\ \{\omega\} \end{Bmatrix}^{s-1} \tag{8.20}$$

where;

$$\begin{aligned}
M_{ij}^{11} &= \frac{1}{\Delta t}\int_{\Omega_e}\Big[\frac{1}{\Delta t}\psi_i\psi_j + \psi_i\Big(\bar{u}_h\frac{\partial\psi_j}{\partial x} + \bar{v}_h\frac{\partial\psi_j}{\partial y}\Big)\Big]dxdy, \\
M_{ij}^{13} &= \frac{1}{\Delta t}\int_{\Omega_e}\psi_i\frac{\partial\phi_j}{\partial x}\,dxdy, \quad M_{ij}^{14} = \frac{1}{Re\Delta t}\int_{\Omega_e}\psi_i\frac{\partial\varphi_j}{\partial y}\,dxdy, \\
M_{ij}^{22} &= \frac{1}{\Delta t}\int_{\Omega_e}\Big[\frac{1}{\Delta t}\psi_i\psi_j + \psi_i\Big(\bar{u}_h\frac{\partial\psi_j}{\partial x} + \bar{v}_h\frac{\partial\psi_j}{\partial y}\Big)\Big]dxdy, \\
M_{ij}^{23} &= \frac{1}{\Delta t}\int_{\Omega_e}\psi_i\frac{\partial\phi_j}{\partial y}\,dxdy, \quad M_{ij}^{24} = -\frac{1}{Re\Delta t}\int_{\Omega_e}\psi_i\frac{\partial\varphi_j}{\partial x}\,dxdy, \\
M_{ij}^{31} &= \frac{1}{\Delta t}\int_{\Omega_e}\frac{\partial\phi_i}{\partial x}\psi_j\,dxdy, \quad M_{ij}^{32} = \frac{1}{\Delta t}\int_{\Omega_e}\frac{\partial\phi_i}{\partial y}\psi_j\,dxdy, \\
M_{ij}^{41} &= \frac{1}{Re\Delta t}\int_{\Omega_e}\frac{\partial\varphi_i}{\partial x}\psi_j\,dxdy, \quad M_{ij}^{42} = \frac{1}{Re\Delta t}\int_{\Omega_e}\frac{\partial\varphi_i}{\partial y}\psi_j\,dxdy, \\
M_{ij}^{12} &= M_{ij}^{21} = M_{ij}^{33} = M_{ij}^{34} = M_{ij}^{43} = M_{ij}^{44} = 0, \\
\tilde{M}_{ij}^{11} &= \tilde{M}_{ij}^{22} = \Big(\frac{1}{\Delta t}\Big)^2\int_{\Omega_e}\psi_i\psi_j\,dxdy, \\
\tilde{M}_{ij}^{31} &= \frac{1}{\Delta t}\int_{\Omega_e}\frac{\partial\phi_i}{\partial x}\psi_j\,dxdy, \quad \tilde{M}_{ij}^{32} = \frac{1}{\Delta t}\int_{\Omega_e}\frac{\partial\phi_i}{\partial y}\psi_j\,dxdy, \\
\tilde{M}_{ij}^{41} &= \frac{1}{Re\Delta t}\int_{\Omega_e}\frac{\partial\varphi_i}{\partial y}\psi_j\,dxdy, \quad \tilde{M}_{ij}^{42} = -\frac{1}{Re\Delta t}\int_{\Omega_e}\frac{\partial\varphi_i}{\partial x}\psi_j\,dxdy, \\
K_{ij}^{11} &= \int_{\Omega_e}\Big[\frac{\partial\psi_i}{\partial x}\frac{\partial\psi_j}{\partial x} + \frac{\partial\psi_i}{\partial y}\frac{\partial\psi_j}{\partial y} + \Big(\bar{u}_h\frac{\partial\psi_i}{\partial x} + \bar{v}_h\frac{\partial\psi_i}{\partial y}\Big)\Big(\bar{u}_h\frac{\partial\psi_j}{\partial x} + \bar{v}_h\frac{\partial\psi_j}{\partial y}\Big)\Big]dxdy, \\
K_{ij}^{12} &= \int_{\Omega_e}\Big(\frac{\partial\psi_i}{\partial x}\frac{\partial\psi_j}{\partial y} - \frac{\partial\psi_i}{\partial y}\frac{\partial\psi_j}{\partial x}\Big)dxdy, \quad K_{ij}^{13} = \int_{\Omega_e}\Big(\bar{u}_h\frac{\partial\psi_i}{\partial x} + \bar{v}_h\frac{\partial\psi_i}{\partial y}\Big)\frac{\partial\phi_j}{\partial x}\,dxdy, \\
K_{ij}^{14} &= \int_{\Omega_e}\Big[\frac{\partial\psi_i}{\partial y}\varphi_j + \frac{1}{Re}\Big(\bar{u}_h\frac{\partial\psi_i}{\partial x} + \bar{v}_h\frac{\partial\psi_i}{\partial y}\Big)\frac{\partial\varphi_j}{\partial y}\Big]\,dxdy, \\
K_{ij}^{21} &= \int_{\Omega_e}\Big(\frac{\partial\psi_i}{\partial y}\frac{\partial\psi_j}{\partial x} - \frac{\partial\psi_i}{\partial x}\frac{\partial\psi_j}{\partial y}\Big)dxdy = K_{ji}^{12}, \\
K_{ij}^{22} &= \int_{\Omega_e}\Big[\frac{\partial\psi_i}{\partial x}\frac{\partial\psi_j}{\partial x} + \frac{\partial\psi_i}{\partial y}\frac{\partial\psi_j}{\partial y} + \Big(\bar{u}_h\frac{\partial\psi_i}{\partial x} + \bar{v}_h\frac{\partial\psi_i}{\partial y}\Big)\Big(\bar{u}_h\frac{\partial\psi_j}{\partial x} + \bar{v}_h\frac{\partial\psi_j}{\partial y}\Big)\Big]dxdy \\
K_{ij}^{23} &= \int_{\Omega_e}\Big(\bar{u}_h\frac{\partial\psi_i}{\partial x} + \bar{v}_h\frac{\partial\psi_i}{\partial y}\Big)\frac{\partial\phi_j}{\partial x}\,dxdy,
\end{aligned}$$

$$
\begin{aligned}
K_{ij}^{24} &= -\int_{\Omega_e}\Big[\frac{\partial\psi_i}{\partial x}\varphi_j + \frac{1}{Re}\Big(\bar{u}_h\frac{\partial\psi_i}{\partial x} + \bar{v}_h\frac{\partial\psi_i}{\partial y}\Big)\frac{\partial\varphi_j}{\partial x}\Big]\,dxdy,\\
K_{ij}^{31} &= \int_{\Omega_e}\frac{\partial\phi_i}{\partial x}\Big(\bar{u}_h\frac{\partial\psi_j}{\partial x} + \bar{v}_h\frac{\partial\psi_j}{\partial y}\Big)\,dxdy = K_{ji}^{13},\\
K_{ij}^{32} &= \int_{\Omega_e}\frac{\partial\phi_i}{\partial y}\Big(\bar{u}_h\frac{\partial\psi_j}{\partial x} + \bar{v}_h\frac{\partial\psi_j}{\partial y}\Big)\,dxdy = K_{ji}^{23},\\
K_{ij}^{33} &= \int_{\Omega_e}\Big(\frac{\partial\phi_i}{\partial x}\frac{\partial\phi_j}{\partial x} + \frac{\partial\phi_i}{\partial y}\frac{\partial\phi_j}{\partial y}\Big)dxdy\\
K_{ij}^{34} &= \frac{1}{Re}\int_{\Omega_e}\Big(\frac{\partial\phi_i}{\partial x}\frac{\partial\varphi_j}{\partial y} - \frac{\partial\phi_i}{\partial y}\frac{\partial\varphi_j}{\partial x}\Big)dxdy = K_{ji}^{43}\\
K_{ij}^{41} &= \int_{\Omega_e}\Big[\varphi_i\frac{\partial\psi_j}{\partial y} + \frac{1}{Re}\frac{\partial\varphi_i}{\partial y}\Big(\bar{u}_h\frac{\partial\psi_j}{\partial x} + \bar{v}_h\frac{\partial\psi_j}{\partial y}\Big)\Big]\,dxdy,\\
K_{ij}^{42} &= -\int_{\Omega_e}\Big[\varphi_i\frac{\partial\psi_j}{\partial x} + \frac{1}{Re}\frac{\partial\varphi_i}{\partial x}\Big(\bar{u}_h\frac{\partial\psi_j}{\partial x} + \bar{v}_h\frac{\partial\psi_j}{\partial y}\Big)\Big]\,dxdy,\\
K_{ij}^{43} &= \frac{1}{Re}\int_{\Omega_e}\Big[\frac{\partial\varphi_i}{\partial y}\frac{\partial\phi_j}{\partial x} - \frac{\partial\varphi_i}{\partial x}\frac{\partial\phi_j}{\partial y}\Big]dxdy,\\
K_{ij}^{44} &= \int_{\Omega_e}\frac{1}{Re^2}\Big(\frac{\partial\varphi_i}{\partial x}\frac{\partial\varphi_j}{\partial x} + \frac{\partial\varphi_i}{\partial y}\frac{\partial\varphi_j}{\partial y}\Big) + \Big[\varphi_i\varphi_j\Big]dxdy\\
G_i^1 &= \int_{\Omega_e}\frac{1}{\Delta t}\psi_i f_x^s\,dxdy, \quad F_i^1 = \int_{\Omega_e}\Big(\bar{u}_h\frac{\partial\psi_i}{\partial x} + \bar{v}_h\frac{\partial\psi_i}{\partial y}\Big)f_x^s\,dxdy\\
G_i^2 &= \int_{\Omega_e}\frac{1}{\Delta t}\psi_i f_y^s\,dxdy, \quad F_i^2 = \int_{\Omega_e}\Big(\bar{u}_h\frac{\partial\psi_i}{\partial x} + \bar{v}_h\frac{\partial\psi_i}{\partial y}\Big)f_y^s\,dxdy\\
F_i^3 &= \int_{\Omega_e}\Big(\frac{\partial\phi_i}{\partial x}f_x^s + \frac{\partial\phi_i}{\partial y}f_y^s\Big)dxdy, \quad F_i^4 = \frac{1}{Re}\int_{\Omega_e}\Big(\frac{\partial\varphi_i}{\partial y}f_x^s - \frac{\partial\varphi_i}{\partial x}f_y^s\Big)dxdy
\end{aligned}
\tag{8.21}
$$

The above completes the least-squares finite element formulation for the problem with the Picard method of linearization.

E. Fictitious Domain Method

Fictitious domain method (FDM) is a technique of resolving the motion of particles inside a fluid, where the motion of the fluid is extended inside the particle with the help of rigid body motion. The fluid motion is governed by the Navier-Stokes equations and the particle motion is obtained with the hydrodynamic integration of the forces and torques on the particle. The governing equations for the fluid motion

are the incompressible Navier-Stokes equations for laminar flows; expressed in the first order form as has been presented before. The *total* stress tensor in the fluid phase is expressed as;

$$\sigma = -pI + \frac{1}{Re}\left[\bigtriangledown \mathbf{u} + \bigtriangledown \mathbf{u}^T\right] \tag{8.22}$$

In the above, $\mathbf{I}$ is the identity tensor, Re is the Reynolds number for the flow, p is the pressure, and $\mathbf{u}$ is the velocity of the fluid. The evaluation of the drag and the lift on the immersed object can be obtained with the help of these forces integrated over the surface area, or alternatively the volume of the object immersed in the fluid.

$$F_p = -\int_{\Gamma_p} \sigma \cdot n \; d\Gamma \tag{8.23}$$

and, the torque integrated over the domain of interest is evaluated as;

$$T_p = \int_{\Gamma_p} (x - x_p) \times \sigma \cdot n \; d\Gamma \tag{8.24}$$

where, $T_p = \Omega_p(i)$ is the boundary of the particle p. For a generic particle in the flow fluid, the particle can be in motion both in linear translational motion as well as rotation. The motion of the particle is obtained from the Newton's law and since we are only dealing with stationary particles we will not present the governing equations for the above. However, the motion of the particle once obtained (for stationary particles the translational velocities and angular velocity are both zero), are extended *inside* the rigid particles with the help of kinematic equations of fluid motion as follows;

$$u(\mathbf{U}) = \mathbf{U}_i + \omega_i \times (\mathbf{X} - \mathbf{X}_i) \tag{8.25}$$

As a first approximation of stationary circular particle in the flow field can be interpreted as flow past a cylinder. We constructed the surface of the cylinder, with the impositions of the velocity boundary conditions. Both the u, and v components of

the velocity vector **U** were specified to be identically equal to zero. It was *assumed* that LSFEM should pick up the correct values of the non-zero pressures inside the particle, and the flow around the cylinder would be replicated faithfully. To avoid the evaluation of the surface integrals to obtain the hydrodynamic integration of the forces and the torque in the particle, the phase indicator function is introduced. The introduction of this function converts the time-consumptive surface tracking and evaluation problem into an area integral in two dimensions. The phase indicator function is obtained as follows;

$$\alpha_i(\mathbf{X}) = \begin{cases} 1 & \mathbf{X} \in \Omega_i \\ 0 & \mathbf{X} \in \Omega_\Gamma \ \Omega_i \end{cases} \tag{8.26}$$

Based on the above assumptions and FDM procedure, we applied LSFEM based Fictitious Domain Method implementation for studying the flow past a cylinder.

F. Flow Past a Cylinder at Low Reynolds Number

The problem considered here is the steady incompressible flow past a cylinder described with the Fictitious Domain method, with the specification of the velocity boundary conditions. The Reynolds numbers studied for this problem are both 20 and 40. For the Reynolds number of 20 we consider the domain of interest as $[0, 0]\times[25, 20]$. A cylinder of unit diameter (1) is present at the location $[10.0, 10.0]$. The x-component of the inlet velocity is specified to be equal to 1.0 and the y-component (v) is set equal to zero. Symmetry boundary conditions, of $\omega = 0$, and $v = 0$, are imposed on the top and the bottom walls. The outflow boundary conditions are imposed in a weak sense through the least-squares functional. With the imposition of the symmetry boundary condition we increase the y-dimension of the domain to twice the stated value. During the minimization statement of the least squares functional we added a weight of 100 into the continuity equation, to enforce better mass conservation as least squares

formulations suffer from extensive loss of mass. It has been misleadingly reported by some researchers that loss of mass can be mitigated easily with the usage of higher order element methods, however one has to be wary with such concepts. Since, the loss of mass is highly problem dependent. For a new problem, just using a very high order expansion will perhaps work to mitigate the loss of mass for some problems, but not all of them.

The non-linear convergence criterion was set at a reduction in the norm of the residual with respect to the initial at a value of 10^{-03}. The linear convergence criterion was set at a reduction in the conjugate gradient residual to 10^{-06}. Picard method of linearization was used for the solution of the problem. It took four non-linear iterations to converge. Both the pressure and velocity non-linear residuals converged to the tolerance set. The total degrees of freedom that were solved for this problem were 52164 and there were a total of 800 elements on the Cartesian product grid that was set up. The usage of a uniform Cartesian grid for the solution of problems with fictitious domain method has been explored as the main advantage of this method over body fitted meshes. Figure 58 presents the closeup of the mesh with finer elements near the location of the cylinder, with a fixed rectangular mesh without body fitted mesh. Also, the figure presents the development of the wake near the cylinder, which is shown with streamline plots. The length of the wake obtained with the fictitious domain method was found 1.2 units in length or alternatively, equivalent to 2.4 cylinder radii. The wake length is slightly higher than the value of 1.88 cylinder radii, as reported by Dennis and Chang. The reason for this difference can also be felt in 15% loss of mass that was reported at the exit of the domain ahead of the presence of the cylinder in the flow field. As can be expected for this huge domain, the exit velocity at the exit of the channel should recover to the undisturbed value at the inlet, however a loss of mass with the minimum value of 0.85 velocity was

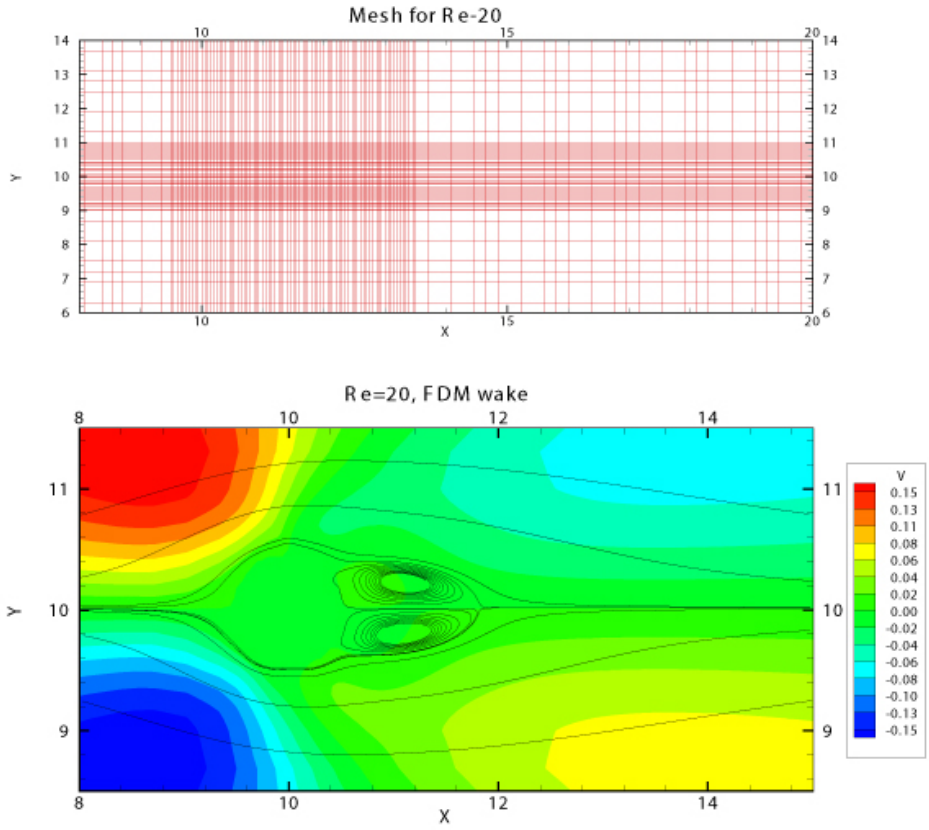

Fig. 58. Re=20, development of wake with FDM

reported for this case for a small strip of elements ahead of the cylinder location in the domain.

For the Reynolds number of 40 we consider the domain of interest as $[0, 0] \times [46, 41]$. A cylinder of unit diameter (1) is present at the location $[15.5, 20.5]$. There were a total of 309444 degrees of freedom in the mesh with a total of 4800 elements. The p_{level} used for this problem was set at a value of 4. Non-linear convergence was declared when the residuals reduced to a value of 10^{-03}. No weight was added to the continuity equation and the least squares finite element formulation was minimized without the consideration of the weight into the functional. The pressure contour

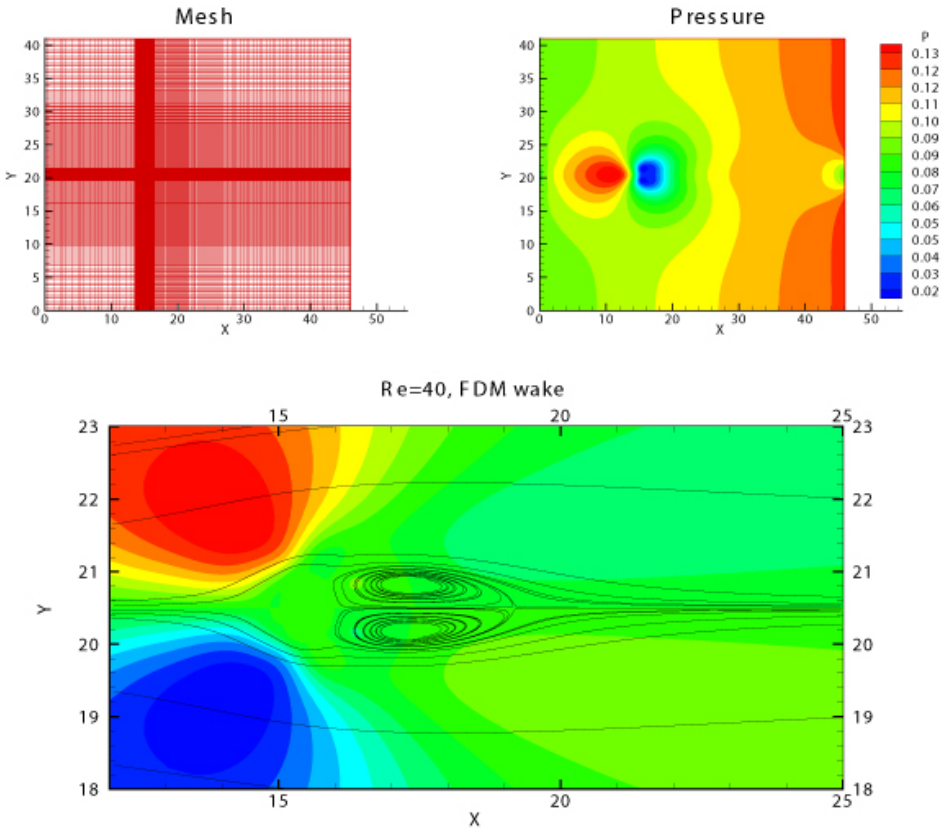

Fig. 59. Re=40, development of wake with FDM

plots and the development of the wake at a higher Reynolds number of $Re = 40$ are reported in Figure 59. The wake length in this case was found to be around 3.0 units, which is also an overestimation of the wake length that has been reported to be around 4.69 cylinder diameter or 2.3, in length. This overestimation of the wake length in both the cases tested, points to the fact that least squares finite element method performs relatively poorly to the imposition of the velocity boundary conditions. The fictitious domain method approach coupled with LSFEM formulations does not provide excellent results, although they may be considered acceptable for engineering analysis, and there is some smearing of the wake over the domain because

of inadequate resolution of the pressure fields near the boundary layers.

G. Forward Facing Step

In this section we consider another geometry namely that of the forward facing step [79]- [80]. The Navier-Stokes equations are set to be valid inside the domain of interest, which has a large contraction region. Of main interest is to be able to check the performance of the least squares finite element methods, for solving this 'difficult' contraction problem. The problem under consideration is that of a channel of height H through which the flow occurs, and in the presence of a constriction of height h [81]-[82]. Due to the presence of the constriction the flow is perturbed which is initially coming from the left, and after the constriction comes out from the right, where the channel height is $H - h$. Let, $r = h/H$ be restriction ratio, namely the ratio of the height of the step height, and the inlet channel height. Only one value of the restriction ratio, $r = 0.50$ was studied for this presentation. The Reynolds number is defined here as the ratio;

$$Re = \frac{\rho U_{ref} L_{ref}}{\nu} \tag{8.27}$$

In the above case, ν is the viscosity of the fluid, and ρ is the constant density of the fluid. All quantities are normalized with respect to the bulk velocity of the fluid entering the forward facing step which is taken as; $U_{ref} = (2/3)U_C$, where U_C is the centerline velocity of the plane incoming Poiseuille flow. At the solid walls, no penetration and no slip conditions were employed. At the outlet to the flow the outflow boundary conditions were employed in a weak sense into the least squares functional. It is seen that the incoming Poiseuille parabola is deformed in the step region, but is re-established at the outflow region [83].

The length of the entrance region was taken at 2 units. The length after the step was set at 20 [84]. The total entrance region height H on the left side was set at 2. The height of the step h was taken as 1. The Reynolds number of the incoming flow was set at 100. The problem was discretized with a set of 2590 spectral elements,with

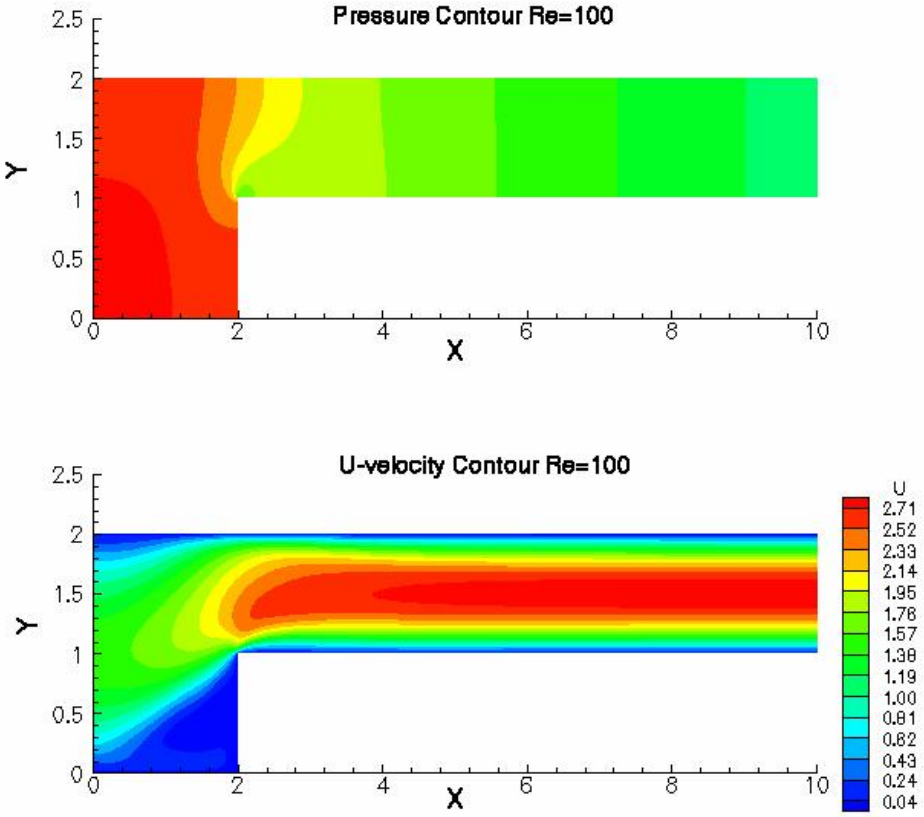

Fig. 60. u-velocity and pressure contours, Re=100

a discretization of 35×30 elements, in the cavity before the front end of the step, and 35×22 elements after the step. The p_{level} of 5 was used inside each element. The total number of degrees of freedom in the problem were 261444. The problem was solved with the Picard method of linearization. The problem took 8 iterations to converge to a tolerance set at 10^{-03}. Figure 60 presents the u-velocity and the

pressure contours inside the step at a Reynolds number of 100. Figure 61 presents

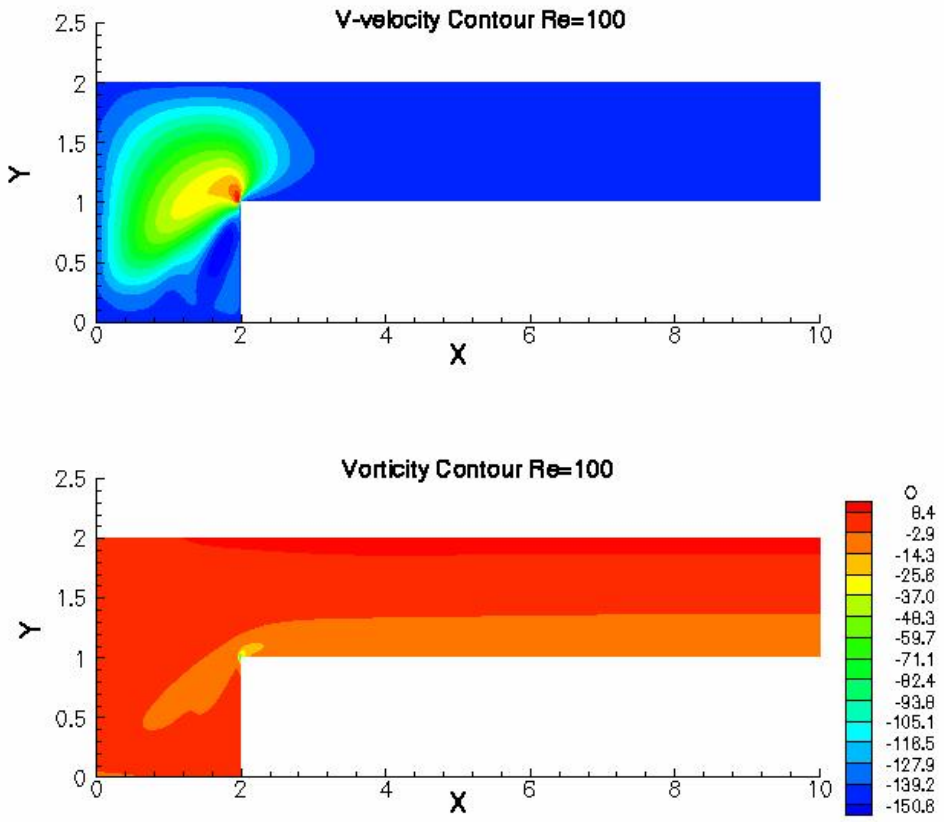

Fig. 61. v-velocity and vorticity contours, Re=100

the v-velocity and the vorticity inside the step geometry. As can be seen from the figure, the unboundedness of the vorticity at the front corner of the step is captured correctly, and demonstrates a high value of -150.57. This corner singularity was handled with an appropriate mesh refinement near the front edge of the step. For studying the problem for a higher reynolds number flow we increased the Reynolds number to 450. For this case, the mesh and the u-velocity contours are presented in Figure 62. This figure also presents the streamline plots inside the forward facing step for $Re = 450$. The reattachment zone on the top of the step is also visible for

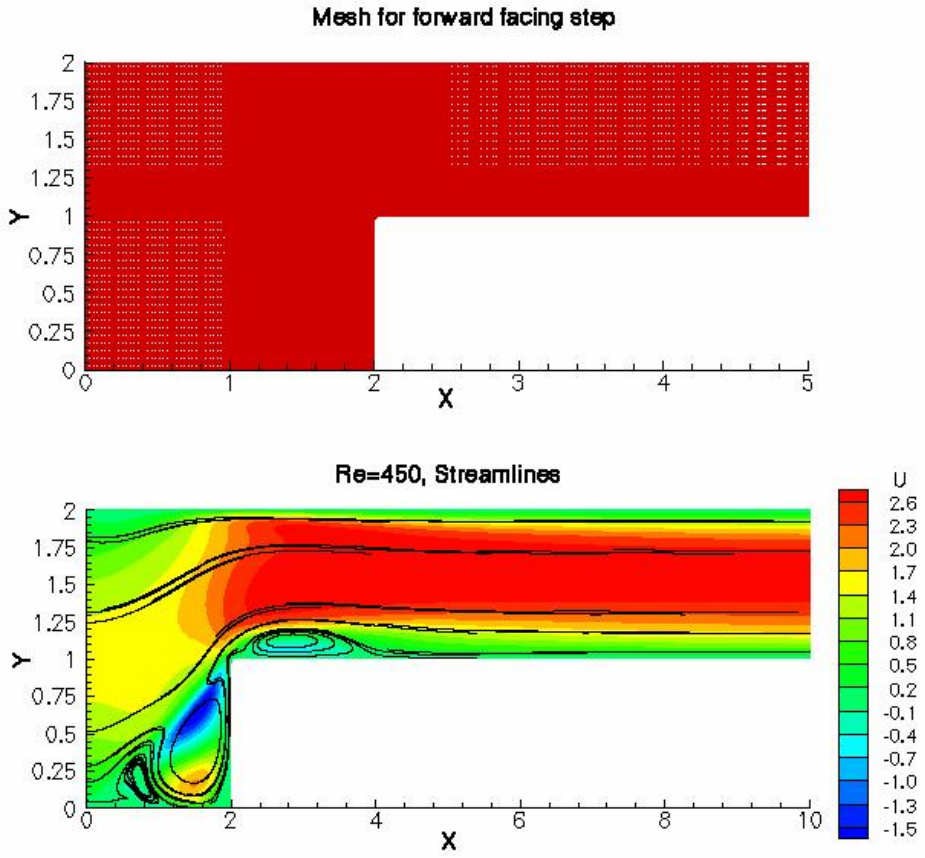

Fig. 62. Mesh and u-velocity contours, Re=450

this case for the higher Reynolds number [85]. Some of these results are being refined at the moment and this is an active area of research at present.

CHAPTER IX

CONCLUSION

A. Summary and Conclusion

In this presentation we covered the applications of higher order spectral *hp* element methods to solving different problems in both structures and computational fluid dynamics areas. We covered the usage of higher order methods for solving problems as encountered with both the mixed and displacement based models for the Timoshenko and Euler-Bernoulli beam theories in chapter II, followed by the usage of such methods for studying plate bending in two dimensions in chapter III. We also considered both isotropic and orthotropic plates, subject to different types of boundary conditions. We considered both linear and non-linear analysis for isotropic plates and orthotropic plates. In chapter IV we considered the usage of such methods for the solutions of large deformation analysis problems with the Updated Lagrangian analysis, for continuum based deformation analysis. We considered both linear and non-linear analysis for large deformation analysis.

Following such studies, we explored the usage of fast linear solvers for the solutions of huge linear systems that arise in course of solutions of Computational fluid dynamics applications. In this context, we explored the usage of element by element bi-orthogonal conjugate gradient solvers and domain decomposition techniques for solutions of both symmetric and non-symmetric operators in chapter V that occur with the p version of finite element analysis. The parallel implementation aspects for the above methods were also illustrated with ideal to super ideal speedups reported for both the methods studied. In chapter VI we studied the usage of multigrid methods for fast solutions of linear systems as obtained from p-version least squares finite

element methods. In this case also we obtained ideal to very good speedups with high performance gains over serial computations of the same. A matrix free technique was used to solve the coarse grid problem making the formulation completely independent of the size of the problem.

In chapter VII we explored the usage of Penalty finite element methods for solving the porous media problem in two dimensions. The usage of Generalized Navier-Stokes equations was explored for solving the coupled convective heat transfer problem along with studying such flows in porous bodies. Both transients, and steady state analysis were studied in the context of Penalty finite element methods. Finally, in chapter VIII we study the usage of least squares finite element methods for the solutions of CFD problems in two dimensions in conjugation with the Fictitious Domain methods and otherwise. In this section we also highlight some of the weaknesses of LSFEM in not capturing the correct pressure metrics for this problem. Further we explore the usage of LSFEM for solving the forward facing step problem.

In summary we demonstrated the usage of higher order methods for studying various different problems as encountered in different areas in engineering. In addition we also explore three different parallel implementations of fast linear solvers which are used extensively in CFD applications with p version SEM methods. In addition the usage of LSFEM, in particular the caution that needs to be exercised while applying LSFEM to new problems are also highlighted in the last chapter. Some of the latest sections of this dissertation are the object of current research efforts and is in a developing stage.

REFERENCES

[1] G. Karniadakis, S. Sherwin, Spectral/hp element methods for CFD, Oxford University Press, Oxford, 1999.

[2] C. Canuto, M. Hussaini, A. Quarteroni, T. Zang, Spectral methods in fluid dynamics, Springer, New York, 1988.

[3] I. Babuska, M. Suri, The p and hp versions of the finite element method, basic principles and properties, SIAM Review 36 (4) (1994) 578–632.

[4] R. Severn, Inclusion of shear deflection in the stiffness matrix for a beam element, The Journal of Strain Analysis for Engineering Design 5 (4) (1970) 239–241.

[5] J. Reddy, C. Wang, K. Lam, Unified finite elements based on the classical and shear deformation theories of beams and axisymmetric circular plates, Communications in Numerical Methods in Engineering 13 (6).

[6] J. Reddy, On locking-free shear deformable beam finite elements, Computer Methods in Applied Mechanics and Engineering 149 (1-4) (1997) 113–132.

[7] P. Bar-Yoseph, D. Fisher, O. Gottlieb, Spectral element methods for nonlinear spatio-temporal dynamics of an Euler-Bernoulli beam, Computational Mechanics 19 (1) (1996) 136–151.

[8] J. Melenk, On condition numbers in hp-FEM with Gauss–Lobatto-based shape functions, Journal of Computational and Applied Mathematics 139 (1) (2002) 21–48.

[9] J. Maitre, O. Pourquier, Condition number and diagonal preconditioning: comparison of the-version and the spectral element methods, Numerische Mathematik 74 (1) (1996) 69–84.

[10] R. Cook, Concepts and applications of finite element analysis, John Wiley and Sons, New York, 1974.

[11] J. Reddy, An introduction to nonlinear finite element analysis, Oxford University Press, Oxford, UK, 2004.

[12] J. Reddy, On the dynamic behaviour of the Timoshenko beam finite elements, Sadhana 24 (3) (1999) 175–198.

[13] J. Pontaza, J. Reddy, Mixed plate bending elements based on least-squares formulation, International Journal for Numerical Methods in Engineering 60 (5) (2004) 891–922.

[14] Y. Urthaler, J. Reddy, A mixed finite element for the nonlinear bending analysis of laminated composite plates based on FSDT, Mechanics of Advanced Materials and Structures 15 (5) (2008) 335–354.

[15] A. DallAsta, A. Zona, Comparison and validation of displacement and mixed elements for the non-linear analysis of continuous composite beams, Computers and Structures 82 (23-26) (2004) 2117–2130.

[16] P. Lou, G. Dai, Q. Zeng, Finite-element analysis for a Timoshenko beam subjected to a moving mass, Proceedings of the Institution of Mechanical Engineers, Part C: Journal of Mechanical Engineering Science 220 (5) (2006) 669–678.

[17] I. Edem, The exact two-node Timoshenko beam finite element using analytical bending and shear rotation interdependent shape functions, International Jour-

nal for Computational Methods in Engineering Science and Mech 7 (6) (2006) 425–431.

[18] J. Reddy, Theory and analysis of elastic plates and shells, CRC Press, Boca Raton, London, 2006.

[19] N. Eratll, A. Aköz, The mixed finite element formulation for the thick plates on elastic foundations, Computers and Structures 65 (4) (1997) 515–529.

[20] A. Houmat, Hierarchical finite element analysis of the vibration of membranes, Journal of Sound and Vibration 201 (4) (1997) 465–472.

[21] A. Houmat, An alternative hierarchical finite element formulation applied to plate vibrations, Journal of Sound and Vibration 206 (2) (1997) 201–215.

[22] S. Adjerid, M. Aiffa, J. Flaherty, Hierarchical finite element bases for triangular and tetrahedral elements, Computer Methods in Applied Mechanics and Engineering 190 (22-23) (2001) 2925–2941.

[23] O. Beslin, J. Nicolas, A hierarchical functions set for predicting very high order plate bending modes with any boundary conditions, Journal of Sound and Vibration 202 (5) (1997) 633–655.

[24] E. Pereira, J. Freitas, Numerical implementation of a hybrid-mixed finite element model for Reissner–Mindlin plates, Computers and Structures 74 (3) (2000) 323–334.

[25] J. Reddy, An introduction to the finite element method, McGraw-Hill, New York, 1993.

[26] B. Osilenker, Fourier series in orthogonal polynomials, World Scientific Pub Co Inc, NJ, USA, 1999.

[27] J. Han, K. Liew, An eight-node curvilinear differential quadrature formulation for Reissner/Mindlin plates, Computer Methods in Applied Mechanics and Engineering 141 (3-4) (1997) 265–280.

[28] B. Donning, W. Liu, Meshless methods for shear-deformable beams and plates, Computer Methods in Applied Mechanics and Engineering 152 (1-2) (1998) 47–71.

[29] M. Cho, R. Parmerter, Finite element for composite plate bending based on efficient higher order theory, AIAA Journal 32 (1994) 2241–2248.

[30] J. Reddy, On laminated composite plates with integrated sensors and actuators, Engineering Structures 21 (7) (1999) 568–593.

[31] P. Heyliger, J. Reddy, A mixed computational algorithm for plane elastic contact problems. I. Formulation., Comp. Struct. 26 (4) (1987) 621–634.

[32] S. Smith, D. Stolle, A comparison of Eulerian and updated Lagrangian finite element algorithms for simulating film casting, Finite Elements in Analysis and Design 38 (5) (2002) 401–415.

[33] L. Jiang, M. Chernuka, N. Pegg, A co-rotational, updated Lagrangian formulation for geometrically nonlinear finite element analysis of shell structures, Finite Elements in Analysis and Design 18 (1-3) (1994) 129–140.

[34] K. Bathe, S. Bolourchi, Large displacement analysis of three-dimensional beam structures, International Journal for Numerical Methods in Engineering 14 (7) (1979) 961–986.

[35] B. Chattopadhyay, P. Sinha, M. Mukhopadhyay, Geometrically nonlinear analysis of composite stiffened plates using finite elements, Composite Structures

31 (2) (1995) 107–118.

[36] R. Zinno, E. Barbero, Total Lagrangian formulation for laminated composite plates analysed by three-dimensional finite elements with two-dimensional kinematic constraints, Computers and Structures 57 (3) (1995) 455–466.

[37] M. Refaat, S. Meguid, On the elastic solution of frictional contact problems using variational inequalities, International Journal of Mechanical Sciences 36 (4) (1994) 329–342.

[38] P. Heyliger, J. Reddy, On a mixed finite element model for large deformation analysis of elastic solids., Int. J. Nonlinear Mech. 23 (2) (1988) 131–145.

[39] P. Fischer, An overlapping Schwarz method for spectral element solution of the incompressible Navier-Stokes equations, Journal of Computational Physics 133 (1) (1997) 84–101.

[40] J. Heys, T. Manteuffel, S. McCormick, L. Olson, Algebraic multigrid for higher-order finite elements, Journal of Computational Physics 204 (2) (2005) 520–532.

[41] C. Dorao, H. Jakobsen, A parallel time–space least-squares spectral element solver for incompressible flow problems, Applied Mathematics and Computation 185 (1) (2007) 45–58.

[42] B. Jiang, The least-squares finite element method, Theory and Applications in Computational Fluid Dynamics and Electromagnetics, Springer, Berlin, 1998.

[43] J. Lottes, P. Fischer, Hybrid multigrid/Schwarz algorithms for the spectral element method, Journal of Scientific Computing 24 (1) (2005) 45–78.

[44] T. Chan, T. Mathew, Domain decomposition algorithms, Acta Numerica 3 (2008) 61–143.

[45] P. Fischer, N. Miller, H. Tufo, An overlapping Schwarz method for spectral element simulation of three-dimensional incompressible flows, Parallel Solution of Partial Differential Equations, P. Bjorstad and M. Luskin, eds., Springer-Verlag, New York (1999) 45–78.

[46] T. Mathew, Domain decomposition methods for the numerical solution of partial differential equations, Springer Verlag, New York, 2008.

[47] L. Pavarino, Domain decomposition algorithms for the p-version finite element method for elliptic problems, Ph.D. thesis, New York University (1992).

[48] V. Prabhakar, J. Reddy, Orthogonality of modal bases in hp finite element models, International Journal for Numerical Methods in Fluids 54 (11) (2007) 1291–1312.

[49] J. Reddy, D. Gartling, The finite element method in heat transfer and fluid dynamics, CRC Press, Boca Raton, London, 2001.

[50] C. Tong, Q. Ye, Analysis of the finite precision bi-conjugate gradient algorithm for nonsymmetric linear systems, Mathematics of Computation 69 (232) (2000) 1559–1576.

[51] C. Tong, Q. Ye, A linear system solver based on a modified Krylov subspace method for breakdown recovery, Numerical Algorithms 12 (1) (1996) 233–251.

[52] U. Ghia, K. Ghia, C. Shin, High-Re solutions for incompressible flow using the Navier-Stokes equations and a multigrid method, Journal of Computational Physics 48 (3) (1982) 387–411.

[53] J. Pontaza, J. Reddy, Space-time coupled spectral/hp least-squares finite element

formulation for the incompressible Navier–Stokes equations, Journal of Computational Physics 197 (2) (2004) 418–459.

[54] J. Pontaza, Least-squares variational principles and the finite element method: theory, formulations, and models for solid and fluid mechanics, Finite Elements in Analysis and Design 41 (7-8) (2005) 703–728.

[55] K. Kim, K. Leem, G. Pelekanos, M. Song, Algebraic multigrid preconditioner for a finite element method in TM electromagnetic scattering, Journal of Computational Analyis and Applications 4 (3) (2009) 597–605.

[56] T. Mifune, N. Obata, T. Iwashita, M. Shimasaki, A parallel algebraic multigrid preconditioner using algebraic multicolor ordering for magnetic finite element analyses, Proceedings of the International Conference ParCo 33 (2005) 237–244.

[57] J. Meza, R. Tuminaro, A multigrid preconditioner for the semiconductor equations, SIAM Journal on Scientific Computing 17 (1) (1996) 118–132.

[58] T. Chan, B. Smith, Domain decomposition and multigrid algorithms for elliptic problems on unstructured meshes, Electronic Transactions on Numerical Analysis 2 (1994) 171–182.

[59] R. Mertens, H. De Gersem, R. Belmans, K. Hameyer, D. Lahaye, S. Vandewalle, D. Roose, An algebraic multigrid method for solving very large electromagnetic systems, IEEE Transactions on Magnetics 34 (5) (1998) 3327–3330.

[60] F. Saied, G. Mahinthakumar, Efficient parallel multigrid based solvers for large scale groundwater flow simulations, Computers and Mathematics with Applications 35 (7) (1998) 45–54.

[61] R. Chen, K. Tsang, An effective multigrid preconditioned CG algorithm for millimeter wave scattering by an infinite plane metallic grating, International Journal of Infrared and Millimeter Waves 21 (6) (2000) 945–963.

[62] G. Mahinthakumar, F. Saied, Distributed memory implementation of multigrid methods for groundwater flow problems with rough coefficients, Proceedings of the 1996 Simulation Multiconference, New Orleans, LA 51 (1996) 52–57.

[63] L. Shi, Y. Yu, N. Bell, W. Feng, A fast multigrid algorithm for mesh deformation, in: ACM Siggraph 2006 Papers, ACM, 2006, p. 1117.

[64] O. Tatebe, The multigrid preconditioned conjugate gradient method, in: 6th Copper Mountain Conference on Multigrid Methods, Copper Mountain, CO, 1993, pp. 610–621.

[65] P. Wesseling, Introduction to multigrid methods, John Wiley and Sons, Chichester, UK, 1995.

[66] A. Greenbaum, Iterative methods for solving linear systems, Society for Industrial Mathematics, Philadelphia, PA, 1997.

[67] C. Riyanti, A. Kononov, Y. Erlangga, C. Vuik, C. Oosterlee, R. Plessix, W. Mulder, A parallel multigrid-based preconditioner for the 3D heterogeneous high-frequency Helmholtz equation, Journal of Computational Physics 224 (1) (2007) 431–448.

[68] D. Gartling, A test problem for outflow boundary conditions-flow over a backward-facing step, International Journal for Numerical Methods in Fluids 11 (7) (1990) 953–967.

[69] J. Pontaza, J. Reddy, Spectral/hp least-squares finite element formulation for the Navier-Stokes equations, Journal of Computational Physics 190 (2) (2003) 418–459.

[70] P. Nithiarasu, K. Seetharamu, T. Sundararajan, Natural convective heat transfer in a fluid saturated variable porosity medium, International Journal of Heat and Mass Transfer 40 (16) (1997) 3955–3968.

[71] R. Ranjan, J. Irudayaraj, S. Jun, Simulation of infrared drying process, Drying Technology 20 (2) (2002) 363–379.

[72] P. Nithiarasu, K. Seetharamu, T. Sundararajan, Effect of porosity on natural convective heat transfer in a fluid saturated porous medium, International Journal of Heat and Fluid Flow 19 (1) (1998) 56–58.

[73] Z. Guo, T. Zhao, Lattice Boltzmann model for incompressible flows through porous media, Physical Review E 66 (3) (2002) 363–374.

[74] Z. Guo, T. Zhao, Lattice Boltzmann simulation of natural convection with temperature-dependent viscosity in a porous cavity, Progress in Computational Fluid Dynamics, An International Journal 5 (1) (2005) 110–117.

[75] J. Reddy, Penalty-finite-element analysis of 3-D Navier-Stokes equations, Computer Methods in Applied Mechanics and Engineering 35 (1982) 87–106.

[76] T. Basak, S. Roy, A. Balakrishnan, Effects of thermal boundary conditions on natural convection flows within a square cavity, International Journal of Heat and Mass Transfer 49 (23) (2006) 4525–4535.

[77] R. Marshall, J. Heinrich, O. Zienkiewicz, Natural convection in a square enclosure by a finite-element, penalty function method using primitive fluid variables,

Numerical Heat Transfer 1 (1978) 315–330.

[78] D. Davis, Laminar natural convection in an enclosed rectangular cavity(Laminar natural convection in enclosed rectangular cavity, discussing temperature gradient effects), International Journal of Heat and Mass Transfer 11 (1968) 1675–1693.

[79] S. Ravindran, Control of flow separation over a forward-facing step by model reduction, Computer Methods in Applied Mechanics and Engineering 191 (41-42) (2002) 4599–4617.

[80] L. Marino, P. Luchini, Adjoint analysis of the flow over a forward-facing step, Theoretical and Computational Fluid Dynamics (2009) 37–54.

[81] D. Wilhelm, L. Kleiser, Application of a spectral element method to two-dimensional forward-facing step flow, Journal of Scientific Computing 17 (1) (2002) 619–627.

[82] D. Wilhelm, C. Härtel, L. Kleiser, Computational analysis of the two-dimensional–three-dimensional transition in forward-facing step flow, Journal of Fluid Mechanics 489 (2003) 1–27.

[83] J. Largeau, V. Moriniere, Wall pressure fluctuations and topology in separated flows over a forward-facing step, Experiments in Fluids 42 (1) (2007) 21–40.

[84] A. Toshitake, T. Shakouchi, Flow characteristics over forward facing step and through abrupt contraction pipe and drag reduction, Research Reports of Faculty Engineering, Mie University 29 (2004) 1–8.

[85] S. Gandjalikhan Nassab, R. Moosavi, S. Hosseini Sarvari, Turbulent forced convection flow adjacent to inclined forward step in a duct, International Journal of

Thermal Sciences 48 (7) (2009) 1319–1326.

VITA

Rakesh Ranjan was born in a small town in (then) Bihar, Ranchi. He joined the Indian Institute of Technology (IIT), Kharagpur in 1995. He graduated from IIT, Kharagpur in 1999, with a undergraduate degree (with Honors) in agricultural engineering. He joined the Pennsylvania State University, University Park, for a masters in agricultural engineering in August 1999. The main idea of his masters work was in mathematical modelling of coupled partial differential equations for simulating transient infrared and convective drying of food materials. He defended his masters thesis on March 27th, 2001.

After a short stint as a software engineer working for a software company in Natick, MA, he worked for a consulting civil engineering company in Pennsylvania from September 2001 through June 2006. From August 2006, he started his Ph.D. program in the Mechanical Engineering Department at Texas A&M University. He defended his Ph.D. on November 2, 2009.

Rakesh Ranjan may be contacted at the email address: ranrakesh@gmail.com, or through Prof. J.N. Reddy at the Mechanical Engineering Department, 3123 TAMU, Texas A&M University, College Station, TX 77843-3123.

This document was typeset in LaTeX by Rakesh Ranjan.